Department of Physics
Indian Institute of Technology Guwahati
Ph.D. Thesis


# Development of Hydroxyapatite based ceramic composites and thin films for biomedical applications

Mr. Apurba Das

**Thesis Supervisor:** Prof. Pamu Dobbidi

March, 2022.

# Development of Hydroxyapatite based ceramic composites and thin films for biomedical applications

*A Thesis submitted for the award of the degree of*
*Doctor of Philosophy in Physics*
*by*

**Mr. Apurba Das**

Thesis Supervisor: **Prof. Pamu Dobbidi**

**Department of Physics**
**Indian Institute of Technology Guwahati**
**Guwahati - 781039, Assam, India**

**March, 2022**

# Statement

This thesis work entitled "**Development of Hydroxyapatite based ceramic composites and thin films for biomedical applications**" has been carried out in the Department of Physics, Indian Institute of Technology Guwahati, India by me under the supervision of Prof. Pamu Dobbidi. The material of this thesis has not been submitted elsewhere for any other degree. Works presented in the thesis are all my own unless the reference is cited in the text.

(Mr. Apurba Das)
March, 2022
Department of Physics
Indian Institute of Technology Guwahati
Guwahati - 781039, India

# Disclaimer

The bibliography included in this thesis is by no means complete but contains the ones consulted thoroughly by me. I apologize for involuntarily missing out on some of the research papers, review articles, and other scientific documents pertaining to the focus of this thesis, which should also have been cited. For illustration purposes, some of the figures in this thesis are taken from other sources and properly cited.

# Certificate

It is certified that the work contained in the thesis entitled "**Development of Hydroxyapatite based ceramic composites and thin films for biomedical applications**" by Mr. Apurba Das (Roll no.-166121008), a Ph.D. student in the Department of Physics, Indian Institute of Technology Guwahati is carried out under my supervision and has not been submitted elsewhere for the award of any other degree.

(Dr. Pamu Dobbidi)
March, 2022
Professor
Department of Physics
Indian Institute of Technology Guwahati
Guwahati - 781039, India

*The thesis is dedicated to Deuta*

*Ma*

*Maina*

*and Gz*

*...*

# Acknowledgement

First and foremost, I would like to express my deepest gratitude to my mentor Prof. Pamu Dobbidi for his continuous guidance and support. In particular, he is acknowledged for teaching me how to proceed in research and developing the most needed patience. I also acknowledge my Doctoral committee members: Prof. S Ravi (Chairman), Prof. S Kanagaraj, and Dr. U N Maiti for their valuable time, insightful remarks and suggestions at every point in time. I also acknowledge all my collaborators, Dr. Lalit M Pandey, and Dr. B L Chittari for the numerous insightful discussions around the clock. It was a great experience working with them, and I have learned a lot from them.

Acknowledgements are also due to Dr. M Ravi Sankar, who had been instrumental in providing various lab support. I also thank all HoDs (Prof. Poulose Poulose, Prof. Subhradip Ghosh, and Prof. Perumal Algarsamy) for the opportunity to work in the department and pursue my research career. I am also grateful to the faculty members of the department of Physics, the technical staff, the academic and non-academic staff of the department, who helped me in multiple ways during my research. It was a great experience interacting with them, and their suggestions indeed helped me to pursue my career. I specially thank Dr. Sidananda Sarma, Basab-da, Aditya-da, Atul-da, Lokesh-da, and Hemanta-da for their support in different research and computer-related issues.

The financial support for the thesis work is provided by the Indian Institute of Technology Guwahati, and Ministry of Human Resource and Development, Government of India. I also acknowledge the facilities provided by Science and Engineering Research Board (SERB), Department of Science and Technology under grant no. CRG/2019/006650. The characterization facilities provided by the Central Instruments Facility, Indian Institute of Technology Guwahati, Centre for Nanotechnology, Indian Institute of Technology Guwahati, and the XRD facility provided by DST, New Delhi, through the FIST program [SR/FST/PSII-020/2009], is also highly acknowledged.

I would also like to acknowledge my Seniors, Dr. T. Santhosh, Dr. P. Mahesh, Dr. Srinivas Pattipaka, Dr. Rasmi R. Behera, Dr. Bipul Deka, Dr. Prahlad Baruah, Dr. Gyan P Bharti, Dr. Rahul Kesarwani, Dr. Pratap Behera, Dr. Viswajit, Dr. Sanjib K Nayak, Dr. Pallabi Gogoi, and Dr. Bibhuti B Dash, for being available at any time and for any discussion. I also like to express my sincerest gratitude to Dr. Ranjan Kalita and Dr. Indu K Dihingia, who has been my source of inspiration and guidance. Special thanks are due to Susmita-ba, Varun-bhaiya, Aman, Rushikesh, Vivek, Anupama, Prajna, Shashi, Sweety, Radhe Shyam, Deepak, Spandana, Bedatrayee, and Konica. Without their help and support, the thesis would have never been completed. I would also acknowledge my juniors Radhika, Karishma, Sunil, and Subingya, for their helping hands and support. I am fortunate enough to have a great friend circle, seniors like Nagendra-bhaiya, Joy-da, Jagan-bhaiya, Karuna-da, Ritupan, Nilamoni, Kajal, Abhishek, Abhilasha, Harish, Pintu, Suman, Akangshu, Debabrat, Rajnandan, Ardhendu-da, Jnanendra-da, Bidyut-da, etc. I thank all of them for their help in shaping my thesis in its current form.

Finally, I thank all of my family members, my nearest and dearest ones, for their constant and rock-solid support and caring about my well-being.

Apurba Das

# Abstract

Hydroxyapatite ($Ca_{10}(PO_4)_6(OH)_2$, HAP) is an immensely favored biomaterial in the biomedical industry, known for its extensive applications in orthopedics and dentistry. Naturally, it appears as an inorganic constituent of natural bones, with substitutions like $Mg$, $Sr$, and other trace ions occupying the $Ca$ sites. To distinguish it from HAP, it is often designated as bone-like apatite or bone apatite in brief. Consequently, it can be perceived that the $Ca/P$ ratio of bone apatites differs from HAP (1.67 for HAP, whereas a ratio $< 1.67$ is obtained for bone apatite). The last two decades have seen an exponential rise in the biomedical industry related to HAP primarily due to its incredible biocompatibility, affinity to bond to living bones when used as implants, and its ability to promote ingrowth of new bones through osteoconduction without having any toxic or inflammatory response to the surrounding tissues. As a testimony to the claim, the recent reports published in Yahoo finance claimed that the HAP market is projected to grow from USD 2.2 billion (currently in 2020) to USD 3.1 billion in 2025 at a compound annual growth rate (CAGR) of 6.8%. It has been forecasted that the Asia-Pacific HAP market will grow at the highest CAGR precisely due to the increase in medical tourism in countries like India, South Korea, and Japan. It has led to the rapid development of the domestic health care sector and is an indicator for exhaustive research in HAP to develop devices and technologies to cater to growing medical tourism.

HAP has an exciting crystal structure. The non-stoichiometric composition with substitutions like $Mg$, $Sr$, and other trace ions as impurities are found to crystallize into the hexagonal ($P6_3/m$) structure. Stoichiometric HAP reportedly crystallizes in the monoclinic structure ($P2_1/b$). The difference between the two structures lies in the arrangement of the $OH$ group inside the crystal lattice, with the hexagonal crystal lattice containing a disordered arrangement of the $OH$ group, resulting in the dipoles generating a "para-electric-like" arrangement. However, the monoclinic structure distinguishes by forming an ordered array of the $OH$ group so that the $OH$ dipoles along the [101] planes are all arranged in the same direction. The dipoles along the [010] planes are directed opposite, thus generating an "anti-ferroelectric-like" arrangement. Synthetically derived HAP is a polymorph containing contributions from the monoclinic and hexagonal phase in quantities that vary concerning the synthesis conditions. There is an exciting but unending debate regarding the crystal structure of HAP in literature. The starting point of the discussion relates to the association of non-linear electrical properties to HAP. It has been mentioned

previously that natural bones display piezoelectricity and ferroelectricity. These properties are understood to be due to the collagen molecules that comprise the organic constituent of the natural bones. Researchers were convinced that synthetic HAP could be associated with non-linear electrical properties. However, the existence of symmetry in the crystal structures (both $P6_3/m$ and $P2_1/b$) restricted the association. Physicists have made many efforts, primarily theoretical, to associate a different crystal structure with synthetic HAP. It was argued that the space group P21 is a possibility in HAP, which can be accounted for piezoelectricity and ferroelectricity. However, the experimental evidence by most of the researchers still supports the existence of space groups $P6_3/m$ and $P2_1/b$. A solid conclusion is yet to be arrived at, and primarily, these differences exist due to the inherently complex crystal structure HAP. Moreover, synthetic HAP is highly sensitive to the preparation conditions, and a slight deviation of the experimental conditions leads to changes in its properties. In conclusion, it can be said that a great deal of effort is still required for reconciling the debate.

The last few decades have seen an increasing interest in exploring the electrical properties of HAP. The interest has been driven by the association of electrical properties of biomaterials with their biological performance. In many instances, the electrical properties have been shown to augment the biological properties of the biomaterials under *in-vivo* environment. Several efforts to modulate the electrical properties have been reported in the literature. One way to do so is by considering the composite of HAP with other components with improved electrical properties. In medical applications, the implanted biomaterials have to endure several challenges to function desirably for intended applications. The implants specially designed for load-bearing should handle compression and shear forces under normal loading conditions. Additionally, they must sustain the corrosion resistance, hardness, aging resistance against the harsh *in-vivo* conditions inside the human body. These properties must be supplemented with biocompatibility, osseointegration, and osteoconductivity to function as a biomaterial properly. It is a difficult task for a single component ceramic to possess all these properties. The biological properties of HAP are superior to most bioceramics; however, poor mechanical properties like fracture toughness, lower Young's modulus, hardness, tensile strength, etc., limit its load-bearing applications. Improving the mechanical properties by retaining the biological properties of HAP can be accomplished by fabricating a ceramic composite of HAP with other ceramic composites that have superior mechanical properties. In terms of electrical properties, the $\epsilon_r$ of HAP is on the lower side ($\sim$5-10 at 1

MHz). As mentioned previously, such a lower $\epsilon_r$ is less valuable if we intend to design implants that can harness the external electric stimulations. The electrical properties can be improved to the desired level by considering composites with a suitable ceramic. A ceramic composite enables the tailoring of properties to suit any application. Sometimes, ceramic composites exhibit properties that are superior to their constituents and can be a boon in several applications.

On similar lines, thin films of HAP have been researched considerably for developing coatings useful in biomedical implants. $Ti$ or its alloys are used for designing the implants due to their biocompatibility, osseointegration abilities, higher strength to weight ratio, and ability to resist corrosion. However, many instances have reported implants loosening due to poor bonding to the host, primarily due to the formation of layers of fibrous tissue at the skeletal tissue/device interface. To do away with the failures, the commonly adopted techniques employ a surface modification of the $Ti$ or $Ti$ alloy implants using several techniques. Biomedical implants are coated with a bioactive layer such as HAP or $CaPO_4$, which readily improves the implants' bond strength and stability, leading to the prolonged service life of the implants. Many techniques have been developed for surface modification of the implants. Among them, biomimetic coating of HAP using chemical route, sol-gel based coating technique, plasma spraying, thermal spraying, electrophoretic deposition, radio frequency (RF) sputtering, and pulsed laser techniques have been reported in the literature. However, the plasma spraying is the only process recognized by the Food and Drug Administration (FDA), USA, for coating biomedical implants. The coating quality in plasma spraying is significantly better than the chemical deposition techniques, making it widely acceptable for commercialization. However, even this technique is not free from shortcomings such as the introduction of impurity phase, limited crystallinity, poor uniformity in the thickness, and low adhesion (although higher than the chemical deposition techniques, it is still on the lower side for achieving the best response). Over the years, several improvements and modifications in the plasma spraying techniques have addressed these issues. Still, other methods are far better and more robust in terms of the properties of the coated layer. The physical vapor deposition (PVD) techniques offer a substantial advantage in terms of the adhesion strength, uniformity of coatings, and the crystallinity of the coated layer. Also, the benefit of coating any complex layer, whether compound, multilayer, insulators, or metallic, can be achieved through the PVD techniques. In this direction, we would focus on the RF sputtering technique, which is a versatile technique to coat biomaterials. It has been previously pointed

out that the trend in biomaterials research is to obtain electrically active coatings that augment the biological properties of such implants. A significant criterion for displaying electrical properties is related to the density of the coating, which has to be significantly high for obtaining superior properties. RF magnetron sputtered coatings have proven to be highly efficient for such purposes. In terms of the coating uniformity and adhesion, the technique is significantly superior to most other processes reported previously. The features for controlling the deposition temperature during the sputtering process allow the phase present in the sputtering target to be transferred to the thin films. This particular feature is unlike plasma spraying. Due to the very high deposition temperature generation, there is a phase evolution from HAP to $\beta$-tricalcium phosphate ($\beta$-TCP), adversely affecting the implants' overall stability and service life. HAP amongst the $Ca-P$ family is known to be the highly crystallized form with the lowest dissolution rate. $\beta$ or $\alpha$-TCP has a significantly higher dissolution rate and is formed due to the loss of the $OH$ group from HAP due to high temperature during synthesis. As of now, there is no known process to control the degree of $\beta$ or $\alpha$-TCP in HAP, and avoiding its formation is considered the best way to retain the stability and integrity of the thin films. Resorting to sputtering provides the best possible alternative to plasma spraying under such circumstances. However, commercialization of the method is yet to be seen, but a change in the perspective is inevitable in the recent future.

Thesis overview:

In this thesis, we reported the synthesis of HAP; we have explored its properties, especially the electrical properties such as the variation of $\epsilon_r$ and conductivity concerning temperature and frequency. We extend our understanding of HAP to prepare ceramic composites of HAP and $SrTiO_3$ (ST) to improve its electrical properties and investigate the biological response of the prepared ceramic composite. We approach the problem by considering a series of composites of varying concentrations of HAP and ST. Thereby, we identify the composite displaying substantially better properties based on the careful investigations of the biological and electrical properties. Subsequently, we introduce the $Ba$ component in ST, leading to the ceramic $Ba_{0.5}Sr_{0.5}TiO_3$ (BST). We found the excellent biological response of ST and ST-based composites, and we expected that the introduction of $Ba$ would enhance the properties of the composites manifold. The same approach of preparing a series of composites was adopted, which led to the identification of the composite blended with the best biological and electrical properties. The results were exciting, and afterward, we have developed scaffolds from the previously identified best compos-

ites of the BST and ST series and probed their biological response to determine their suitability in tissue engineering applications. Finally, we developed coatings over $Ti$ substrate from the identified best composite of ST and HAP series using RF magnetron sputtering. We fabricated our in-house sputtering target, developed a series of thin films of various thicknesses, and probed their preliminary biological and electrical properties. Based on the analyses, we were able to identify the thickness with optimized properties that would be suitable for coating implants, and would be used for bioelectronics and orthopedics applications. We also deposited bilayered coatings of HAP and BST over $Ti$ implants, to understand the usefulness of bilayers in orthopedic or dental applications. We have analyzed the bilayered films' interfacial, electrical, and biocompatibility aspects that helped us understand the properties from a broader perspective. The sole aim had been to understand the importance of electrical properties, which highly augments the biological properties, resulting in enhancing the service life of the implants or any gadgets used in biomedical applications. In this thesis, we have made a humble effort to adopt the already existing methodology of impedance spectroscopy in biomaterials research to composites, which have shown tremendous potential for biomedical applications. The thesis comprises seven working chapters. The preliminary five chapters are committed to understanding the composites' basic properties. The sixth chapter highlights applying these understanding to plausible devices for prospective clinical usage in the near future. A chronological description (in brief) of each chapter is included below. The seventh chapter gives the summary and future scope of the work.

Chapter 1 provides a general overview of the thesis and a general introduction to the research problem. We also discuss the preparation methodology of the monoliths and discuss the characterization techniques in detail. In brief, we prepare HAP using the sol-gel technique, and the ST and BST have been prepared using the solid-state reaction methodology. Once the monoliths are ready, the composites are prepared by mixing the monoliths in different compositions. These composites are then characterized using different techniques for understanding their microstructural, electrical, and biological properties. The microstructural techniques include X-ray diffraction (XRD), Field emission scanning electron microscopy (FESEM) and Field emission transmission electron microscopy (FETEM). The study of electrical properties includes the variation of $\epsilon_r$ with respect to temperature and frequency and understanding their loss mechanisms. The study of biological properties includes understanding the protein adsorption behavior, cytocompatibility, and finally, the

bioactivity of the specimens.

In chapter 2, a discussion on the preparation methods and characterization techniques adopted in the thesis for preparing the monoliths, composites, sputtering target, and thin films are discussed elaborately.

In chapter 3, we study in detail the preparation methodology of HAP and focus on extracting its physiochemical properties. We find that synthetically derived hydroxyapatite, HAP, exists in the hexagonal phase where the adjacent $OH$ groups point opposite each other. The $OH$ group pointing in the same direction forms a monoclinic phase. The different pointing directions of the two phases show variations in physicochemical properties. The hurdle in obtaining the single crystals of such complex HAP results in most conventional synthesis methods producing the polymorphic phases that often show promising properties over the single crystals. We present a detailed temperature-dependent structural evolution of the synthetically derived polymorphic phase of hydroxyapatite (HAP). As prepared samples of HAP using the sol-gel method at room temperature showed the polymorphic phase of monoclinic and hexagonal symmetries. The prepared samples show the monoclinic phase with a vol.% of 45.94% at 303 K. When subjected to the temperature, HAP predominantly shows the monoclinic phase vol.% of 57.77% at 573 K. The dominant growth of single-phase in HAP lead to the monotonic $OH$ group reorientation with the temperature. From micro Raman spectroscopy, we confirm the reorientation of the $OH$ group with changes in the vibrational spectra.

Additionally, a detailed study of the temperature-dependent optical properties of HAP reveals the presence of defects, which endows it with photoluminescence properties (PL), and the results correlated the bandgap calculations ($E_g \sim 3.91$eV). The PL studies revealed that HAP specimens have positive thermal quenching (PTQ) behavior that resulted from the defect transitions from a radiative to a non-radiative state. By deconvoluting the PL spectra, it is established that the intensity of the PL spectra peaks in the orange emission (approximately $\sim$ 630 eV) and are consequences of deep level defects near the center of the forbidden region. Further, the dielectric spectroscopy is used to attribute the $OH$ ions orientation; the calculated activation energy is in the range of rotational transformation of $OH$ ions. The temperature tunable polymorphic HAP exhibit different physical properties that can have applications in bioimaging and biomedical devices.

In chapter 4, we discuss the interplay of structural, electrical, and surface properties in determining the collective behavior of HAP and ST composites. Synthesizing the monoliths by sol-gel (HAP) and solid-state reaction (ST), respectively, they are

mixed in different At.% (20, 40, 60, and 80 At.%) to prepare a series of composites. The prepared composites are subjected to X-ray diffraction and Raman analysis to probe the microstructural aspects. The analysis revealed no evidence of a phase that the reaction between the two monoliths might form. The crystallite sizes are in the range of 27.2-37.3 nm, and it increases with the content of ST in the composites. The Raman analysis revealed crucial information about the presence of rutile $TiO_2$ that is later found to be the link in displaying bone-like apatite nucleation ability in the monolith ST and its composites. The FESEM analysis revealed that the grain sizes are between the monoliths (64 nm-144 nm) and are found to follow a trend similar to the crystallite size. The variation in $\epsilon_r$ with the temperature ranges from 5-35 (1 MHz) at 310 K for all the specimens. The dependence of $\epsilon_r$ on the grain size of the composites follows a nearly exponential relation. The bone-like apatite forming ability of the composites is studied by incubating the specimens in simulated body fluid (SBF). Additionally, selected specimens' cytocompatibility (MG63 cell lines), and protein adsorption (bovine serum albumin, BSA) are also studied to comprehensively understand the delicate relationship between the electrical and biological properties. The protein adsorption is primarily related to the surface charge, and its dependence is found linear.

Additionally, the $\epsilon_r$ of the composites is less than 35, which compliments the protein adsorption behavior of the specimens. The amount of adsorbed protein for all the specimens considered in the present study lay in 3-32 $\mu$g/ml. Furthermore, the specimens exhibited excellent cell viability of more than 90%. Based on the physical and biological investigations, $20H - 80S$ is the best specimen that blends the characteristic feature of both monoliths. We also present the conductivity ($\sigma$) analysis of the composite specimens that are crucial to relate the biological properties with the electrical properties of the composites. The $\sigma$ is very low ($\sim 10^{-8} S/cm$), and the porous structure of the composites revealed from the micrographs is one of the factors for such low $\sigma$. From a plethora of conduction mechanisms, Motts' variable range hopping (VRH) conduction is projected as the most appropriate mechanism that appropriately describes the conduction process in the composites. Mott's VRH is also related to the polarization mechanism associated with the development of electrets. The study points towards the practical potential of applying the designed bio-composites in generating bio-electrets or understanding the electrical properties at the forefront of research in developing electro-active smart scaffolds for bone tissue engineering applications.

Chapter 5 investigates electrically active ceramic composite of HAP and BST

for biomedical applications. Based on the studies conducted in the previous chapter on HAP and ST-based composites, this chapter goes a step ahead by introducing $Ba$ in ST. Similar to the approach adopted previously, the chapter proceeds by fabricating a series of composites, focusing on the dielectric and biological properties and their relationships. The article primarily emphasized extracting the $\epsilon_r$ of the specimens (that lay in the range of 3-65) and related them to microstructural properties like the grain size and At.% of BST. A broad outlook on the importance of $\epsilon_r$ in determining the suitability of bioceramics for clinical applications is presented. Bioactivity analysis of the specimens led to probing the negative surface charges, and it was found crucial to the growth of dense apatite layers. Furthermore, the cytocompatibility of the specimens displayed cell viability above 100% for day 1, which increased substantially for day 3. Protein adsorption studies using BSA and fetal bovine serum (FBS) were carried out to reveal other biological properties of the composites. Electrostatic interactions govern the adsorption, and the mathematical dependence on surface charges is linear. The protein adsorption is also linearly correlated with the $\epsilon_r$, intrinsic to the biomaterials. We delve deeper into protein-biomaterials interactions by considering the evolution of the secondary structure of BSA adsorbed into the specimens. Based on the investigations, 20 At.% HAP-80 At.% BST ($20H-80B$) was established as a suitable composite comprising the desired features of HAP and BST. Such explorations of electrical and biological properties are interesting for modulating the behavior of bioceramic composites. The results project the suitability of $20H-80B$ for designing electrically active innovative scaffolds for the proposed biomedical applications and are expected to incite further clinical trials. Furthermore, electrical modeling of the ceramic composites is done using the Cole-Cole formalism. The $\sigma$ mechanisms of the composites are also analyzed, and Mott's VRH conduction is the most appropriate formalism that successfully describes the conduction process. The established Mott's VRH is also related to the polarization mechanisms active in the specimens. The study projected an exciting correlation between the electrical and biological properties from the perspective of impedance spectroscopy that will be helpful for biomaterials research.

Chapter 6 has three components, the first part of the chapter deals with the fabrication and analysis of the properties of scaffolds designed explicitly for bone tissue engineering applications. We discuss the fabrication, microstructural analysis, mechanical and biological properties of scaffolds synthesized from composites $20H-80S$ and $20H-80B$. The compositions were endowed with significantly bet-

ter properties, as evident from the studies conducted in the previous chapters. The microstructural analysis reveals the presence of reflections from both the monoliths and smaller-sized grain in $20H-80S$ ($92.2 \pm 4.5$ nm). $20H-80B$ has a higher grain size ($110.3 \pm 5.1$ nm) and higher porosity, and its biomineralization capability ($Ca/P-1.64$) is found higher compared to $20H-80S$ ($Ca/P-1.52$). The higher porosity is also reflected in high protein adsorption on 20H-8B. The scaffolds' cytocompatibility revealed cell viability $> 90\%$ for the entire period analyzed in the experiment.

The second part, deals with the thin films prepared from the $20H-80S$ composite sputtering target on $Ti$ substrates. We developed three thickness variations of $20H-80S$ thin films. The preliminary studies of the thin films establish that thicker composite films have improved microstructural properties. The films were found to be cytocompatible with improved cell viability of more than 100 % for all the films, which is desirable for inducing various metabolic reactions *in-vivo*. The electrical properties of the thin films are probed by considering the frequency and temperature variation of the dielectric properties. The improved dielectric properties of the thin films augment the biological responses of implants by enabling expedited healing. The mechanism is related to the polarization of the dipoles that forms an exciting study, elaborated in the chapter. Also, associated with the polarization are the loss mechanisms that continuously disrupt the polarization, hindering the faster healing process of bone fractures. A comprehensive analysis of such loss mechanisms is detailed in the chapter. The study on $20H-80S$ composite films closes with the electrical blueprint of the thin films in the form of a parallel QR circuit (Q denoting constant phase element and R the resistor) obtained by Cole-Cole analysis. Understanding the electrical properties from the biological perspective makes the article interesting. It provides fresh insights on the behavior of thin films for designing bioelectronics gadgets and electro-active implants.

The third part of the chapter deals with bilayered thin films of BST and HAP. On $Ti$ substrate, we develop layered thin films (of 100 nm each) so that we deposit HAP films first followed by BST in one set of thin films, and the other set deposits BST on the bottom followed by HAP top layer. From a biological perspective, the films were bioactive, hydrophobic, and cytocompatible. The dielectric properties of the films displayed a modest $\epsilon_r$ in the range of 35-45. The article relied on the external stimulations used for treating fractures to divulge the relation between electrical and biological properties. The coatings (associated with the implants) were dielectric; they inherently underwent polarization under the electric field. This polarized field

continued to generate the electric field *in-vivo* even after the removal of the external field. Furthermore, the leakage current in the films unveiled a new way to choose the exposure parameters (of the external stimulations) meticulously based on the properties of the films to minimize the fracture healing time.

Chapter 7 presents the future work and directions that we can adopt in the future to carry out our research. We present a short discussion on how we can carry forward our products for *in-vivo* testing and finally marketing our products to the industry. Several processes are detailed, leading to the realization of our products into the market.

# List of Publications

## Refereed Journal Publications

(1) A. Das, and P. Dobbidi, Materials Science and Engineering C, **101**, 7 (2019).

(2) A. Das, and P. Dobbidi, ACS Biomaterials Science and Engineering, **7**, 2296 (2021).

(3) A. Das, A. Bhardwaj, S. Rabha, L. M. Pandey, A. Deoghare, and P. Dobbidi, Journal of the American Ceramic Society, **105**, 1790 (2022).

(4) A. Das, and P. Dobbidi, ACS Omega, **6**, 25916 (2021).

(5) A.Das, E. Barua, S. K. Mushahary, A. Bhardwaj, V. Saxena, L. Pandey, A. Deoghare, and P. Dobbidi, Materials Letters, **304**, 130668 (2021).

(6) A.Das, P. Dobbidi, A. Bhardwaj, V. Saxena, and L. M. Pandey, Scientific Reports, **11**, 22304 (2021).

(7) A. Das, V. Saxena, A. Bhardwaj, S. Rabha, L. M. Pandey, and P. Dobbidi, Surfaces and Interfaces, **31**, 102063 (2022).

(8) A. Das, A. K. Chikkala, G. P. Bharti, R. R. Behera, R. S. Mamilla, A. Khare, and P. Dobbidi, Journal of Alloys Compounds, **11**, 22304 (2021).

(9) A. Das, S. Kornepati, J. Rabha, and P. Dobbidi, AIP Conference Proceedings, **2115**, 030053 (2019).

## Patents

(1) "Hydroxyapatite (HAP) comprising of mixed polymorphs of monoclinic and hexagonal phases obtained by sol-gel process", Apurba Das, and Pamu Dobbidi, Indian Patent Application No. **202031029208** dated **09/07/2020**.

(2) "Synthesis and processing of ST sputtering target material to obtain single phase thin films", Pamu Dobbidi, Susmita Rabha, and Apurba Das, Indian Patent Application No. **202131004326** dated **01/01/2021**.

## Publications not related to Thesis

(1) R. Shyam, D. Negi, M. Gupta, P. Vasistha, G. Gupta, A. Das, P. Dobbidi, K. Awasthi, and S. R. Nelamarri, Applied Surface Science, **575**, 151794 (2022).

(2) R. K. Behera, A. Das, A. Hasan, D. Pamu, L. M. Pandey, and M. R. Sankar, Journal of Alloys Compounds, **842**, 155683 (2020).

(3) E. Barua, A. Das, D. Pamu, A. B. Deoghare, P. Deb, S. D. Lala, and S. Chatterjee, Ceramics International, **45**, 26265 (2019).

(4) R. Shyam, D. Negi, M. Gupta, P. Vasistha, G. Gupta, A. Das, P. Dobbidi, K. Awasthi, and S. R. Nelamarri, Applied Physics A, **126**, 1 (2022).

(5) R. Shyam, A. Das, P. Dobbidi, F. Singh, P. Vasistha, G. Gupta, and S. R. Nelamarri, Journal of Alloys and Compounds, **823**, 153794 (2020).

(6) V. S. Yadav, A. Kumar, A. Das, D. Pamu, L. M. Pandey, and M. R. Sankar, Materials Letters, **270**, 127732 (2020).

## Under Review/Just Accepted

(1) A. Das, P. Dobbidi, and B. L. Chittari, ***Defect dynamics, origin of photoluminescence and temperature dependent OH dipoles orientation in synthetically derived Hydroxyapatite,*** Under review Physical Review Materials.

(2) A. Das, S. Rabha, V. Saxena, A. Bhardwaj, L. M. Pandey, K. A. Emmanuel, and P. Dobbidi, ***The role of electrical property in determining the response of 20H-80S composite thin films fabricated for biological applications,*** Just accepted in Journal of Materials Science.

## Workshops/Conferences attended

(1) *Introduction to MATLAB,* **Indian Institute of Technology Guwahati**, Guwahati, India, 10 August, 2019.

(2) *63rd DAE Solid State Physics Symposium,* **Guru Jambheshwar University of Science and Technology**, Haryana, India, 18-20 December, 2018.

(3) *International Conference on Nano Science and Technology (ICONSAT-2020),* **S. N. Bose National Centre for Basic Science**, Kolkata, India, 5-7 March, 2020.

(4) *North-East Atmospheric Radar Workshop (NEAR-2019),* **Indian Institute of Technology Guwahati**, Guwahati, India, 8-9 August, 2019.

(5) *International Conference on Advanced Ceramics and Nanomaterials for Sustainable Development (ACEND-2018),* **Christ University**, Bangalore, India, 19-21 September, 2018.

(6) *Nanomaterials and Smart Devices,* **Indian Institute of Technology Guwahati**, Guwahati, India, 17-21 September, 2018.

(7) *International Conference on Sophisticated Instruments in Modern Research (ICSIMR-2017),* **Indian Institute of Technology Guwahati**, Guwahati, India, 30 June-13 July, 2017.

(8) $2^{nd}$ *International Conference on Nano Science and Engineering Applications-2018,* **Jawaharlal Nehru Technological University Hyderabad**, Hyderabad, India, 04-06 October, 2018.

(9) *One-Day Workshop on Vacuum Technology and its Applications in Optical Science,* **Indian Institute of Technology Guwahati**, Guwahati, India, 19 August, 2019.

(10) *One-Day Workshop on Vacuum Technology and its Applications in Optical Science,* **Indian Institute of Technology Guwahati**, Guwahati, India, 19 August, 2019.

(11) *Research Conclave-2018,* **Indian Institute of Technology Guwahati**, Guwahati, India, 8-11 March, 2018.

# Contents

# List of Figures

# List of Tables

# List of Symbols

| | |
|---|---|
| $\epsilon_r$ | Dielectric constant |
| GPa | Giga Pascal |
| MPa | Mega Pascal |
| m | Meter |
| $\mu$m | micrometer |
| $d_{33}$ | Piezoelectric constant |
| pC/N | Pico Coulomb per Newton |
| S/cm | Siemens per centimeter |
| nm | Nanometer |
| $Ti$ | Titanium |
| $Ti-6Al-4V$ | Titanium alloy (90% $Ti$, 6% $Al$, 4%$V$, 0.25% $O$, 0.25% $Fe$) |
| MG63 | osteoblastic cell-line |
| SaOS2 | Human osteosarcoma cell-line |
| h | hour |
| K | Kelvin |
| s | Second |
| min | Minutes |
| rpm | Revolutions per minute |
| mm | Millimeter |
| cm | Centimeter |
| mbar | Millibar |
| $\sigma$ | Conductivity |
| $\rho$ | Resistivity |
| $\zeta$ | Decay length of localized wave function |
| $\alpha^{-1}$ | Decay length of localized wave function |
| $k_B$ | Boltzmann constant |
| $E_a$ | Activation energy |

| | |
|---|---|
| Hz | Hertz |
| kHz | Kilo Hertz |
| $\theta$ | Bragg's angle |
| $D$ | Crystallite size |
| $^{\circ}$ | Degree |
| $\mathring{A}$ | Angstrom |
| hkl | Miller indices |
| $Cu$ | Copper |
| $Ni$ | Nickel |
| $K_{\alpha}$ | X-ray radiation (Siegbahn notation) |
| $K_{\beta}$ | X-ray radiation (Siegbahn notation) |
| $E_g$ | Bandgap |
| eV | Electron volt |
| $\lambda$ | Wavelength of X-ray |
| mL | Millilitre |
| $\nu_1$ | Raman mode in $(PO_4)^{3-}$ group |
| $\nu_2$ | Raman mode in $(PO_4)^{3-}$ group |
| $\nu_3$ | Raman mode in $(PO_4)^{3-}$ group |
| $\nu_4$ | Raman mode in $(PO_4)^{3-}$ group |
| $tan\delta$ | Loss factor |
| $Ar$ | Argon |
| $N(E_F)$ | Density of states |
| $R$ | Hopping length |
| $W$ | Hopping energy |
| $mV$ | Decay length of localized wave function |
| Q | Constant phase element |
| $Ca$ | Calcium |
| $Ba$ | Barium |
| $Sr$ | Strontium |
| $P$ | Phosphorous |
| mJ | Millijoule |
| mg | Milligram |
| kV | Kilovolt |
| $\mu$A | Microampere |

# Chapter 1

# Introduction

.

This chapter provides the motivation for carrying out the thesis work. By a careful literature survey, the chapter discusses the subtle literature gaps that inspired us to carry out the research work.

## 1.1 Brief overview of Biomaterials

Leading experts in the field of biomaterials science have defined the term "biomaterials" as: "A material intended to interface with biological systems to evaluate, treat, augment or replace any tissue, organ or function of the body" [1]. However, a broader definition was introduced by Williams *et al.* [2] wherein the term has been redefined to: "A biomaterial is a substance that has been engineered to take a form which, alone or as part of a complex system, is used to direct, by control of interactions with components of living systems, the course of any therapeutic or diagnostic procedure in human or veterinary medicine." The history of biomaterials dates back to antiquity when Egyptians used sutures for stitching wounds that were designed from animal sinew. In the current state, biomaterials research lies at the intersection of medicine, chemistry, biology, physics, and more recently, tissue engineering and materials science. The state-of-the-art biomaterials research embodies smart, functional biomaterials that can provide specific bioactive signals to modulate their immediate biological environment for materials integration and wound healing. These materials can be metals, polymers, or ceramics. Ceramics, predominantly bioceramics, for instance, can function as joint or tissue replacements,

Part of this chapter is published in A. Das, and P. Dobbidi, Materials Science and Engineering C **101**, 539 (2019)

coatings of metallic implants as well as feature as drug delivery agents to cancerous cells [3–18].

The design of a biomaterial largely depends on the area of its application. For effectively functioning as a biomaterial, a material should possess properties that include biocompatibility, bio-inertness, bio-functionality, and most importantly, the material should not induce any form of toxicity or inflammatory response to the receptor. The range of applications of biomaterials can be diverse. Undoubtedly, the most widely explored area of biomaterial research is tissue engineering, drug delivery, and bone regeneration. A schematic diagram illustrating various applications of biomaterials has been shown in Figure 1.1.

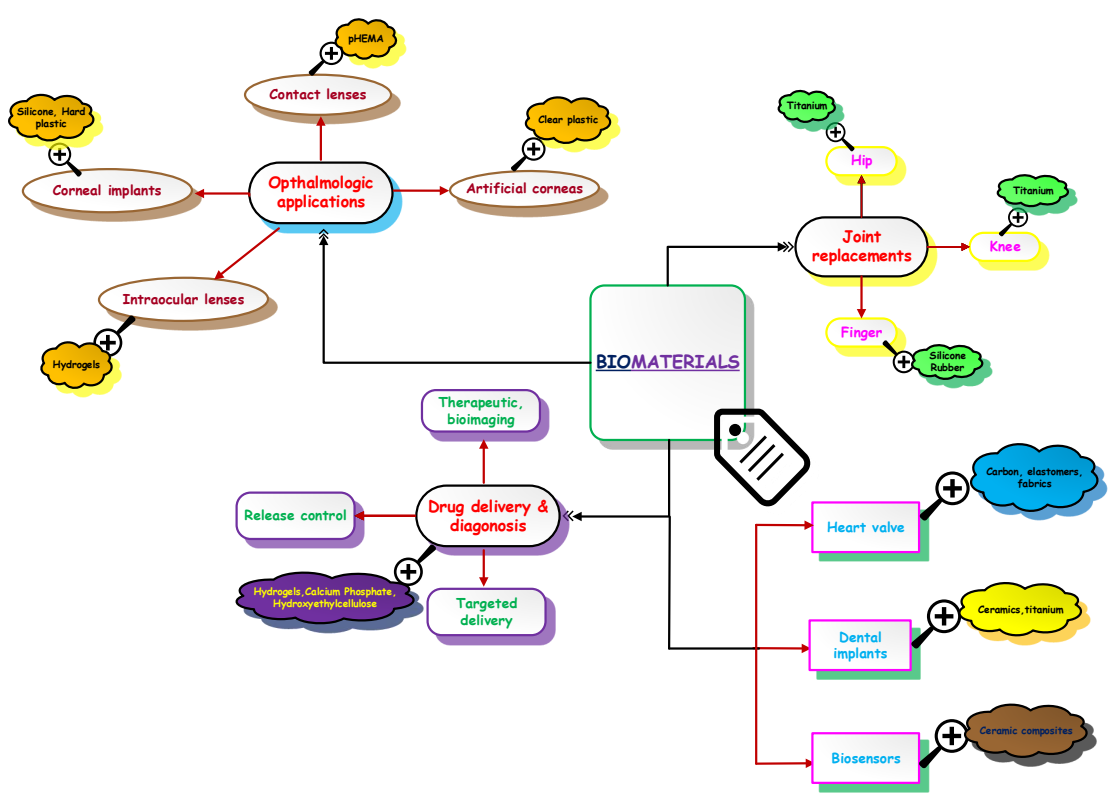


**Figure 1.1:** A Schematic representation of different biomaterials and their applications in various fields.

Restoring normal functioning of the diseased or impaired tissues of the body can be challenging from a medical perspective. The design of remarkable biomaterials that can alleviate pain, survive the especially harsh *in-vivo* biological conditions, and render support to the body for the normal functioning of a patient has been the greatest accomplishment of biomaterials research in the past few decades [19]. The increasing demand for developing biomaterials suitable for tissue engineering (regen-

erative medicine) has been associated with the fact that traditionally, the methods adopted for developing damaged tissues were associated with transplanting tissue from one site to another from the same patient. In some cases, the transplantation was done by taking tissues from one patient and transplanting it to another. This process, however, leads to severe issues like infection and hematoma, ultimately leading to the rejection by the host body [20]. It is a severe cause of concern for the patient as revision surgeries have to be performed to remove the malfunctioned component and replace them with new transplants. This leads to a financial burden on the patient apart from the severe discomfort he has to undergo. On the other hand, tissue engineering aims to regenerate the damaged tissues rather than replace them by engineering suitable biological substitutes, significantly reducing the risks of infection and improving tissue function. It clearly explains the increasing interest in the research community for exploring biomaterials.

## 1.2 Classes of biomaterials

Four categories of biomaterials are defined in the literature. These are polymers, metals, ceramics, and composites [21]. Polymers form the largest category of biomaterials and are usually applicable for soft and hard tissue applications. Based on its origin, polymers can be either natural (which includes collagen and cellulose) or synthetic (silicone rubber, poly(methylmethacrylate)(PMMA), poly(vinyl chloride)) [22]. Metals are mostly applicable for dental and orthopedic applications, and some common examples include $Ti$ and its alloys, stainless steel, $Co-Cr$ alloy. Ceramics are predominantly used for hard tissue repair and bone regeneration, especially in areas with no load-bearing requirement. They are also frequently used as coatings for metallic implants, especially to enhance the biocompatibility of metallic coatings. Common examples of biocompatible ceramics are the calcium phosphates ($CaP$), bioglass, alumina ($Al_2O_3$) and zirconia ($ZrO_2$). From a wider perspective, composites may refer to a combination of materials with different physical and chemical properties. The combination can be a ceramic-polymer, polymer-polymer, or ceramic-ceramic composite. The idea is to create a material with specialized properties and the targeted application. Some common examples of composites in the context of biomaterials can be hydroxyapatite $(Ca_{10}PO_4)_6(OH)_2$, HAP)-$BaTiO_3$, HAP-PMMA, polylactide (PLA)-poly(trimethylene carbonate) (PTMC) [23].

Interestingly, ceramics are further classified based on the following categories.

1. Based on its interaction with the host: bioinert, bioactive, and biodegradable

or resorbable.

2. On the type of application, they are intended for: structural and non-structural ceramics.

3. Based on the characteristics of the ceramics.

### 1.2.1 Based on the interaction with the host

Based on the nature of interaction with the host, three categories of ceramics are defined:

*Bioinert*: They usually refer to those ceramics which can maintain their stability (in terms of their physical and mechanical properties) when implanted into the host body. Implants designed from such ceramics usually do not bond to the bones. $\alpha - Al_2O_3$, $ZrO_2$ are some of the typical examples.

*Bioactive*: This class of bioceramics forms strong bonding with the adjacent tissues. The bonding occurs through a carbonated apatite layer that includes the interface of union between the host and the implant. HAP and bioglass are typical examples of such ceramics.

*Biodegradable or resorbabale*: These ceramics are dissolved into the body over time and are gradually replaced with natural tissues. From an experimental perspective, these ceramics are ideal as they would be available only up to the point their functions are required. The disadvantage of such ceramics is the rate of resorption, which is difficult to control. Additionally, the decline of mechanical strength with the resorption is a significant concern. A common example of resorbable ceramic is tricalcium phosphate.

### 1.2.2 Type of application

Two categories of ceramics are defined based on the type of application:

*Structural ceramics*: Ceramics that are of very high mechanical strength and inert nature are termed structural ceramics. Typical examples of such ceramics are $\alpha - Al_2O_3$ and $ZrO_2$.

*Non-structural ceramics*: Bioceramics, which are biodegradable/bioactive, either dense or porous with significantly low mechanical strength, and cannot support high loads, are classified under non-structural ceramics. Examples of such ceramics are HAP and tricalcium phosphates.

### 1.2.3 Characteristics of the ceramics

There are four categories of ceramics based on their characteristics:

*Dense but inert ceramics*: Inert ceramics that do not have any porosity are classified under this category. The bonding of these ceramics with bone is by the growth of tissues in the irregularities of the implants, and in some cases, these ceramics are fitted by pressure into the defects. A typical example of this type of ceramic is polycrystalline $Al_2O_3$.

*Porous but inert ceramics*: In this category of biomaterials, the bonding occurs by mechanical means, and the fixation occurs biologically. There is a growth of bone in the pores of the implants. A common example of such ceramic is porous polycrystalline $Al_2O_3$.

*Dense but porous bioactive ceramics*: These classes of ceramics are characterized by a bond that is chemical, and the fixation is bioactive. Examples are HAP and bioglass.

*Dense and resorbable ceramics*: The class of implants under slow dissolution to be finally replaced by bones. Tricalcium phosphates are such classes of ceramics. Plaster of Paris is another typical example of this category of ceramics.

## 1.3 Properties of biomaterials

Biomaterials portray a wide range of physical and chemical properties. Biomedical applications in physiology, surgery, and medicine demand a thorough understanding of mechanical properties [24]. An in-depth analysis of the mechano-tribological effects of the implant material is necessary for determining the reliability of long-term load-bearing application of orthopedic and dental implants. Properties such as the elastic modulus should closely match the adjacent bones to integrate the implant material to the host [25]. On the one hand, biomaterials with poor mechanical properties are incapable of providing sufficient support for tissue regeneration (in load-bearing applications); on the other hand, quite stiff biomaterials could stagnate regeneration of new bones tissues due to the stress shielding phenomenon [25]. Achieving an optimum balance of mechanical properties is therefore of prime importance for the smooth functioning of biomedical devices. It has also been observed that the cells in various tissues can sense the elasticity of the extracellular matrix and can transduce the mechanical signal into physiological responses. So, for a better reconstruction of defective bone tissues, the synergy of mechanical proper-

ties of the biomaterials with the surrounding tissue is of utmost importance [26]. Apart from these, other significant properties like roughness, surface wettability, and chemical stability are amongst the crucial factors that a biomaterial must comply. For instance, surface wettability refers to the hydrophilicity or hydrophobicity of the biomaterial surface. They are determined by the contact angle measurements. They are determining factors when biomaterials are used in the design of medical devices or implants, as drug delivery systems, and in bioreactors. The wettability of biomaterials is mostly determined by the surface tension and surface energy of the materials that are considered intensive thermodynamic properties [27].

These properties of biomaterials must be augmented by their biological properties, such as biocompatibility, osteoinductivity, osteoconductivity, and biodegradability, to name a few [28]. All these properties collectively determine the success of an implanted biomaterial *in-vivo*. The biocompatibility ensures that there is no toxic or inflammatory response of the implanted biomaterial, whereas osteoinductivity refers to the capacity of the biomaterials to stimulate differentiation of cells into preosteoblasts [1]. Biodegradability refers to the property of a biomaterial to dissolve after a specific time so that the new bones and soft tissues developed in the implanted site can function naturally without any support. Osteoconductivity is the ability of a bioactive biomaterial to induce the growth of bone tissues and cells over its surface or pores so that after biodegradation, the new bones can function coherently with the older bones [1]. The discussion clarifies that a synergy between the mechanical, interfacial, and biological responses is of utmost necessity for the success of an implanted biomaterial.

There has been a tremendous effort by researchers to develop advanced functional biomaterials with tailored mechanical and biological properties for many decades now. Several years of constant innovation have led to the development of biologically inspired processes to generate different biomaterials for bone tissue engineering. The human body is a beautiful creation of nature. A thorough understanding of its functioning has led researchers to understand that several exquisite electrical properties like piezoelectricity and streaming potential are constantly engaged in bone remodeling [29]. Piezoelectricity, for instance, as a consequence of "Wolff's law," is the manifestation of the stress-induced in bones due to daily activities that help in bone remodeling [30]. The natural design has inspired the biomaterials community to consider the electrical properties of biomaterials from a profound perspective. The design and development of electrically active biomaterials have shown promising properties by promoting tissue formation, and an expedited healing

process [31]. Clinical applications have increasingly resorted to the application of external electric stimulations for bone repair [32]. The use of biomaterials endowed with electrical properties as scaffolds or bone implants has dominated biomaterials research in the past few years. Inspired by these developments, we discuss the necessary electrical properties of biomaterials that bear significance in biomaterials research in the following sections.

## 1.4 Electrical properties of biomaterials

### 1.4.1 Dielectric properties

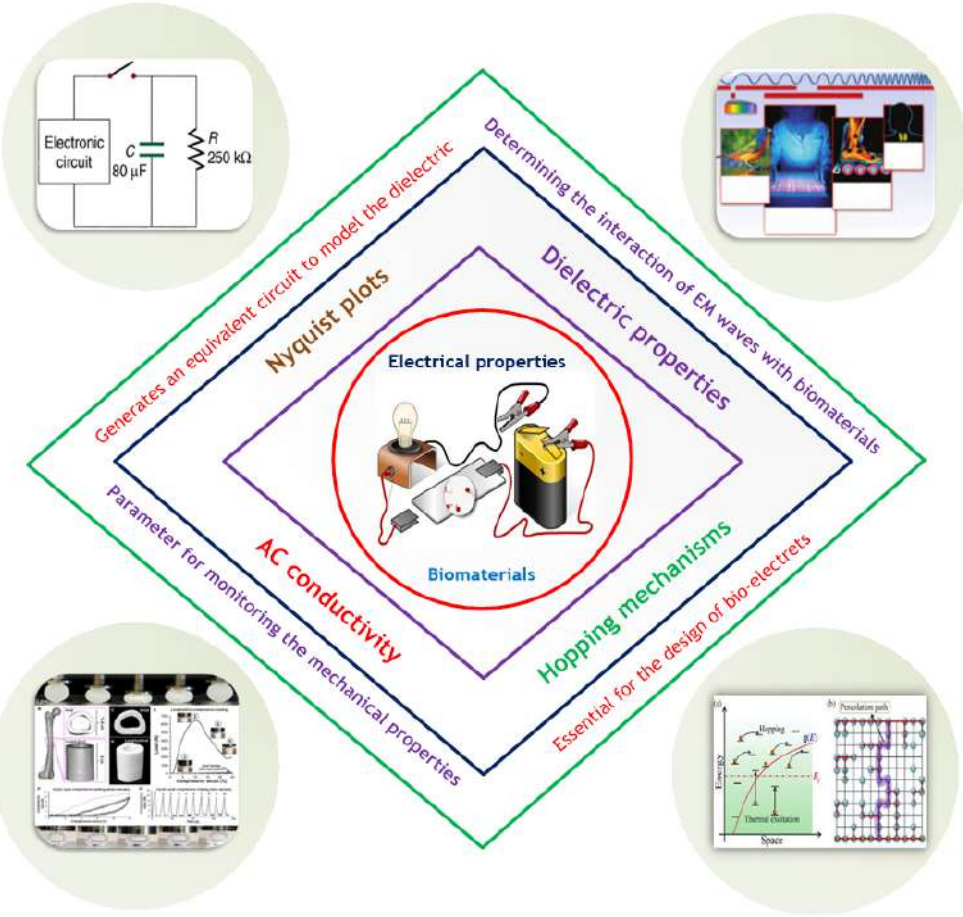


**Figure 1.2:** An illustration of the importance of electrical properties of biomaterials in the context of bone tissue engineering.

The dielectric constant ($\epsilon_r$) represents an intrinsic property of a biomaterial to

interact with the electric field. Biomaterials (in particular bioceramics) are mostly insulators and undergo polarization on interaction with an electric field. Polarization refers to the orientation of the dipoles within a dielectric favorably in the direction of the applied field [33]. A higher $\epsilon_r$ implies a greater degree of polarization. The advantage of polarization directly relates to the insulator's ability to produce an electric field after removing the external field. This fact can generate an internal field in the wounded site by the implanted biomaterial, which will lead to an expedited healing process. It has already been discussed in the previous section that electric stimulations are used to treat fractures, and delayed unions and non-unions of the fractured bone [34]. Biomaterials designed to harness this electric field to generate an internal field without external stimulations are revolutionary. However, insulators with higher $\epsilon_r$ are related to more considerable losses, meaning there is a disruption/decay of the polarization due to several conduction mechanisms [33]. Understanding dielectric properties in a broader sense includes the loss mechanisms, which can severely affect the performance of biomaterials. The techniques of impedance spectroscopy that are already used in clinical applications to detect cancerous cells and tumors can be a handy tool to analyze the electrical properties of biomaterials. A schematic diagram illustrating the importance of electrical properties of biomaterials in bone tissue engineering applications is illustrated in Figure 1.2.

### 1.4.2 Piezoelectricity and Ferroelectricity

Piezoelectricity, discovered by Pierre Curie in 1880, refers to the property of certain crystals, whereby they undergo electrical polarization on the application of mechanical stress. This process is sometimes also termed as the "direct piezoelectric effect" also has a counterpart termed as "converse piezoelectric effect," where a crystal is observed to be strained on the application of an electric field. Ferroelectricity is another attractive electrical property exhibited by certain crystals, in which a spontaneous dipole moment is observed. All the ferroelectric materials are naturally piezoelectric, whereas the converse is not true. Quartz is a ubiquitous example of a piezoelectric that is non-ferroelectric by nature. In biomedical applications, $BaTiO_3$ has received considerable attention due to its ferroelectric and piezoelectric properties. It is biocompatible and has the ability to generate an electric field after implantation as a bone substitute.

The introduction of non-linear electrical properties like piezoelectricity and ferro-

electricity in biomaterials draws inspiration from discovering such non-linear effects in natural bones and tissues several decades earlier [35]. Piezoelectric biomaterials develop charges on opposites faces (thus generating an internal electric field) under mechanical stress that leads to cell stimulation and bone remodeling [36]. Ferroelectricity in biological applications has demonstrated substantial momentum for researchers to use them in galvanotaxis, wound healing, cellular migration, and tissue regeneration, to name a few [37]. However, from a broader perspective, the demonstrated possibilities are yet to be seen in biological applications. The reasons involve insufficient research and improper understanding of the underlying mechanism that can allow researchers to modulate their properties for biomedical applications. It is worth noting that there is a significant gap in the time frame of the discovery of non-linear effects in bones and its induction to biomaterials. It is due to the fact that the underlying mechanisms of piezo and ferroelectricity in natural systems took a great deal of time to be apprehended [38]. Moreover, the researchers were quite conservative about the compatibility of existing piezoelectric and ferroelectric materials in biological applications. It is only at the beginning of the $21^{st}$ century that researchers started exploring the traditional piezo and ferro-active materials for biological applications [39, 40]. However, despite the efforts, there are still a lot of unanswered questions, and a lack of comprehensive theory to explain these effects has inspired researchers from materials science, physics, biosciences, and engineering disciplines to pursue the problem and create a generation of smart biomaterials.

## 1.5 A brief history of ceramics in biomedical applications

The selection of materials and design of implants for hard tissue replacement so that it is mechanically and chemically stable is a prime area of research in bone tissue engineering. Several combinations of bioinert, biodegradable and bioactive materials have been considered plausible candidates for hard tissue replacement. The introduction of bioceramics as implants was done for the first time during the 1980s. Among them, HAP has been most widely explored due to its structural and chemical similarity to the natural bones [41]. Before HAP, highly dense and pure alumina ($\alpha - Al_2O_3$) was the first bioceramic that had been used clinically [3]. Excellent corrosion resistance, biocompatibility, high wear resistance, and high strength made it suitable for hip prostheses and dental implants. The Young's

modulus of alumina is, however, on the higher side (380 GPa) as compared to cortical bones (7-25 GPa) and cancellous bones (0.05-0.5 GPa). Therefore using alumina in load-bearing applications leads to stress shielding of the bones (preventing the bones from being loaded), which must be avoided at all costs for the bones to remain healthy and robust [3]. In older patients (above 50 years and suffering from arthritis and osteoporosis), it was found that stress shielding might result in cancellous bones atrophy and loosening of the acetabular cup [42]. Consequently, it is essential to consider the patient's age, the nature of the joint, and most importantly, the biomechanics of repair before using the prosthesis designed from the alumina ceramics.

From dense ceramics, the research moved to porous ceramic implants, which had advantages such as the inertness and the highly stable interface developed when the bones grow into the pores of the ceramic implant. However, it is evident from the discussion that porous ceramics are limited to areas of low-load or non-load bearing applications. For instance, the *in-vitro* aging of porous alumina implants in saline solution (for four weeks) reduces the effective mechanical strength by 35 to 40%. Similarly, another high strength porous ceramic: calcia stabilized zirconia ($ZrO_2$), is seen to undergo a significant decrease in strength, much similar to calcium aluminates. Thus, the aging phenomenon was seen to lead to a significant reduction of the strength of porous ceramics, which posed a serious question towards the long-term applications of these classes of materials. By then, the $CaP$ based ceramics had been discovered, and it had earned popularity among researchers and clinicians due to its biodegradability and bioactivity. Its range of applications included dental implants, periodontal treatment, alveolar ridge augmentation, orthopedics, spinal surgery, and many more. The calcium phosphate ceramics displayed different phase and depending upon their applications, the appropriate phase (bioactive or resorbable) were used. The stability of different $CaP$ ceramics is based on the physiological conditions the ceramics are subjected. At pH $< 4.2$ and body temperature (310 K), the most stable phase is dicalcium phosphate ($CaHPO_4.2H_2O$), and at pH $>4.2$, it is HAP. At very high temperatures ($>$ 1273 K), the stable phase is $\beta$-tricalcium phosphate ($Ca_3(PO_4)_2$, TCP) and at further higher temperatures ($>$ 1398 K) it transforms to $\alpha$-TCP. In terms of the resorption, $\alpha$-TCP has the highest rate of resorption followed by $\beta$-TCP, and HAP is known to be the most stable form, which has the least rate of resorption [43]. A table comparing the mechanical properties of the different ceramics discussed here is presented in Table 1.1 [44].

**Table 1.1:** A summary of the mechanical properties of various ceramics used for biomedical applications.

| **Materials** | **Density ($g/cm^3$)** | **Young's Modulus (GPa)** | **Fracture toughness ($MPa.m^{1/2}$)** |
|---|---|---|---|
| $Al_2O_3$ | 3.9-4.0 | 380.0 | 4.2-5.9 |
| $ZrO_2$ (3 mol% $Y_2O_3$) | 6.0-7.0 | 150.0-205.0 | 7.0-12.0 |
| $BaTiO_3$ | 6.0 | 70.0 | 2.0 |
| $HAP$ | 3.1 | 80.0-100.0 | 0.6 |
| Natural Bones | 2 | 3.0-80.0 | 2.0-12.0 |

A comprehensive literature survey points out that HAP has been the most favored biomaterial that has been explored to the maximum possibility. Special attention to HAP has been provided due to several reasons. HAP is biocompatible, osteoconductive and the ease with which they can be processed into matrices with interconnected pores is unmatched with other ceramics [41]. Moreover, amongst the $CaP$ ceramics, its biodegradability rate is the least. Furthermore, it has the capacity to form chemical and mechanical bonds directly with the bones that leads to a strong bone-implant interface, thus making the biological properties of HAP incredible [43]. During the adsorption process, the HAP has a reputation for not causing denaturation of bio-related substance, which makes it useful as an absorbent for chromatography. In bone grafting applications, the HAP is used as porous and dense ceramics, coating layers, cement and granules. The reason for such diverse applications of HAP is its mechanical and chemical properties that are highly dependent upon the sintering temperature and duration, and most importantly, the $Ca/P$ ratio (1.67 for stoichiometric HAP). These parameters are tunable, and as a result, the properties of HAP can be modulated for the above applications. Despite these advantages (even after appropriate tuning), the mechanical properties such as fracture toughness (0.6 $MPa.m^{1/2}$) poised limitation in its application as a bone substitute, especially in those areas where there is a need for load-bearing [45]. Extensive experiments have revealed that the $CaP$ based ceramics show absymal performance under tensile loads. Consequently, Hench *et al.* proposed that HAP or $CaP$ based ceramics be used only for the following cases [3]:

(a) unloaded implants (smaller dimension), especially in the middle ear.

(b) dental implants with supporting metal posts ($Ti/Ti$-based alloys).

(c) low-loaded porous implants where bone growth needs to occur.

(d) bioactive phase in composites: either polymer-ceramic or ceramic-ceramic.

The advantages of HAP outweigh the shortcomings (which are far too few), and as a result, have gained immense popularity among clinicians and researchers. At present, the research in HAP is not just limited to mechanical or biological applications. Several new aspects that explore the electrical properties, photoluminescence, and microstructure (primarily related to its space group) have featured in the last few years and have revived the research in HAP. Some of these exciting features have been discussed in the following section, and along with that, we point out the gaps existing in the literature that motivated us to carry out research in HAP.

## 1.6 An overview of HAP

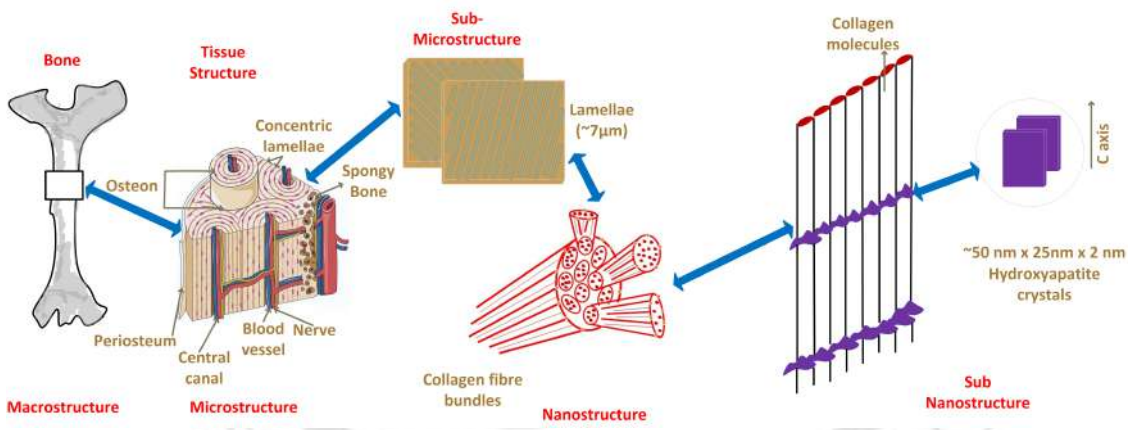


**Figure 1.3:** A schematic representation of the hierarchical structure of bones at different scales.

HAP is an immensely favored biomaterial in the biomedical industry, known for its extensive applications in orthopedics and dentistry. The versatility of its properties has expanded the scope of its applications to column chromatography for antibody purification, drug delivery, autogenous bone graft substitute, alveolar ridge, and ear implants [46–48]. Naturally, it appears as an inorganic constituent of natural bones, with substitutions like $Mg$, $Sr$, and other trace ions occupying the $Ca$ sites [49]. It is often designated as bone-like apatite or bone apatite, in brief, to distinguish it from HAP. As a consequence, it can be perceived that the $Ca/P$ ratio of bone apatites differs from HAP (1.67 for HAP, whereas a ratio $< 1.67$ is

obtained for bone apatite) [50]. An illustration showing the natural occurrence of bone apatite is displayed in Figure 1.3. The last two decades have seen an exponential rise in the biomedical industry related to HAP primarily due to its incredible biocompatibility, affinity to bond to living bones when used as implants, and its ability to promote ingrowth of new bones through osteoconduction without having any toxic or inflammatory response to the surrounding tissues. As a testimony to our claim, the recent reports published in Yahoo finance claimed that the HAP market is projected to grow from United States dollar (USD) 2.2 billion (currently in 2020) to USD 3.1 billion in 2025 at a compound annual growth rate (CAGR) of 6.8 % [51]. It has been forecasted that the Asia-Pacific HAP market will grow at the highest CAGR precisely due to the increase in medical tourism in countries like India, South Korea, and Japan [51]. This has led to the rapid development of the domestic health care sector and is an indicator for exhaustive research in HAP to develop devices and technologies to cater to growing medical tourism.

HAP has an exciting crystal structure. The non-stoichiometric composition with substitutions like $Mg$, $Sr$, and other trace ions as impurities are found to crystallize into the hexagonal ($P6_3/m$) structure [52]. Stoichiometric HAP reportedly crystallizes in the monoclinic structure ($P2_1/b$) [53]. The difference between the two structures lies in the arrangement of the $OH$ group inside the crystal lattice, with the hexagonal crystal lattice containing a disordered arrangement of the $OH$ group, resulting in the dipoles generating a "para-electric-like" arrangement [53]. However, the monoclinic structure distinguishes by forming an ordered arrangement of the $OH$ group in such a way that the $OH$ dipoles along the [101] planes are all arranged in the same direction. The dipoles along the [010] planes are directed opposite, thus generating an "anti-ferroelectric-like" arrangement [53]. Synthetically derived HAP is but a polymorph containing contributions from the monoclinic and hexagonal phase in quantities that vary with respect to the synthesis conditions. There is an interesting but unending debate regarding the crystal structure of HAP in literature. The starting point of the debate relates to the association of non-linear electrical properties to HAP. It has been mentioned previously that natural bones display piezoelectricity and ferroelectricity. These properties are understood to be due to the collagen molecules that comprise the organic constituent of the natural bones. Researchers somehow were convinced that synthetic HAP could be associated with non-linear electrical properties [52]. The existence of symmetry in the crystal structures (both $P6_3/m$ and $P2_1/b$), however, restricted the association. Physicists have made many efforts, mostly theoretical, to associate a different crystal structure with

synthetic HAP. In this regard, substantial work done by Haverty *et al.* must be highlighted [52]. It was argued that the space group $P2_1$ is a possibility in HAP, which can be accounted for piezoelectricity and ferroelectricity. However, the experimental evidence by most of the researchers still supports the existence of space group $P6_3/m$ and $P2_1/b$ [54, 55]. A solid conclusion is yet to be arrived at, and primarily, these differences exist due to the inherently complex crystal structure HAP. Moreover, synthetic HAP is highly sensitive to the preparation conditions, and a slight deviation of the experimental conditions leads to changes in its properties. In conclusion, it can be said that a great deal of effort is still required for reconciling the debate.

## 1.7 Brief introduction to HAP based ceramic composites as biomaterials

Ceramic-composite is defined as a class of materials formed by combining two or more ceramics as components for inducing enhanced properties of the resultant matrix compared to the individual monoliths [56]. In medical applications, the implanted biomaterials have to endure several challenges to function desirably for intended applications. The implants specially designed for load-bearing should handle compression and shear forces under normal loading conditions [57]. Additionally, they must sustain the corrosion resistance, hardness, aging resistance against the harsh *in vivo* conditions inside the human body. These properties must be supplemented with biocompatibility, osseointegration, and osteoconductivity to function as a biomaterial properly [58]. It is indeed a difficult task for a single component ceramic to inherently possess all these properties. The biological properties of HAP are superior to most bioceramics; however, poor mechanical properties like fracture toughness, lower Young's modulus, hardness, tensile strength, *etc.*, limit its load-bearing applications. Improving the mechanical properties by retaining the biological properties of HAP can be accomplished by fabricating a ceramic composite of HAP with other ceramic composites that have superior mechanical properties. In terms of electrical properties, the $\epsilon_r$ of HAP is on the lower side ($\sim$5-10 at 1 MHz). Such a lower $\epsilon_r$ is less valuable if we intend to design implants that can harness the external electric stimulations, as mentioned previously. The electrical properties can be improved to the desired level by considering composites with a suitable ceramic. A ceramic composite enables the tailoring of properties to suit any

application [59]. Sometimes, ceramic composites exhibit properties that are superior to their constituents and can be a boon in several applications.

Needless to mention that there are several works reported by various researchers on HAP-based ceramic composites. In line with the theme of the dissertation, the focus would be on those articles where the composites report an improvement in electrical properties. $BaTiO_3$ (BT) has been one of the foremost ceramics that has been considered for addition to HAP for inducing piezoelectricity in HAP [60]. The results were astonishing as a composite of HAP and BT could induce osteogenesis in jawbones of dogs at least one week ahead of HAP [61]. The study established that BT is a biocompatible component that can be utilized for biomedical applications. In another report, the piezoelectric coefficient ($d_{33}$) was reported for a composite containing 10 vol. % of HAP and 90 vol. % of BT [62]. To support bone ingrowth, the ceramic composite was made porous, and the $d_{33}$ coefficient was found to be comparable to natural bones ($2.85 \pm 0.1$ pC/N) [62]. In yet another study by Bowen *et al.*, [60], the dielectric and conduction properties of HAP-BT ceramic composites were considered. The $\epsilon_r$ of the designed ceramic composites were comparatively higher as the incorporation of BT, which reportedly has a high $\epsilon_r$ (typically $> 1000$ at 1 kHz), lead to the improvement of the charge storage capacities. The conductivity of the ceramic composites was low ($< 10^9$ S/cm at 1 kHz), which indicates that once polarized, the decay of the polarized field will take substantial time. This was an indicator of the suitability of the material as scaffolds that will be able to generate an internal polarized field capable of healing the bone fractures at an expedited rate. The trend in biomaterials research also advocates using biomaterials with superior electrical properties in the design of bio-electronic gadgets.

Electrets are one such area where HAP has shown promising properties. At this point, it would be justified to take a slight detour and explain the concept and application of electrets from a biomaterials perspective. Electrets are constituted of dielectric materials capable of generating an electrostatic field (quasi-permanent) due to charges with dipole moments [33]. The electrets are in high demand for power generators used in energy harvesting. The electrets are excellent candidates in low-powered electric devices for power generation and can be potential candidates for bio-electronic gadgets that require low power. In wound healing applications, electrets display the potential to be used as advanced wound healing bandages, which are capable of generating electric fields to stimulate the healing process [63]. Against such backdrops, the use of HAP and BT ceramic composites can be highly recommended.

It has to be understood that BT is a ferroelectric and piezoelectric material. Ferroelectric materials are often preferred for generating ceramic composites due to their high $\epsilon_r$ [64]. A significant drawback associated with such materials, however, limits their applications to electrets. It is well known that ferroelectrics are associated with a remanent polarization that stores electric energy decreasing the discharge efficiency of the electrets. Also, the addition of ferroelectric components decreases the overall breakdown strength of the composites and results only in a minor development in the energy storage density of the composites [65]. These can adversely affect the power generation capability in devices that uses such composites. It was pointed out previously that BT has a significantly high value of $\epsilon_r$ and HAP has a meager value of $\epsilon_r$ [60]. The result of intermixing will produce an inhomogeneous electric field, adversely affecting the breakdown strength of the composite. The best alternative solution is a paraelectric material, with a relatively high $\epsilon_r$ and no remanent polarization. Such paraelectric can support in generating composites with subsequently better electric properties. $SrTiO_3$ (ST) has been the preferred choice as a paraelectric for addition to HAP. There have been several efforts to prepare a ceramic composite of HAP and ST for various biomedical applications. The first evidence in favor of ST for biomaterials applications was put forward by Xin *et al.* [66] by considering ST nanotube arrays that were capable of delivering $Sr$ ions for stimulating bone formation and inhibiting bone resorption. $Sr$ is of paramount importance in biomedical applications. Mainly $Sr$ based drugs are used in medicine for healing postmenopausal osteoporosis [67].

Against such backdrops, researchers were looking for platforms that can result in $Sr$ delivery in a sustained manner. There was no better alternative than ST, which has proven its effectiveness by supporting the precipitation of bone-like apatite from simulated body fluid (SBF), indicating its superior biocompatibility. Further, the cell adhesion and cell proliferation abilities performed by SaOS2 cells on ST nanorods showed that the cells could proliferate normally and adhered firmly over the interface [66]. In yet another study on $ST$ nanoparticles infused with $TiO_2$ nanorods were able to determine the exact concentration of $Sr$ ions that supported the cell proliferation and spreading of SaOS2 cells without inducing any toxic response [68]. The exact concentration of $Sr$ ions identified by them was 1.4 ppm, and concentrations above 3.0 ppm were identified to inflict adversity on the cells. A few research groups have considered composites of ST and HAP, and in one particular study containing 50 wt.% of HAP and ST was prepared, and their properties were studied by comparing them with the respective monoliths. The elastic modulus of the composite (54 $\pm$

4 GPa) was reportedly better than the monolith HAP (46 ± 10 GPa) but was lower than ST (153 ± 19 GPa) [67]. The results were expected as HAP is a brittle ceramic; however, the brittleness decreased due to the introduction of ST, improving Young's modulus. Interestingly, there has been no attempt at exploring the electrical properties of ST and HAP-based composites.

There is another interesting ceramic $Ba_{0.5}Sr_{0.5}TiO_3$ (BST) that can be of considerable importance when considered as a composite with HAP. BST introduces $Ba$ in ST, and from a biomaterials perspective, the presence of $Ba$ and $Sr$ could positively influence its biological properties. Like ST, BST is also paraelectric, and to the best of our knowledge, its biological properties have not been reported to date. Together with ST, exploring the biological and electrical properties of BST composites with HAP can be prominent for designing biomedical devices like scaffolds, coatings for implants, and components of bioelectronic gadgets. It must be apparent from the previous discussions that research on composites of ST and HAP, as well as BST and HAP, are in the nascent stage, and with the promising properties reported in some literature, there is a high potential for these composites to be an essential part of the biomedical industry in the foreseeable future.

## 1.8 HAP and its composite thin films

Thin films of HAP have been researched considerably for developing coatings useful in biomedical implants. $Ti$ or $Ti$-based alloy such as $Ti-6Al-4V$ have been the preferred choice of substrates for thin films [69]. $Ti$ or its alloys are used for designing the implants owing to their biocompatibility, osseointegration abilities, higher strength to weight ratio, and their ability to resist corrosion [70]. However, many instances have reported implants loosening due to poor bonding to the host, primarily due to the formation of layers of fibrous tissue at the skeletal tissue/device interface [71]. To do away with the failures, the commonly adopted techniques employ a surface modification of the $Ti$ or $Ti$ alloy implants using several techniques. Biomedical implants are coated with a bioactive layer such as HAP or $CaPO_4$, which readily improves the bond strength and stability of the implants, leading to the prolonged service life of the implants. Many techniques have been developed for surface modification of the implants. Among them, biomimetic coating of HAP using chemical route, sol-gel based coating technique, plasma spraying, thermal spraying, electrophoretic deposition, radio frequency (RF) magnetron sputtering, and pulsed laser techniques have been reported in literature [72].

The biomimetic coating, chemical-based deposition technique, or sol-gel technique are effective for coating $Ti$ or $Ti$-based alloys and are usually associated with significantly fewer complexities. A severe drawback associated with such a process is the bonding strength of the HAP layer over the implants [73]. Over time, it has been observed that the coating layer dissociates during its service due to the adverse conditions inside the body. The disassociation is particularly alarming in the case of chemical-based deposition techniques, which presents a severe disadvantage for its commercialization. Among these processes, plasma spraying is the only process recognized by the Food and Drug Administration (FDA), USA for coating of biomedical implants [74]. The quality of coating in plasma spraying is significantly better than the chemical deposition techniques, which makes it widely acceptable for commercialization. However, even this technique is not free from shortcomings such as the introduction of impurity phase, limited crystallinity, poor uniformity in the thickness, and low adhesion (although higher than the chemical deposition techniques, is still on the lower side for achieving the best response) [74]. Over the years, several improvements and modifications in the plasma spraying techniques have addressed these issues, but other techniques are far better and more robust in terms of the properties of the coated layer.

The physical vapor deposition (PVD) techniques offer a substantial advantage in terms of the adhesion strength, uniformity of coatings, and the crystallinity of the coated layer. Also, the advantage of coating any complex layer, be it compound, multilayer, insulators, or metallic, can be achieved through the PVD techniques [75]. In this direction, we have focussed on the RF magnetron sputtering technique, which is a versatile technique to deposit biomaterials. It has been previously pointed out that the trend in biomaterials research is to obtain electrically active coatings that augment the biological properties of such implants. A significant criterion for displaying electrical properties is related to the density of the coating, which has to be significantly high for obtaining superior properties. RF magnetron sputtered coatings have proven to be highly efficient for such purposes. In terms of the coating uniformity and adhesion, the technique is significantly superior to most of the other processes reported previously [76]. The features for controlling the deposition temperature during the sputtering process allow the phase present in the sputtering target to be transferred to the thin films [77]. This particular feature is unlike the plasma spraying, where due to the generation of very high deposition temperature, there is a phase evolution from HAP to $\beta$-TCP, adversely affecting the overall stability and service life of the implants. HAP amongst the $Ca-P$ family is known to

be the highly crystallized form with the lowest rate of dissolution [78]. $\beta$ or $\alpha$-TCP has a significantly higher rate of dissolution and are formed due to the loss of $OH$ group from HAP due to high temperature during synthesis [78].

As of now, there is no known process to control the degree of $\beta$ or $\alpha$-TCP in HAP, and avoiding its formation is considered the best way to retain the stability and integrity of the thin films. Resorting to sputtering provides the best possible alternative to plasma spraying under such circumstances. From an economic perspective, the instance of the semiconductor industry can be cited where RF sputtering is the technique through which all the integrated circuit fabrication is carried out. The process is economically quite viable, and in biomaterials research, the technique has shown potential for various biomedical purposes [77]. However, commercialization of the technique is yet to be seen, but in the recent future, a change in the perspective is inevitable. In the following sections, we briefly present the literature review of sputtered HAP thin films along with the compound thin films and discuss their properties for various applications.

## 1.9 RF sputtered HAP thin films and their properties

In one of the reports by Ding *et al.*, RF sputtering was used to obtain HAP/$Ti$ composite coatings for improving the bonding strength of the HAP over $Ti-6Al-4V$ [79]. The experiment was motivated by some of the previous experiments on HAP coatings over $Ti-6Al-4V$, which showed decreasing bonding strength after immersing in SBF. The peeling of the HAP films occurred due to the presence of micropores or cracks in the sputtered films that allowed SBF to penetrate in between the interface of HAP and $Ti-6Al-4V$, weakening the strength of the films [80]. To avoid such events, a multilayered coating of HAP/$Ti$ coating was reported by depositing $Ti$ and HAP layers alternatively, which led to a spectacular increase in the stability of the coatings under SBF along with the bonding strength (that remained constant above 60 MPa for the maximum duration considered in the experiment). In fact, the bonding strength of the coating was restricted by the measuring apparatus, and it was projected that the actual strength could be much higher than the reported values [80]. The process reports an innovative approach to tackle the issue of HAP layer adsorption into the bone tissue by initially coating a $Ti$ layer over the substrates, which prevents the substrate from coming into direct contact with the bone tissue, thereby reducing the chance of implant loosening.

A similar concept was reported by Nelea *et al.*, by depositing a buffer layer of

$TiN$ on $TiAlFe$ substrates to obtain better adherence of the coated HAP layer upon the substrates [81]. The mechanical properties of the coatings that had the buffer layer was compared with that of coatings without the buffer layer. The hardness for both set of coatings remained similar (4.9 GPa in both cases); however, slight differences in the elastic modulus was obtained (147 GPa without buffer layer and 151 GPa with the buffer layer). The introduction of the buffer layer posed to be a brilliant alternative in enhancing the mechanical stability of the sputtered films [81]. In another work by Synders *et al.*, mechanical properties of HAP thin films deposited by RF sputtering was measured experimentally, and the results were compared to theoretical models [82]. The nano-indentation results reported values of $10 \pm 1$ GPa for hardness and 147 $\pm$ 10 GPa as Young's modulus for the thin films. The values were in good agreement with theoretical results that yielded 132.1 GPa, a deviation of 10% from the experiment. The Young's modulus of $Ti-6Al-4V$ is close to 110 GPa, and the values reported for HAP thin films were comparatively higher, which indicates superior mechanical properties of the sputtered films [82]. There are several other reports that have successfully reported the deposition of HAP films by sputtering. However, even more reports are available that reported the formation of secondary phases like $CaO$ and $\beta$-TCP during the deposition process [75].

A careful selection of the deposition conditions like the substrate temperature, deposition pressure, RF power, and target to substrate distance needs to be done for successfully obtaining phase pure thin films of HAP. Additionally, it must be evident from the above discussion that no solid efforts are made to extract the electrical properties of the thin films, which further requires substantial research. Even in dealing with the biological properties, several studies are still required to be conducted. The extraction of properties of thin films is challenging, especially considering that most of the properties are thickness dependent, and some of the properties, like the electrical properties, need special arrangements for their extraction. Furthermore, bilayered coatings on $Ti/Ti$ alloys have received significant attention due to their superior ability to generate high-quality medical coatings that, have produced superior responses on the lab scale [83]. In this regard, BT based bilayer coatings have been reported, and these coatings are found to be bioactive and cytocompatible [84]. One of the prime advantages of using bilayers over implants lie in the less material consumption of costly components like $Ba_xSr_{1-x}TiO_3$ or BT that are conducive for inducing electrical properties in the coatings. Using bilayers provides an additional advantage of tuning the material properties by collectively incorporating the behavior of both the layers, thus making them suitable for *in-vivo* environments [85].

In the case of bone implants, one component which has better bone regeneration ability will help in bonding with the surrounding tissues, and the other layer with superior electrical properties will aid in faster healing of the fractures [85]. Thus, bilayers have the potential of being exceptionally favorable for avoiding component failures and faster bone healing. In this context, the coating technology adopted for obtaining bilayers is vital to developing economically viable implants and has superior electrical and biological properties. Such a versatile method is undoubtedly the RF magnetron sputtering, which can produce high-quality uniform coatings over implants while maintaining a high degree of adhesion with the substrate [86].

## 1.10 Objectives

The objectives that we aim to accomplish in this thesis are as follows,

(1) Successfully prepare HAP and analyze the structural variation with temperature (using X-ray diffraction (XRD) and Raman spectroscopy techniques), the variation of $\epsilon_r$ with respect to frequency and temperature, bandgap, photoluminescence, and most importantly, obtain a correlation between the results described by each of these techniques.

(2) Develop ceramic composites of HAP and ST of varying concentrations and improve their electrical properties. The emphasis is on identifying the composite with the superior electrical and biological response. Establishing a correlation between the observed electrical and biological properties of the composites and devising a mechanism to understand how one augments the other would be the prime motivation.

(3) Introduce the $Ba$ component in ST, prepare BST, and investigate its influence on biological and electrical properties. Understanding how a composite of BST and HAP stands compared to HAP and ST would be interesting. We follow a similar methodology in fabricating ceramic composites of different concentrations. Hence, identifying the composite with a superior blend of electrical and biological properties would be an objective of the study.

(4) Develop scaffolds from the composites (which have enhanced biological and electrical properties) as identified in the previous steps and make a preliminary analysis of their mechanical and biological properties. From the study, identification of the scaffolds which have significantly better properties shall be made.

(5) Develop thin film coatings from sputtering targets (developed in the laboratory) using the identified best composites in the previous chapters and analyze the

microstructural, electrical and biological properties to investigate the possibility of using the coatings in $Ti$ implants for tissue engineering.

## 1.11 Overview of the thesis

In this thesis, we reported the synthesis of HAP and explored its properties especially the electrical properties such as the variation of $\epsilon_r$ and conductivity with respect to temperature and frequency. We extend our understanding of HAP to prepare ceramic composites of HAP and ST to improve its electrical properties and investigate the biological response of the prepared ceramic composite. We approach the problem by considering a series of composites of varying concentrations of HAP and ST. Thereby, we identify the composite displaying substantially better properties based upon the careful investigations of the biological and electrical properties. Subsequently, we introduce the $Ba$ component in ST, leading to the ceramic $Ba_{0.5}Sr_{0.5}TiO_3$. We found strikingly good biological response of ST and ST containing composites, and we expect that the introduction of $Ba$ would enhance the properties manifold. The same approach of preparing a series of composites was adopted that led to the identification of the composite blended with better biological and electrical properties. The results were exciting, and afterward, we developed scaffolds from the previously identified best composites of the ST and BST series and probed their biological and mechanical response to determine their suitability in tissue engineering applications. Finally, we developed coatings over $Ti$ substrate from the identified best composite of ST and HAP series using RF magnetron sputtering. We fabricated our in-house sputtering target, developed a series of thin films of various thicknesses, and probed their preliminary biological and electrical properties. Based on the analyses, we were able to identify the thickness with optimized properties that would be suitable for coating implants that would be used for bioelectronics and orthopedics applications. We also develop bilayered coatings of HAP and BST over $Ti$ implants, with the sole aim of understanding the usefulness of bilayers in orthopedic or dental applications. We analyzed the interfacial, electrical, and biocompatibility aspects of the bilayered films that helped us to understand the properties from a broader perspective. The sole aim had been to understand the importance of electrical properties, that highly augments the biological properties, resulting in enhancing the service life of the implants or any gadgets used in biomedical applications. We have not discovered any new technique for analyzing the properties but have made a humble effort to adopt the already existing method-

ology of impedance spectroscopy in biomaterials research to composites, which have shown tremendous potential for biomedical applications. The thesis comprises seven working chapters. The preliminary five chapters are committed to understanding the fundamental properties of the composites, and the final chapter highlights the application of this understanding to plausible devices for prospective clinical usage in the near future. A chronological description (in brief) of each chapter is included below.

### 1.11.1 Chapter 1

Chapter 1 begins with the general introduction to biomaterials, their classification categories, properties, and area of application. Briefly, a discussion on the mechanical and biological properties of biomaterials is presented. After that, based on the trend in biomaterials research, we introduce the electrical properties and how they augment the effective functioning of biomaterials. Based on a careful literature survey, we present a justification for choosing HAP as one of the starting materials for the thesis. It is followed by more literature surveys on ceramic composites and thin films. The central theme upon which the survey revolves around is how a ceramic composite developed with HAP can lead to the improvement of its electric properties keeping intact the biological properties, which is essential for all *in-vivo* applications. Towards the end of the chapter, we present the objectives of the thesis, followed by a summary of the work contained in each chapter.

### 1.11.2 Chapter 2

In this chapter, we discuss in detail the experimental procedures adopted throughout the thesis for the exploration of microstructural, electrical, and biological properties of the monoliths and ceramic composites. The chapter comprehensively discusses the process of preparation of sputtering targets and deposition of thin films from the fabricated target. Further, the process of extraction of the microstructural, surface, electrical and biological properties have been discussed. This discussion will help understand the results of the different experiments included in the following chapters.

### 1.11.3 Chapter 3

In Chapter 3, we study in detail the preparation methodology of HAP and focus on extracting its physiochemical properties. We find that synthetically derived HAP, exists in the hexagonal phase where the adjacent $OH$ groups are pointing opposite to each other, and the $OH$ group pointing in the same direction forms a monoclinic phase. The different pointing directions of the two phases show variations in physicochemical properties. The hurdle in obtaining the single crystals of such complex HAP results in most conventional synthesis methods producing the polymorphic phases that often show promising properties over the single crystals. We present a detailed temperature-dependent structural evolution of the synthetically derived polymorphic phase of HAP. As prepared samples of HAP using the sol-gel method at room temperature showed the polymorphic phase of monoclinic and hexagonal symmetries. The prepared samples show the monoclinic phase with a vol.% of 45.94% at 303 K. When subjected to the temperature, HAP predominantly shows the monoclinic phase vol.% 57.77% at 573 K. The dominant growth of single-phase in HAP lead to the monotonic $OH$ group reorientation with the temperature. From micro Raman spectroscopy, we confirm the reorientation of the $OH$ group with changes in the vibrational spectra. Additionally, a detailed study of the temperature-dependent optical properties of HAP reveals defects, which endows it with photoluminescence properties (PL), and the results correlated with the bandgap calculations ($E_g \sim 3.91$ eV). The PL studies revealed that HAP specimens have positive thermal quenching (PTQ) behavior that resulted from the defect transitions from a radiative to a non-radiative state. By deconvoluting the PL spectra, it is established that the intensity of the PL spectra peaks in the orange emission (approximately $\sim$ 630 eV) and are consequences of deep level defects near the center of the forbidden region. Further, the dielectric spectroscopy is used to attribute the $OH$ ions orientation; the calculated activation energy is in the range of rotational transformation of $OH$ ions. The temperature tunable polymorphic HAP exhibit different physical properties that can have applications in bioimaging and biomedical devices.

### 1.11.4 Chapter 4

In chapter 4, we discuss the interplay of structural, electrical, and surface properties in determining the collective behavior of HAP and ST composites. Synthesizing the monoliths by sol-gel (HAP) and solid-state reaction (ST) respectively, they are mixed in different At.% (20, 40, 60, and 80 At.%) to prepare a series of composites.

The prepared composites are then subjected to X-ray diffraction (XRD) and Raman analysis to probe the microstructural aspects. The analysis revealed no evidence of a phase that the reaction between the two monoliths might form. The crystallite sizes are in the range of 27.2-37.3 nm, and it increases with the content of ST in the composites. The Raman analysis revealed crucial information about the presence of rutile $TiO_2$ that is later found to be the link in the display of bone-like apatite nucleation ability in the monolith ST and its composites. The field emission scanning electron microscopy (FESEM) analysis revealed that the grain sizes are between the monoliths (64 nm-144 nm) and are found to follow a trend similar to the crystallite size. The variation in $\epsilon_r$ with the temperature ranges from 5-35 (1 MHz) at 310 K for all the specimens. The dependence of $\epsilon_r$ on the grain size of the composites follows a nearly exponential relation.

The bone-like apatite forming ability of the composites is studied by incubating the specimens in SBF. Additionally, the cytocompatibility (MG63 cell lines) and protein adsorption (Bovine serum albumin, BSA) of selected specimens are also studied to comprehensively understand the delicate relationship between the electrical and biological properties. The protein adsorption is primarily related to the surface charge, and its dependence is found linear. Additionally, the $\epsilon_r$ of the composites is less than 35, which compliments the protein adsorption behavior of the specimens. The amount of adsorbed protein for all the specimens considered in the present study lay in the range of 3-32 $\mu$g/ml. Furthermore, the specimens exhibited excellent cell viability of more than 90%. Based on the physical and biological investigations, $20H - 80S$ is established as the best specimen that blends the characteristic feature of both the monoliths. We also present the conductivity analysis of the composite specimens that are crucial to relate the biological properties with the electrical properties of the composites. The conductivity is very low ($\simeq 10^{-8}$ S/cm), and the porous structure of the composites revealed from the micrographs is one of the factors for such low conductivity. From a plethora of conduction mechanisms, Motts' variable range hopping (VRH) conduction is projected as the most appropriate mechanism that appropriately describes the conduction process in the composites. Mott's VRH is also related to the polarization mechanism associated with the development of electrets. The study points towards the practical potential of applying the designed bio-composites in generating bio-electrets or understanding the electrical properties that are at the forefront of research in designing electro-active smart scaffolds for bone tissue engineering applications.

### 1.11.5 Chapter 5

Chapter 5 investigates the electrically active ceramic composite of HAP and BST for biomedical applications. Based on the studies conducted in the previous chapter on HAP and ST-based composites, this chapter goes a step ahead by introducing $Ba$ in ST. Similar to the approach adopted previously, the chapter proceeds by fabricating a series of composites, focussing on the dielectric and biological properties and their relationships. The article emphasized primarily on extracting the $\epsilon_r$ of the specimens (that lay in the range of 3-65) and related them to microstructural properties like the grain size and At.% of BST. A broad outlook on the importance of $\epsilon_r$ in determining the suitability of bioceramics for clinical applications is presented. Bioactivity analysis of the specimens led to probing the negative surface charges, and it was found crucial to the growth of dense apatite layers. Furthermore, the cytocompatibility of the specimens displayed cell viability above 100% for Day 1, which increased substantially for Day 3.

To reveal other biological properties of the composites, protein adsorption studies using BSA and fetal bovine serum (FBS) were carried out. Electrostatic interactions govern the adsorption, and the mathematical dependence on surface charges is linear. The protein adsorption is also linearly correlated with the $\epsilon_r$, intrinsic to the biomaterials. We delve deeper into protein-biomaterials interactions by considering the evolution of the secondary structure of BSA adsorbed into the specimens. Based on the investigations, 20 At.% HAP-80 At.% BST ($20H - 80B$) was established as a suitable composite comprising the desired features of HAP and BST. Such explorations of electrical and biological properties are interesting for modulating the behavior of bioceramic composites. The results project the suitability of $20H - 80B$ for designing electrically active smart scaffolds for the proposed biomedical applications and are expected to incite further clinical trials. Furthermore, electrical modeling of the ceramic composites is done using the Cole-Cole formalism. The conductivity mechanisms of the composites are also analyzed, and Mott's VRH conduction is the most appropriate formalism that successfully describes the conduction process. The established Mott's VRH is also related to the polarization mechanisms active in the specimens. The study projected an exciting correlation between the electrical and biological properties from the perspective of impedance spectroscopy that will be helpful for biomaterials research.

### 1.11.6 Chapter 6

Chapter 6 has three components, the first part of the chapter deals with the fabrication and analysis of the properties of scaffolds designed explicitly for bone tissue engineering applications. We discuss in detail the fabrication, microstructural analysis, mechanical and biological properties of scaffolds synthesized from composites $20H-80S$ and $20H-80B$. The compositions were endowed with significantly better properties, as evident from the studies conducted in the previous chapters. The microstructural analysis reveals the presence of reflections from both the monoliths and smaller-sized grain in $20H-80S$ ($92.2 \pm 4.5$ nm). This resulted in improved mechanical strength compared to $20H-80B$, which has a larger grain size ($110.3 \pm 5.1$ nm) and higher porosity along with the biomineralization of $20H-80B$ ($Ca/P-1.64$), which is found higher compared to $20H-80S$ ($Ca/P-1.52$). The higher porosity also reflected in high protein adsorption on $20H-8B$. The scaffolds' cytocompatibility revealed the cell viability $> 90\%$ for the entire period analyzed in the experiment.

In the next part, we deal with the thin films prepared from $20H-80S$ composite sputtering target on $Ti$ substrates. We developed three thickness variations of $20H-80S$ thin films. RF magnetron sputtering has been used to deposit the thin films due to its several advantages. Specifically, the ability to deposit stoichiometric thin films with uniformity makes it a deposition technique of choice among researchers. The preliminary studies of the thin films establish that thicker composite films have improved microstructural properties. The films were found to be hydrophobic, and the cytocompatibility analysis complemented the wettability studies by showing improved cell viability of more than 100 % for all the films, which is desirable for inducing various metabolic reactions *in-vivo*. The electrical properties of the thin films are probed by considering the frequency and temperature variation of the dielectric properties. The improved dielectric properties of the thin films augment the biological responses of implants by enabling expedited healing. The mechanism is related to the polarization of the dipoles that forms an exciting study, elaborated in the chapter. Also associated with the polarization are the loss mechanisms that continuously disrupt the polarization, hindering the faster healing process of bone fractures. The study on $20H-80S$ composite films closes with the electrical blueprint of the thin films in the form of a parallel QR circuit (Q denoting constant phase element and R the resistor) obtained by Cole-Cole analysis. Understanding the electrical properties from the biological perspective makes the article interesting and provides fresh insights on the behavior of thin films for designing

bioelectronics gadgets and electro-active implants.

The final part of the chapter deals with bilayered thin films of BST and HAP. On $Ti$ substrate, we develop layered thin films (of 100 nm each) in a way that we deposit HAP films first followed by BST in one set of thin films and the other set deposits BST on the bottom followed by HAP top layer. From a biological perspective, the films were bioactive, hydrophobic, and cytocompatible. The dielectric properties of the films displayed a modest $\epsilon_r$ in the range of $35 - 45$. The article relied on the external stimulations used for treating fractures to divulge the relation between electrical and biological properties. As the coatings (associated with the implants) were dielectric, they inherently underwent polarization under the electric field. This polarized field continued to generate the electric field *in-vivo* even after the removal of the external field. Furthermore, the leakage current in the films unveiled a new way to choose the exposure parameters (of the external stimulations) meticulously based on the properties of the films to minimize the fracture healing time.

### 1.11.7 Chapter 7

Chapter 7 summarizes the entire thesis work. It contains two sections. The first section on Conclusions describes the important conclusion drawn out from the various work performed in the thesis. In the second part, we discuss the scope of the future work and the various extensions that can be explored in the future.

# Chapter 2

# Preparation methods and Characterization techniques

This chapter presents the preparation methodology and measurement techniques used to characterize $Ca_{10}(PO_4)_6(OH)_2$ (HAP), $SrTiO_3$ (ST), and $Ba_{0.5}Sr_{0.5}TiO_3$ (BST) bulk ceramics and their thin films. In the first part of the chapter, we discuss the methodology adopted to prepare the ceramics HAP, ST, and BST. It is followed by the discussing the calcination, sintering, and pelletization process. We then discuss the methodology adopted to extract the microstructural, electrical, and biological properties of the ceramics. Towards the second part of the chapter, we discuss the radio frequency (RF) magnetron sputtering that is used to deposit the thin films.

## 2.1 Preparation of the monoliths: HAP, ST and BST

This section, discusses in detail the procedure adopted in preparing the monoliths. We have used both the solid-state reaction and sol-gel process to process and prepare the monoliths that were later used to prepare the composites. It is worthwhile to mention that the HAP monolith were prepared using the sol-gel process, whereas the ST and BST was prepared using the solid-state reaction method.

### 2.1.1 Sol-gel process for preparation of HAP

The sol-gel process adopted for the preparation of HAP converts monomers into a colloidal solution (known as sol) which acts as a precursor to generating an integrated network (gel) of particles that are discrete or polymers [87]. The advantages

of this technique lie in its cost-effectiveness, low processing temperature, high solubility, control of stoichiometry, and is capable of dispersing the dopants homogeneously. The ability to prepare end products with precise size control, improved microstructure, and density is counted as a significant advantage of this process. Oxide nanoparticles are thus preferred to be prepared using alkoxide precursors by using the sol-gel route [87].

To prepare HAP, we used $Ca(NO_3)_2.4H_2O$ (Sigma Aldrich, USA) and $P_2O_5$ (Sigma Aldrich, USA) precursors and $C_2H_5OH$ (Merck laboratories, India) as the mixing media. The precursors were mixed to maintain the $Ca/P$ at 1.67. This was done by considering two beakers containing 25 mL that are continuously stirred in two magnetic stirrers (Tarsons, India). A stoichiometric amount of the precursors ($Ca(NO_3)_2.4H_2O$ and $P_2O_5$) weighed as per the ratio 10:6 was added into the beakers separately (in stirring mode) naming them as $Ca$ solution and $P$ solution, respectively [88]. By undergoing vigorous stirring for 30 minutes, a complete dissolution of both the components was ensured. With a sufficiently low flow rate, we considered adding together the stirred $Ca$ and $P$ solution so that the resultant solution remained clear at every instant. Following the completion of the mixing process, the solution was stirred continuously for 24 hours and allowed to remain undisturbed for another 24 hours [88]. This process is called the aging of the resultant solution and is crucial for HAP formation. The mixture transforms into a dense transparent gel on successful aging, which was taken up for drying in a hot air oven (Optics Technology, India) at 363 K overnight. The process converted the gel into powder, which was finally calcined (LHT 01/17 D, Nabertherm, Germany) at 773 K for 2 hours to completely remove the unreacted components [88].

### 2.1.2 Solid-state reaction for preparation of ST and BST

We have adopted the solid-state route for synthesizing the monoliths ST and BST. There are several reasons for choosing this procedure. The chief among which is its cost-effectiveness, environment-friendly nature, selectivity of a wide range of precursors such as oxides and carbonates [89]. In this process, it is essential to understand that the starting materials do not react at room temperature, and hence, it is imperative to apply higher temperatures with optimized heating and cooling rates to prepare the finished product. Thus, it is clear that both the thermodynamic and kinetic factors are equally responsible for the solid-state reaction method in which the precursors are observed to react in the absence of any solvent [89].

The second component ST was prepared following the conventionally adopted inexpensive solid-state processing route. The initial precursors required for the preparation consists of $SrCO_3$ (Sigma Aldrich, USA) and anatase $TiO_2$ (Sigma Aldrich, USA), which are mixed in stoichiometric amounts according to the reaction

$$SrCO_3 + TiO_2 \rightarrow SrTiO_3 + CO_2 \uparrow \tag{2.1}$$

The precursors were weighed (AG 135, Mettler Toldedo, Switzerland) and ground repeatedly in a planetary ball mill (Pulverisette 6, Fritsch, Germany) using propanol as the grinding media [88]. The jar used for mixing was made from zirconia, and the balls were of diameter 10 mm made out of the same materials as the jar. The milling of powders was carried out at revolutions per minute (rpm) of 250 for five hours. After repeated grinding, the powders were calcined at 1473 K for 4 h to ensure phase formation and discarding any unwanted components in the resultant powder.

The third component BST is prepared according to the following reaction,

$$BaCO_3 + SrCO_3 + 2TiO_2 \rightarrow 2Ba_{0.5}Sr_{0.5}TiO_3 + 2CO_2 \uparrow \tag{2.2}$$

The initial precursors required for the preparation consisted of $BaCO_3$ (Sigma Aldrich, USA), $SrCO_3$ (Sigma Aldrich, USA), and anatase $TiO_2$ (Sigma Aldrich, USA), which were mixed in stoichiometric amounts according to the above reaction [90]. The grinding conditions were similar to those adopted during the processing of ST. After the grinding, the contents of the ball mill were dried and calcined at 1373 K for 4 h.

### 2.1.3 Preparation of the composites and specimens for analysis

Two composites were considered in the thesis for study. The first series of composites were prepared from ST and HAP. The recipe for preparation for the specimens are summarized in Table 2.1. The precursors' HAP and ST for the composites were weighed according to the stoichiometry and ground finely in a planetary ball mill using propanol for uniformly mixing the components (150 rpm for 5 h) [88]. After ball milling, the contents were dried at an elevated temperature (473 K) to obliterate the propanol. The other series of BST and HAP were prepared following the same procedure and the recipe followed are included in Table 2.2.

**Table 2.1:** The composition of different compact discs and their codes.

| Monolith | Monolith | Scheme | Code |
|---|---|---|---|
| HAP | ST | 100 At.% HAP | HAP |
| | | 20 At.% HAP & 80 At.% ST | 20H-80S |
| | | 40 At.% HAP & 60 At.% ST | 40H-60S |
| | | 60 At.% HAP & 40 At.% ST | 60H-40S |
| | | 80 At.% HAP & 20 At.% ST | 80H-20S |
| | | 100 At.% ST | ST |

**Table 2.2:** The composition of different compact discs and their codes.

| Monolith | Monolith | Scheme | Code |
|---|---|---|---|
| HAP | BST | 100 At.% HAP | HAP |
| | | 20 At.% HAP & 80 At.% BST | 20H-80B |
| | | 40 At.% HAP & 60 At.% BST | 40H-60B |
| | | 60 At.% HAP & 40 At.% BST | 60H-40B |
| | | 80 At.% HAP & 20 At.% BST | 80H-20B |
| | | 100 At.% BST | BST |

Once the composites were prepared, they were converted into compact cylindrical discs. Poly-vinyl alcohol (PVA, Loba Chemie, India) was added to the finely mixed powder, which served as the prepared composites' binding agent. The powders were then pressed into cylindrical green compacts using a hydraulic press (M 30, Technosearch instruments, India), applying a uniform pressure of 25 $kg/cm^2$. Several compacts were prepared for each composition under the same conditions are finally sintered at 1073 K for 3 h for densification and compaction of the resultant cylindrical compacts.

### 2.1.4 Thin films: Preparation and deposition technique

The deposition of thin films is an integral part of our thesis work, and in this section, a detailed description of the deposition technique is provided. Thin films are

defined as three- dimensional entities, such that one of its dimensions (especially the thickness) is in the range of a few nanometres to micrometers. The research interest in thin films is due to their exceptional properties, which are pretty different from their bulk counterparts and attributed to quantum effects with the reducing thickness along a particular dimension. Usually, the deposition of thin films over a substrate takes place atom by atom over nuclei favorably oriented for the incoming atoms to settle down. In general, it is observed that at an initial time, since the atoms deposit over the substrate, the effect of the substrate dominates [86]. Especially in terms of the lattice parameters, that leads to the introduction of strain. With more incoming atoms, as the thickness of the films increase, the substrate effect starts getting insignificant. Thus, it is clear from the discussion that there is a variation in strain with the thickness of the thin film, and gives rise to some of its interesting physical and chemical properties. There are a variety of deposition techniques available in practice, and each has its advantage and associated disadvantages. The thesis focuses on the physical vapor deposition technique viz. radio frequency (RF) magnetron sputtering There are several reasons to adopt this process, and this includes (a) uniform growth of thin films, (b) excellent texture, (c) controlled thickness, (d) excellent mechanical properties, and (e) controllable stoichiometry [91].

Sputtering was initially observed by Grove as early as 1852 [91]. Since then, several developments have been made, and the process has established itself as the most favored technique for the semiconductor industry. There are two variants of sputtering: direct current sputtering (DC) and RF sputtering. DC sputtering is mostly used in the case of metals, and RF sputtering is used in the case of semiconductors or insulators. In the thesis, RF sputtering has been used as the deposition technique to obtain the thin films. Henceforth only the RF sputtering technique shall be discussed in detail [91]. In a sputtering chamber, it is of prime importance to creating a high vacuum (as high as $10^{-6}$ mbar) as it is imperative to have thin films of high purity in order to meet the stringent requirements of device fabrication. Apart from that, the RF sputtering unit contains a cathode where the dielectric materials to be sputtered are fitted in the form of a cylindrical target [91]. The target is prepared in the laboratory to have a diameter $\sim$ 62 mm and thickness 3-5 mm. The substrates ($Ti$, $n$-type Si, and quartz) are attached over a stainless steel circular plate to be fitted in the anode configuration. As shown in Figure 2.1, the distance between the target and the substrate is adjustable, and temperature can be applied to the anode for stoichiometric or microstructural modifications necessary in the

deposited thin films. Below the cathode, a magnetron generates the magnetic field lines parallel to the cathode surface and an electric field normal to the cathode. The combination of the magnetic and electric field in the RF sputtering helps increase the deposition rate by confining the electrons near the cathode so that there is an enhanced ionization in the system. The sputtering usually works by applying an RF power to the anode and the cathode at a frequency of 13.56 MHz. The deposition process is discussed subsequently.

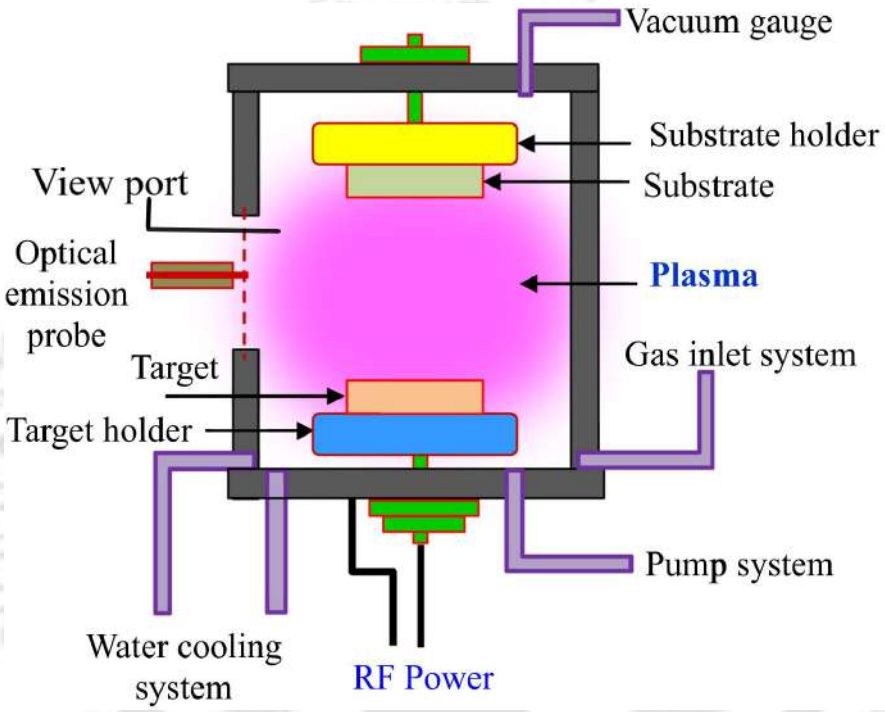


**Figure 2.1:** A schematic diagram of the sputtering operation. The figure is reproduced with permission from [92].

Once the target and substrates were loaded, the deposition chamber was evacuated to a base pressure of $10^{-6}$ mbar. This was accomplished using the turbo-molecular pump in concoction with the rotary pump. Once the pressure levels were reached, $Ar$ was introduced into the deposition chamber so that the pressure levels in the chamber raised to $10^{-2}$ mbar. The introduction of $Ar$ into the chamber was done using a mass flow controller (MFC) that helped to maintain the pressure levels constant at $10^{-2}$ mbar, with the help of a gate valve that remained partially closed, thus helping the pressure levels to be maintained at the specified level by preventing the turbo-molecular pump from driving out all the $Ar$ gas. The plasma was generated by applying an RF power ($\sim$ 50 watts), which started the deposition process. Depending upon the requirements, the RF power was increased or decreased, and

the target to substrate distance adjusted to obtain an optimum level of deposition rate. To determine the deposition rate at a particular power and gas pressure while maintaining the target to substrate distance fixed, the thickness of the deposited layer can be obtained either by taking a transmittance spectrum or by the surface profilometry image of the thin films. An image of the RF sputtering setup available in our laboratory is shown in Figure 2.2. The process of preparing the sputtering target and the substrate has been discussed elaborately in the following section.

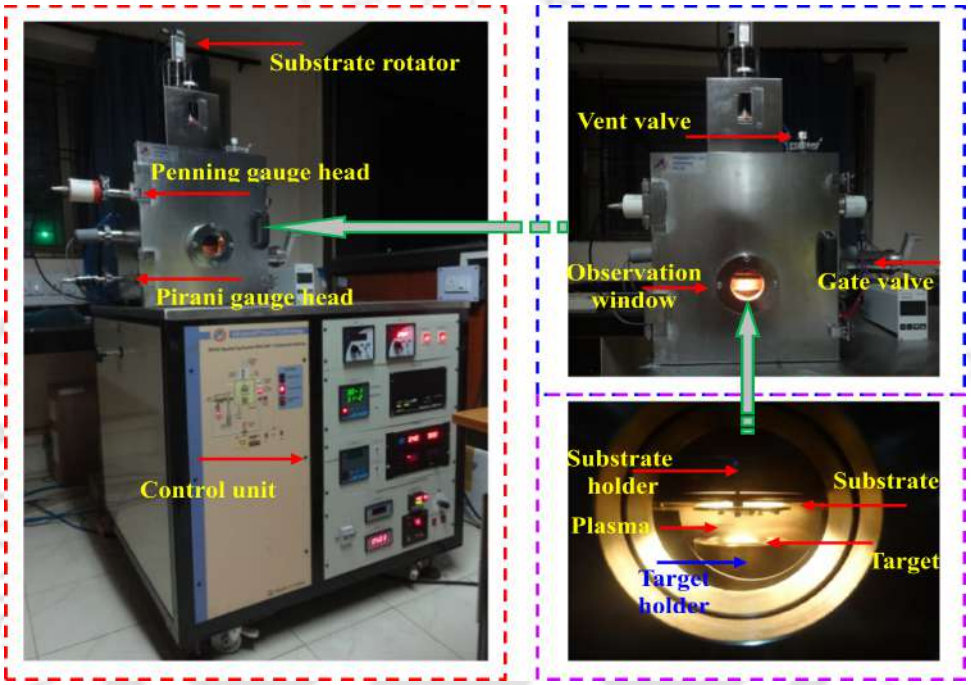


**Figure 2.2:** A view of the RF sputtering unit (Advanced Process Technology, India) available in our laboratory. The figure is reproduced with permission from [92].

### 2.1.5 Preparation of sputtering target

Preparing the sputtering targets was precisely similar to preparing the pellets, as described in the previous section. For the thesis work, we have prepared three sputtering targets. One is a composite target of $20H - 80S$, and the other two are HAP and BST sputtering targets, respectively. For preparing the composite target, 40 grams of $20H - 80S$, prepared by the process described in the previous section, was considered and adequately ground in an agate mortar, simultaneously adding PVA that serves as the binding agent. The powder was then pressed in a die of diameter 62 mm to convert it into a sputtering target. The green target was finally

sintered at 1273 K for three hours to achieve compaction. The process converted the green target into the sputtering target of diameter 62-64 mm and thickness 3-5 mm. A similar procedure prepared the HAP and BST targets. After preparing the HAP and BST powders as described in the previous section, the process of adding PVA was carried out. In both cases, 40 grams of powder was taken and converted into cylindrical targets for the final deposition of the thin films.

### 2.1.6 Preparation of the substrates

Three substrates have been used in the entire thin film deposition process. $Ti$, $n$-type Si, and quartz have been used to deposit and characterize the thin films. $Ti$ has been chosen for the thin films' deposition due to their biocompatibility with additional properties such as high strength, rigidity, fracture toughness, and reliability based on mechanical properties. The properties of $Ti$ allow them to be a suitable replacement for hard tissues. The $n$-type $Si$ has been used for the deposition process solely to extract the electrical properties of the films; the conductive $n$-type $Si$ allows the films to be deposited in capacitor configuration. With a top electrode over the deposited thin film, the electrical properties can be extracted to correlate them with the thin films' biological properties. On the other hand, quartz is a transparent substrate and allows the extraction of the optical properties of the thin films.

However, it must be noted that the thin films need a unique preparation process before the film deposition can be carried out. Substrates of appropriate dimensions (1 cm x 1 cm) must be cut out from the larger dimensional wafers/sheets and cleaned thoroughly. For the $Ti$ substrates, the cleaning process consists of mechanical polishing using silicon carbide papers of various grit sizes starting from 200, 500, 700, 1000, and 1200 to smoothen the surface and remove any dirt that might have adhered on the surface. It was followed by ultrasonic cleaning in three solvents in the order: deionized water: acetone, propanol-2. The sonication process was carried out for 30 minutes with each of the solvents, after which the substrates were dried using an air blower in a clean environment. The exact process was repeated for each of the solvents. Once the process was completed, the substrates were stored in a vacuum desiccator until they were introduced into the sputtering chamber for deposition. The $n$-type $Si$ and quartz substrates need not be mechanically polished and required only ultrasonic cleaning using the three solvents in the same order as detailed previously.

## 2.2 Characterization of the composites and monoliths

### 2.2.1 Structural characterization

In the thesis, the structural characterization of the composites and the monoliths has been accomplished using the X-ray diffraction (XRD) technique. XRD is versatile and non-destructive structural characterization tool that provides a plethora of information regarding the materials' property and their behavior. In the thesis, two XRD sources have been used. The first of these used a $Cu$ source of wavelength $\lambda = 1.5406\mathring{A}$ (Xpert$^3$ MRD XL, PANalytical, UK). This diffractometer used the Bragg-Brentano geometry ($\theta - 2\theta$ mode) to perform temperature variation XRD measurements for the monolith HAP. The data was collected in the $2\theta$ range of $20 - 55°$. The X-ray photons at a step size of 0.01° were collected with a scan time of 1s. Temperature variation of the specimens was achieved by heating the specimen stage starting from 303 K to 573 K. The temperature variation XRD data were later refined using the Rietveld refinement program by the FullProf software. The other diffractometer used for collecting the room temperature data also used a $Cu$ source of wavelength $\lambda = 1.5406\mathring{A}$ (TTRAX III, Rigaku, Japan). The diffractometer used a scintillation detector to collect the X-ray photons arranged to rotate along the circumference of a vertical circle. A $Ni$ filter was used to cut off the $K_\beta$ from the $K_\alpha$ radiation. The sample stage for the diffractometer was placed precisely at the center, and the goniometer was provided for the rotation of the source and detector. For the thin films, the data was collected in the $2\theta$ mode, and the rest of the details were the same as in the case of bulk specimens. In this mode, the X-ray source does not move but was fixed in such a way that the x-rays were incident on the thin films at a glancing angle of 0.5°. It was to ensure that the diffraction pattern was mostly comprised of the thin films and not from the substrate. Finally, the identification of the different (hkl) planes apparent from the XRD was accomplished by comparing with the International Centre for Diffraction Data (ICDD).

### 2.2.2 Surface morphology and Microstructure

The surface morphology and the microstructure of the composites and monoliths were analyzed using field emission scanning electron microscopy (FESEM) (Sigma 300, Zeiss, Germany). The microscopes work under secondary electron mode to probe the microstructure of the composites and the monoliths and the thin films used in the thesis. For the analysis of the elementary compositions, an elementary

dispersive X-ray spectroscopy (EDS, Oxford Instruments, UK) was used that comes as an attachment with the FESEM. The principle of detection of the elementary atomic composition is intriguing and involves the use of X-rays emitted from the specimen. During the analysis, when the electrons from the source of FESEM hit the specimen, the inner electrons of the specimens are knocked out, resulting in the creation of inner vacancies. These are later filled by an outer electron making an immediate transition to the vacant sites. As a result, an X-ray photon is released and detected in the EDS. The energy of the photons is unique to the elements present in the specimen. This phenomenon helps in the identification/detection of the possible elements present in the specimen.

The specimen preparation part was exciting as the samples, in our case, are insulating. So to get the FESEM images, a thin layer of platinum ($\sim$ 10 nm) was coated by sputtering over the surface that will be exposed to the electrons coming from the source. A similar methodology was also adopted for the EDS of the specimens. For the thin films, the specimens deposited over the $Ti$ substrates were used that are specially prepared to have dimensions of 2 mm x 5 mm. Similar to the bulk specimens, a thin layer of platinum was coated over the specimens. They were attached to the FESEM sample holder using a double-sided carbon tape conducting in nature.

Atomic force microscopy (AFM) is another characterization technique that has been used to generate a 3D surface profile of the samples on the nanoscale. The AFM works by measuring the force between the tip of the probe that remains attached with a cantilever and the surface of the thin film specimen [93]. The AFM probe raster scans the specimen's surface based on a predefined program controlled by a controller unit. The surface topography of the specimen is thus generated using the signal processing unit based on the interactions between the atoms at the tip and the surface of the specimen. In the scanning process, when the tip of the AFM is brought close to the specimen, the Van der Wall's force acting between the tip atoms and the surface atoms deflects the cantilever [93]. A laser reflection detects the deflection, and this information is fed to a photodetector. The photodetector instructs the electronic feedback circuit connected to the AFM tip to keep the force constant between the surface and the tip. These feedback signals are utilized to generate the 3D image of the specimen with both phase and amplitude. In the thesis, the AFM images of the specimens were generated using an Atomic Force Microscope (Cypher, Oxford Instruments, UK). The image processing was done using the Gwyddion software.

### 2.2.3 Raman, Photoluminiscence and time resolved photoluminiscence Analysis

Raman Spectroscopy is another non-destructive technique used to obtain a plethora of information regarding the specimens. Raman analysis does not require any specific sample preparation. Usually, it probes the molecular vibrations to generate the Raman spectrum, which is a plot of the Raman intensity (in arbitrary units) versus the Raman shift (wavenumber units). The sample for analysis is irradiated with a monochromatic laser beam, and the incident light scattered from the specimen is collected to generate the spectrum. When the monochromatic radiation interacts with the specimen, inelastic scattering of the laser light leads to a change in the frequency of the scattered light [94]. Generally, the scattered radiation has a frequency higher than the incident light (Anti-Stokes radiation) or lesser than the incident radiation (Stokes radiation). Also, it contains a fraction of the radiation that will have frequency unchanged. The unchanged frequency is due to elastic scattering of the laser photons and leads to Rayleigh scattering [94]. As the intensity of the Stokes radiation is higher than the Anti-Stokes radiation, the Raman spectrometer records only the Stokes photons. The Anti-Stokes photons are used for generating the fluorescence spectra, as the Stokes radiation is found to significantly overlap with the fluorescence bands [93]. It is interesting to note that the Raman shift is independent of the wavelength of the incident radiation and has the advantage that, like XRD, the spectrum can be generated with the specimens being constantly heated or cooled. The temperature variation Raman spectra are critical for generating information relating to structural phase transitions of the specimens. In the thesis, the room temperature Raman measurements (Jobin Yvon LabRAM, Horiba, Japan.) were performed using an $Ar$-ion laser of wavelength 514.5 nm. The temperature variation Raman was performed using a source for wavelength 488 nm, and the temperature was varied from 303 K to 573 K at an interval of 10 K with an exposure time of 10s. The temperature variation in the specimen stage was carried out by heating the sample at 10 K/min. In both cases, the scattered photons were collected in the wavelength range of 100 to 1200 $cm^{-1}$. A highly sensitive charge coupled device (CCD) detector detects the intensity of scattered Raman light. Before the operation, the Raman spectrometer was calibrated using a standard Silicon wafer for which a shift was obtained at 523.88 $cm^{-1}$.

The photoluminiscence (PL) spectra were recorded with the same Raman spectrometer with which the Raman spectra were recorded. The temperature variation

PL (t-PL) spectra were obtained sequentially at 10 K from the same spot in the sample using the same laser source of 488 nm. The time-resolved PL (TRPL) spectra were obtained with a laser excitation of 475 nm closest to the laser used for the PL spectra. A picosecond time-resolved luminescence spectrometer (FSP920, Edinburg Instruments, UK) was used for recording the TRPL spectra with an instrument response time of ∼50 ps.

### 2.2.4 Dielectric and electrical characteristics

Impedance analyzer (4991A, Agilent Technologies, USA) was used to analyze the dielectric properties, which measures the dielectric constant ($\epsilon_r$) for the frequency range 1 MHz-1 GHz. The impedance analyzer has the added advantage of measuring $\epsilon_r$ with respect to temperature variation (133 K-523 K). The temperature variation was carried out using a temperature control system (BDS 2300 Novocontrol, Germany), which used liquid nitrogen to produce temperature variation. The frequency sweep was carried out once the temperature stabilized after an interval of 10 K starting from 133 K. It is worth mentioning that the interval of 10 K is chosen as a matter of convenience for collecting the data by using the temperature variation program. The sample for measuring the $\epsilon_r$ was a cylindrical disc prepared by the procedure described in the previous section. Once the compact cylindrical discs were obtained after the sintering, they were converted into capacitors of metal-insulator-metal (MIM) configuration. This is done by coating a layer of silver (from silver paste procured from Sigma Aldrich, USA) on both the plane faces of the cylindrical disc. After coating the silver, the capacitors were dried in an oven at 423 K to solidify the silver paste. Once the silver paste dried, it was ensured that proper continuity was established for the coated silver paste. Finally, the capacitors were loaded into the sample holder and inserted into the temperature control chamber for the frequency variation of the $\epsilon_r$ at different temperatures.

An LCR meter (1J43100, Wayne Kerr, UK) was also used for recording the variation of $\epsilon_r$ at lower frequencies from 10 Hz-1 MHz. The specimen for the LCR meter was of the same configuration as mentioned previously. The variation in the $\epsilon_r$ was measured using the LCR meter for the thin films. The LCR meter has a slightly modified sample holder for the thin film. However, the thin film samples were considered in the metal-oxide-semiconductor (MOS) configuration. Silver electrodes were deposited on the thin films using sputtering to convert the thin films to the capacitor. These samples were then used for recording the variation of the

$\epsilon_r$ with frequency at different temperatures. Along with the $\epsilon_r$, the conductivity of the specimens (thin films and cylindrical discs) were also measured with variations in the frequency and temperature. During the measurement of $\epsilon_r$, $tan\delta$ and conductivity, the impedance's real and imaginary part of the impedance (viz. $Z'(f)$ and $Z''(f)$) were also measured, which was essential for the Cole-Cole analysis using the ZSimpWin software (Princeton Applied Research, USA). The Cole-Cole plot is a significant analysis that helps generate the specimens' electrical blueprint under analysis. The analysis is especially useful for directly correlating the complex dielectric system to an idealized model circuit consisting of discrete circuit elements such as capacitors and resistors. These models can be useful in understanding the electrical nature of the biomaterials and is of immense importance in designing bioelectronics gadgets where accurate mapping of the electrical properties is of utmost necessity.

The current-voltage (I-V) characteristics of the thin films were measured in a Keithley Parametric analyzer (4200A, Tektronix, USA). For the measurements, the thin films were converted to MOS capacitors as described previously.

### 2.2.5 Determination of thickness of thin films

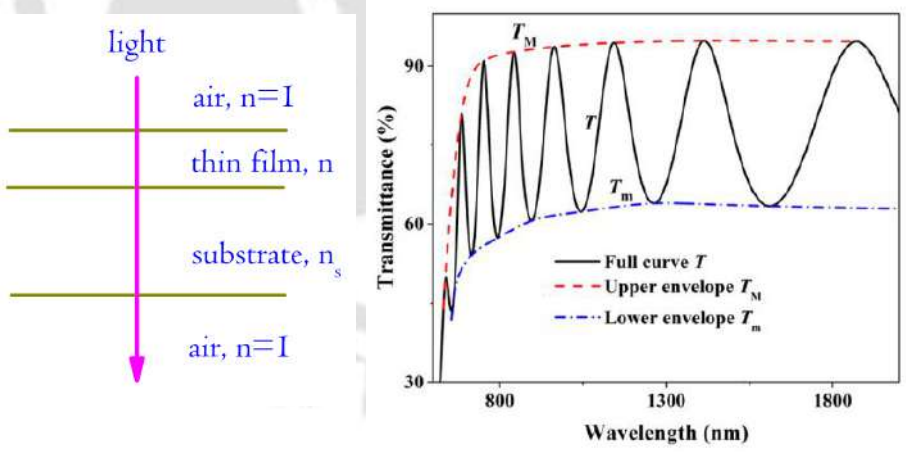


**Figure 2.3:** Illustration of the interference pattern in thin films and the corresponding transmittance spectra. The different values of $n$ represents the characteristic refractive index of the different layers.

Measurement of the thickness of the thin films is an important analysis and involves the use of two methods. In one such technique, a surface profilometer (Vecco Dektak 150, USA ) was used where a diamond tip stylus was used for scanning the

thin films. In this process, a stage carrying the thin film specimen moves with high precession so that the tip can scan the specimen for its thickness. The sample was prepared in a way that a portion of it is masked from the deposition. As the tip scans the specimen, the tip has to make vertical displacements in order to scan the surface variations. These precession displacements are converted to electrical signals, which are further converted into digital signals that can be displayed on a screen. The analysis time and the resolution of the displacements can be tuned with the help of adjustable parameters such as scan length and speed which can be user controlled by specific programs in the computer.

In addition, the transmittance was also measured by the the ultraviolet-visible (UV-Vis) (Lambda 950, PerkinElmer, USA) spectrometer by scanning the specimen in the wavelength range of 200-1500 nm that gave us the thickness of the thin films using the Swanepoel envelope method [95]. When the thin films deposited on a transparent substrate is exposed to light in the specified wavelength, it undergoes interference as the reflected and the transmitted light originated from the coherent source in the spectrophotometer. As shown in Figure 2.3, the condition for maxima in the interference pattern is

$$2nd = m\lambda \tag{2.3}$$

where, $m$ is the order of the interference, $n$ is the refractive index of the material of the thin film and $d$ is the thickness. Now, the refractive index of the thin films can be calculated using the following equation

$$n = (N + (N^2 - n_s^2)^{1/2})^{1/2} \tag{2.4}$$

where,

$$N = 2n_s \frac{T_M - T_m}{T_M T_m} + \frac{n_s^2 + 1}{2} \tag{2.5}$$

and

$$n_s = \frac{1}{T_s} + (\frac{1}{T_s^2 - 1})^{1/2} \tag{2.6}$$

here, $T_M$ and $T_m$ are the transmittance maxima and minima as shown in Figure 2.3. $T_s$ denotes the transmittance of the transparent substrate without the thin film. The rest of the quantities are already illustrated in Figure 2.3. Now, if $n_1$ and $n_2$ are the refractive index of the thin film at two successive maxima at wavelengths $\lambda_1$

and $\lambda_2$, then the interference maxima condition modifies to

$$2n_1 d = m_1 \lambda_1 \tag{2.7}$$

and

$$2n_2 d = m_2 \lambda_2 \tag{2.8}$$

Solving the above two equation (knowing that $m_2 - m_1 = 1$), we can determine the unknown thickness d of the thin films according to the following equation

$$d = \frac{\lambda_1 \lambda_2}{2(n_1 \lambda_2 - n_2 \lambda_1)} \tag{2.9}$$

### 2.2.6 Preparation of SBF and bioactivity analysis

Simulated body fluid (SBF) is the most favored solution for evaluating the bioactivity in materials. Specimens incubated in SBF that are capable of inducing bone-apatite on their surface are termed bioactive. The bioactive surfaces show enhanced biological properties due to their capacity to bond with the soft tissues mediated by forming a bone-like apatite layer. SBF simulates the inorganic component of the human blood plasma. This is ensured by maintaining the concentration of the ions in SBF so that it replicates the inorganic component of the blood plasma. To achieve the target, the methodology adopted for preparation on SBF is followed from Kokubo and Takadama and the preparation procedure is elaborated below [96].

In preparing the SBF, we followed the exact procedure reported by Kokubo and Takadama with the minor modification that the concentration of the SBF prepared for the thesis was 1.5 times higher than the SBF prepared by Kokubo and Takadama [96].The reagents required in preparation of the solution are listed below:

a) Sodium Chloride ($NaCl$) from Sigma Aldrich, USA.

b) Sodium Hydrogen Carbonate ($NaHCO_3$) from Sigma Aldrich, USA.

c) Potassium Chloride ($KCl$) from Sigma Aldrich.

d) Di-Potassium hydrogen phosphate trihydrate ($K_2HPO_4$) from Sigma Aldrich, USA.

e) Magnesium Chloride Hexahydrate ($MgCl_2.6H_2O$) from Sigma Aldrich, Japan.

f) Calcium Chloride ($CaCl_2$) from Sigma Aldrich, India.

g) Sodium Sulfate ($Na_2SO_4$) from Merck, Germany.

h) Tris-Hydroxymethyl Aminomethane ($(HOCH_2)_3CNH_2$) from Sigma Aldrich, USA.

i) 1 M Hydrochloric acid from Merck, India.

**Table 2.3:** Reagents required for preparation of 1.5 SBF.

| Order | Reagents | Weighing apparatus | Molecular mass (g/mol) |
|---|---|---|---|
| 1 | $NaCl$ | weighing paper | 58.4430 |
| 2 | $NaHCO_3$ | weighing paper | 84.0068 |
| 3 | $KCl$ | weighing bottle | 74.5515 |
| 4 | $K_2HPO_4.3H_2O$ | weighing bottle | 228.2220 |
| 5 | $MgCl_2.6H_2O$ | weighing bottle | 203.3034 |
| 6 | $CaCl_2$ | weighing bottle | 110.9498 |
| 7 | $Na_2SO_4$ | weighing bottle | 142.0428 |
| 8 | Tris | weighing paper | 121.1356 |
| 9 | 1 M $HCl$ | syringe | - |

We intended to prepare 1000 ml of 1.5 SBF. A scratch-free plastic beaker (Tarsons, India) containing 700 ml of distilled water along with a stirring bar was introduced into a heating magnetic stirrer (AN-MSH-680, Antech, India). The pH measuring electrode of the pH meter (pH700, Eutech Instruments, Singapore) was introduced into the beaker, and the initial pH value was recorded. By increasing the temperature of the magnetic stirrer in small steps, it was adjusted to 309.5 $\pm$ 1.5 K. The reagents in sequential order as mentioned in Table 2.3 were added one by one. For comparison with 1.5 SBF, the ionic concentrations of blood plasma and calcium phosphate solution are presented in Table 2.4.

When the temperature of the solution reached 309.5 $\pm$ 1.5 K, we start adding the reagents one by one, ensuring that the reagent added earlier was fully dissolved before the next one was added. This was done to ensure that no precipitation occurs when the solution was being made. The pH of the solution after adding each reagent was noted. While adding $CaCl_2$, extreme care should be taken because $CaCl_2$ is available in granular form and takes much time to dissolve. It plays a great role in apatite precipitation, so we must look out that one granule dissolved completely before the other one was added. The reagents such as $KCl$, $K_2HPO_4.3H_2O$, $MgCl_2.6H_2O$, $CaCl_2$, $Na_2SO_4$ should be measured in weighing bottles in an as short time as possible because these are hygroscopic. Once reagents from 1 to $8^{th}$ order have dissolved completely, the pH of the solution was adjusted between 2.0 $\pm$ 1.0. This was done by adding $HCl$ drop by drop, taking note of the pH change after the addition of each drop. Once the pH was adjusted to the desired value, we started adding Tris, maintaining the temperature of the solution between 308 and 311 K. After adding

a little amount of Tris, the pH was allowed to reach a constant value before adding more amounts. Once the pH reached $7.45 \pm 0.05$, we made sure that the temperature of the solution was maintained at $309.5 \pm 0.05$ K. Now, we started adding $HCl$ drop by drop in a syringe to bring down the pH to $7.42 \pm 0.01$, taking care that the pH does not decrease below 7.40. The remaining amount of Tris was to be added alternately with $HCl$ so that the final pH was exactly 7.40 at 309 K.

**Table 2.4:** Comparison of ionic concentrations of 1.5 SBF, SBF, and blood plasma.

| **Ion** | **Blood plasma** | **SBF** | **1.5 SBF** |
|---|---|---|---|
| $Na^+$ | 142.0 | 142.0 | 213.0 |
| $K^+$ | 5.0 | 5.0 | 7.5 |
| $Mg^{+2}$ | 1.5 | 1.5 | 2.25 |
| $Ca^{+2}$ | 2.5 | 2.5 | 3.75 |
| $Cl^-$ | 103.0 | 147.8 | 221.7 |
| $HCO_3^-$ | 27.0 | 4.2 | 6.3 |
| $HPO_4^{2-}$ | 1.0 | 1.0 | 1.5 |
| $SO_4^{2-}$ | 0.5 | 0.5 | 0.75 |
| pH | 7.2-7.4 | 7.40 | 7.40 |

The pH electrode was then removed from the solution, rinsed thoroughly with distilled water, and the washings added to the solution. The as-prepared solution was then transferred into a volumetric flask of 1000 mL capacity. The beaker was then thoroughly rinsed with distilled water, and the washings were again added to the final solution. Deionized water was finally poured into the volumetric flask to adjust the solution to 1000 mL. Closing the lid of the flask with a plastic cover it was allowed to cool naturally for some time and finally transferred into a refrigerator. This solution prepared can be used to deposit bone-like apatite for 30 days from the date of preparation.

The motive was to obtain bone-like apatite layers under physiological conditions. So the deposition was to be carried out at 310 K. For this purpose, we used hot air oven to maintain the temperature at our desired value. However, before immersing substrates, the 1.5 SBF solution stored in the refrigerator was to be heated up to raise its temperature to 310 K. We took a small amount of the solution in a plastic beaker and heated it using the magnetic stirrer. Once the temperature of the sensor indicated 310 K, the heating was stopped, and the solution was poured into small plastic watch boxes which were being numbered serially using a code. With forceps,

the cylindrical discs and $Ti$ substrates were carefully taken out from the petri dish and dipped into the solution. The petri dish was then sealed and placed in the ultrasonic bath setting its temperature to 310 K. To obtain apatite layers at an enhanced deposition rate, we refreshed the solution in the petri dish every 24 hours. The old solution inside the petri dish was removed using a syringe, and new 1.5 SBF solution was introduced, taking care not to disturb the position of the specimens. Once finished, the petri dishes were sealed again and returned to the temperature bath. Allowing the films to deposit for 12 days, the specimens were removed one by one with forceps, rinsed in deionized water, dried with a blower, and finally stored in a hot air oven for 24 h with the temperature is adjusted to 333 K. The dried specimens were finally analyzed using FESEM and XRD to check the growth of bone-like apatite.

### 2.2.7 Protein adsorption and zeta potential measurements

Following the biomineralization process, the protein adsorption of the ceramic composites is one of the most important analysis that we considered for analyses of the biological properties of the specimens. Bovine serum albumin (BSA), and fetal bovine serum (FBS), were used as the model protein for analyzing the protein adsorption on the surface of the synthesized discs. The procedure for studying the adsorption of proteins is discussed in brief. To start, BSA (500 $\mu$g/mL, Sigma Aldrich, USA) and FBS (10 % v/v, Sigma Aldrich, USA) solution were prepared in phosphate buffer saline (PBS) [27]. The specimens (compact discs) were weighed and incubated in protein solution for one hour at room temperature for adsorption. The adsorbed protein was desorbed from the specimens by immersing them in 5 % sodium dodecyl sulfate (SDS, Sigma Aldrich, USA) solution by shaking incubation (180 rpm) at 310 K for another one hour. The Bicinchoninic acid assay (BCA Assay kit, Sigma Aldrich, USA) was used to quantify the adsorbed proteins by measuring the absorbance at 562 nm using a microplate reader (Infinite 200 Pro, Tecan, Switzerland). The change in the secondary structure of the adsorbed proteins was further studied using the Fourier transform infrared (FTIR) analysis. The analysis was performed by recording the FTIR spectrum (Spectrum Two, Perkin Elmer, USA) in the Amide-I region (1590-1710 $cm^{-1}$). The observed spectra in the region were fitted with Gaussian curves to obtain the relative percentage of the secondary structures ($\alpha$-helix, $\beta$-sheet, $\beta$-turn, random coils, and side chains).

Protein adsorption is one of the preliminary events that take place on the surfaces

of biomaterials when they are implanted *in vivo* [88]. In fact, the human blood plasma contains numerous proteins, and a dynamic protein exchange will take place on the surfaces when these proteins adhere to the biomaterials. It has been observed that the preferential adsorption of proteins on the surface of the biomaterials, such as the bone-related proteins, might be related to the osteoinduction of the specimens. Albumin is one of the most abundant proteins in the blood plasma [97]. BSA has been used to test the protein adsorption behavior of ceramics as the analog of albumin. BSA is also known as the globular protein. The other protein FBS is a widely used component in cell culture studies [98]. BSA is the major component of the FBS. Analyzing the secondary structure of proteins is an essential component of proteins adsorption. In general, the Amide-I band has been used to quantify the secondary structure of the proteins [99]. However, analyzing the secondary structure in the Amide-I region is a complex phenomenon and involves the deconvolution or resolving of the overlapping bands since the Amide-I region is single broadband [98]. The deconvolution of the Amide-I band has been achieved through the Origin software (Origin lab corporation, USA). The associated procedures and techniques are discussed at appropriate places in Chapter 3 and Chapter 4 of the thesis.

The zeta potential measurements were performed in a Litesizer particle size analyzer (Litesizer 500, Anton Paar, Austria) by dispersing the powdered form of the ceramics in deionized water and/or PBS at pH 7.4.

### 2.2.8 Cytocompatibility

The 3-[4,5-dimethylthiazol-2-yl]-2,5-diphenyltetrazolium bromide (MTT) assay on specimens at varying concentration of the specimens (for instance 0.5, 0.2, and 0.1 mg/ml), was carried out in sterilized MilliQ water on MG63 bone-like cell line in a 24 well plate [100]. $1 \times 10^4$ cells/well were seeded in each well and incubated for 24 hours. Cells were incubated in Dulbecco's Modified Eagle Medium (DMEM) supplemented with 10 % FBS and 1 % Penstrap antibiotic in a $CO_2$ incubator at 5 % $CO_2$ and 310 K, after which the material was seeded into the wells. After each specified time interval, 20 $\mu$L of MTT (0.5 mg/mL) was added to the wells after removing the consumed DMEM media and incubated in a $CO_2$ incubator for 4 h. Post incubation, the formed formazan crystals were dissolved in 100 $\mu$L filtered dimethylsulfoxide (DMSO). Absorbance was measured at 570 nm (Infinite 200 Pro, Tecan, Switzerland). Cell viability (%) was calculated and compared to control wells (cells without any material incubation), taken as 100 %.

MTT assay was first introduced in 1983 by Tim Mosmann and is very useful for the determination of the cell viability, toxicity, and cell proliferation [101]. The assay is fast and can be rapidly performed on a microplate assay and read on a spectrophotometer at an absorbance of 573 nm [97]. In MTT assay, the tetrazolium MTT is reduced to insoluble formazan by the action of the cell lines, which are solubilized and liberated and are readily quantified colorimetrically [88]. For determining cytocompatibility, the MG63 cell lines have been used primarily due to their similarity to human osteoblasts. For many years now, MG63 cell lines have been used as a primary model for bone research. These cell line share similarities with primary osteoblasts, such as expression of most integrin subunits, similar internal cellular structures organization, and can adhere to physically and chemically modified surfaces [102]. It makes MG63 cell lines extremely useful for *in-vitro* analysis of biomaterials properties. Moreover, the cell lines allow numerous biological repeats, and the reproducibility of results can be an important factor behind choosing any cell lines for biological analysis.

## 2.3 Field emission transmission electron microscopy analysis (FETEM)

Field emission transmission electron microscopy (FETEM) is a critical microstructural analysis and can be used to reveal several crucial pieces of information about the specimen under study. FETEM is a highly specialized imaging technique that spans several orders of magnitude in magnification ranging from $\mu$m to nm. The latest developments in state-of-the-art technology relating to TEM have enhanced the spatial resolution and the chemical analysis of the specimens. A FETEM is typically used with an energy dispersive spectrometer and a mapping arrangement that helps to determine the chemical composition and the distribution of the elements in different portions of the specimen. The mapping of high-resolution surface features of the specimens is commonly known as the scanning transmission electron microscope (STEM), and such features make FETEM a unique tool to characterize the nanostructures with pinpoint accuracy in the imaging part with the highest spatial and energy resolutions.

The working principle of the FETEM (2100F, JEOL-JEM, Japan) involves an electron source that produces an electron beam traveling through a vertical column under a vacuum. Electromagnetic lenses are used to focus the electron beam to a

very tight spot, and this beam is allowed to pass through the specially prepared specimen. The directed electron beam interacts with the specimens and hits the detector positioned below the specimen holder. A fluorescent screen is attached with the detector to facilitate the operator for searching of the samples dispersed on the grid. Since the TEM analysis is based on the electron beam passing through the specimen, the specimen must be made as thin as possible. It involves a particular set of procedures that must be followed while preparing the specimen for analysis. Analysis of powdered specimens is straightforward and involves using grids that are commonly available in the market at affordable prices. The grid is a circular frame designed from metal with a carbon film layer over it. In the thesis, the specimens (in powdered form) were dispersed in a solvent (either acetone or propanol-2), and the solution was sonicated for at least an hour. Following sonication, the solution was cast on the grid using a micropipette. The grid was then dried in a hot air oven overnight at 343 K. The grid is then loaded in the sample holder and inserted into the slot for loading specimen in TEM. Following the insertion, the vacuum pump is started in the TEM setup, and after the vacuum reaches a predefined level, the beam is switched on to analyze the specimen. Also, the high-resolution TEM images are usually captured at a resolution of 1-10 nm provides the images of lattice planes, which can be used to calculate the interplanar spacings correlated to the ICDD patterns relating to the XRD analysis.

## 2.4 Conclusions

This chapter briefly discussed the various experimental techniques and processes used in the thesis work. The process is concisely described, targeting the generalized procedure of specimen preparation and the characterization technique adopted in the thesis. However, certain precise conditions and parameters chosen during the measurement have been detailed at appropriate places in the subsequent chapters. The chapter provides the framework for understanding the results presented in the following chapters and would be helpful for the reproduction of the results.

# Chapter 3

# Defect dynamics, origin of photoluminescence and temperature dependent $OH^-$ dipoles orientation in synthetically derived Hydroxyapatite

This chapter presents the preliminary investigation of the properties of Hydroxyapatite ($Ca_5(PO_4)_3OH$, HAP) which forms the backbone of the thesis work. The preparation methodology is elaborated and is further supplemented with the analysis of crucial properties such as its photoluminescence (PL) and time-resolved PL. The temperature-induced dynamics in HAP is another focal point of the entire chapter. These studies have rarely been investigated in literature and form the basis for application in several biomedical imaging devices.

## 3.1 Introduction

HAP having a non-stoichiometric composition due to impurities and with a disordered arrangement of $OH^-$ ions, naturally crystallizes to hexagonal ($P6_3/m$) structure [52, 103–106]. The stoichiometric composition and ordered arrangement of

The contents of this chapter is under review as A. Das, P. Dobbidi, and B. L. Chittari *Defect dynamics, origin of photoluminescence and temperature dependent $OH^-$ dipoles orientation in synthetically derived Hydroxyapatite* in Physical Review Materials.

$OH^-$ ions make the HAP acquire monoclinic ($P2_1/b$) symmetry [38, 107, 108]. Interestingly, the synthetically derived HAP is predominantly interpreted as mixed-phase of monoclinic (23%) and hexagonal (77%) by the National Institute of Standards and Technology (NIST) [53, 109, 110]. In a polymorphic structure, where both the monoclinic and hexagonal arrangement is fused, the dominant fraction of a monomorph dictates the properties. Individually, in the monoclinic phase, the $OH^-$ dipoles lying in columns parallel to the [101] plane are all arranged in the same direction [111]. The dipoles in the next plane along the [010] direction are directed opposite, thereby generating an "anti-ferroelectric-like" arrangement [112]. Furthermore, the hexagonal phase has dipoles arranged in different orientations, generating a disordered "para-electric-like" arrangement [113]. These properties make the synthetically derived HAP an interesting polymorph that can be switched by tuning the two-phase in a specimen during the synthesis [113–116].

Recently, the formation of the monoclinic phase has been associated with the low-temperature synthesis process ($\leq$ 373 K) [117]. The structural defects in HAP (vacancies in $Ca$ and $O$ sites being most common) is mainly related to the synthesis procedure that endows it with the exciting prospect of PL. The display of luminescence by HAP can open new possibilities for biomedical imaging and diagnostics that constantly demand biologically favorable materials that do not induce any toxic response to the host. In this regard, researchers have considered rare-earth dopants in HAP for tuning the PL response to the desired level [118]. Unfortunately, the toxicity associated with rare earth elements limit its commercialization in medical diagnostics. Instead, luminescence in defect-induced polymorphic HAP at physiological temperature (310 K) offers the most innovative approach with the additional possibility of temperature modulated tunability for biomedical imaging.

This chapter presents the synthesis of HAP polymorph and shows the possibility of switching between two phases under mild temperatures. Further, we used Rietveld refinement to establish the phases in the synthesized polymorphic HAP. We explore the temperature-induced effects in polymorphic HAP using the temperature-dependent X-ray diffraction (t-XRD) and temperature-dependent micro-Raman spectroscopy (t-Raman). The HAP shows a rearrangement of $OH^-$ ions with temperature under micro-Raman and dielectric spectroscopy measurements that detected the local distortions of $OH^-$ ions. The Arrhenius plots (a derivative of dielectric spectroscopy), which determine the activation energy ($E_a$), are used to probe the dynamics of $OH^-$ motions (dipole) induced by the temperature. The Physics of defect structures in HAP have been probed using PL and supplemented by the electronic

structure calculations using ultraviolet-visible (UV-Vis) spectroscopy. Interesting dynamics of defects inherent in HAP are correlated to the observation of PL. Such optical response of HAP makes it an exciting candidate in bio-imaging, adding more dimensions to its versatility.

We firmly believe that the properties of HAP vastly remain unexplored to this date. Specifically, very few studies are dedicated to the temperature-induced changes in polymorphic HAP. To bridge the gaps in the literature, we explored in detail the temperature-induced changes in HAP that can reveal the undiscovered fundamental properties of HAP. Series of exciting correlations were found in associating the dynamics of $OH^-$ reorientations through XRD, Raman, and Dielectric spectroscopy. Moreover, the scarcity of available data for temperature variations in PL studies prompted us to explore the detailed mechanisms, and we found PTQ behavior in polymorphic HAP. This led to an important conclusion that the PL intensity of HAP will be higher near-physiological temperatures, an exciting result that can be tuned for biomedical imaging. We delve deeper into exploring the optical properties by probing the bandgap of polymorphic HAP, which presents an indirect bandgap in the range related to defect states in the forbidden region, reaffirming the results obtained from PL. The existence of vacancies and defect states reveals interesting Physics and glorifies HAP with several features.

## 3.2 Synthesis and Characterization methods

HAP has been prepared using the sol-gel process, which has been elaborated in Chapter 2. After successful preparation of HAP, the specimen preparation was initiated with the obtained powder using a hydraulic press by pressing them under a pressure of 25 $kg/cm^2$ to obtain cylindrical green discs. These discs were finally sintered in a furnace at 1073K for compaction, which resulted in compacted discs of thickness $\sim$1 mm and diameter $\sim$10 mm.

The t-XRD spectra of the specimens were recorded in a diffractometer by employing the Bragg- Brentano geometry in the $2\theta$ range of $20-55^\circ$ (Xpert$^3$ MRD XL, PANalytical, UK). The X-ray photons at a step size of $0.01^\circ$ were collected with a scan time of 1s. Temperature variation of the specimens was achieved by heating the specimen stage starting from 303 K to 573 K. The t-XRD data were later refined using the Rietveld refinement program by the FullProf software.

The Raman spectra of the specimens were collected from a micro-Raman spectrometer for the frequency shifts of 100 to 1200 $cm^{-1}$, with an excitation wavelength

of 488 nm. The intensity of scattered Raman light was detected using a highly sensitive charged couple device (CCD) detector. Before the operation, the Raman spectrometer was calibrated using a standard $Si$ wafer for which a shift was obtained at 523.88 $cm^{-1}$. The temperature variation in the specimen stage was carried out by heating the sample at 10 K/min. The readings are taken from room temperature (303 K) to 573 K at an interval of 10 K with an exposure time of 10s.

The PL spectra were recorded with the same Raman spectrometer with which the Raman spectra were recorded. The temperature variation PL (t-PL) spectra were obtained sequentially at 10 K from the same spot in the sample using the same laser source of 488 nm. The band structure of HAP was analyzed using the UV-Vis absorption spectra recorded using a spectrophotometer (Lambda 950, PerkinElmer, USA). The time-resolved PL (TRPL) spectra were obtained with a laser excitation of 475 nm closest to the laser used for the PL spectra. A picosecond time-resolved luminescence spectrometer (FSP920, Edinburg Instruments, UK) was used for recording the TRPL spectra with an instrument response time of ∼50 ps.

Dielectric constant ($\epsilon_r$) measurements of the specimens were recorded in an LCR meter in the temperature range from 303 K to 593 K at different frequencies. The LCR meter usually measures the capacitance of a specimen from which the $\epsilon_r$ is extracted using the well-known relation $\epsilon_r = \frac{Cd}{\epsilon_0 A}$, where $C$, $d$, $A$ & $\epsilon_0$ stands for capacitance, thickness, area, and permittivity of free space. The other losses in electrical energy occurring in a material due to various physical processes such as electrical conduction, dielectric relaxation, and dielectric resonance can be measured by the factor $\tan\delta$, an integral element in the dielectric spectroscopy of materials. To obtain the spectra, the specimens had to be initially coated with silver paste on both sides to transform them into a metal-insulator-metal (MIM) arrangement and then dried sufficiently before inserting them into the LCR meter.

## 3.3 Results and Discussions

### 3.3.1 Structural Analysis

The as-prepared samples of synthetically derived HAP show mixed-phase (monoclinic, $P2_1/b$ and hexagonal, $P6_3/m$) polymorph. For refining the XRD spectra, the two-phase refinement is carried out considering the monoclinic (space group $P2_1/b$, No. 14) and hexagonal (space group $P6_3/m$, No. 176) phases. The Rietveld refinement of the XRD pattern obtained at 303 K and 573K is shown in Figure 3.1(a),

revealing the mixed polymorphic phases with an increasing fraction of monoclinic phase with the temperature. Figure 3.1 shows that the monoclinic volume fraction increases to 57.77 (45.94)%, and the remaining 41.28 (55.06)% represents the hexagonal phase at 573 K (303 K). The continuous change of volume fractions of two phases is observed for intermediate temperatures between 303 K to 573 K, as shown in Figure 3.1(b) with the increasing temperature. This helps us illustrate (see Figure 3.1(c)) that the volume fraction change can be a function of temperature, with the possibility that one can achieve the dominant volume fraction of the Hexagonal phase for lower temperatures.

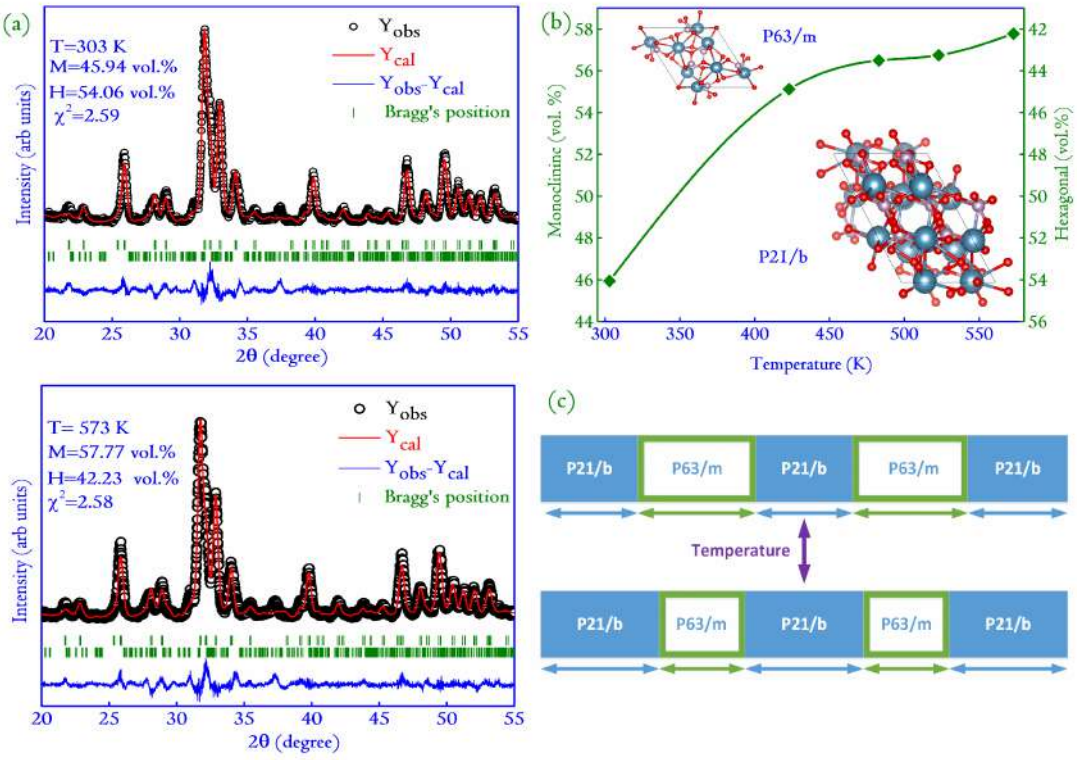


**Figure 3.1:** (a) XRD of HAP and its refined pattern at temperatures 303 K and 573 K, the volume fraction of monoclinic (M) and hexagonal (H) phase has been drastically changed with the temperature. The black circular dots ($Y_{obs}$) represents the experimentally observed data points obtained from the diffractometer. The red line ($Y_{cal}$) is the fitted theoretical curve obtained from the FullProf program. The goodness of the fit represented by the $\chi^2$ value is adjusted to 2.59 and 2.58, respectively, for the refinement. (b) The volume fraction of monoclinic ($P6_3/m$) and hexagonal ($P2_1/b$) phases in polymorph HAP as a function of temperature continuously changes. (c) We illustrate that the two phases in the synthetically derived HAP samples get changed with the temperature.

The close observation of the t-XRD peaks near larger Bragg angles show a systematic shift (see Figure 3.2(a)) in the peak positions with the temperature that

gives the first evidence for the reorientation motion of the $OH$ group in the synthetically derived HAP. The Bragg shift is observed for the peak positions (130), (213), (321), (042), and (141), without any change in the intensities of the peaks. The marginal shift in the peaks (Figure 3.2(b-d)) indicates a slight structural deformation of HAP with the temperature. As presented previously, the principle change in the structures of monoclinic and hexagonal HAP is linked with the orientation of the $OH^-$ group. In a similar study, the X-ray scattering of oxygen ($O$) atoms is found to be non-negligibly smaller [119, 120], and theoretically, it is also shown that the detection of $OH$ ions in the reorientation is difficult [52]. A better alternative to present the structural transformation subjected to the temperatures is explained in Section 3.3.2 and 3.3.4 with the help of micro-Raman spectroscopy and the dielectric response.

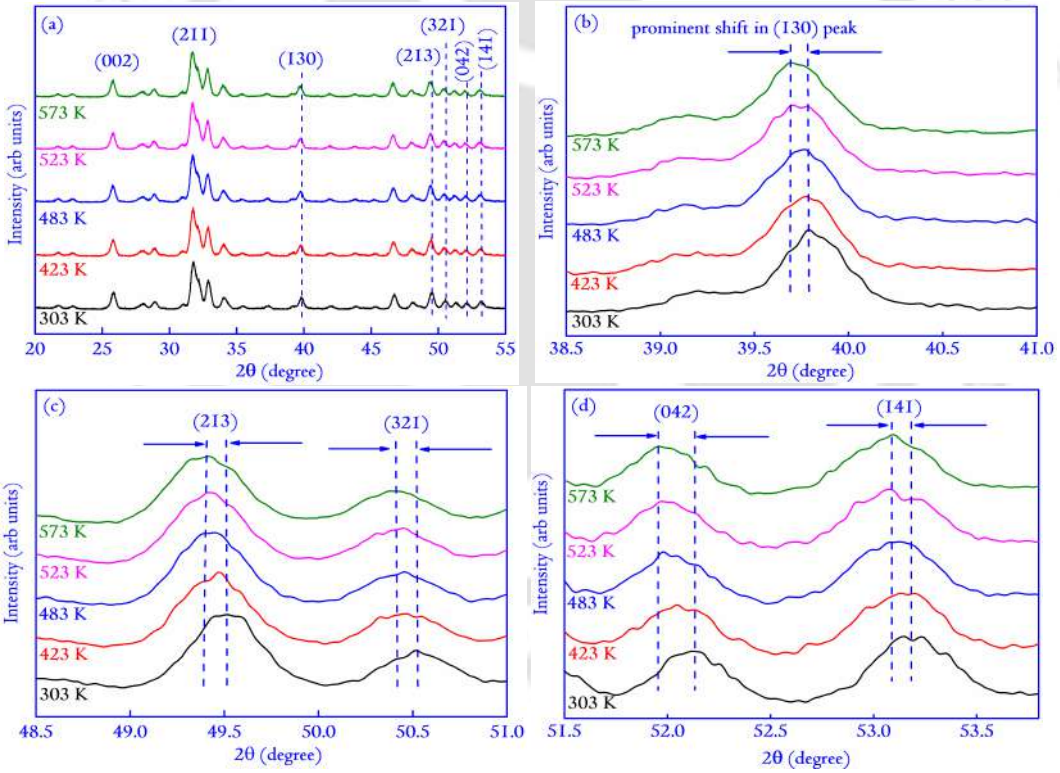


**Figure 3.2:** (a) XRD spectra of HAP at different temperatures. The spectra indicate a shift towards lower Bragg angles at higher temperatures. The shift is seen only in a few peaks and separated from the rest by a blue dotted line. A zoomed-in view of the shifted peaks is shown by explicitly targeting the Bragg's angle near which the peaks appear in Figure 3.2(b),(c), and (d), respectively.

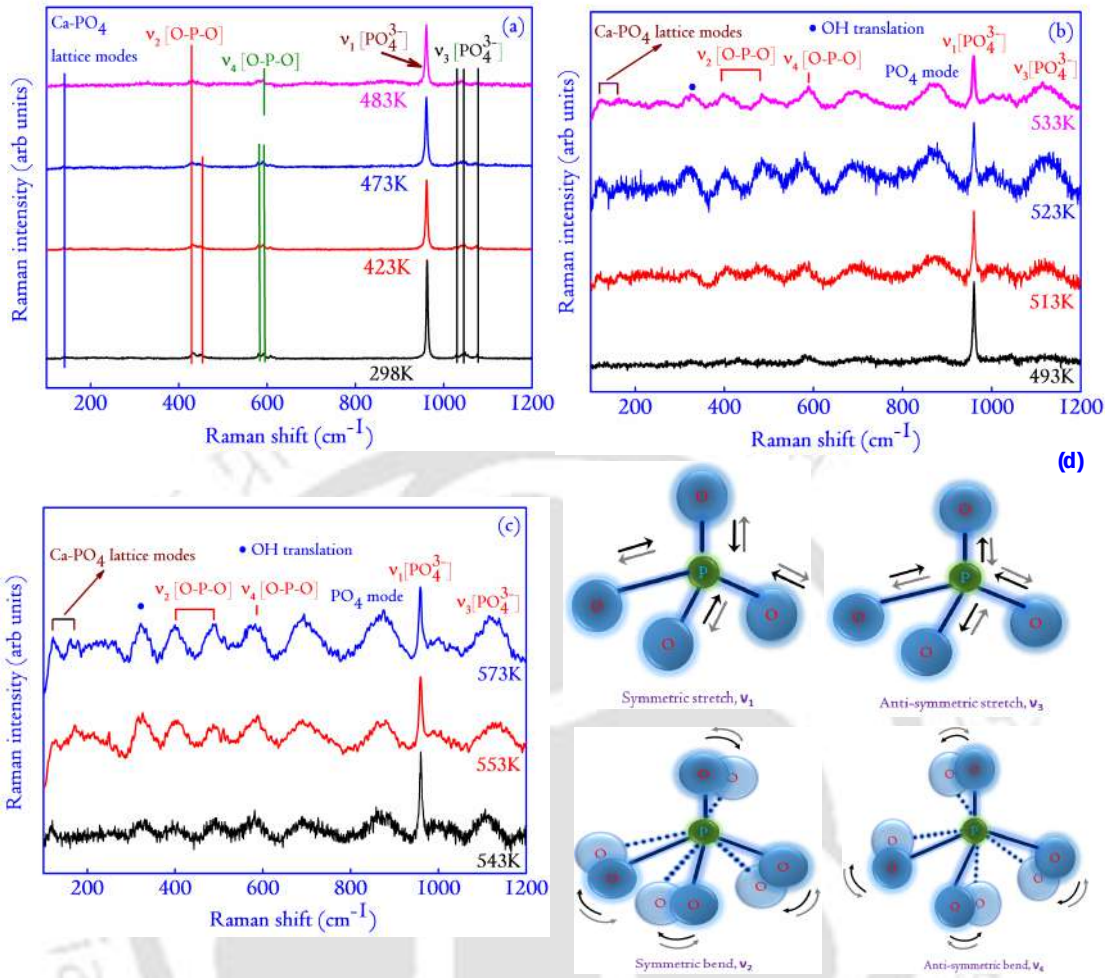


**Figure 3.3:** (a),(b),(c) The temperature variant Raman spectra showing the bands with their assignments. The bands depict the decrease in intensity of the most intense bands with rising temperatures. After 483 K, the appearance of additional bands is observed, which were not present at lower temperatures. In the adjacent Figure 3.3(d), the different modes of vibration of the $(PO_4)^{3-}$ group responsible for generating the most prominent bands in the Raman spectra are illustrated graphically. In the figure, the green circle shows the $P$ atom, and the blue circle stands for the $O$ atom. The straight arrows (in black and grey font) represent the direction of linear symmetric or anti-symmetric stretch ($\nu_1$ & $\nu_3$), and the curved arrows denote the symmetric and the anti-symmetric bending motion of the $PO_4^{3-}$ group ($\nu_2$ & $\nu_4$).

### 3.3.2 Temperature dependent Raman Spectroscopy

The micro-Raman spectroscopy is highly sensitive to structural displacement with changes in the polarizability [120] that helps to pursue temperature-driven non-negligible structural transitions, especially the reorientation motions of $OH$ ions, which we observe with a slight variation in the t-XRD of HAP. The t-Raman spec-

tra of the HAP are shown in Figure 3.3, where we plotted Raman spectra at different temperatures between 298 K to 573 K. The synthetically derived HAP show vibrational modes originating from the $PO_4^{3-}$, $OH^-$ and $Ca^{+2}$ ions when illuminated with an excitation source of 488 nm. As we know, the hexagonal phase has 129 optical modes; among them, the Raman active modes are 52 for the $C_{6h}$ symmetry and 102 for $C_6$ symmetry, are distributed as $12E_{2g} + 12A_{2g} + 8E_{1g}$ and $21A + 21E_1 + 22E_2$, respectively [121]. In the monoclinic phase, there are 132 Raman active modes $(66A_g + 66B_g)$ from the total 261 vibrational modes for the $C_{2h}$ symmetry [121]. From Figure 3.3(a), the strong, intensive peak at $\sim$960 $cm^{-1}$ is from the internal modes of tetrahedral $PO_4$. It is important to note that the vibrational modes originated from the $PO_4$ are classified as, $\nu_1$, $\nu_2$, $\nu_3$, and $\nu_4$ bond modes. The symmetric stretching of $P-O$ bonds belongs to the $\nu_1$ mode. The bending mode of $O-P-O$ is for $\nu_2$, which is doubly degenerate, whereas $\nu_3$ mode arises from the triple degenerated asymmetric stretching of $P-O$ bonds. The $\nu_4$, represents triply degenerate anti-symmetric bending of $O-P-O$ bonds [122]. The internal modes of vibrations of $PO_4$ are illustrated in Figure 3.3(d).

#### 3.3.2.1 Lower wavenumber region (100-900 $cm^{-1}$)

It is observed from the temperature variation of Raman spectra in Figure 3.3(a) that in the lower wavenumber region, a small intensity band appears at 140 $cm^{-1}$ (marked by the blue line in Figure B.1a) which belongs to the $Ca-PO_4$ lattice modes [123]. Interestingly, this band disappeared for a temperature above 493 K. Moreover, two new bands at 120 $cm^{-1}$ and 163 $cm^{-1}$ (marked in Figure 3.3(b)) arise as the temperature further increased, and, later, these vibrational bands attains prominence after 523 K. These observations are in conjunction with several theoretical studies [105], [121]. The temperature-dependent dominant variations are observed for the region 300-900 $cm^{-1}$. Notably, a new band arise at 325 $cm^{-1}$ (marked by a blue dot in Figure 3.3(b) and 3(c)) for the temperatures $\geq$473K associated with the translational modes of $OH$ ions [124]. As the temperature is raised, the orientation motion of the $OH$ group initiates, creating a disordered structural arrangement of the $OH$ group at the region of higher temperatures. The appearance of new vibrational bands indicates the structural onset transformation followed by the disturbance of $OH$ ions vibration by rearranging itself at a specific temperature threshold. From Figure 3.3(b) and 3.3(c), the reorientation of $OH$ ions increased monotonically with temperature until 523 K and might be saturated for further temperatures. Another behavior could be the reorientation starts at 473 K and continues thereafter.

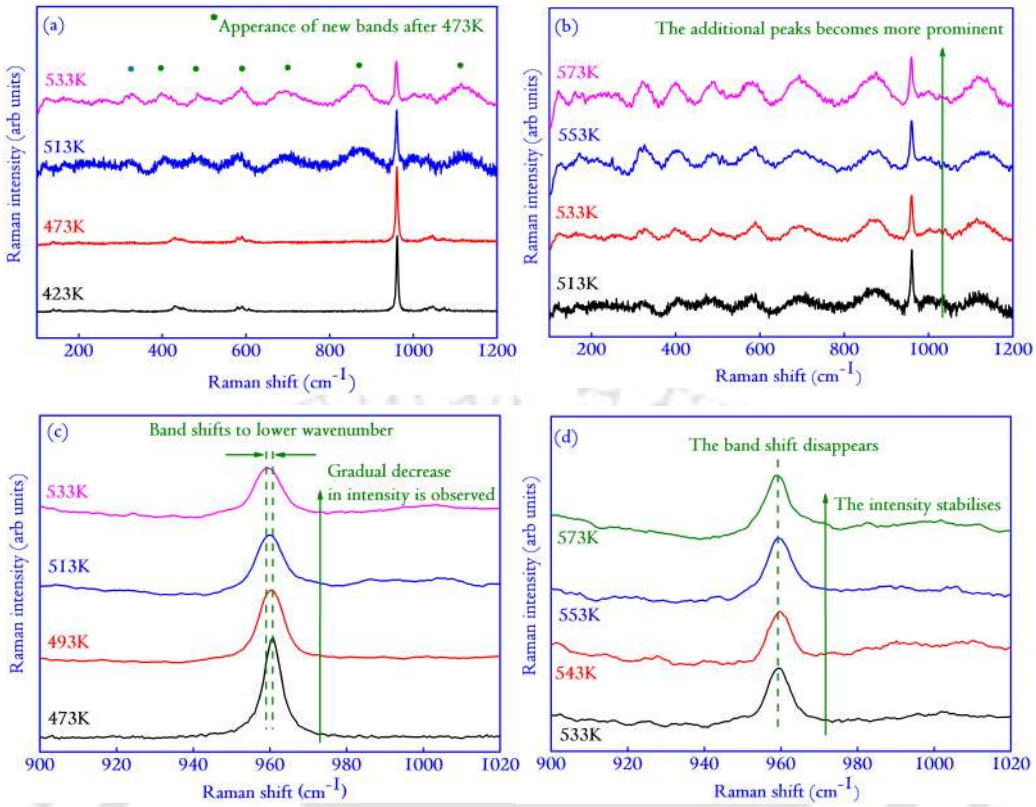


**Figure 3.4:** (a) Temperature-dependent Raman spectra showing the appearance of additional bands after 473 K, (b) the other bands becoming more prominent with an increase in the temperature. The spectra recorded at 553K and 573 K depict that no additional bands or intensity changes are observed with a further increase in temperature. (c) The zoomed-in view of the shift in bands with an increase in temperature and decreasing intensity of the most prominent $\nu_1$ $[PO_4^{3-}]$ band, and (d) the relative stabilization in the band shift and intensity with further increase in temperature in HAP.

However, these transformations induced by the change in the structural ordering of the $OH$ group can also occur by rotational transformation. Since the $OH$ group translation or rotational nature can be identified by observing the associated dipole moment, these details are further discussed in Section 1.3.4. It is also observed that many new bands at 431 $cm^{-1}$, 447 $cm^{-1}$, 579 $cm^{-1}$, 591 $cm^{-1}$ appear (see Figure 3.4(a)). These vibrational modes are attributed to the $PO_4$ tetrahedra; the intensity of these peaks is found to decrease, proportionately increasing the width of the peak with increasing temperature. The bands at 579 $cm^{-1}$ and 591 $cm^{-1}$ arises for the spectra compared for the temperatures 298 K and 423 K (marked by two green lines at lower temperature and a single green line at 483 K in Figure 3.4(a)), the intensity drastically reduced, the bands are broadened and merged as a hump at 483 K. Moreover, these merged bands are found to be arising again with the

further increase in the temperature. The splitting of these merged band vibrations is attributed to a lower symmetry monoclinic structure [125].

#### 3.3.2.2 Higher wavenumber region (900-1200 $cm^{-1}$)

The bands appearing in this region are primarily due to the vibrational mode of the $PO_4$ group. The most notable band is the one appearing at 960 $cm^{-1}$, which is the most prominent high-intensity band in the Raman spectra of HAP. Among the bands, the most drastic visible changes due to temperature are perceived in this particular band, which is assigned to the $\nu_1$ vibration mode. As the temperature is increased, the band starts to shift to lower wavenumber (see Figure 3.4(c)). The redshift continues until the temperature of ∼523 K is reached, beyond which the shift disappears, as shown in Figure 3.4(d). The temperature-induced effects of a polymorph of synthetically derived HAP would differ from a monomorphic phase containing hexagonal or monoclinic phase. No such shift was observed for the temperature-dependent $\nu_1$ band in the Raman spectra of $Pb_{10}(PO_4)_6(OH)_2$ [121]. However, in a theoretical study on the vibrational spectra of HAP, it was predicted that the bands in this region are succeptible to Lyddane-Sachs-Teller (LST) shift due to the long-range Coulomb effect [126]. This LST shift is influenced by the $\epsilon_r$. The LST shift is most significant for smaller $\epsilon_r$ and decreases for higher values of $\epsilon_r$. It is reported that the calculated shift is found to be up to 18 $cm^{-1}$ in the bands for $\epsilon_r$ of ∼5 (in both monoclinic and hexagonal) [126]. The bands at higher wavenumbers, especially between 950 $cm^{-1}$ and 1100 $cm^{-1}$, are particularly sensitive to such shifts. In the following section, the temperature variation of dielectric spectroscopy would reveal that the $\epsilon_r$ of the synthesized HAP was in the range of ∼9-12, and for such a value of $\epsilon_r$, the shift gets progressively smaller. Finally, the bands appearing after 960 $cm^{-1}$ also are susceptible to changes induced by the transition from a monoclinic to the hexagonal structure. Particularly the three bands appearing around 1026, 1047, and 1077 $cm^{-1}$ are attributable to $\nu_3$ $PO_4$ mode are found to decrease in intensity with the increasing temperature finally reappearing again at 513 K at lower wavenumbers.

### 3.3.3 Temperature dependent PL spectra, band structure and TRPL analysis

The PL spectra, in general, can be a starting point to explore defects (specifically point-like defects in materials) that can lead to exciting Physics [127]. The shape of

the PL bands, their intensity, and dependence on temperature are of immense importance in identifying the nature of the defects. For instance, the defect-related bands are broader in shape due to strong electron-phonon coupling, which are characteristics of deep-level defects [128]. The PL associated with such defects slightly changes their shape with increased temperature. In Figure 3.5, the t-PL of HAP shows broad, continuous emission spectra with a plateau-like region in the wavelength range of 550-700 nm (corresponding to the visible region of the electromagnetic spectrum).

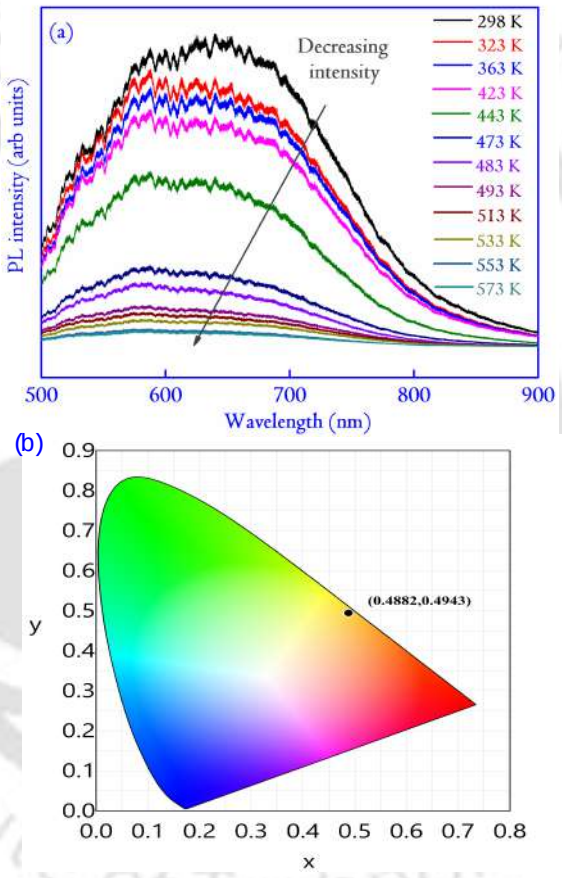


**Figure 3.5:** (a) show the temperature variation of the PL spectra of HAP. The intensity of the PL spectra decreases with temperature. This points to the PTQ behavior in the specimen. Also, the broad PL spectra are indicative of point-like defects in the specimens. Since $Ca^{+2}$ or the $PO_4^{3-}$ is incapable of showing PL, the luminescence in HAP must come from the defect structures introduced during the preparation. In (b), the Commission International d'Eclairage (CIE) chromacity coordinates at 298 K are shown. The co-ordinates (0.4882, 0.4943) specified (by the dot) in the CIE diagram are known as the chromacity co-ordinates [129]. Typically three co-ordinates (x, y, z) are required to specify chromacity. However, the z coordinate is always dependent on the other two coordinates and hence not specified. The co-ordinates typically infer the emission colors of an LED if constructed from the specimen under study.

The continuous increase in the PL intensity with increasing wavelength is observed for the entire temperature variation considered in the study. However, an increase in the measurement temperature leads to the flattening of the observed PL response. Such monotonic decrease in the PL intensity with increasing temperature indicates the positive thermal quenching (PTQ) behavior of HAP [129]. The thermal quenching of PL due to defects thrives on the assumption that the defect transitions from a radiative to a non-radiative state. The model, commonly referred to as the Seitz-Mott mechanism in literature, states that at low temperatures, most defects remain in the ground state [127]. With a rise in temperature, a random defect may overcome the energy barrier separating the excited and ground state. The difference energy may be released not as a photon but in multiple phonons. Quantitative estimation of the PTQ [Figure 3.6] can be performed using the following Arrhenius equation,

$$I(T) = \frac{I_0}{1 + A\exp(\frac{-E_{ae}}{K_B T})} \tag{3.1}$$

Where $I(T)$ and $I_0$ are the integrated PL intensities at $T$ K and 0 K, respectively. A is a constant, $K_B$ is the Boltzmann constant, and $E_{ae}$ is the activation energy of the non-radiative process explained earlier.

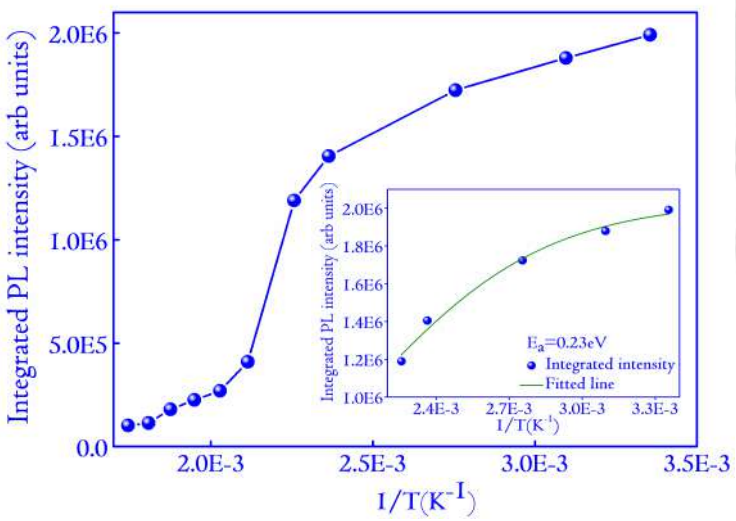


**Figure 3.6:** The variation in the integrated PL intensity as a function of the inverse temperature. The variation represents the PTQ behavior in the specimens, arising from a transition from radiative to a non-radiative state. In the inset, the Arrhenius fit in the temperature region (298 K to 443 K) is shown. The $E_{ae}$ for the fitted region corresponds to 0.23 eV.

To determine $E_{ae}$ for HAP, the experimental data is fitted with equation (3.1) in the temperature region (298 to 443 K). The $E_{ae}$ for the selected temperature range is 0.23 eV, and it gives a quantitative estimation of the non-radiative process occurring in the specimens [129]. It is proposed that in the forbidden band, the $OH^-$ and $O^-$ vacancies generate a series of energy levels in the forbidden band. These forbidden bands can play an essential role in the recombination of electron-hole that displays PL due to strong electron-photon coupling [128, 130]. A careful literature survey points to the origin of such defects within the HAP matrices to the synthesis and processing technique employed to prepare the parent compound. A series of experimental parameters, such as the reaction pressure, time, temperature, *etc.*, are primarily reported to determine the kinetics of defect formation. Mapping such defects by controlling the experimental parameters is, therefore, challenging [130].

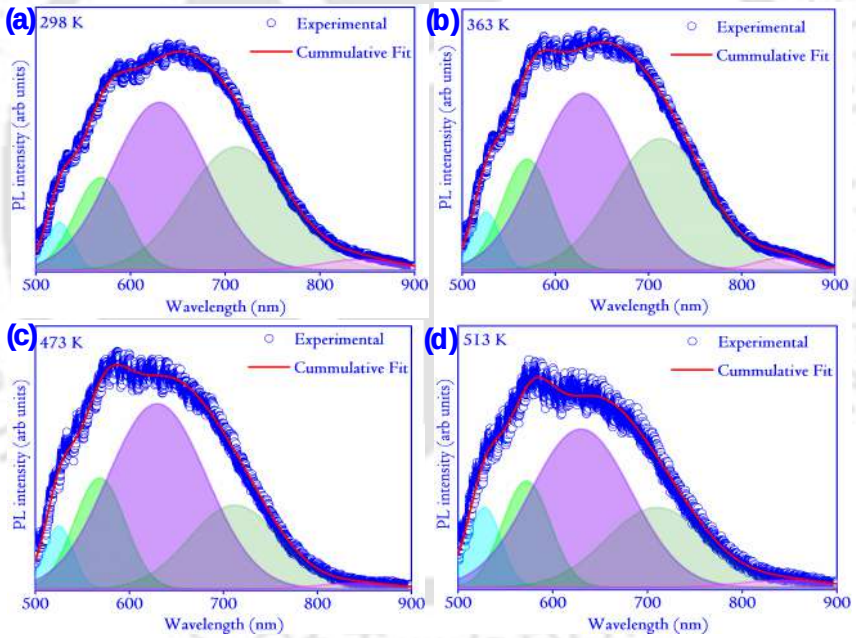


**Figure 3.7:** The deconvolution of the PL spectra at fur different temperatures of 298 K, 363 K, 473 K, and 513 K, respectively. The deconvoluted peaks correspond to the peak wavelength of ∼525 nm (2.36 eV, represented by the blue peak), ∼570 nm (2.17 eV, represented by green peak), ∼630 nm (1.97 eV, represented by the violet peak), ∼712 nm (1.74 eV, represented by the light green peak), and ∼844 nm (1.47 eV, represented by the magenta peak), respectively.

The broad PL emission of HAP further reveals that luminescence is composed of multiple emission bands, and these components can be deconvoluted using Gaussian curves centered at energies of 2.36, 2.17, 1.97, 1.74, and 1.47 eV, respectively.

The parameters associated with the deconvoluted bands are tabulated in Table A.1 (Appendix A). Interestingly, the deconvoluted peaks have energy lower than the bandgap ($E_g$) energy of HAP (3.91 eV, determined in the next section), and the excitation source (488 nm, 2.54 eV) also has lower energy than the $E_g$. The set of events points towards the defective centers lying in the forbidden gap of HAP are the main components contributing to all the emissions observed in the PL spectra [131]. HAP is widely recognized as a wideband semiconductor with a high degree of structural flexibility, due to which the vacancies, structural defects, and ionic substitutions are easily stabilized [130]. This attribute of HAP complements several energy states, leading to a complex electronic structure for the specimens. Also, the full width at half maximum (FWHM) of the deconvoluted peaks carries information about the homogeneous or inhomogeneous nature of the broadening in the linewidth associated with the electronic transition (shown in Table A.1, Appendix A) [130]. The Gaussian curves chosen for the deconvolution of the PL spectra relate to the inhomogeneous broadening generated by impurities, defects, or vacancies in the specimens. The single crystals displaying PL spectra are deconvoluted using the Lorentzian curves that signify the natural or homogeneous broadening related to the electron-phonon coupling in the specimens [130]. The deconvoluted band centered at 2.36 eV is associated with the defects in the bulk of the specimen in the form of Calcium vacancies ($V_{ca}$), distortion in the $PO_4$ groups, or sometimes interstitial defects [131]. It is inferred that defects related to the loss of symmetry in $[CaO_9]$, $[CaO_7H]$, and $[PO_4]$ clusters exist in HAP, which is characteristic of the low-temperature synthesis of HAP. The loose arrangement of $Ca$ and its significantly high mobility is associated with the $V_{ca}$ in the $Ca$ clusters, which causes the loss of symmetry. In consideration of the above facts, the mechanism of the PL emission in HAP can be described by a model based on the Kröger-Vink notation according to the following equations

$$2[V_{Ca}^{x}O_9] + 3[PO_4]_d^x \rightarrow [V'_{Ca}O_9] + [V''_{Ca}O_9] + 3[PO_4]^{\bullet} \tag{3.2}$$

$$2[V_{Ca}^{x}O_7H] + [PO_4]_d^x \rightarrow [V'_{Ca}O_7H] + [V''_{Ca}O_9] + [PO_4]^{\bullet} \tag{3.3}$$

$$[CaO_9]_O^x + [PO_4]_d^x \rightarrow [CaO_9]'_O + [PO_4]^{\bullet} \tag{3.4}$$

$$[CaO_7H]_O^x + [PO_4]_d^x \rightarrow [CaO_7H]'_O + [PO_4]^{\bullet} \tag{3.5}$$

Where equations (3.2) and (3.3) represent the $Ca$ vacancy contributions and equations (3.4) and (3.5) represent the contribution from structural defects in HAP. In the above equations, $[V_{Ca}^{x}O_9]$ and $[V_{Ca}^{x}O_7H]$ represents the neutral $Ca$ vacancies; $[V_{Ca}^{\prime}O_9]$ and $[V_{Ca}^{\prime\prime}O_9]$ are $Ca$ vacancies that received one and two electrons, respectively. The distorted or disordered $PO_4$ clusters are represented by the $[PO_4]_d^x$ and $[PO_4]^{\bullet}$ with $x$ and $\bullet$ representing a neutral state and a cluster with one hole [130]. The equations comprehensively describe the PL mechanisms in HAP due to the formation of the vacancies. In addition, it is reported that the loss of symmetry in the clusters due to vacancies or defects results in the formation of donor or acceptor levels in the forbidden gap. These levels are classified in the literature as deep or shallow-level defect states. The shallow levels are formed close to the conduction bands and/or valance bands; hence are more and are responsible for the bluish or violet PL emissions. The orange, yellow, green, and red emissions are due to the deep-level defects and are located near the center of the forbidden region. It is clear from Figure 3.7 that the deconvoluted intensity peaks for ∼630 nm (1.96 eV) corresponds to the orange emissions, and the previous discussion elucidates that these are due to deep-level defects [131].

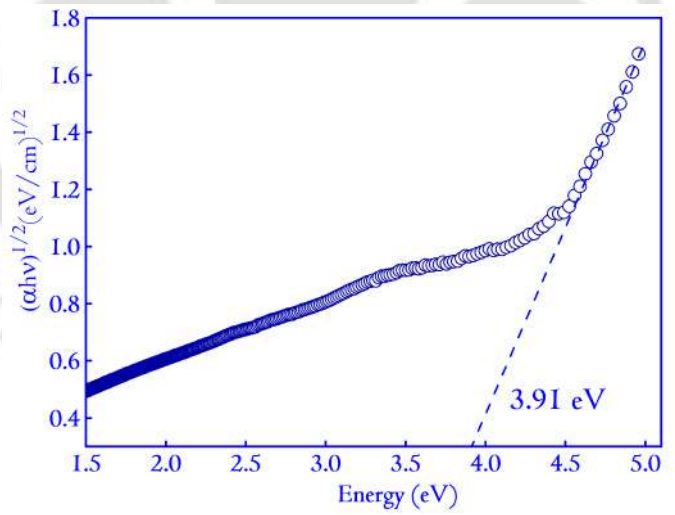


**Figure 3.8:** The Tauc's plot for the determination of the bandgap of HAP. The intercept to the x-axis produces a bandgap of 3.91 eV. The $E_g$ value is related to the photocatalysis of HAP under persistent UV illumination.

Along with PL, the bandgap of HAP is calculated and shown in Figure 3.8. The bandgap of HAP is assumed to be indirectly allowed, and accordingly, the Tauc's

relation can be expressed as [105]

$$(\alpha h\nu)^{\gamma} = A(h\nu - E_g) \tag{3.6}$$

Where $A$ is a constant, $E_g$ is the bandgap, and $\gamma$ is the power coefficient that determines the nature of the transition. For indirectly allowed transition, it assumes the value of 1/2. Plotting $(\alpha h\nu)^{1/2}$ versus h$\nu$, the $E_g$ can be determined by the intercept of the line to the region where there is an inflection of the curve [132]. The $E_g$ for HAP is found to be 3.91 eV [133]. With respect to the PL spectra where the excitation wavelength corresponding to 1.37 eV (900 nm)-2.48 eV (500 nm), it can be concluded that as the $E_g$ (3.91 eV) is higher, the band-to-band electronic transition has negligible influence on the PL response [130]. The $E_g$ value reaffirms our earlier assumption of the presence of the defect levels in the forbidden region of the band diagram. It is proposed that $E_g$ values close to 4.00 eV indicates vacancies from an entire $OH$ group and/or oxygen from the $PO_4$ group [134]. These results are also in conjunction with the earlier PL results. The $E_g$ value of HAP in the range of 3.40-4.00 eV has been related to observing the photocatalysis of HAP under persistent UV illumination [135]. The root of photocatalysis is related to an oxygen vacancy in the $PO_4$ group, introducing a fully occupied state in the lower half of the bandgap. The photoionization of this level (due to wreckage of either $P-O-P$ or $O-H-O$ bridge bonds) most likely explains the onset of photocatalysis [128].

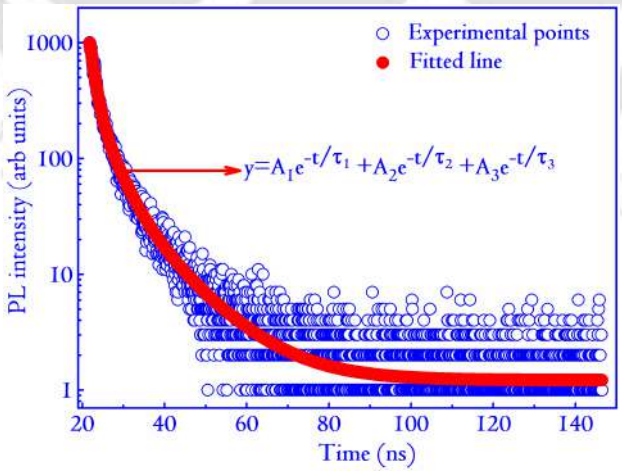


**Figure 3.9:** The TRPL response of HAP, on excitation by a laser of wavelength 475 nm, is close to 488 nm used to obtain the PL spectra. The experimental data is best fitted with a tri-exponential function represented in the figure. The different parameters used for describing the tri-exponential function are appropriately described in the text. The average lifetime of the carriers is determined to be 7.958 ns.

The TRPL measurements were carried out to investigate the recombination dynamics, and we observe that the decay spectrum in our case fits well with a tri-exponential decay function of the form (Figure 3.9),

$$y = A_1 \exp(\frac{-t}{\tau_1}) + \exp(\frac{-t}{\tau_2}) + \exp(\frac{-t}{\tau_3}) \tag{3.7}$$

Where, $A_1$, $A_2$, and $A_3$ represents the amplitude of the three decay process specified by the equation (3.7) of magnitudes 39.58, 37.59, and 22.82. $\tau_1$, $\tau_2$ and $\tau_3$ are the carrier lifetimes and have the magnitudes of 1.18, 3.99, and 11.45 ns, respectively and $t$ denote instantaneous time. Using the expression, $\tau_{av} = \sum \frac{A_i \tau_i^2}{A_i \tau_i}$, we complete our discussion by determining the average lifetime for the excitation at 475 nm as 7.95 ns.

### 3.3.4 Temperature dependent dielectric response

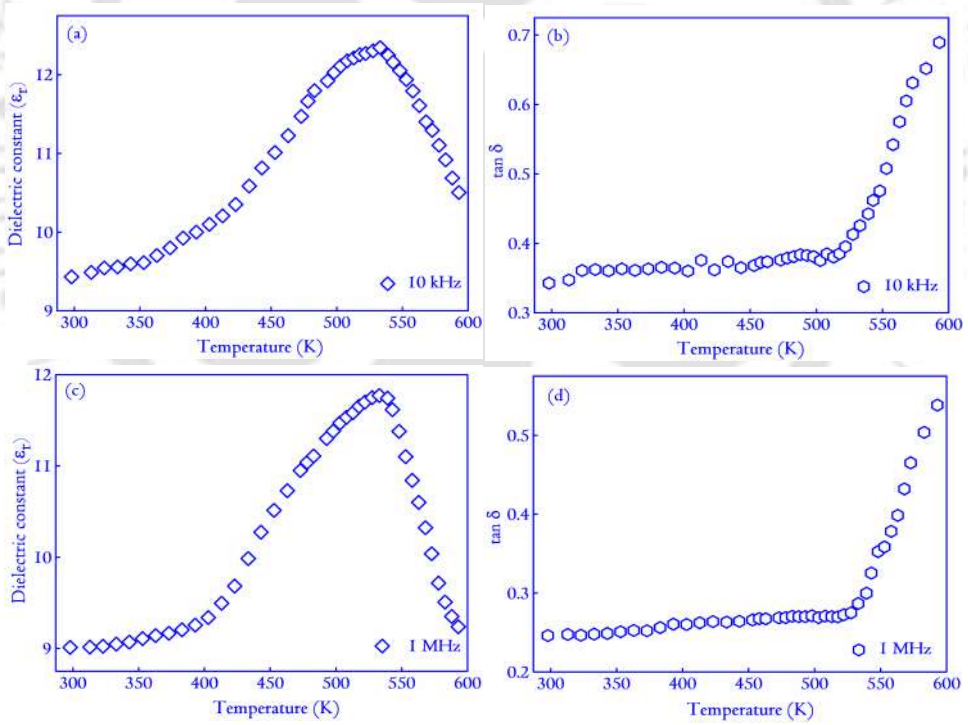


**Figure 3.10:** Temperature-dependent (a, c) dielectric spectra and (b, d) tan$\delta$ of HAP measured at two different frequencies: 10 kHz and 1 MHz. The figures form the basis for calculating conductivity and determination of the $E_a$ of the specimens by the Arrhenius plots depicted in Figure 3.11.

The attributes of $OH$ ions that determine the dielectric properties of HAP can be probed by the temperature-dependent dielectric spectroscopy presented in Figure

3.10 measured at 10 kHz and 1 MHz. The measurements with two other frequencies (50 kHz and 100 kHz) are presented in Appendix A as Figure A.1. It is reported that the $OH$ ions in HAP form one-dimensional chains that behave as dipoles and are capable of reorientations upon suitable excitation. We presented these re-orientation motions as modifications to the t-XRD and t-Raman spectra discussed in the previous Section 3.3.1 and 3.3.2. These reorientations are further confirmed by two mechanisms, firstly, it involves the direct rotation of the $OH$ ions about a suitable axis, and secondly, it incorporates the translational motion that can proceed by rupturing the existing $OH$ bonds and forming new ones. In such cases, measurement of the dielectric spectra is considered an important tool to exploit and understand the underlying reorientation mechanisms [114]. Additionally, it estimates the energy barrier associated with such re-orientation motion. From Figure 3.10, in all the probed frequencies, the HAP has the lower value of $\epsilon_r$ ($\sim$9 at 298 K). With the gradual increase in the temperature, the value of $\epsilon_r$ increases and reaches a peak value of $\epsilon_r \sim 12$ for the temperature 533 K and is found reducing for higher temperatures. The anomaly occurring in dielectric spectra is ascribed to the change in the ordering of the $OH$ groups from a para-electric-like to an anti-ferroelectric-like arrangement [111, 136]. This transformation of $OH$ groups is associated with the energy supplied by the externally applied temperature. Further, the dielectric loss characterized by tan$\delta$ (see Figure 3.10(b & d)) is also found to increase with temperature, which is in conjunction with the $\epsilon_r$. The increase is, however, more prominent at the onset of 533 K. The estimate of transformation energy of $OH$ ions arrangement can be obtained from the activation energy calculation derived from the $\epsilon_r$ and tan$\delta$ with the temperature. The activation energy of the transformation is estimated from the calculated conductivity ($\sigma$) by using the following relation [137],

$$\sigma = \epsilon_0 \epsilon_r \omega tan\delta \tag{3.8}$$

Where $\sigma$ is the conductivity, $\epsilon_0$ is the permittivity of free space ($8.854 \times 10^{-14} F/cm$), $\omega$ is the angular frequency ($2\pi f$, $f$ is the frequency at which the data is obtained). The plots depicting the variation of $\sigma$ with temperature are shown in Figure 3.11 for the frequency range presented in Figure 3.10. The other frequencies are included in Figure A.2 of Appendix A. The calculated $\sigma$ is related to the reorientation energy or the activation energy of reorientation, $E_a$ as defined in the equation below [138, 139]

$$\sigma = \sigma_0 \exp(\frac{-E_a}{K_B T}) \tag{3.9}$$

Where $\sigma_0$ is the pre-exponential factor that describes the temperature independent part of the conductivity, $K_B$ is the Boltzmann constant, and $T$ is the absolute temperature. Taking natural logarithm on both sides of the equation and rearranging the terms, equation (3.10) turns out to be Arrhenius equation as written below,

$$ln[\sigma] = ln[\sigma_0] - \frac{1000}{T}(\frac{E_a}{1000K_B}) \tag{3.10}$$

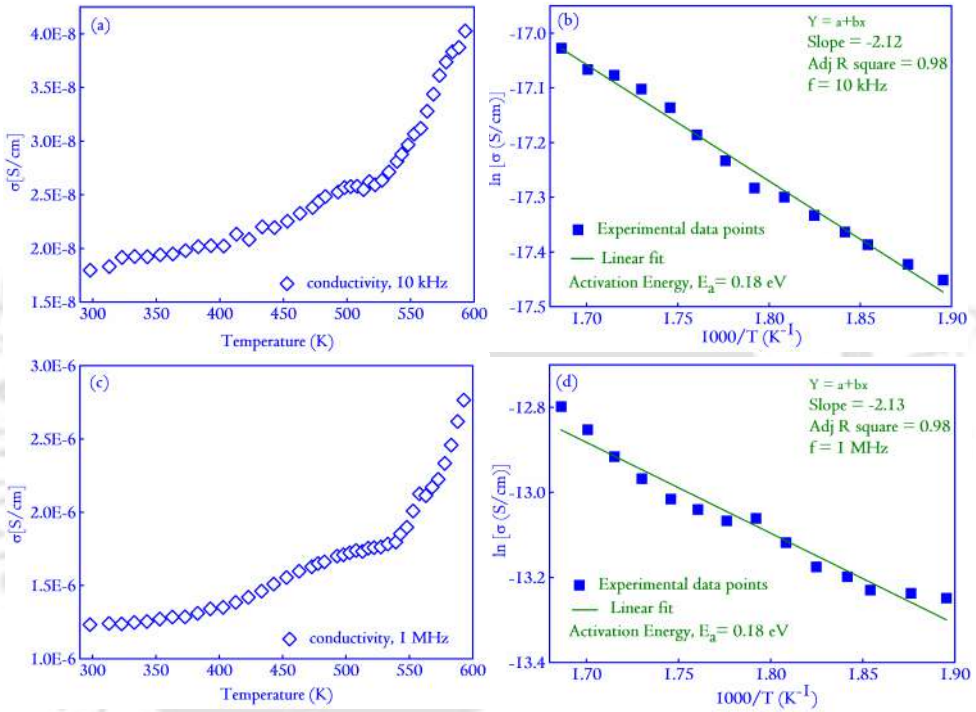


**Figure 3.11:** (a, c) Variation of conductivity with the temperature at two different frequencies: 10 kHz and 1 MHz. The conductivity has been derived from the plots of $\epsilon_r$ versus $T$ as well as tan$\delta$ versus $T$ in Figure 3.10. In (b, d), the corresponding Arrhenius plots for determining the energy of reorientation characterized by $E_a$ are plotted. The reorientation energy lies in the range of 0.18-0.20 eV, signifying that the reorientation occurs by rotation of the $OH$ group.

A plot of ln$[\sigma]$ versus $1000/T$ would yield a straight line with the slope providing for the $E_a$, the activation energy of reorientation motion of the $OH$ ions in HAP. The Arrhenius plots with the calculated $E_a$ for different frequencies are shown in Figure 3.10(b-d). The other plots are included in Figure A.2 of Appendix A. The values of $E_a$ for the frequencies considered are in the range of 0.18 eV to 0.20 eV, consistent with previously reported values between 0.016-0.630 eV corresponds to the rotational transformation, and the range of 0.84-0.89 eV to translational transition [140–142].

This indicates the $OH$ ions reorientation in the HAP is basically from the rotational transformation of an ordered anti-ferroelectric arrangement to a disordered para-electric arrangement upon the temperature increase. The higher energy in the range of 0.84-0.89 eV, representing the translational transition, supports the breaking up of $OH$ bonds. An ordinary rotational flip does not involve any bond wreckage, and hence it has lower transformation energy.

## 3.4 Conclusions

We present an exciting outlook towards temperature-dependent effects on the synthesized polymorphic HAP. $OH$, being a dominant group, its dynamics play a significant role in determining the temperature-induced structural changes. Exploring the $OH$ ion reorientation with the high polarizability from the micro-Raman spectroscopy in conjunction with dielectric spectroscopy ($OH$ being a dipole) displays the temperature-dependent volume fraction change to the polymorph HAP. The micro-Raman spectroscopy revealed the reorientation motion of the $OH$ group, and dielectric spectroscopy established that the reorientation is purely rotational transformation due to the temperature aided activation energy. It is further understood that the rotation is not a collective motion but occurs monotonically, with the temperature reaching a maximum near 523 K. The defect dynamics in HAP are understood by considering the PL and UV-Vis studies. The display of PL by HAP is intrinsically related to the defect structures. It is proposed that the PL in HAP is due to an oxygen vacancy from $PO_4$ and/or an entire group of $OH$. An exciting consequence of defects reflects in the bandgap study that pointed at the possibility of photo-catalysis of HAP under continuous illumination of UV light. This phenomenon is related to the vacancy in the $PO_4$ group that produces energy levels in the forbidden gap (towards the lower half, near the valence band). The dynamics of the defects in the HAP structure are further probed with TRPL, and the results revealed an average lifetime of 7.95 ns for the excitation. Such insights are useful in mapping the fundamental properties of HAP and hold the possibility of opening new avenues of its application in areas related to bioimaging and bio-electronic gadgets. The upsurge of research in biomedical imaging, where there is a continuous search for biocompatible materials (such as HAP), would be beneficial for in-situ investigations in surgery and the detection and imaging of cancer cells.

# Chapter 4

# Physical, chemical, electrical and biological investigations of $SrTiO_3 - Ca_{10}(PO_4)_6(OH)_2$ composites

This chapter discusses the effect of adding $SrTiO_3$ (ST) to $Ca_{10}(PO_4)_6(OH)_2$ (HAP). By a thorough investigation of the microstructural, biological, and electrical properties, an attempt to identify the composition displaying sufficiently the blend of all the properties is identified. This composite is later chosen to develop scaffolds, further discussed in Chapter 6.

## 4.1 Introduction

This chapter, reported electrically active materials that have received widespread attention in biological applications due to their unique properties of piezoelectricity, pyroelectricity, and ferroelectricity that aid in several healing processes [38]. The human body makes use of multiple electrical properties to perform a series of metabolic activities [143]. For instance, piezoelectric materials have been explored in generating smart scaffolds, which are reported to enhance cell adhesion, differentiation, and cellular migration. The idea is mostly inspired by the discovery of

The contents of this chapter is published in A. Das, A. Bhardwaj, S. Rabha, L. M. Pandey, and P. Dobbidi, Journal of the American Ceramic Society **105**, 1790 (2022) and A. Das, and P. Dobbidi, ACS Omega **6**, 25916 (2021)

piezoelectricity in collagen molecules (1957), a principal organic constituent of natural bones [144]. Collagen, being endowed with a polar structure, has the natural ability to show pyroelectricity in addition to piezoelectricity. Both of these effects are the most significant contributors to the bone remodeling process in living bodies [38, 145].

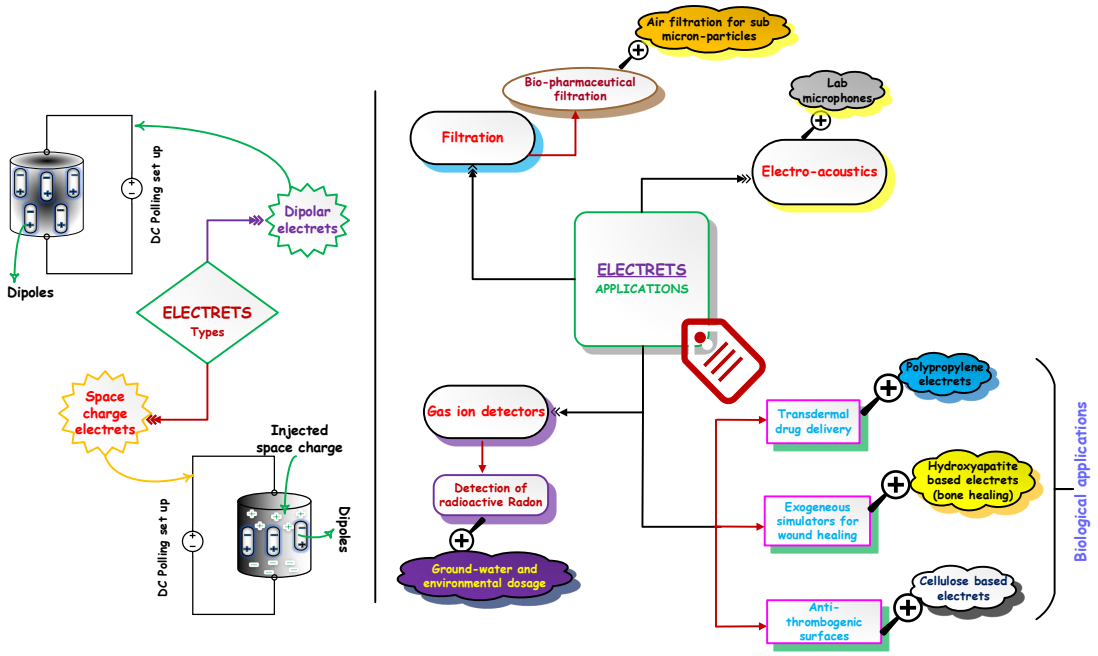


**Figure 4.1:** The different classifications of electrets and their mode of formation are graphically illustrated in the figures' left partition. These electrets have numerous technical applications, and some of them are schematically presented in the right section.

The ability to generate internal electric fields by ferroelectric materials leads to their applications in many low-powered biomedical devices such as pacemakers and defibrillators [36]. Many significant phenomena such as trapping biological molecules, induction of electro-kinetic process, and modulation of biological systems have hinted at the extensive use of ferroelectric materials. Researchers have investigated the possibility of ferroelectrics like $LiNbO_3$, $Fe$ doped $LiNbO_3$, $BaTiO_3$ (BT), and polyvinylidene fluoride for such applications [36, 60, 64, 146, 147]. Most recently, biological electrets have developed into a fertile research area, and it is being explored for developing various new devices in biomedical applications [148]. A schematic diagram showing the application of electrets in various fields with special attention to biological applications has been shown in Figure 4.1. Electrets can store charges for a sufficiently long time; they are quite handy in generating weak electric fields sufficient for regulating complex metabolic processes in the human body. Bio-

materials such as $Ca_{10}(PO_4)_6(OH)_2$ (HAP) as bio-electrets have been researched, and interestingly, the sparkling discovery of ferroelectricity and piezoelectricity has compelled researchers to consider its applications from a technological perspective [39, 86]. HAP is a dielectric, and its capability of generating a weak electric field can be related to the electrization of dielectric material by applying a high electric field. Especially HAP-based electrets have been shown to promote new bone formation along with the polarized electrets that have demonstrated superior responses on living cells, and tissues [149–152]. The exploration is not limited to biological applications; they are even considered in power generating systems [148, 153]. For applications in power generating systems, electrets are usually made from insulators with sufficiently high permittivity. However, the permittivity of HAP is on the lower side ($\simeq 5-10$ at 1 MHz) [154]. To improve the charge storage capacity in electrets, dielectric constant ($\epsilon_r$) of HAP has to be improved. To that extent, researchers [155–157] have explored composites made of HAP and BT specifically for their electrical properties. $CaTiO_3$, along with HAP, has also been explored for applications relating to orthopedic implants [154, 158]. The use of ceramics composites in biomedical applications has crucial advantages. For instance, ceramic composites exhibit properties that are superior to their constituents, and in some cases, they can even evolve characteristics absent in their monoliths. Additionally, the freedom to tailor the properties to suit any application is a boon in many experiments [159].

In this chapter, the emphasis has been laid on developing a ceramic composite of ST and HAP. ST is a perovskite widely explored in varistors, as anodes in fuel cells, and many other significant applications [159, 160]. Ferroelectrics are usually the most preferred choice for addition to a composite as they display substantially high $\epsilon_r$ [161]. However, they are associated with a remnant polarization that stores electric energy, and the presence of remnant polarization decreases the discharge efficiency of electrets [64]. Using a paraelectric such as ST eliminates this drawback and, at the same time, augments in generating a composite with high $\epsilon_r$. Specifically, in biomedical applications, there is an upsurge use of external stimuli like an alternating electric field in areas of bone injury for achieving a faster healing response [143]. Clinicians use scaffolds for such tissue engineering applications. Scaffolds derived from ceramics can undergo electrical polarization under alternating fields that would continue to augment the external field even after its removal [33]. An accelerated healing response can be achieved from such scaffolds, which would largely depend on the electrical properties like the $\epsilon_r$ of the ceramic. A higher $\epsilon_r$ leads to a strong polarized field and contributes to a faster healing process. However, the elec-

trical properties must be balanced by the biological properties of the composites to be suitable for biomedical applications. In this regard, ST has an improved $\epsilon_r$, and in one such study, the bioactive nature of the ST nanotube array is established [65]. The slow and effective release of $Sr$ ions from such nanotube arrays is demonstrated, which is found to be crucial for bone formation and improving osteoblast replication [66]. Fewer studies have also demonstrated the effective enhancement of the elastic modulus on the addition of ST to HAP (46 $\pm$ 10 GPa for monolith HAP and 54 $\pm$ 4 GPa for a composite containing HAP and ST (both at 50 wt.%)) [67]. In another study, the release of $Sr$ ions from ST nanoparticles in a heterostructure-based arrangement with $TiO_2$ nanoparticles has proven its effectiveness in cell proliferation of osteosarcoma cells [162]. Such release of $Sr$ nanoparticles effectively inhibits the osteoclast cells that help prevent vertebral or hip-fracture-related issues. Despite such advantages, in literature, only a few reports are available on the composite of HAP and ST, and protein adsorption investigations are scarce. When a biomaterial is implanted, one of the initial reactions on its surfaces is the adsorption of protein [163]. The adsorbed layer acts as the mediator for various cellular reactions later on the implants' surface. Proteins like albumin, which are polymers of amino acid residues, are highly useful in conducting such experiments as albumins are considered very well studied due to their abundance in blood plasma. Adsorbed protein is also known to enhance the osseointegration and biocompatibility of the surface [164]. Thus, protein adsorption studies can lead to a series of vital information about the behavior of a biomaterial.

In this study, by varying the concentrations of HAP and ST, an attempt is made to understand the changes in the microstructure of the prepared composites' electrical properties. The composites have been developed without any sophisticated high-end techniques for densifying the resultant compacts. This is done to keep in mind that such compacts will inherently be porous, and such a porous structure can be efficient for cell adhesion, bone formation, and ingrowth [90, 165]. In analyzing the electrical properties, it has to be understood that higher $\epsilon_r$ is associated with higher loss. Therefore, the lower conductivity ($\sigma$) specimens are beneficial for longer retention of the polarization and are essential from a biomedical perspective. Choosing a material for designing scaffolds must be preceded by a thorough investigation of its electrical permittivity and understanding its loss mechanisms. The elegant framework of Impedance spectroscopy (IS) is a vital tool for extracting such properties and is slowly gaining its edge in biomaterials research [90]. Inspired by the exciting developments, this chapter incorporates the study of the temperature

dependence of conductivity in the composites in the range of 133-523 K. In the chosen temperature range; the $\sigma$ is in the range of ($< 10^{-7} S/cm$), which is relatively low, making it suitable for electret design [166]. The range is selected to include the physiological temperature $\sim$ 310 K, and higher, which would be helpful to predict its usability in the design of bio-electrets. To the best of our knowledge, such mechanisms have never been applied to biomaterials design. It presents a fresh perspective of investigating the biomaterials' suitability by employing the Impedance spectroscopy techniques that can be the starting point for designing and analyzing advanced biomaterials.

## 4.2 Experimental details

### 4.2.1 Synthesis of the precursors and compact discs

As discussed in the previous chapter, the HAP and ST powders are prepared by the sol-gel processing and solid-state reaction method, respectively. The powders are then pressed into cylindrical green compacts applying a uniform pressure of 25 $kg/cm^2$. Several compacts are prepared for each composition under the same conditions and are finally sintered at 1073 K for 3 h for densification and compaction of the resultant cylindrical compacts. The compositions are already mentioned in Chapter 2. However, for clarity, the compositions and their respective codes are mentioned in Table 4.1.

**Table 4.1:** The composition of different compact discs and their codes.

| Monolith | Monolith | Scheme | Code |
|---|---|---|---|
| HAP | ST | 100 At.% HAP | HAP |
| | | 20 At.% HAP & 80 At.% ST | 20H-80S |
| | | 40 At.% HAP & 60 At.% ST | 40H-60S |
| | | 60 At.% HAP & 40 At.% ST | 60H-40S |
| | | 80 At.% HAP & 20 At.% ST | 80H-20S |
| | | 100 At.% ST | ST |

## 4.2.2 Characterization techniques

### 4.2.2.1 Micro structural, electrical and surface morphology

The characterization techniques adopted for a systematic analysis of the prepared specimens' properties involve X-ray diffraction (XRD) and Raman spectroscopy for crystal structure evaluation. The diffracted x-ray photons were obtained for the specimens in the $(2\theta)$ range of $20 - 55°$, scanning at the rate of $3°$/min. The data was collected at an interval of $0.03°$ (TTRAX III, Rigaku, Japan). The XRD patterns were then matched to the standard International Center for Diffraction Data (ICDD) files. The Raman spectra, on the other hand, was collected for a Raman shift of 100-1200 $cm^{-1}$ using a micro-Raman spectrometer (Jobin Yvon LabRAM, Horiba, Japan). The Raman spectrometer utilized an argon ion laser operated at a wavelength of 514.5 nm. The dielectric spectra for the prepared specimens have been obtained in the frequency range of 1 MHz-1 GHz, varying the temperature from 133 K to 523 K using an impedance analyzer (4991A, Agilent Technologies, USA) equipped with a temperature control system (BDS 2300, Novocontrol, Germany). The temperature controller used liquid nitrogen for temperature control, and the frequency sweep was done after the temperature stabilized at an interval of 10 K each (starting from 133 K). For measuring the conductivity, the same Impedance analyzer was used, where the fabricated MIM capacitors are loaded into a sample holder. By varying the frequency in the range of 1 MHz-1 GHz, the data for the conductivity of the specimens were collected.

The morphology of the specimens was observed using field emission scanning electron microscopy FESEM (Sigma 300, Zeiss, Germany). The FESEM images have also been used for determining the grain sizes of the specimens using the Image J software. The elemental composition of the specimens were also determined using the EDS (Oxford Instruments, UK) facility attached to the FESEM.

To supplement FESEM images, the field emission transmission electron microscopy (FETEM) (2100F, JEOL-JEM, Japan) images were recorded along with the high-resolution transmission electron microscopy (HRTEM) images.

For studying the biological properties of the sintered discs, the protein adsorption of the compacts was studied. Bovine serum albumin (BSA) (Sigma Aldrich, USA) was used for the protein adsorption study of the synthesized specimens, and the details of the procedure are reported elsewhere [27]. 3-[4,5-dimethylthiazol-2-yl]-2,5-diphenyltetrazolium bromide (MTT) assay of the specimens with varying concentrations (0.5, 0.2, and 0.1 mg/ml) is carried out on MG63 cell line using

MTT assay following the protocol previously described by our research group [27]. Samples were dispersed in MilliQ water, followed by autoclave sterilization. $10^4$ cells/well were seeded in each well and incubated for 1, 3, and 5 days. Cells were incubated in Dulbeccos' modified eagle medium (DMEM) in $CO_2$ incubator at 5% $CO_2$ and 310 K. After each specified time interval, 50 $\mu$l of MTT (0.5 mg/ml) containing fresh DMEM media was removed and incubated in $CO_2$ incubator for 4 h. Post incubation, formazan crystals were dissolved in 100 $\mu$l filtered dimethyl sulfoxide (DMSO). Absorbance was carried out at 570 nm (Infinite 200 Pro, Tecan). Cell viability (%) was calculated and compared to control wells without samples. The assay was carried out in triplicate.

Finally, the *in-vitro* bone-like apatite nucleation ability of the specimens was analyzed using the simulated body fluid (SBF). The specimens were incubated in 1.5 SBF solution for 12 days at 310 K, ensuring that the old solution was refreshed every 24 hours. The 1.5 SBF solution was prepared using the protocol suggested by Kokubo *et al.* [167] with a slight modification that the concentration of ions in the solution was enhanced to 1.5 times the original concentration [52]. Following incubation, the specimens were washed and dried for 24 hours at 333 K. Further, the growth of bone-like apatite was analyzed using FESEM for understanding the phase and surface morphology of the apatite layer. To measure the zeta potential of the specimens, the specimens were dispersed in phosphate buffer saline (PBS) (pH 7.4) and analyzed in a Litesizer particle size analyzer (Litesizer 500, Anton Paar, Austria).

## 4.3 Results and Discussions

### 4.3.1 Structural analysis

XRD is an exquisite technique employed to reveal a plethora of information regarding the phase composition, microstructure, strain, and mechanical properties of the material under analysis. The compositional phase of the sintered discs is systematically depicted in Figure 4.2. The phase analysis of the different compositions has been achieved by comparing the patterns with the existing ICDD files #009-0432 for HAP and #073-0661 for ST. A careful analysis of the XRD patterns ruled out the possibility of obtaining any phase corresponding to $CaTiO_3$ or $Sr_{10}(PO_4)_6(OH)_2$. All the peaks individually correspond to the parent monoliths that have been mixed in different percentages. However, owing to the closeness of the Bragg positions of

ST [(110) and (211)], and HAP [(112) and (300)], there is an overlap of the XRD peaks to some extent at these values. It can be observed in $80H - 20S$ that the (112) peak (of ST) at 32.2° and (112) of HAP at 32.5°, is distinguished by a small depression in intensity. The depression tends to vanish as the content of ST in the composite increases. Further, the depression is reduced into a single individual peak of ST for $20H - 80S$.

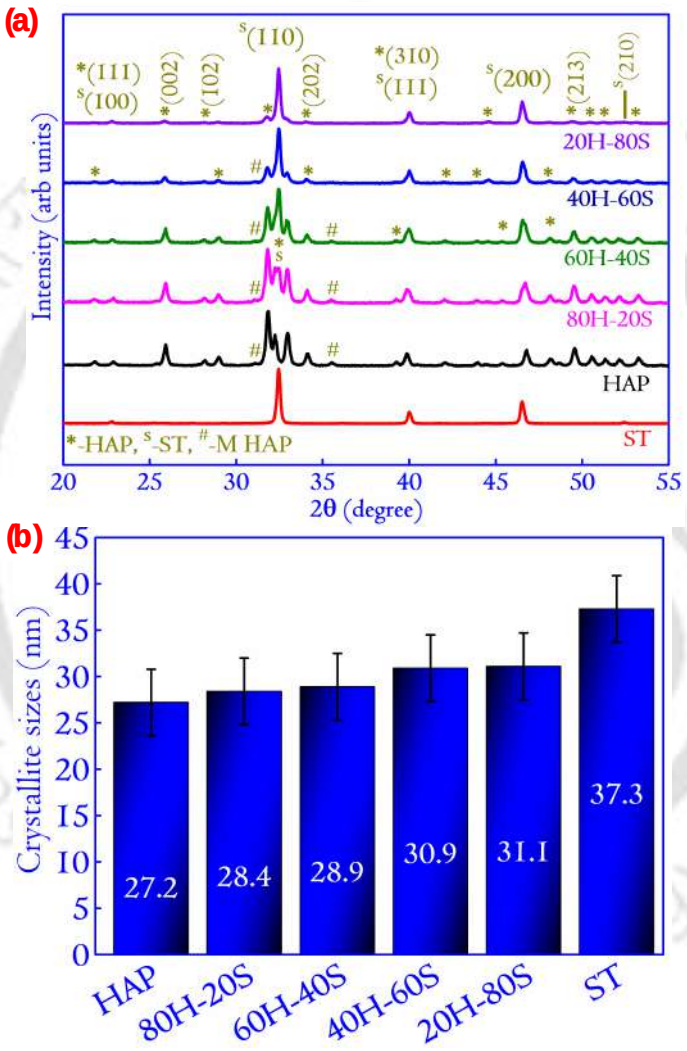


**Figure 4.2:** (a) The XRD spectra of the composites and their monoliths. The spectra do not reveal any trace of phase that the monoliths' reaction may form. However, at certain $(2\theta) \sim 32°$, there is an overlap of X-ray reflections from the monoliths. (b) The variation in composites' crystallite sizes and the monoliths in the form of a bar diagram. The variation shows that the composites' crystallite sizes lie between the monoliths.

Interestingly, the XRD pattern of HAP reveals two small intensity peaks that correspond to the monoclinic HAP (M HAP) phase. The monoclinic structure of

HAP is usually associated with an ordered arrangement of $OH^-$ ions and, at a temperature of $\simeq$ 483 K, undergoes a phase transition to the hexagonal structure, which is characterized by a disordered arrangement of the $OH^-$ ions [109, 140]. These two peaks continuously decrease in intensity with increasing ST content in the specimens and are suppressed entirely for $20H-80S$. The increase in the content of ST might be related to the suppression in the monoclinic peaks of the specimens [168]. Since the hexagonal phase is the predominant phase, it can be concluded that at a mixing percentage of 80 At.% of ST, the hexagonal phase is stabilized. A similar stabilization of the cubic form of $La_2Mo_2O_9$ is also observed by Subasri *et al.* [169], where it is inferred that adding $CaO$ up to 4 mol.% to $La_2Mo_2O_9$ could stabilize the cubic structure at room temperature. The broadening of the XRD peaks can be utilized to determine the crystallite sizes in the specimens. An ideal diffraction pattern of specimens demands the peaks to be sharp without any broadness (*i.e.,* a line). The finite crystallite size and internal strain often limit the diffraction pattern from being ideal and produce broad peaks [161]. The composites' average crystallite size has been calculated using the Scherrers' equation, which can be expressed as

$$Crystallite\ size\ (D) = \frac{k\lambda}{\beta \cos\theta} \tag{4.1}$$

where $k$ is the Scherrers' constant (0.8-0.9), $\beta$ is the full width at half maximum (FWHM) in radians, $\lambda$ denotes the wavelength of X-ray, and $\theta$ is the Bragg angle. The crystallite sizes of each specimen are calculated and plotted in Figure 4.2(b). From Figure 4.2(b), it is found that the crystallite size shows a gradual increase with ST content in the specimens. HAP has a smaller crystallite size (27.2 nm) than ST (37.3 nm), and in the case of composites, the presence of one component can restrict the growth of the other. ST can be predicted to be the dominant phase from the calculations as with an increasing ST content, the crystallite size tends to improve.

The crystallite size obtained from the Scherrer formula for HAP is similar to other reports for HAP specimens sintered in the range of 973 K-1173 K [170, 171]. The crystallite size is a temperature-dependent parameter and usually increases with temperature. In the case of ST, the crystallite sizes obtained by most researchers are in the range of 20-30 nm [172, 173]. It is observed that the synthesis process in most of these cases is the sol-gel process, which produces ultra-fine powders that require lower calcination temperatures and hence lesser crystallite size. The solid-state reaction route adopted for synthesizing ST requires the powder to be calcined at very high temperatures (>1273 K) and therefore produces powder with larger

crystallite sizes that need higher sintering temperatures for improved densification [174].

### 4.3.2 Raman analysis:

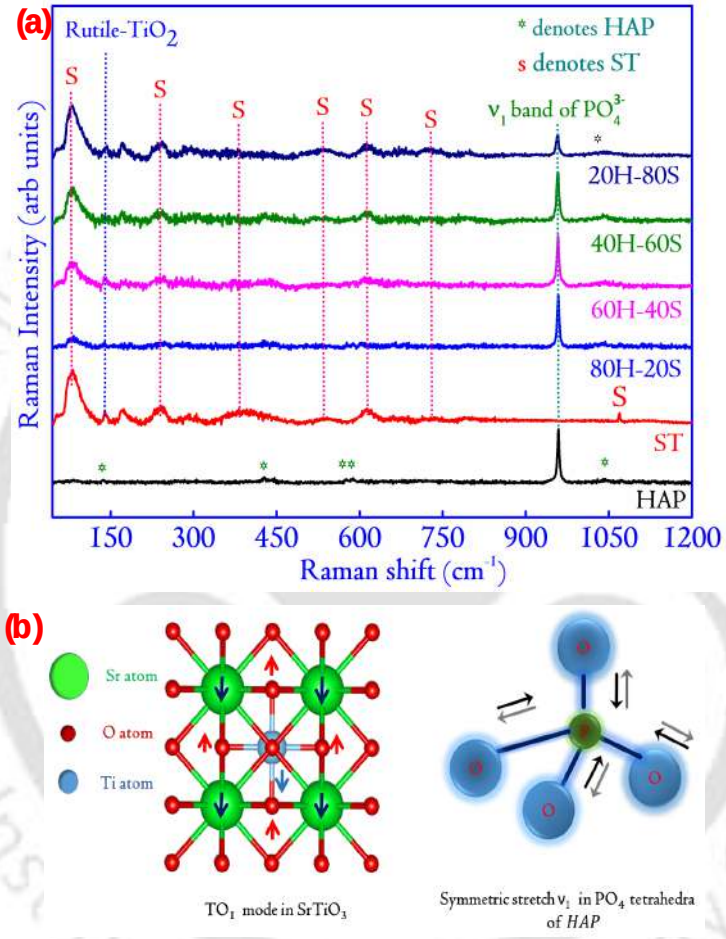


**Figure 4.3:** (a) The Raman spectra of the composites and their monoliths are presented. The Raman spectra reveal specific details like the presence of unreacted rutile $TiO_2$, which plays a crucial role in the apatite nucleation ability of the specimens. In conjunction with XRD, the Raman spectra did not present any trace of phase that a reaction between the two monoliths might form, and (b) the graphical illustration of the $TO_1$ mode in ST and $\nu_1$ mode in HAP. These are a few selected modes of vibrations in ST and HAP, illustrated for a clear understanding of the incident laser beams' interactions with the microstructure of the composites. Much detailed description of all the possible modes of vibration in ST and HAP can be found in the text.

The Raman spectra of the prepared composite are depicted in Figure 4.3. Interestingly, the Raman spectra of the composites revealed a low-intensity band at

approximately 140 $cm^{-1}$ for all the specimens except HAP, which is attributed to rutile $TiO_2$ [175]. The source of rutile $TiO_2$ can be traced out to anatase $TiO_2$ used as the precursor in preparing ST. At 1073 K, any amount of unreacted anatase $TiO_2$ converts to rutile $TiO_2$, which is the most stable polymorph of $TiO_2$ [176]. Similarly, the band at 171 $cm^{-1}$, which appears for ST and other composite containing higher At.% of ST, is a specimen-dependent band originating due to impurities in the microstructure of ST [177]. Bands from ST mostly dominate the Raman spectra for the specimens. A summary of all the bands, and their assignments, have been tabulated in Table 4.2. ST crystallizes in a cubic lattice (space group $Pm3m$), with all atoms lying at the center of inversion [178]. From symmetry, all the first-order bands of ST are prohibited, and the observed bands are due to second-order Raman scattering [175]. Researchers have predicted four doubly degenerated transverse optic modes ($TO_1, TO_2, TO_3, TO_4$), four longitudinal optical modes ($LO_1, LO_2, LO_3, LO_4$), a transverse acoustic mode (which is doubly degenerate (TA)), and a longitudinal acoustic mode ($LA$) that accounts for a total of 10 phonon branches to explain the observed variation of the Raman spectra [109]. A graphical depiction of the $TO_1$ mode of vibration in ST is illustrated in Figure 4.3(b). All the observed Raman bands in the spectra can be explained by the addition or difference combinations. The other component HAP has the maximum intensity Raman band appearing at 960 $cm^{-1}$ and is attributed to the $\nu_1$ mode of free $(PO_4)^{3-}$ tetrahedron. The bands are dominated by the vibrational modes of tetrahedral $(PO_4)^{3-}$ ions in HAP. These modes are normal modes of vibration and give rise to four frequencies classified in the literature as $\nu_1$, $\nu_2$, $\nu_3$, and $\nu_4$. The origin of these modes can be sourced to the symmetric stretching of $P-O$ bonds, which leads to the generation of the frequency $\nu_1$. $\nu_2$ is related to the bending mode of $O-P-O$ vibrations that are doubly degenerate, whereas $\nu_3$ mode arises from the asymmetric stretching of $P-O$ bonds and is triply degenerate. The $\nu_4$ band is triply degenerate and is due to the bending of $O-P-O$ bonds in the lattice. An illustration of the $\nu_1$ vibrational mode in HAP is depicted in Figure 4.3(b). Apart from the $(PO_4)^{3-}$ bands, bands pertaining to the $Ca-PO_4$ lattice modes are also found at lower wavenumbers corresponding to 84 $cm^{-1}$, 132 $cm^{-1}$, and 269 $cm^{-1}$, which are of very weak intensities. It is interesting to note that, like XRD, the Raman bands' intensity varies regularly with the At.% of the components in the specimens. For instance, the bands at 81 $cm^{-1}$ due to ST and 960 $cm^{-1}$ due to HAP show the pristine specimens' highest intensities. However, with a reduction in At.% of the composites, the respective bands' intensity continuously decreases.

**Table 4.2:** The Raman bands and their assignments for different bonds in the composite and the monoliths.

| **Bands** ($cm^{-1}$) | **Assignments** | **Intensity** |
|---|---|---|
| 81 | $TO_2 - TA_1$<br>$TO_2 - TO_1$ | very<br>sharp |
| 84 | Translational modes of $Ca^{+2}$ and $(PO_4)^{3-}$ | weak |
| 132 | $Ca - PO_4$ lattice modes | weak |
| 140 | $B_{1g}$ (Rutile $TiO_2$) | weak |
| 171 | band originating due to impurity in ST | medium |
| 244 | $2TA$<br>$2TO_1$ | medium |
| 269 | $Ca - PO_4$ lattice modes | weak |
| 300 | $TO_2 + TA_1$<br>$TO_2 + TO_1$<br>$TO_4 - TO_2$<br>$TO_1 + LO_1$<br>$TO_2 + LA$ | small |
| 384 | $LO_1 + TA$<br>$TO_4 - TO_1$<br>$TO_4 - TA$<br>$2TO_2$ | medium |
| 428 | $\nu_2$ band of $PO_4$ | medium |
| 446 | $\nu_2$ band of $PO_4$ | medium |
| 543 | $TO_4$ | small |
| 575 | $\nu_4$ band of $PO_4$ | medium |
| 583 | $\nu_4$ band of $PO_4$ | medium |
| 613 | $TO_4 + TA$<br>$TO_4 + TO_1$<br>$2TO_3$ | medium |
| 674 | $TA + LO$<br>$TO + LO$ | very<br>small |
| 734 | $TO_4 + TO_2$<br>$LA + LO_4$ | very<br>small |
| 960 | $\nu_1$ band of $PO_4$ | very sharp |
| 1042 | $\nu_3$ band of $PO_4$<br>$2TO_4$ | medium |
| 1069 | $2LO_2$<br>$LO_1 + LO_4$ | medium |

### 4.3.3 Surface Morphology and EDS analysis

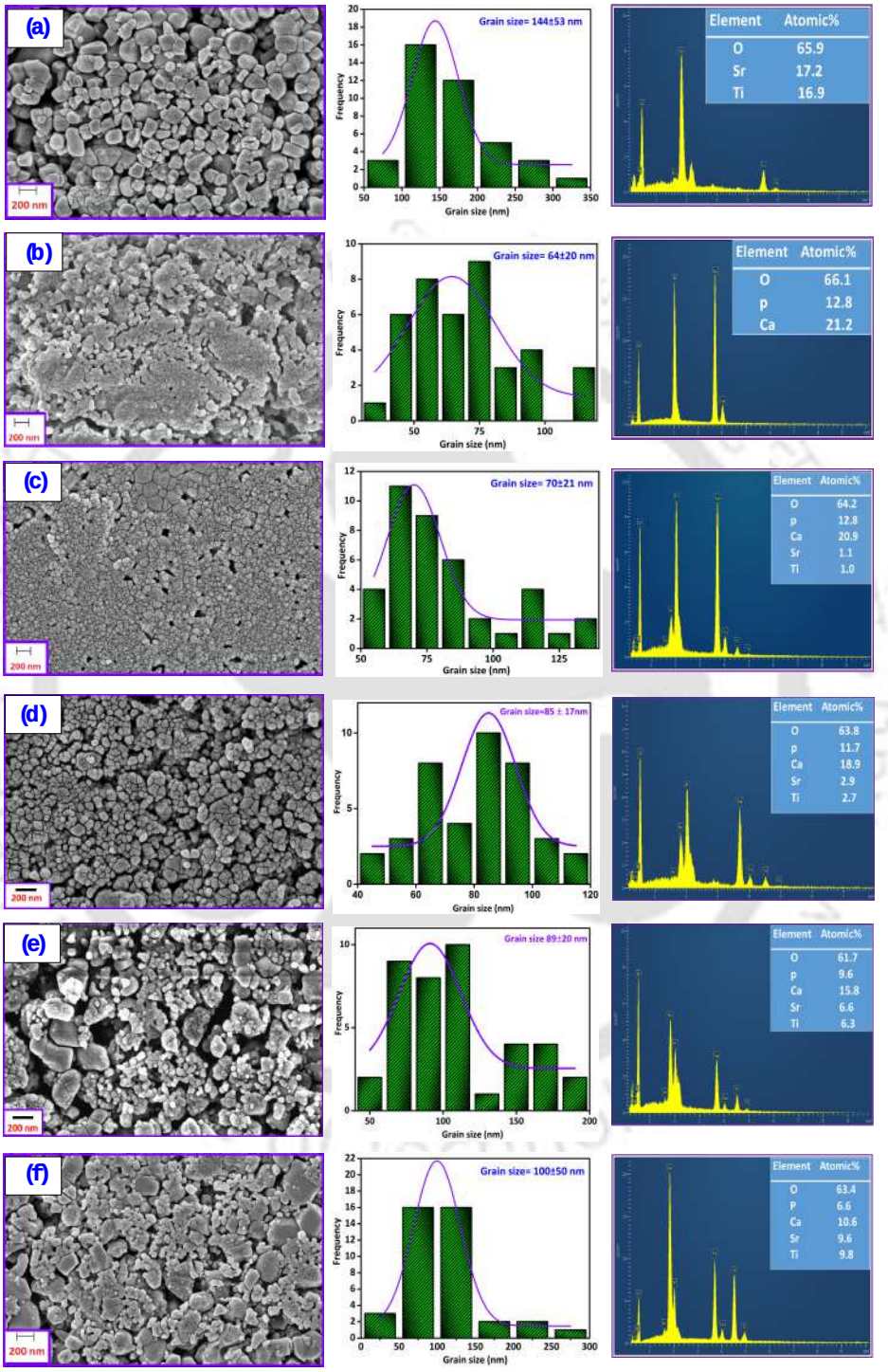


**Figure 4.4:** The FESEM, grain size estimation, and EDS of (a) ST, (b) HAP, (c) $80H-20S$, (d) $60H-40S$, (e) $40H-60S$, and (f) $20H-80S$. For estimating the grain size, the ImageJ software is used, and a Gaussian curve is fitted to extract the average grain size of the distribution.

The surface morphology and the quantitative estimation of the At.% of various elements (equation 4.2, 4.3, and 4.4, where we assume that the compound has the general formula $A_xB_yC_z$) in the prepared specimens are depicted in Figure 4.4.

$$At.\,\%\,of\,A = \frac{N_A * 100\%}{N_A + N_B + N_C}, \tag{4.2}$$

$$At.\,\%\,of\,B = \frac{N_B * 100\%}{N_A + N_B + N_C}, \tag{4.3}$$

$$At.\,\%\,of\,C = \frac{N_C * 100\%}{N_A + N_B + N_C}. \tag{4.4}$$

where $N_A$, $N_B$ and $N_C$ are number of atoms of A(=x), B(=y) and C(=z) respectively.

The FESEM micrographs depict the presence of porosity in the specimens. The larger grains corresponding to ST and the smaller HAP grains complement each other so that the empty spaces between the larger grains are filled up by, the smaller HAP grains. Additionally, ceramics like ST requires a higher temperature (>1273 K) along with the enhanced soaking time of several hours for improved densification [179]. In the present scenario, to avoid disintegration of HAP into secondary phases like $\beta$-TCP, the sintering temperature is fixed at 1073 K. It has been reported previously that above 1073 K, HAP might undergo dehydration resulting in the formation of secondary phases [180]. This lower sintering temperature might be one of the primary causes of porosity in most specimens. Although no specific morphology of ST and HAP specimens is observed, most ST grains are characterized by polyhedral structures, and the HAP grains are primarily spherical. However, in the case of ST, the grains are well separated from one another, having well-defined grain boundaries. On the contrary, HAP grains coalesce, forming an aggregate with no clear grain boundaries. The calculation of grain sizes revealed that the grains are primarily nanoparticles with dimensions less than 100 nm for HAP. The surface-to-volume ratio of the nanoparticles is usually large, leading to increased surface energy. By agglomeration, an interface with lower energy is formed, reducing the surface energy [181]. The average grain sizes of the composites and monoliths have been shown in Figure 4.4. The composites' grain sizes follow the same trend as the crystallite sizes calculated in Figure 4.2(b). Since the grain sizes are larger than the crystallite sizes, the grain is an agglomeration of several crystallites. However, as no trace of a phase is bought about by a reaction between the parent compounds (as identified from XRD and Raman spectra in Figure 4.2 and Figure 4.3), the

possibility of inducing a reaction between the constituent phases by thermal energy (by actuating the coalesce of HAP and ST grains) can be ruled out. So the grains retain their identity in the composite at a sintering temperature of 1073 K.

**Table 4.3:** The elementary atomic composition of various elements in the composites.

| Specimens | Elements | Ca | P | O | Sr | Ti | Ca/P |
|---|---|---|---|---|---|---|---|
| 80H-20S | Observed | 20.9 | 12.8 | 64.2 | 1.1 | 1.0 | |
| | Theoretical | 21.50 | 12.90 | 59.13 | 1.07 | 1.07 | 1.64 |
| | Relative error (%) | 3.00 | 1.00 | 9.00 | 3.00 | 7.00 | |
| 60H-40S | Observed | 18.9 | 11.7 | 63.8 | 2.9 | 2.7 | |
| | Theoretical | 19.74 | 11.84 | 59.21 | 2.63 | 2.63 | 1.61 |
| | Relative error (%) | 4.00 | 1.00 | 8.00 | 10.00 | 3.00 | |
| 40H-60S | Observed | 15.8 | 9.6 | 61.7 | 6.6 | 6.3 | |
| | Theoretical | 16.95 | 10.17 | 59.32 | 5.08 | 5.08 | 1.64 |
| | Relative error (%) | 10.00 | 8.00 | 7.00 | 5.00 | 2.00 | |
| 20H-80S | Observed | 10.6 | 6.6 | 63.4 | 9.6 | 9.8 | |
| | Theoretical | 11.90 | 7.14 | 59.52 | 9.52 | 9.52 | 1.60 |
| | Relative error (%) | 11.00 | 8.00 | 7.00 | 3.00 | 3.00 | |
| HAP | Observed | 21.2 | 12.8 | 66.1 | - | - | |
| | Theoretical | 23.00 | 14.00 | 59.00 | - | - | 1.65 |
| | Relative error (%) | 8.00 | 9.00 | 12.00 | - | - | |
| ST | Observed | - | - | 65.9 | 17.2 | 16.9 | |
| | Theoretical | - | - | 60.00 | 20.00 | 20.00 | - |
| | Relative error (%) | - | - | 10.00 | 14.00 | 15.00 | |

The EDS spectra of the specimens show the At.% of various elements. A comparison of the theoretically calculated At.% and experimentally obtained values for multiple elements in selected composites have been shown in Table 4.3. The formulas adopted for calculating the At.% are included in equations 4.2, 4.3, and 4.4. The EDS analysis shows a fair agreement in atomic composition between the experimentally observed values and the theoretically estimated ones [182]. In biocomposites, the $Ca/P$ ratio is a crucial factor that determines the specimens' behavior *in-vivo*. The biodegradation of calcium phosphate-based compounds in aqueous media are

entwined to the $Ca/P$ ratio, and this behavior highly dictates the bone remodeling behavior around the implants [183]. For HAP, it is 1.65, and it has been observed that with an increase in the $Ca/P$ ratio, the biodegradation rate decreases [184]. However, composites, the $Ca/P$ ratio slightly decreased than HAP due to the presence of ST. In all the specimens with HAP monolith, the $Ca/P$ ratio is found to be more than 1.60, and in literature, this ratio is confined to the range 1.50-2.00 for variants of calcium phosphate-based ceramics [185].

### 4.3.4 Dielectric properties of the composites

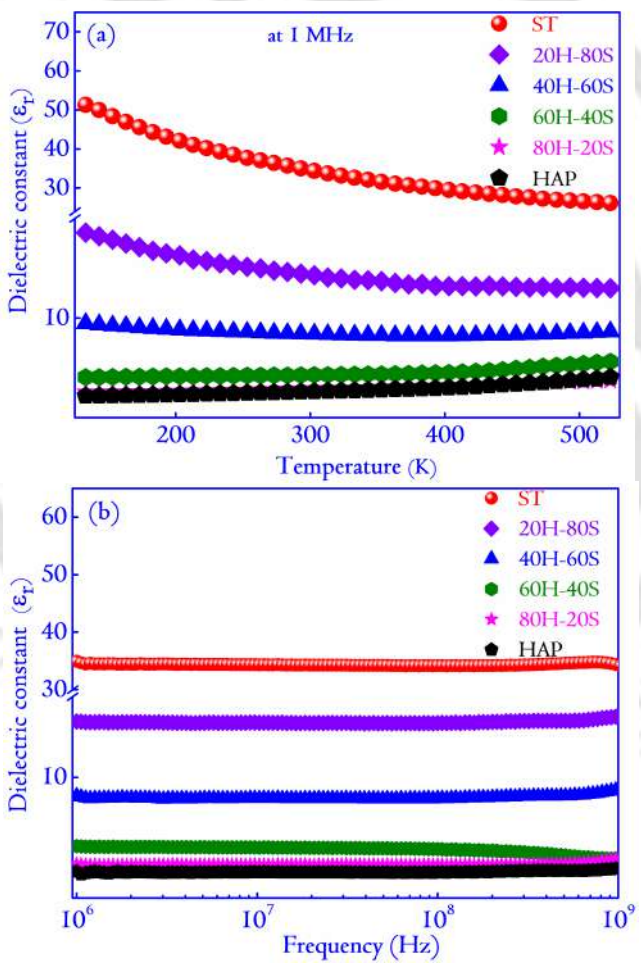


**Figure 4.5:** The variation in the values of $\epsilon_r$ of the composites and their monoliths are shown with respect to variations in (a) temperature at 1 MHz and (b) the frequency at room temperature. For the complete range of temperature and frequency, the values of $\epsilon_r$ for the composites lie between the monoliths. The probed frequency range of $10^6$ to $10^9$ Hz spans the RF spectrum and bears special significance for applying the composites in specific biomedical applications detailed in the chapter.

The variation in dielectric properties of the composites has been studied with respect to frequency and temperature, and the plots have been depicted in Figure 4.5. The frequency range adopted for the present analysis ranged from $10^6$ to $10^9$ Hz, which spans the RF spectrum. Detailed studies are available in the literature that wonderfully describes the behavior of both the individual components in the frequency range spanning from 10 to $10^6$ Hz [186, 187]. However, the range probed in this study is not usually considered, especially for materials with potential biological applications. The justification for probing the said frequency regime may be found from the reports of Sharp *et al.* [188], where it is reported that application of RF pulses is an effective treatment of delayed union and non-union of bone fractures. Individual reports [177] have cited the paramount importance of exposure to low-intensity RF electromagnetic fields in cancer treatment. Recent research has also hinted at the importance of studying the dielectric properties of HAP thick films in the GHz range because HAP films are investigated for biosensing applications [189, 190].

In Figure 4.5(a), a variation in the $\epsilon_r$ of the composites with respect to temperature is seen. In Table 4.4, the values of tan$\delta$ at 1 MHz measured at various temperatures have been included. Usually, the $\epsilon_r$ tends to increase with the application of temperature. This is attributed to the orientation of the dipoles along the applied field with increased thermal energy. Interestingly, in this case, $\epsilon_r$ is found to reduce with temperature for specimens containing a more significant fraction of ST [191]. The decrease can be associated with the phase transition of ST at a temperature of 105 K, which tends to increase $\epsilon_r$ abruptly at the phase transition temperature $T_C$ [192]. Since $\epsilon_r$ is highly dependent on the structure, and a structural transition usually accompanies a phase transition, it leads to a sudden jump in $\epsilon_r$. However, for the other specimens: HAP, $80H - 20S$, and $60H - 40S$, $\epsilon_r$ remains constant for most of the temperature range and exhibits a minor rise towards high temperature due to thermally activated conduction mechanism. Since the conduction in HAP is mostly ionic, it occurs mainly in the columns of $OH^-$ along the c-axis either by the flipping of $OH^-$ ions or exchange of proton vacancies along the $OH^-$ chains or hopping of the $OH^-$ ions in the specimens [193]. The values of $tan\delta$ at various temperatures have been shown in Table 4.4. The values of $tan\delta$ are quite low, and with a temperature rise, improvements in the values of $tan\delta$ are observed. Such variations are usually observed with a rise in temperature, the kinetic energy of the conducting species increases leading to losses in the ceramic composites. The low losses in the ceramic composites can be helpful in electret-based applications

that generally require low losses for a longer lifetime of such devices.

Moreover, in this study, we found that the $\epsilon_r$ of ST at 1 MHz is $\sim 35$ at room temperature. The reported value of $\epsilon_r$ of ST at room temperature is $\sim 10 - 500$ (1 kHz), which is very high compared to the observed value [178]. $\epsilon_r$ is a parameter that depends largely on density/porosity, microstructure, grain size, and to a large extent, on the processing parameters and conditions [114]. Also, the sintering temperature is kept at 1073 K, which is not very high in comparison to the traditional ceramics that are fired at $>$ 1273 K. The FESEM micrographs too revealed the fact that a considerable amount of pores are retained in the ST specimens and those that contained a higher amount of ST. A similar value of $\epsilon_r$ at 1 MHz is also reported by Wong *et al.* [194], where no dispersion in the behavior of $\epsilon_r$ is reported in the probed frequency domain. In Figure 4.5(b), the variation of $\epsilon_r$ with frequency is plotted. The specimens show very little dispersion of $\epsilon_r$, and the values remain constant for the considered range of frequencies. The frequency independence of the $\epsilon_r$ implies that the major polarization processes have relaxed and do not contribute to the $\epsilon_r$.

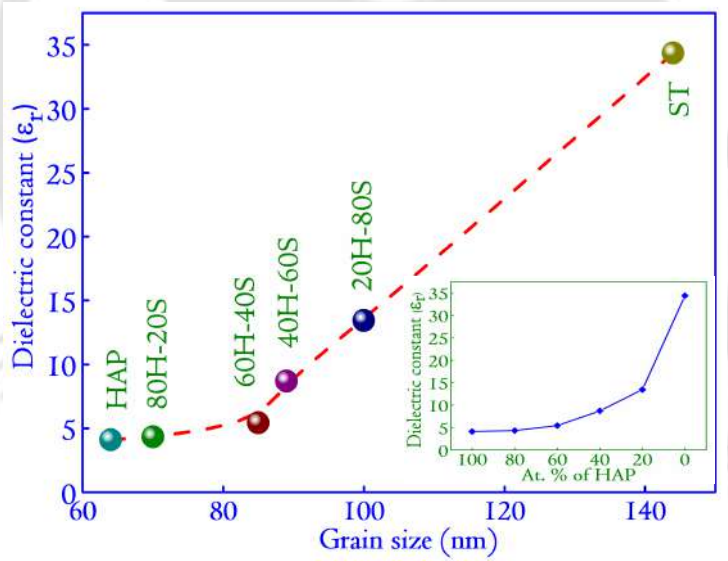


**Figure 4.6:** The variation in the values of $\epsilon_r$ of the composites and their monoliths at 1 MHz is shown with respect to variations in grain size and At.% of HAP (inset). In both cases, the variations are exponential. In the first case, the $\epsilon_r$ exponentially increases with grain size when there is an increase in the content of ST (At.% of ST) in the specimens. In the other scenario (refer inset), the $\epsilon_r$ shows a steady increase (nearly exponential) with the At.% of HAP, an exciting feature detailed in the description.

The variation in $\epsilon_r$ with grain size and At.% of HAP and ST is plotted in Figure 4.6. The values for $\epsilon_r$ are extracted at 1 MHz and plotted to understand grain size influence on $\epsilon_r$. In Figure 4.6, a steady increase in $\epsilon_r$ with grain size and At.% of

ST is observed. The FESEM micrographs in Figure 4.4 revealed that ST specimens have the largest grain sizes. The grain sizes steadily decreased with At.% of ST in the composites. The results also imply that ST, which had a larger grain size, strongly influenced the composites' electrical properties. A similar variation in $\epsilon_r$ with grain sizes is also reported by Wong *et al.* [195], Tang *et al.* [196], and Horiuchi *et al.* [114]. It is a widely known fact that the grains are relatively more conducting than grain boundaries, and smaller grain sizes tend to affect $\epsilon_r$ adversely [114]. Non-ferroelectric grain boundaries reportedly have lower $\epsilon_r$ and are often termed in literature as "dead layer." The proportionate increase in the fraction of grain boundaries with a decrease in the grain size will lead to a decline in the values of $\epsilon_r$ [197].

**Table 4.4:** Variation of $tan\delta$ at 1 MHz at selected temperatures.

| **Specimens ↓** | **283K** | **323K** | **373K** | **423K** | **473K** |
|---|---|---|---|---|---|
| ST | 0.00219 | 0.00349 | 0.00319 | 0.00299 | 0.00616 |
| HAP | 0.00147 | 0.00244 | 0.00914 | 0.01672 | 0.04376 |
| 20H-80S | 0.00941 | 0.00428 | 0.00805 | 0.02948 | 0.02588 |
| 40H-60S | 0.00641 | 0.00548 | 0.00681 | 0.00739 | 0.00812 |
| 60H-40S | 0.00114 | 0.00679 | 0.02004 | 0.03253 | 0.05314 |
| 80H-20S | 0.00225 | 0.00335 | 0.00465 | 0.00777 | 0.00909 |

### 4.3.5 $\sigma$ and hopping mechanisms

The variation in $\sigma$ of the composites with respect to temperature is shown in Figure 4.7. From a biomedical perspective, the frequency range of $10^6$ to $10^9$ Hz (the radio frequency (RF) domain) is used as an effective course of treatment for non-union of bones and fracture healings [198]. Electrical stimulations in the form of RF pulses are frequently used for such applications, and although the mechanism is inconclusive, the results are pretty impressive. Biomedical research has hinted at the use of radiofrequency energy to produce superior hemostasis in bones without any healing complications [199]. Clinicians also have resorted to the use of bipolar RF energy-based devices to avoid necrosis in several applications [200]. It has to be understood that in such applications of RF, the clinicians are yet to arrive at a particular configuration (exact frequency and amplitude of RF that would be suitable

for the intended applications) [200]. To the best of our knowledge, there is no standard available that determines specific settings of RF for inducing the best healing response [201]. Deriving motivation from such applications, the chapter is dedicated to understanding the electrical properties (specifically, the behavior of biomaterials to augment the fracture healing process should be understood before their *in-vivo* applications). In Figure 4.7, the $\sigma$ plots show a significant temperature dependence after 300 K when the $\sigma$ rises compared to the dependence at low temperatures. A temperature range of 303 K to 523 K has been chosen for the $\sigma$ analysis primarily for two reasons. The first is the incorporation of physiological temperature, at which most of the biophysical reactions take place [123]. Secondly, the increasing research interest in developing electrets of biomaterials useful in devices like low-powered electrostatic induction generators involves sufficiently high temperatures (310 K–473 K) [202]. Thus, understanding the conduction mechanisms is of prime importance in these temperature ranges.

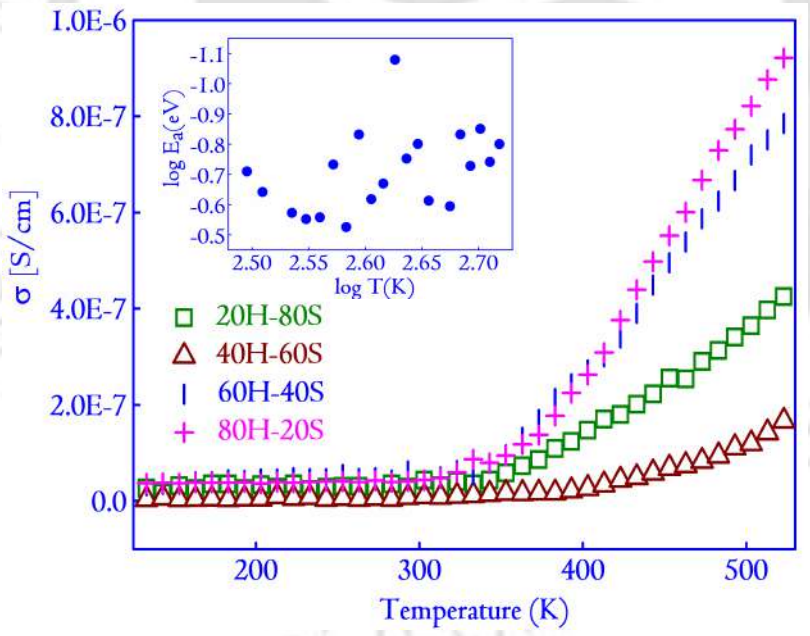


**Figure 4.7:** Variations in $\sigma$ with temperature for the composites are plotted. In the inset of the figure, a variation in the $E_a$ with temperature is plotted in log scale to demonstrate the variation in the $E_a$ with temperature for $20H - 80S$. Also, the variations in $\sigma$ of the specimens with respect to frequency are shown in Figure B.1(a-b) (Appendix B), along with the temperature variation of the $\sigma$ of the monoliths shown in Figure B.2(b) (Appendix B). For the other samples, the $E_a$ versus T plot is shown in Appendix B (in Figure B.3). In the thermally activated conduction mechanism, $E_a$ remains constant over a specific temperature range. In the present study, the variation in $E_a$ with temperature points towards the hopping conduction mechanism. The variations are considered in the temperature range of 303 K to 523 K.

A model that describes the conduction process is mathematically formulated as [148]

$$\sigma = \sigma_0 exp(\frac{-E_a}{k_B T}) \tag{4.5}$$

where $\sigma_0$ is the pre-exponential factor (a constant), $K_B$ is the Boltzmann constant, $T$ is the temperature and $E_a = -\frac{d[ln\sigma]}{d[\frac{1}{k_B T}]}$ is the activation energy of bulk conduction specific to the process [203]. The previous expressions' versatility lies in their ability to determine the $E_a$ of the conduction process irrespective of the mechanism active within the specimens'. At non-zero temperatures, specifically in insulators like bioceramics, the free carriers' concentration is close to zero. The density of defects, impurities, and trapping centers for the electrons are higher. Therefore, hopping is the main conduction mechanism until the room temperature and even higher [204]. There are two types of hopping mechanisms relevant to bioceramics *viz.* the nearest-neighbor hopping conduction (NNH) and the variable range hopping conduction (VRH). In the NNH mechanism, the hopping takes place to the nearest neighboring empty sites, and in literature, it is cited that the $E_a$ of such conduction process must be valued constantly for a particular range [205]. However, it is clear from the inset of Figure 4.7 that $E_a$ is a temperature-dependent function. The variable nature of $E_a$ indicates the existence of VRH mechanisms in the specimens, consistent with the VRH theory.

Understanding the hopping mechanism from the perspective of resistivity ($\rho = (1/\sigma)$) can reveal a plethora of information about the mechanism of conduction within the specimens'. The conclusions extracted from resistivity ($\rho$) or $\sigma$ plots equally apply even if $\sigma$ instead of resistivity is chosen for analysis. In the VRH process, the charge carriers hop between levels close to the Fermi level without dependence on their spatial distribution [206]. Unlike NNH, the VRH process is categorized by the variable hopping distance. Two types of VRH are defined in literature *viz.* the Efros-Shklovskii (ES-VRH) and the Motts' 3D VRH. The following equations can appropriately describe the models [201]

$$\rho = \rho_0 exp(\frac{T_0}{T})^p \tag{4.6}$$

where $\rho_0$ is the pre-exponential factor ($\rho_0 = 1/\sigma_0$, a constant), $T_0$ is the characteristic temperature relevant to the prevalent conduction mechanism, and $p = 1/2$ or $1/4$ respectively, depending on the density of states (DOS) at the Fermi level. In disordered systems without Coulomb interactions, $p = 1/4$ leads to the Mott's VRH

mechanism that thrives on the assumption that the DOS remains constant near the Fermi level [207–209]. The ES-VRH model is derived by considering $p = 1/2$, and it justifies the existence of Coulomb interaction between the initial and final hopping states for the long-range electron hopping [207]. In this model, there is a quadratic diminishing of the DOS near the Fermi level.

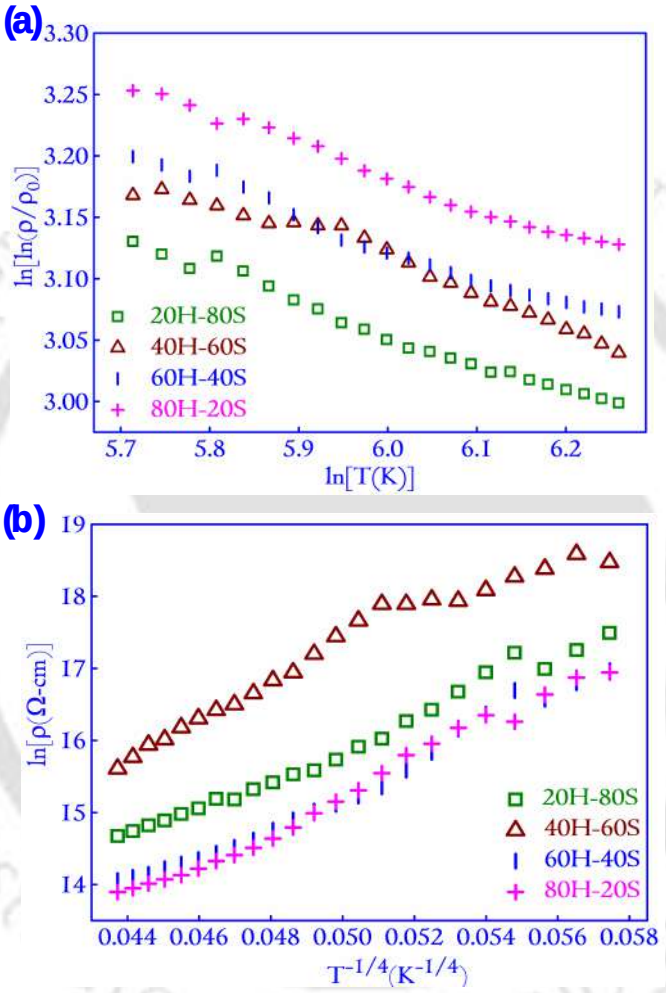


**Figure 4.8:** (a) shows the plot of $ln[ln(\rho/\rho_0)]$ versus $ln[T]$ that helps to identify the VRH mechanism in the composite in a temperature range of 303 K to 523 K. (b) The plot of $ln[\rho]$ versus $T^{-1/4}$, which enables the calculation of the DOS that is intrinsic to the Motts' VRH mechanism.

Identifying the dominant conduction mechanism from a diverse set of available models largely depends on fitting the appropriate model to the $\sigma/\rho$ data. The choice between $p = 1/2$ or $1/4$ is typically made by fitting the above equation 4.6 with different values of $p$. The value of $p$ that best fits the equation gives the dominant conduction mechanism in the probed temperature range. However, fitting

the model with different values of $p$ is quite a tedious task, and instead, we adopt a different approach by considering a slight modification of equation 4.6,

$$ln[ln(\rho) - ln(\rho_0)] = p[ln(T_0) - ln(T)] \tag{4.7}$$

which is an equation of the form $y = mx + c$, with $m = -p$, $y = ln[ln(\rho/\rho_0)]$ and $x = ln(T)$. The mathematical manipulation provides us with the straight-line slope to determine the nature of the conduction mechanism active within the specimens. These variations are shown in Figure 4.8. In all the composites, the slopes are close to 1/4, suggesting Motts' VRH to be the dominant mechanism in the specimens (in the considered temperature range). A plot of the linear fitting is shown in the Figure 4.9. This determination of $p$ is identified as the Zabrodskii analysis and is an unbiased and quantitative method of identifying the conduction mechanism [210]. In all the cases, the linear fit of $ln[\rho]$ versus $T^{-1/4}$ (see Figure 4.10) matches the experimental data quite appropriately with the adj. R square value in each of the plots greater than 0.9. It again confirms that Motts' VRH mechanism can describe the data more satisfactorily in the chosen temperature range.

It is stated earlier that $T_0$ in equation 4.6 and hence equation 4.7, is the characteristic temperature dependent upon the active conduction mechanism in the specimen. Incidentally, the parameter $T_0$ forms an important quantity in the determination of DOS near the Fermi level $N(E_F)$ [210]. The easiest way to extract $T_0$ is by making a plot of $ln[\rho]$ versus $T^{-1/4}$, which ought to be straight line (see equation 4.8). The value of $T_0$ is inversely proportional to the DOS that can be extracted using the following equation [202]

$$\rho = \rho_0 exp(\frac{T_0}{T})^{1/4} \tag{4.8}$$

$$N(E_F) = \frac{16}{T_0 k_B \zeta^3} \tag{4.9}$$

where $\zeta(= \alpha^{-1})$ is the decay length of the localized wave function and signifies the spatial extension of the wave function ($e^{-\alpha R}$) associated to the localized states ($R$ denoting the hopping length). There is a dearth of literature on the value of $\zeta$ for the chosen composite. Deriving from the case of $BaTiO_3$, $\zeta$ is considered to be approximately 0.40 nm [148, 202]. This particular value is chosen for calculation of $N(E_F)$ using equation 4.9. The calculated values are $3.51 \times 10^{19}, 2.81 \times 10^{19}, 2.66 \times 10^{19}$, and $2.12 \times 10^{19}$ for $20H - 80S$, $40H - 60S$, $60H - 40S$, and $80H - 20S$, respectively.

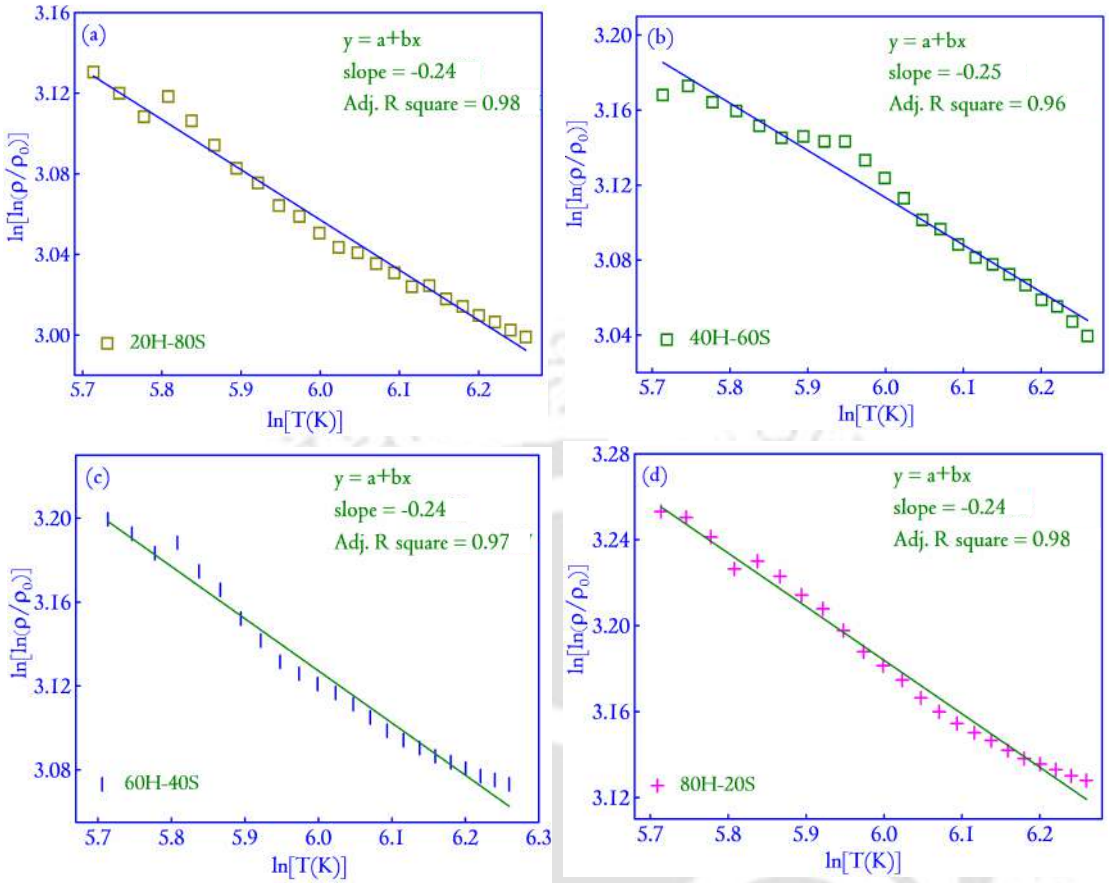


**Figure 4.9:** The slope of the linear fit of $ln[ln(\rho/\rho_0)]$ versus $ln[T]$ that shows that the slope is approximately 0.25 for (a) $20H-80S$, (b) $40H-60S$, (c) $60H-40S$, and (d) $80H-20S$. This further verifies that Motts' VRH mechanism is the dominant conduction mechanism.

Finishing the discussion, two critical parameters *viz.* the hopping length ($R$) and the hopping energy ($W$) is determined from the Motts' VRH model using the following equations [203].

$$R = \frac{3}{4}[\frac{3\zeta}{2\pi N(E_F)k_BT}]^{1/4} \; and \; W = [\frac{3}{4\pi R^3 N(E_F)}] \tag{4.10}$$

The values calculated for $R$ and $W$ are shown as a function of temperature $T$ in Figure 4.11. For all the composites, the value of $R$ and $W$ show a linear variation with temperature $T$ [210]. Also, the essential conditions $W \geq k_BT$ and $R/\zeta \geq 1$ is satisfied in all the cases by the ceramic composites that confirm the validity of the approach (see Table 4.5).

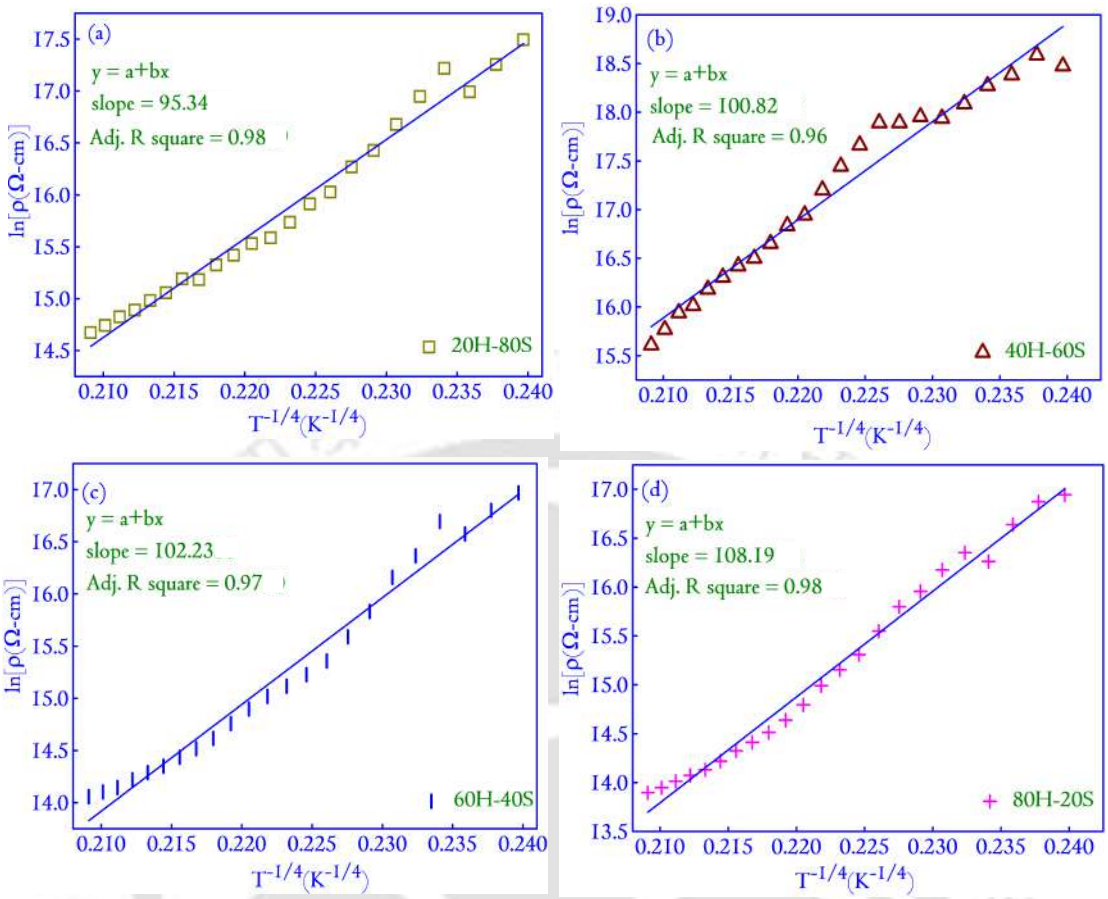


**Figure 4.10:** The plot of $ln[\rho]$ versus $T^{-1/4}$, which shows the linear fit for (a) $20H-80S$, (b) $40H-60S$, (c) $60H-40S$, and (d) $80H-20S$. This fit is used to determine the characteristic temperature.

**Table 4.5:** Variation of the DOS and verification of the essential conditions $W \geq k_BT$ and $R/\zeta \geq 1$ at 310 K. At 310 K, the value of $k_BT$ is 0.026110, which is lesser than all the tabulated values of $W$. Also, in all the cases $R/\zeta$ is greater than 1

| **Sample** | $\mathbf{N(E_F)(eV^{-1})(cm^{-3})}$ | $W$ | $R/\zeta$ |
|---|---|---|---|
| 20H-80S | $3.51 \times 10^{19}$ | 0.30 | 2.83 |
| 40H-60S | $2.81 \times 10^{19}$ | 0.32 | 2.99 |
| 60H-40S | $2.66 \times 10^{19}$ | 0.32 | 3.04 |
| 80H-20S | $2.12 \times 10^{19}$ | 0.34 | 3.21 |

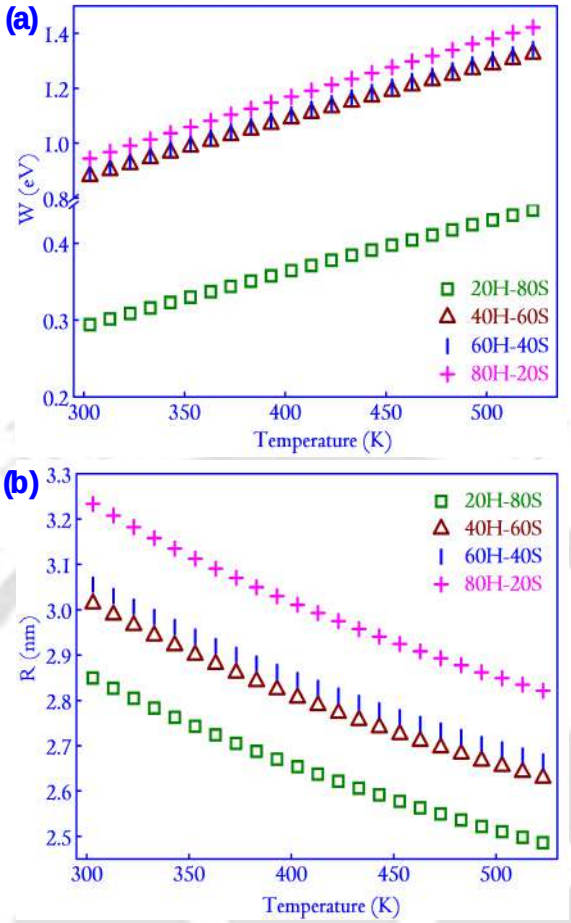


**Figure 4.11:** (a) The variation of the hopping length $R$, and (b) hopping energy $W$ as a function of temperature.

### 4.3.6 In-vitro bone-like apatite formation

The bone-like apatite formation of the specimens is studied by incubating the compact discs in SBF for 12 days. The *in-vitro* mineralization of bone-like apatite from 1.5 SBF can help determine the compact discs' ability to bond with the surrounding tissue when such a system is implanted *in-vivo*. It is reported that a biomaterials' ability to bond to the surrounding tissue may be linked up with the apatite layer that it induces on its interface, provided there are no other toxic or immune responses to the surrounding tissue [211]. Experiments have also been conducted that relate the bone-forming ability of a biomaterial to the amount of bone-apatite that can be nucleated from SBF [190]. Based on such evidence, the apatite nucleation ability of the specimens is studied. Following incubation, the specimens are washed thoroughly in deionized water to dissolve the nucleated salts [212, 213] and ensure that the deposited layers on the discs are composed entirely of bone-like apatite.

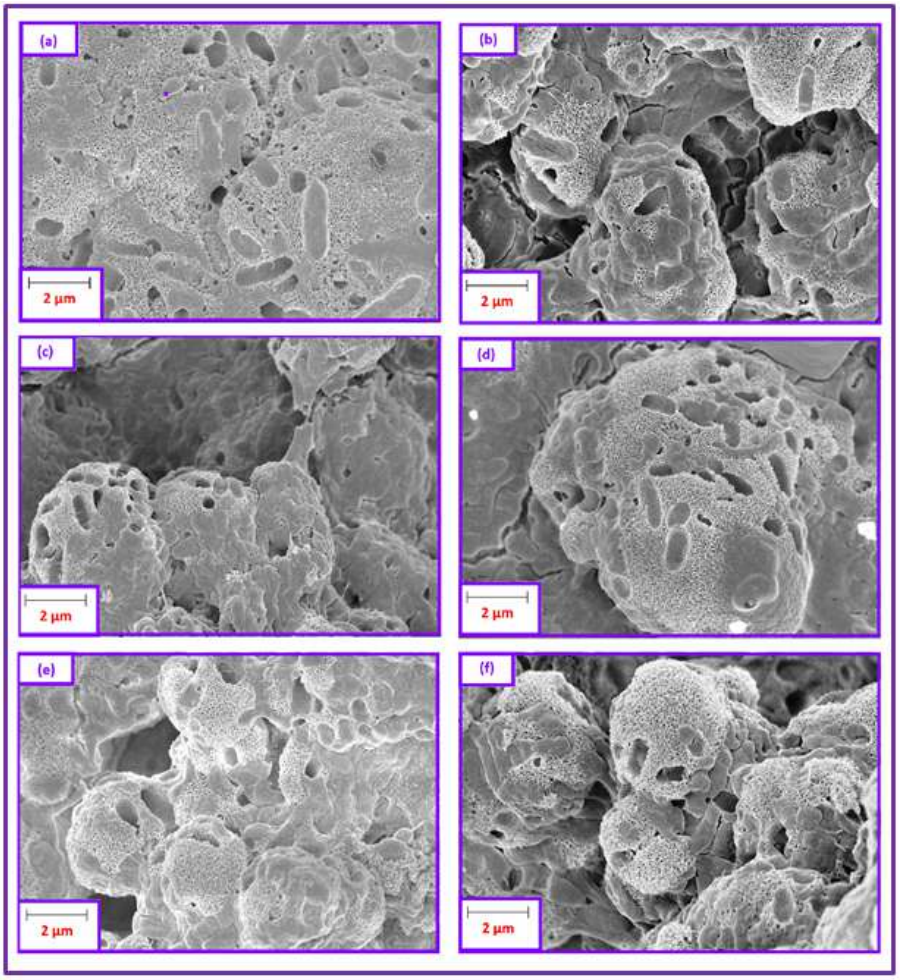


**Figure 4.12:** The FESEM micrographs of the composites and their monoliths after the SBF test. The tests have been carried out to determine the bone-like apatite forming ability of the specimens. In serial order, the specimen code denotes (a) ST, (b) HAP, (c) $80H - 20S$ and (d) $20H - 80S$. Bone-like apatite growth is evident in all the specimens with characteristic pores, which helps in better bone ingrowth, increasing the bonding strength of the composite materials and their monoliths in *in-vivo* applications.

SBF solution triggers the deposition of layers of bone-like apatite on the surface of incubated specimens. In Figure 4.12, FESEM micrographs of the apatite layer deposited on the compacts are shown. The figure depicts that the apatite growth is very dense on all the composites containing HAP. In ST, significantly fewer thick apatite layers are found, which might be due to fewer nucleation centers for apatite crystals to deposit. All the structures' plate-like morphology is similar to the apatite structures found in bones [123, 214]. Numerous micron-sized pores are also observed on the apatite structures and are characteristic of bone-like apatite nucleated from SBF [197]. The growth of apatite from SBF can be understood from a

series of mechanisms put forward by various researchers [92, 123]. The isoelectric point of HAP lies between 5-7, much lower than the SBF (buffered at 7.4) [215]. When synthetic HAP compact discs are incubated in SBF, it exposes the negatively charged $OH^-$ and $(PO_4)^{3-}$ ions in its crystal structure, which tends to impart an overall negative charge on the surface (measurements of zeta potential of selected specimens have shown negative charge and have been included in the section 4.3.8). The negatively charged surface draws $Ca^{+2}$ on its surface and terminates by forming a $Ca$-rich surface capable of drawing $(PO_4)^{3-}$ ions *via* electrostatic attraction. An amorphous calcium phosphate layer is therefore generated, and because apart from apatite, the solubility of other calcium phosphates is very low in the water, the amorphous layer transforms to apatite by incorporating $OH^-$ ions in the crystal structure. This may be due to the fact that the crystal phase of apatite is thermodynamically the most stable in an aqueous medium amongst all the calcium phosphate variants [216]. Thermodynamical calculations have also revealed that SBF is a metastable supersaturated solution with respect to apatite crystals. Once apatite starts nucleating over a surface by the mechanism described above, it grows by consuming the $Ca^{+2}$ and the $(PO_4)^{3-}$ ions from the solution forming dense layers of bone-like apatite. Furthermore, the FESEM images depict that the composites containing HAP have induced the growth of dense apatite layers. The HAP sites in the composites also provide sufficient nucleation centers for the apatite crystals accelerating the growth process and increasing the volume of apatite nucleated over the surface. It necessitates the presence of HAP in the compact discs for higher bone-like apatite nucleation ability in the specimens.

However, it is essential to understand that there is a different mechanism of apatite nucleation over ST surfaces. During the FESEM study, it is observed that patches of bone-apatite are scattered over the ST compacts. The growth is in no way dense and does not cover the entire surface area of the compact. The mechanism behind the growth of apatite structures in ST compacts involves an intermediate $TiO_2$ on the compact discs' surface, as discovered previously in the monoliths' Raman spectra. Coreño *et al.* [217] described a possible mechanism of apatite growth on $CaTiO_3$, and similarly, the growth of apatite on ST can be proposed. ST behaves like a mixed oxide in aqueous suspension. This behavior in an aqueous solution can likely be a combination of an insoluble oxide and $TiO_2$, and a partially soluble inorganic salt [218]. In SBF, the $TiO_2$ sites develop a negative charge at a pH of 7.4 as the isoelectric point of $TiO_2$ is reported to be around pH 5 [219]. The development of negative charge is crucial to draw the $Ca^{+2}$ ions from the

solution. Once the region is covered by $Ca^{+2}$ ions, the $(PO_4)^{3-}$ ions are drawn by electrostatic forces of attraction, generating an amorphous calcium phosphate layer. The conversion of amorphous calcium phosphate to bone apatite then proceeds similarly to the mechanism discussed previously [220–222]. The unreacted $TiO_2$ in the ST specimen would likely induce the apatite nucleation selectively in those areas where the concentration of $TiO_2$ is more. It explains why the apatite growth over the ST compacts is in patches. A graphical illustration of the entire deposition process is depicted in Figure 4.13.

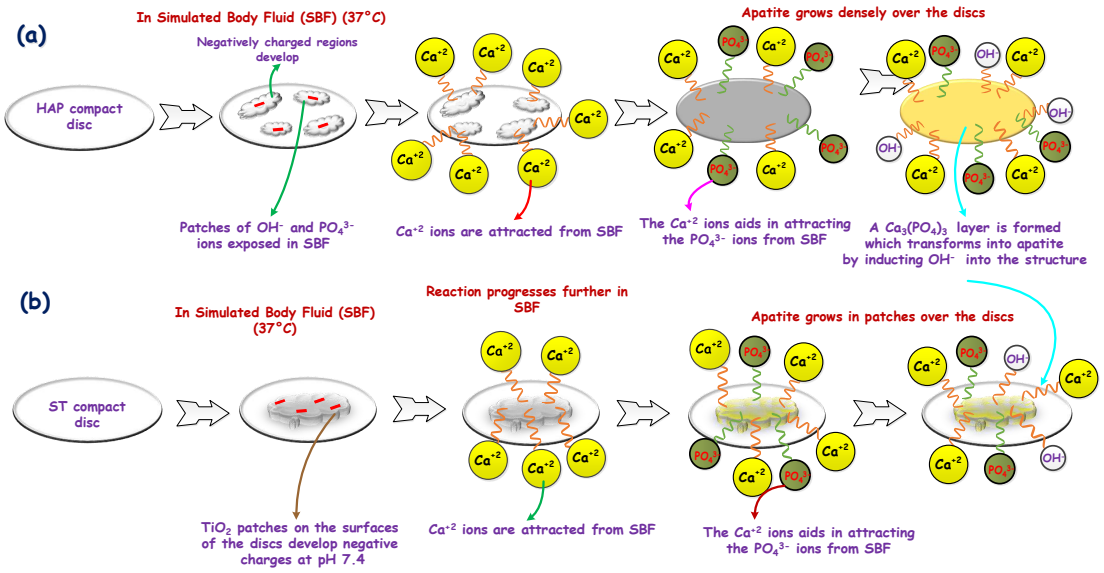


**Figure 4.13:** Graphical illustration of the mechanism of nucleation of bone-like apatite from SBF onto the surface of the compact discs. In (a), the compact discs develop a negative charge in SBF that facilitates the induction of $Ca^{+2}$ due to electrostatic interactions. The positive charge of $Ca^{+2}$, in turn, attracts the negatively charged $(PO_4)^{3-}$ charges forming an amorphous $CaPO_4$ layer that proceeds to form HAP by undergoing hydrolysis. In (b), the reaction proceeds by the $TiO_2$ patches, which form the negatively charged regions that facilitate the attraction of $Ca^{+2}$ followed by $(PO_4)^{3-}$. The reaction finally follows a reaction path similar to (a).

### 4.3.7 Protein adsorption

The protein adsorption behavior of selected specimens (HAP, ST, $20H-80S$, and $80H-20S$) is determined by incubating with BSA in PBS for 1 h. BSA adsorption is found to increase as ST $>$ $20H-80S$ $>$ $80H-20S$ $>$ HAP (Figure 4.14). Protein adsorption on a biomaterial surface is reported to depend on its physical and chemical properties such as surface chemistry, hydrophobicity, and surface charge

[27, 222]. In this direction, a new understanding of the protein adsorption on ceramic biomaterial surfaces is pointed upon by Rubinstein *et al.* [223], and it hinged upon the role of $\epsilon_r$ of the surface over which protein adsorption is considered. As the interaction of a protein with an inorganic biomaterial surface is mostly electrostatic, the $\epsilon_r$ of the surfaces play a critical role. The report reveals that oxide ceramics with $\epsilon_r \leq 35$ offers a surface favourable for protein interactions [224]. As $\epsilon_r$ of the specimens lay in this range (Figure 4.5), it supported the favorable adsorption of BSA on the surfaces (Figure 4.14). Furthermore, the investigation on the wettability of ST ceramics by Sahoo *et al.* [67] revealed that the surfaces are highly hydrophilic, and the extent of hydrophilicity is greater than HAP. This can also be a reasonable justification of higher protein adsorption on ST-containing surfaces, as highly wettable surfaces have been shown to enhance protein adsorption in biological environments. Thus, the protein adsoprtion studies can reveal a lot of information of the specimen under study and the adsorption behavior is governed by a number of factors as discussed previously.

The surface charge (zeta potential) of the specimens in PBS (pH 7.4) is measured and found to be the maximum for HAP (-25.82 mV) and the least for ST (-20.12 mV) [225]. The Zeta potential of composites lies between these two values. The justification for using PBS is that it replicates the essential conditions like the osmolarity, ion concentration, and its pH is similar to that found inside a human body. The surface charge values measured in PBS are, therefore, most likely to remain the same under *in-vivo* environments. In fact, the Zeta potential primarily depends (but is not restricted to) the pH of the system or the dispersant [218]. Further, the surface charge value $\geq \pm 20$ mV indicates the colloidal stability of prepared materials [219]. For the successful integration of an implant surface with the physiological microenvironment, favorable adsorption of the various protein species present in the complex physiological microenvironment is crucial. The protein-surface interactions are followed by cell-surface interactions due to the higher diffusivity of proteins [225]. Electrostatic interaction is one of the major forces involved in bio-interfacial interactions. Further, competitive adsorption among different biomacromolecules takes place on surfaces [226]. In this study, albumin is used for adsorption, a major constituent of serum. Thus, the surface charge, depicted by the zeta potential measurement, is mostly related to the protein adsorption that might occur on the surface. Therefore, the nature of the surface charge might drive the adsorption of the various protein molecules present in its vicinity [226]. To investigate the nature of the relationship between the adsorbed proteins and surface charge, the adsorbed

protein is modeled to the surface charge, and it is seen that the adsorbed amount of BSA is linearly related to surface charge (shown in Figure 4.14(b)). Furthermore, BSA possesses a net negative charge at pH 7.4 in PBS [227]. Hence, a higher adsorbed amount is observed on less negatively charged surfaces (ST) than HAP. This also highlighted the role of electrostatic interactions during the adsorption of BSA on ceramic surfaces [228]. Following adsorption of BSA, it becomes crucial to investigate the cytocompatibility of the prepared surfaces for deciding its applicability in clinical applications. Therefore, the following section presents the cytocompatibility of the ceramic composites.

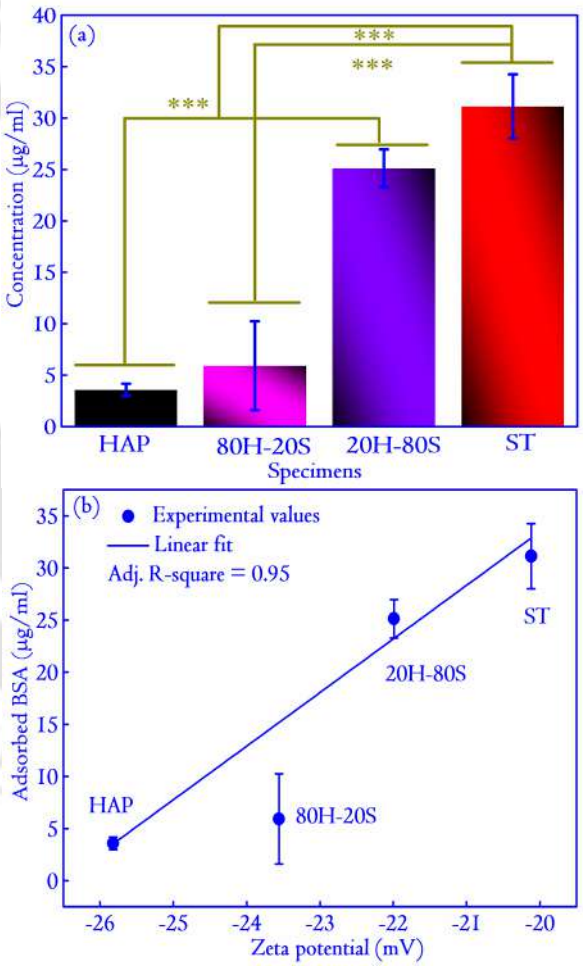


**Figure 4.14:** (a) Protein adsorption (BSA) on selected composites and their monoliths. ST shows very high protein adsorption values co-related to the $\epsilon_r$ of the specimens (see text for detailed description). Also, in (b), a plot of zeta potential versus the concentration of adsorbed proteins on the surfaces is presented. The displayed behavior is linear with respect to the zeta potential of the surfaces. The $***$ represents statistical significance of $p < 0.0001$.

### 4.3.8 Cytocompatibility Assay

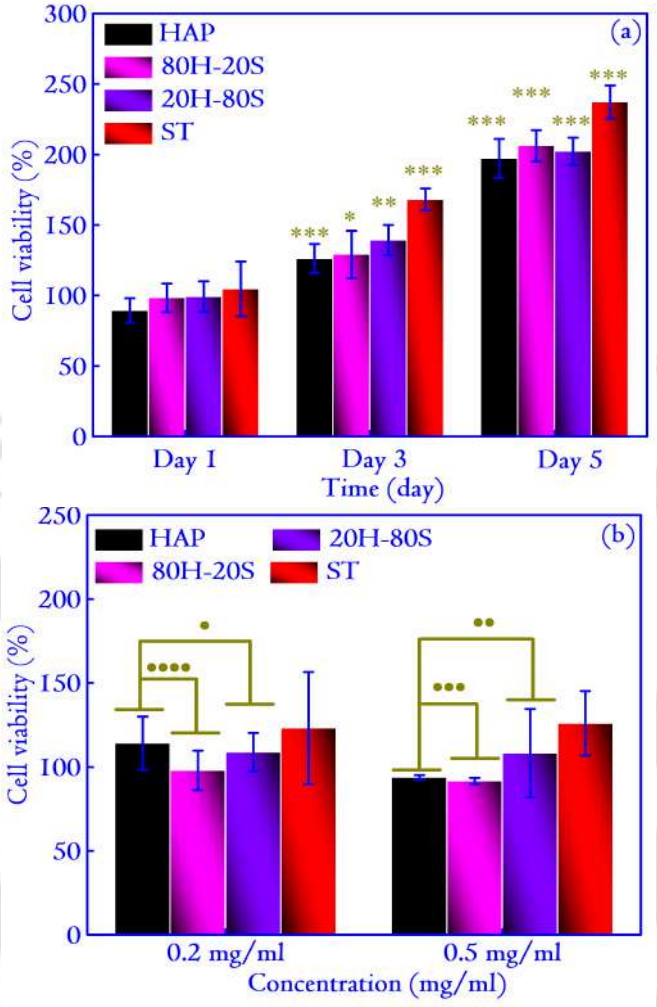


**Figure 4.15:** (a) MTT assay of selected composites and their monoliths. The cell viability is analyzed for 1, 3, and 5 days, and for all the specimens, the cell viability is $> 90$ %, indicative of a high cytocompatibility of the investigated specimens. The concentration adopted for the study is 0.1 mg/ml. The statistical significance of the data is calculated with respect to the data of Day 1, and the $*$, $**$, $***$ represents the $p$ values of 0.003, 0.0001, and $<$0.0001, respectively. Also, in (b), the variation in cell viability of the specimens with higher concentrations such as 0.2 mg/ml and 0.5 mg/ml is shown for Day 1 to analyze the specimens' behavior at other concentrations. In this case, too, the specimens displayed cytocompatibility $> 90$ %. The •, ••, •••, and •••• signify $p$ values (statistical significance) 0.5, 0.2, 0.04, and 0.07, respectively.

MTT assay is carried out after incubating specimens with MG63 cell line ($10^4$ cells/well) for 1, 3, and 5 days. Figure 4.14(a) shows the cell viability versus incubation time (in days) of different surfaces. Initially, cells are incubated with 0.1 mg/ml concentration of all the samples for 1, 3, and 5 days. All the samples show

cell viability > 90 % after one day of incubation, which confirmed the excellent cyto-compatibility of prepared materials. Better cell viability is observed for the ST specimen. It is reported that the porous ST ceramics helps in the release of $Sr^{+2}$ that is highly responsible for the enhanced cytocompatibility of ST [67]. The release of $Sr^{+2}$ ions is responsible for the positive response of osteoblast (MG63 cell lines), and is desirable for pre-osteoblastic cell differentiation, proliferation and also helps in suppressing the osteoclast differentiation [68]. Further, the cell viability increased gradually with the incubation period up to 5 days (Figure 4.15(a)). P-value is also calculated from the experimental cell viability data as compared to control (cells without samples) and is shown in Figure 4.15(a) and (b). This also highlighted no significant decrease in cell viability in the presence of different samples. Following these interesting results at 0.1 mg/ml concentration, the materials are tested at higher concentrations of 0.2 and 0.5 mg/ml. Interestingly, cell viability in the presence of all the samples is > 90 % (Figure 4.15(b)). It reaffirmed the cytocompatibility of the prepared materials and indicated their suitability for *in-vivo* biomedical applications. Thus, it can be concluded that the presence of ST in the ceramic composite is a key factor in deciding the biological properties of ceramic composites.

### 4.3.9 TEM Analysis

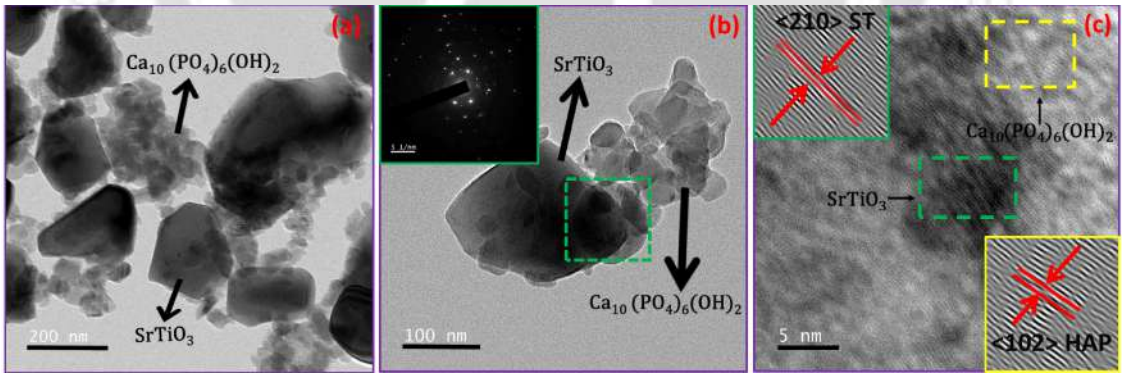


**Figure 4.16:** (a) FETEM image of the specimen $20H - 80S$, showing particles of ST and HAP. Also, in (b), a higher magnification image of the same specimen and its SAED pattern (in the inset) for the region marked by the green dotted rectangle is shown. (c) The HRTEM images of the dotted green rectangle. The green rectangle shows the lattice fringes of ST, subjected to inverse FFT (see inset located in the top left corner) to estimate the interplanar d spacing for ST. A similar area marked by a yellow dotted rectangle shows the lattice fringe.

Out of the series of composites studied so far, based on the electrical properties,

we can conclude that ST demonstrated better dielectric properties having an improved $\epsilon_r$. The $\epsilon_r$ of the composite material can be highly useful in its performance in implantable medical devices [229]. The dielectric properties of a material measure its ability to interact with electromagnetic fields. As most biological tissues are non-magnetic, the electric fields' role is vital in understanding these properties. Ceramics undergo polarization on the application of electric fields. The polarization persists even after removing the external field, and the extent of polarization in ceramics is usually greater for materials with higher $\epsilon_r$ [33]. The purpose of adding ST with HAP is to improve its $\epsilon_r$ so that the polarized electric field can be maximized to augment the fracture healing process in bones. The idea is that external electric fields are applied to the fractured regions in clinical applications to expedite the healing process [29]. Scaffolds made of composite materials (ST and HAP) implanted in the injured regions will retain this external field by undergoing polarization and generate the electric field (even after its removal) that will supplement the faster healing process. The $\epsilon_r$ of ST is higher than the HAP, and with increasing content of ST in the composite, the $\epsilon_r$ is found to improve. At the other extreme, biocompatibility is another aspect that requires significant attention, especially for biomedical implants [230]. Considering both the perspectives, the composite $20H-80S$ exhibited a better dielectric response (highest $\epsilon_r$) and *in-vitro* mineralization of bone apatite. Although ST showed a better dielectric response in the explored frequency range, it failed to show improved bio-mineralization. The protein adsorption studies and the MTT also supplement the significantly superior response of $20H-80S$. This justifies the selection of $20H-80S$ as the composite with improved electrical and biological properties. Accordingly, to have a better understanding of the ceramic composite, the FETEM analysis is carried out. In Figure 4.16(a), the images in two specific areas have been shown along with the selected area electron diffraction (SAED) pattern of the composite (in Figure 4.16(b)). In Figure 4.16(c), the HRTEM images of the composite are displayed, and lattice fringes corresponding to both the monoliths are seen, which corresponds to (210) plane of ST and (102) plane of HAP. The planes are also apparent in the XRD analysis of the specimens. The HRTEM analysis complements the XRD analysis, and the area chosen for the HRTEM analysis showed no trace of any phase formed due to the reaction between the monoliths, similar to the conclusion derived from the XRD analysis. Additionally, on similar lines to FESEM images, we could see the HAP particles in aggregation along with larger-sized ST grains. Also, the sizes reported in the XRD analysis are crystallite sizes that aggregate to form grain. Therefore, the grains/particles observed in

TEM are larger than the crystallite sizes observed from the XRD analysis. The high-resolution surface features of the composite are studied by scanning transmission electron microscope (STEM) mapping, which gives the distribution of various elements and has been included in Figure 4.17(a-f). The area selected for mapping analysis is chosen from Figure 4.16(b), which contained ST and HAP particles.

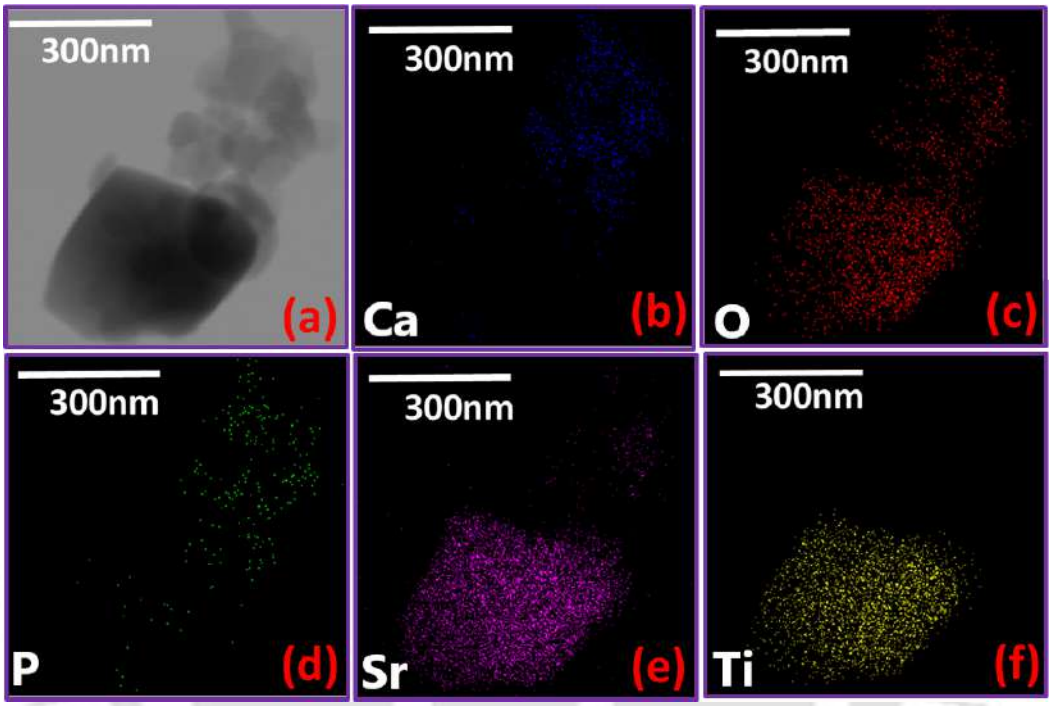


**Figure 4.17:** (a) STEM mapping of the dotted region in Figure 4.16(b). (b-f) shows the individual distribution of the elements in the selected region of the composite with different colors, as indicated in the images above. From Figure 4.17(a-f), it is clear that the larger grain that is visible in the STEM image is an ST grain. The agglomeration in the upper part of the image is HAP, confirmed from the distribution of $Ca$ and $P$. $O$ being common to ST and HAP is distributed symmetrically in both the regions.

## 4.4 Conclusions

The use of smart materials in biological applications has been a recent trend, and an increasing interest in developing biologically compatible smart materials has encouraged scientists to develop new materials for bone tissue engineering applications. Driven by such a motive, this article reports a series of composites with varying ST and HAP concentrations, and the composite with the best property is identified amongst the prepared specimens. Microstructural analysis involving XRD and Raman is used to probe the details of the composite structures. Two interesting ob-

servations are apparent from the analysis: the presence of the monoclinic phase in the HAP, and the second is the identification of rutile $TiO_2$. The crystallite sizes are evaluated from the XRD and observed to range between 27.2-33.3 nm for the specimens. The grain size from FESEM analysis follows a similar trend as the crystallite sizes, and the FESEM images further reveal the presence of pores in the synthesized composites. The pores are introduced in composites as no specific measures to densify the compacts are adopted in view of the fact that pores can enhance the biological properties. The bone-like apatite nucleation ability revealed that excluding ST, the specimens could induce dense nucleation of bone apatite from SBF, which is desirable for *in-vivo* applications and complements the other biological studies. The nucleation in ST is very low, and the mechanism of apatite nucleation over this surface revealed the role of rutile-$TiO_2$, which is identified from Raman spectra to be present in trace amounts over ST surfaces.

The impedance spectra of the specimens that determine the dielectric behavior show the $\epsilon_r$ to lie in the range of 5-35. The porous nature of the composites is identified as a factor related to the lowering of $\epsilon_r$. The study points at an interesting association of the service life of electrets and the active conduction mechanisms. We remark that the lower $\sigma$ ($\simeq 10^{-8}$S/cm) can serve as an indirect way for estimation of the service life. Also, the lower $\sigma$ is related to the inherently porous nature of the specimens, which reduces the effective contact area between the grains, reducing the $\sigma$ drastically. Theoretical advances in the study of electrical properties (specifically in the field of $\sigma$ mechanisms) are yet to be rigorously considered in the design of bioelectrets. The chapter will serve to bridge the gap between theory and industry. A ceramic composite of HAP and ST, specifically for electrets, can be a strong starting point in this direction. The results established in the study can be beneficial for designing prototype electrets and scaffolds in biomedical applications.

The biological properties that involve studying the role of protein adsorption over the synthesized surface show a linear dependence with the surfaces' zeta potential. This dependence implies the governing role of electrostatic interactions in protein adsorptions. Exploring the relation between the $\epsilon_r$ and the protein adsorption in biocomposites is unique and is expected to provide a new dimension towards understanding the protein adsorption over ceramic biomaterials. Further, the surfaces' cell viability is found >90% which reaffirms the cytocompatibility of the surfaces and points towards the high potential of the surfaces for clinical applications. Based on the above studies that include the variation of the dielectric properties and the bio-mineralization of bone apatite, $20H - 80S$ is identified to exhibit the best prop-

erty. The protein adsorption studies and the cytocompatibility assay supported the obtained results by showing relatively higher protein adsorption and cell viability for the selected specimen. The results are quite exciting and establish the potential role of a ceramic composite (HAP and ST) in designing electrically active smart scaffolds. The scaffolds designed from electrically active materials are expected to support the faster healing of wounds by exhibiting a synchronization of the electrical and biological properties. Such exploration of electrically active ceramics is still in the preliminary stage, and in the near future, it is expected to dominate biomedical research with tremendous potential for industrial applications. Specifically using 3D printing technology, the proposed scaffolds can be fabricated that could be used for future biomedical applications.

# Chapter 5

# Microstructural, electrical and biological activity in $Ca_{10}(PO_4)_6(OH)_2 - Ba_{0.5}Sr_{0.5}TiO_3$ ceramic composites

This chapter explores $Ca_{10}(PO_4)_6(OH)_2$ (HAP) and $Ba_{0.5}Sr_{0.5}TiO_3$ (BST) based composites. Introducing the $Ba$ component into $SrTiO_3$ (ST) and analyzing its impact on the microstructural, electrical and biological properties are the prime objectives of this chapter. Based on the study, a suitable composite is identified for developing scaffolds and considered in Chapter 6.

## 5.1 Introduction

In the last chapter, we have explored the composites of HAP and ST specifically for bone tissue engineering applications. The results were extremely illuminating, and in this chapter, we move on to introduce the $Ba$ component in ST to specifically investigate the role of $Ba$, particularly from a biomedical perspective. It was pointed out previously that the dielectric constant ($\epsilon_r$) of HAP is typically on the lower side ($\simeq$5-15 at 1 MHz), and it can be tuned by designing a ceramic composite of HAP with another ceramic having higher $\epsilon_r$. The bulk of the research in the ceramic

The contents of this chapter is published in A. Das, P. Dobbidi, A. Bhardwaj, V. Saxena, and L. M. Pandey, Scientific Reports, **11**, 22304 (2021) and A. Das, and P. Dobbidi, ACS Biomaterials Science and Engineering, **7**, 2296 (2021)

composite is mostly focussed on mixing up a ferroelectric counterpart (of higher $\epsilon_r$) for improving the energy/charge storage capacity. However, such traditional ferroelectrics have a significant value of remnant polarization that often decreases the amount of energy stored in these ceramics [65]. As the power consumption in implantable bioelectronics devices is usually low, therefore dielectrics with moderate permittivity (∼30-100) could be helpful for such implants [231] (see Figure 5.1). BST is an important component that can be considered for a composite with HAP. Composites of HAP with $BaTiO_3$ have already been considered for biomedical applications [231]. The results are inspiring and have motivated us to consider the introduction of the $Sr$ component in $BaTiO_3$. $Sr$ ions have a tremendous role in clinical applications as the use of drugs containing $Sr$ nanoparticles have been useful in preventing vertebral, peripheral fractures and osteoporosis [67, 162]. Recently, radio-pacifiers for implant fixation in the treatment of compression fractures have suggested the use of $Ba$ as cross-linking agents [232]. The results are motivated by the fact that $Ba$ as cross-linking agents have been seen to significantly improve the radiopacity without any adverse effects on the cell viability of MG63 cells [233]. Therefore, including $Ba$ and $Sr$ in biological applications apart from HAP can be an interesting construct.

The biocompatibility in ceramics is regulated by a series of biointerfacial reactions like protein surface and cell-surface interactions. Various efforts are made to design multifunctional biomaterials (biomaterial composites) to modulate intermolecular interactions for tuning biointerfacial interactions [232]. Inspired by the developments, a ceramic composite of monoliths BST and HAP is synthesized by varying the concentrations of HAP and BST. By bridging the literature gaps, the study presented in this article is expected to provide new insights into the biological and physical processes in the presence of BST and HAP simultaneously. However, considering the vastness of the subject matter, the article is focused only on exploring the electrical properties of ceramic composites and correlating them with their biological properties. To keep matters simple, the composites have been developed without adopting any high-end techniques for densifying the compacts [234]. Special priority on the dielectric properties has been given that are analyzed in the RF regime: $10^6 - 10^9$ Hz. The motivation behind choosing the RF regime lies in its application in clinical settings for treating delayed unions and non-unions of bone fractures [200, 235]. Additionally, the Impedance spectroscopy (IS) and conductivity ($\sigma$) mechanisms and their related aspects form an elegant formalism to understand the biomaterials behavior in terms of the polarization disruption mechanisms. Thus,

understanding the electrical properties can be useful for modeling biomaterials before *in-vivo* applications. Such mechanisms have been elaborately discussed in the chapter. Furthermore, the protein adsorption on the surface of the composites is studied using bovine serum albumin (BSA) and fetal bovine serum (FBS) as the model proteins. The adsorption behavior is related to the dielectric properties, which is the unique aspect of the chapter. The ceramic-protein interactions are studied by understanding the evolution of the secondary structures of the adsorbed proteins. Such studies provide fresh perspectives in considering bioceramic composites with specific biological and electrical properties to design a new generation of advanced biomedical devices like electro-active scaffolds and self-healing bandages containing electrets. Below, we present a perspective that encompasses the vital role played by electrical properties of bioceramics in bone tissue engineering.

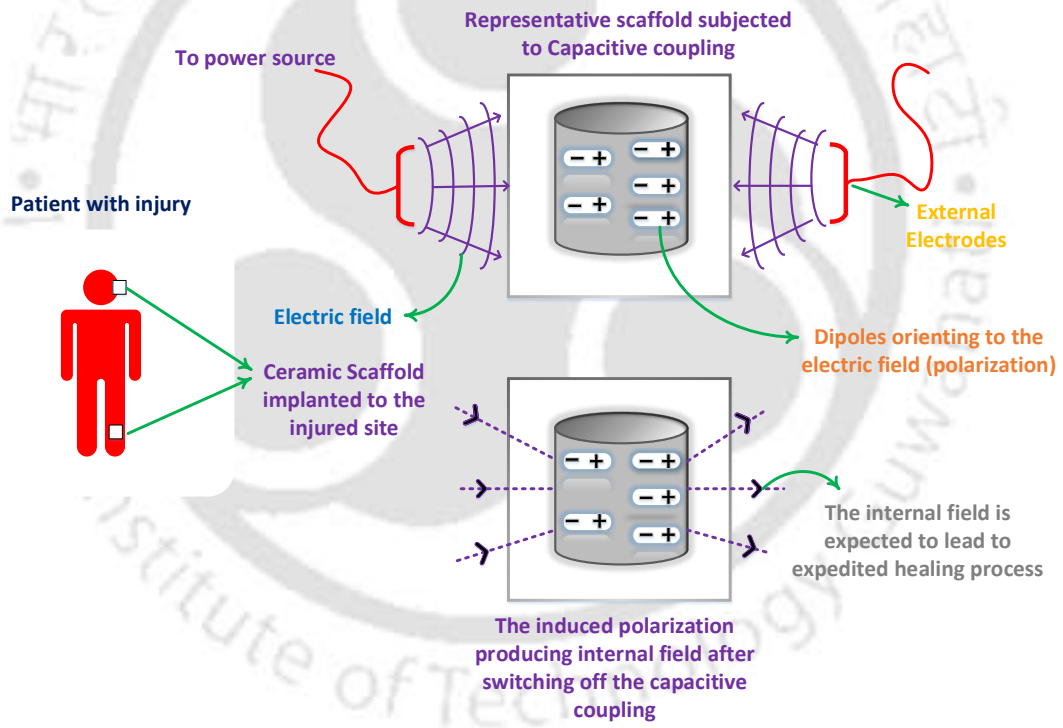


**Figure 5.1:** An illustration of the effect of ceramic scaffolds that inherently can undergo polarization when the external stimulations are applied upon the injured site for enhanced bone growth. The polarization helps maintain the electric field even after removing of the external field (capacitive coupling in this case). The extent of polarization directly depends upon the $\epsilon_r$ of the ceramics that can be tuned for achieving a stronger internal electric field. The possibility of such tuning can be done by adding another ceramic, which has been elaborated in the study. The illustration has been created using Visio 16 available at https://support.microsoft.com/en-us/office.

## 5.2 Experimental details

### 5.2.1 Synthesis of the precursors and compact discs

The monoliths for preparing the composites were processed by sol-gel and solid state processing technology, respectively. The process is described comprehensively in Chapter 2. Once the monoliths preparation is complete, several compacts were prepared for each composition under the same conditions and were finally sintered at 1073 K (3 h) for densification and compaction of the resultant cylindrical compacts. For clarity, the different compositions of the composite are tabulated in Table 5.1 below.

**Table 5.1:** The composition of different green discs and their codes.

| Monoliths | | Scheme | Code |
|---|---|---|---|
| HAP | BST | 100 At.% HAP | HAP |
| | | 20 At.% HAP & 80 At.% BST | 20H-80B |
| | | 40 At.% HAP & 60 At.% BST | 40H-60B |
| | | 60 At.% HAP & 40 At.% BST | 60H-40B |
| | | 80 At.% HAP & 20 At.% BST | 80H-20B |
| | | 100 At.% BST | BST |

### 5.2.2 Characterization of the surfaces

#### 5.2.2.1 Micro structural, electrical and surface morphology

The characterization techniques adopted for a systematic analysis of the prepared specimens' properties involved X-ray diffraction (XRD) for crystal structure evaluation. The diffracted x-ray photons were obtained for the specimens in the ($2\theta$) range of $20 - 55°$, scanning at the rate of $3°$/min and collecting the data points at a frequency of $0.03°$ (TTRAX III, Rigaku, Japan). The XRD patterns were then matched to the standard International Center for Diffraction Data (ICDD) files. The dielectric spectra for the prepared specimens were obtained at a frequency of 1 MHz, varying the temperature from 133 K to 523 K using an impedance analyzer (4991A, Agilent Technologies, USA) equipped with a temperature control system

(BDS 2300, Novocontrol, Germany). The data points were collected at an interval of 10 K. The morphology of the specimens was observed using field emission scanning electron microscopy (FESEM) (Sigma 300, Zeiss, Germany). The FESEM pattern were also used to determine the specimens' grain sizes using the ImageJ software. The elemental composition of the specimens was also determined using the elementary dispersive X-ray spectroscopy (EDS) (Oxford Instruments, UK) attached to the FESEM. To supplement FESEM images, the field emission transmission electron microscopy (FETEM) (2100F, JEOL-JEM, Japan) images were recorded along with the high-resolution transmission electron microscopy (HRTEM) images.

#### 5.2.2.2 In vitro bioactivity and surface electricity

The *in-vitro* bioactivity of the specimens was analyzed using the simulated body fluid (SBF) solution. The specimens were incubated in 1.5 SBF solution for 12 days at 310 K, ensuring that the old solution was refreshed every 24 hours. The 1.5 SBF solution was prepared using the protocol suggested by Kokubo *et al.* [96]. Following incubation, the specimens were washed and dried for 24 hours at 333 K. Further, the growth of bone-like apatite was analyzed using FESEM for understanding the surface morphology of the apatite layer. The zeta potential measurements were performed in a Litesizer particle size analyzer (Litesizer 500, Anton Paar, Austria) by dispersing the powdered form of the ceramics in deionized water at pH 7.4.

#### 5.2.2.3 Protein adsorption, evolution of secondary structure and cytocompatibility analysis

Following the biomineralization process, the protein adsorption of the ceramic composites was analyzed. BSA, along with FBS, was used as the model protein for analyzing the protein adsorption on the surface of the synthesized discs as described elsewhere [27]. The procedure for studying the adsorption of proteins is discussed in brief. To start, BSA (500 $\mu$g/mL) and FBS (10 % v/v) solution was prepared in PBS. The specimens (compacted discs) were weighed and incubated in protein solution for 1 hour at room temperature for adsorption. The rest of the procedures are already detailed in Chapter 2. The change in the secondary structure of the adsorbed proteins was further studied using Fourier transform infrared analysis (FTIR). The analysis was performed by recording the FTIR spectrum (Spectrum Two, Perkin Elmer, USA) in the Amide-I region (1590-1710 $cm^{-1}$). The observed spectra in the region were fitted with Gaussian curves to obtain the relative percentage of the

secondary structures ($\alpha$-helix, $\beta$-sheet, $\beta$-turn, random coils, and side chains). The 3-[4,5-dimethylthiazol-2-yl]-2,5-diphenyltetrazolium bromide (MTT) assay on specimens at varying concentration (1.000, 0.500, 0.250 and 0.125 mg/mL), was carried out in sterilized MilliQ water on MG63 bone-like cell line in a 24 well plate, using the protocol previously described by our research group [236]. $1 \times 10^4$ cells/well were seeded in each well and incubated for 24 hours. Cells were incubated in Dulbeccos' modified eagle medium (DMEM) supplemented with 10 % FBS and 1 % Penstrap antibiotic in a $CO_2$ incubator at 5 % $CO_2$ and 310 K, after which the material was seeded into the wells. After each specified time interval, 20 $\mu$L of MTT (0.5 mg/mL) was added to the wells after removing the consumed DMEM media and incubated in a $CO_2$ incubator for 4 h. Post incubation, the formed formazan crystals were dissolved in 100 $\mu$L filtered dimethyl sulfoxide (DMSO). Absorbance was measured at 570 nm (Infinite 200 Pro, Tecan, Switzerland). Cell viability (%) was calculated and compared to control wells (cells without any material incubation), taken as 100 %.

## 5.3 Results and Discussions

### 5.3.1 Structural analysis

XRD presents a non-destructive technique to probe the microstructure of synthesized composites. In the present study, the XRD patterns of the composite and monoliths have been shown in Figure 5.2. The phase identification has been made by comparing the resultant XRD patterns with standard ICDD files (card no. # 39-1395 for BST and # 009-0432 for HAP) [90]. Apart from the monoliths, the peaks corresponding to ($Sr_5(PO_4)_3(OH)$, SAP) (card no # 002-0761) are also seen, which presumably are formed due to substitution of $Sr$ ions in the $Ca$ site of HAP [90, 237]. The intensity of peaks corresponding to SAP is highest for $80H - 20B$ and decreases monotonously for the other composites in the series. The substitution might have occurred during the process of sintering the at 1073 K. A possible reaction occurring between the monoliths that leads to the formation of SAP can be understood from the following equation

$$\delta Ca_5(PO_4)_3(OH) + 10Ba_{0.5}Sr_{0.5}TiO_3 \rightarrow 10Ba_{0.5\delta}Sr_{0.5-0.5\delta}Ca_{0.5\delta}TiO_3 + \delta Sr_5(PO_4)_3(OH) \quad (5.1)$$

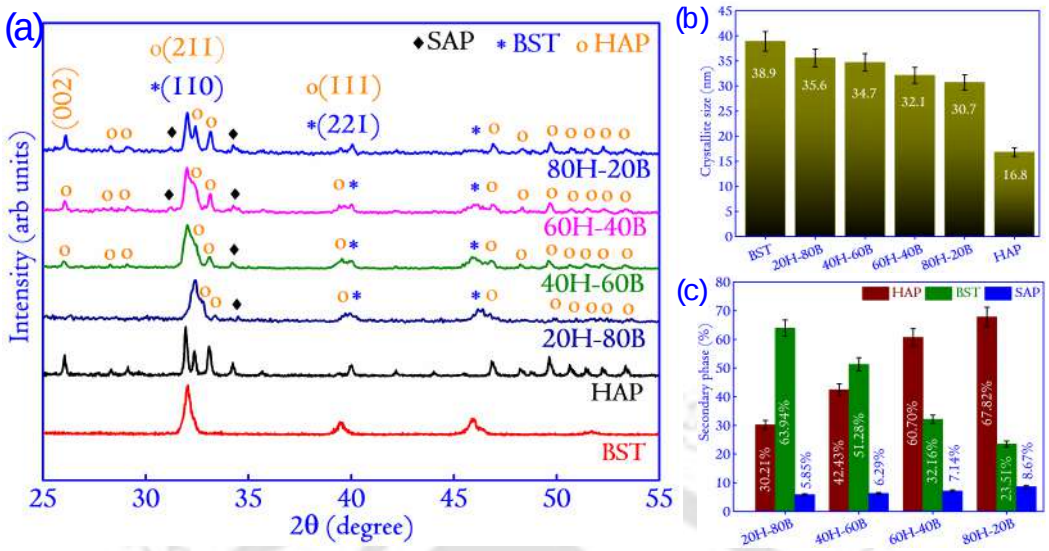


**Figure 5.2:** (a) XRD patterns of the composites show the peaks corresponding to both the monoliths and the appearance of additional peaks corresponding to the SAP phase. The XRD patterns of the monoliths are also presented along with the composites. The patterns reveal a large extent of overlapping in the peaks due to the closeness of the Bragg's angle in those positions. The dominance of the planes in the composite is observed, which corresponds to the more significant concentration of the monoliths. The (hkl) planes are identified by comparing the planes with the standard ICDD files: card no. 39-1395 for BST, 009-0432 for HAP, and card no. 002-0761 for SAP. (b) The variation in crystallite size of the ceramic composites and (c) shows the variation in the secondary phases identified in the XRD of the ceramic composites.

However, it is interesting to note that the substitution of $Ca$ by $Sr$ is by no means complete, and the substitution occurs only for a small fraction of $Ca$. This substitution occurs due to the differences in the reduction potential of $Ca$ (1.76 V) and $Sr$ (1.95 V). Further, the standard reaction potential of $Ba$ is higher than $Ca$, and the atomic radius of $Ba$ (217 pm) is more significant than $Sr$ (215 pm). Hence, it becomes difficult for the $Ba$ ions to occupy a $Ca$ site. Thus there is no substitution of $Ca$ by $Ba$ ions. The quantification of the amount of SAP has been shown in Figure 5.2(c), and the following formula has been used to calculate the amount of $Sr_5(PO_4)_3(OH)$ in the composites

$$wt.\%\ of\ secondary\ phase\ = \frac{I_{phase\,i}}{\Sigma I_{phase\,i}} \times 100\% \tag{5.2}$$

where, $I_{phase\,i}$ is the peak intensity of all the peaks in the XRD spectra of the specimen corresponding to that particular phase and $\Sigma$ denotes the sum over all the peak intensities. The approximate values of the different phases are shown in Figure 5.2(c). The calculated values show that the percentage of the amount of SAP in

all the composites are less than 10%. Also, to get an estimate of the effect of the formation of SAP on the crystal structure, the crystallite size of the composites as well as the monoliths have been calculated using the well-known Scherrer formula and the same have been included in Figure 5.2(b). The composites display crystallite sizes in between the monoliths and such similar behavior of the crystallite sizes are also apparent from the studies conducted on $Ca$ substituted $BaTiO_3$, in which the substitutions are brought about during the process of sintering of the composites [185].

### 5.3.2 Surface morphology and EDS analyses

The FESEM patterns of selected specimens are shown in Figure 5.3. The patterns reveal that HAP is composed of spherical granulite with an average grain size of 77.9 ± 4.9 nm. The BST is composed of polyhedral structures with an average grain size of 131.4 ± 8.1 nm. The FESEM of BST contains pores that might have been incorporated due to the lower sintering temperature of 1073 K. Ceramics such as BST needs high sintering temperature with enhanced soaking time for achieving compaction and a high-density [90, 179, 238]. However, in the present scenario, to avoid the generation of other phases of HAP (such as $\beta$-TCP), the sintering temperature is kept lower than 1273 K [90, 236]. In the case of the composite, it is seen that the lower grain-sized HAP reduces the porosity between bigger-sized BST grains by occupying the voids. The grain sizes of the composites are expected to lie in between the monoliths HAP and BST [90].

The EDS spectra of the composites and the monoliths are also shown in Figure 5.3. The $Ca/P$ values of the composites are calculated, and the $Ca/P$ ratio shows a decreasing trend with the increasing concentration of BST in the composites. It is apparent that in the case of composites with a higher concentration of HAP, the EDS for $Ca$ and $P$ will be better, leading to a higher $Ca/P$ ratio compared to composites that have lower HAP concentration. The $Ca/P$ ratio in HAP-based ceramics is vital in determining its biological properties *in vivo* [90]. A deviation in the $Ca/P$ ratio from the value of 1.67 indicates variation in the dissolution behavior of the ceramics [90, 239]. The dissolution behavior (rate of dissolution) is found to increase with the decrease in the $Ca/P$ ratio of the ceramics [90, 185]. For $Ca/P$ ceramics, the ratio usually lies in between 1.5-2.00, and in this regard, the obtained values lie within the experimentally reported range [90, 236].

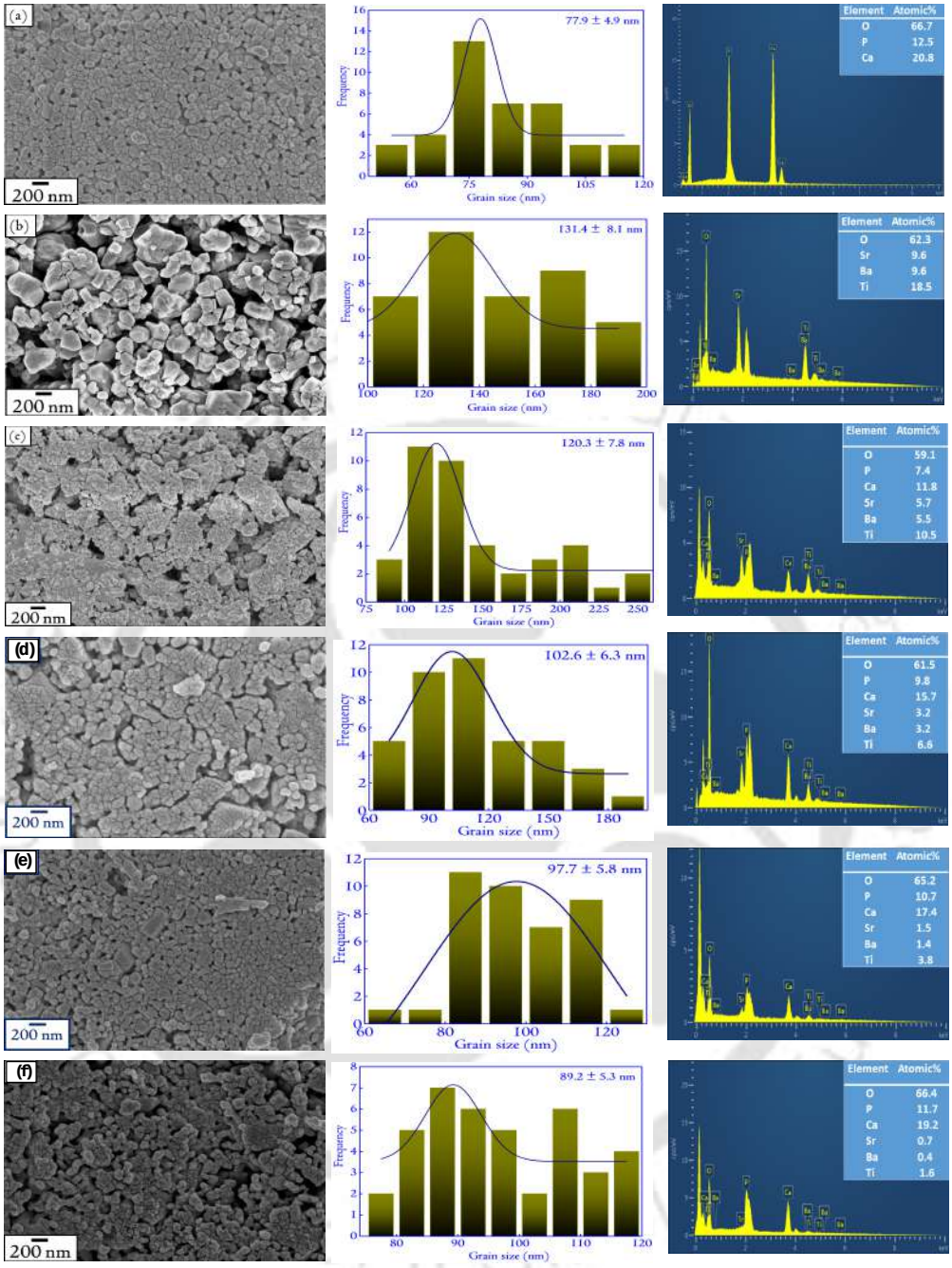


**Figure 5.3:** The FESEM pattern clearly show the evolution of grains of the composites and their monoliths. The variation in the grain sizes and EDS composition for (a) HAP, (b) BST, (c) $20H-80B$, (d) $40H-60B$, (e) $60H-40B$ and (f) $80H-20B$ has also been included to get the quantitative estimate of the same. Like the crystallite size, the grain size is the largest for the monolith BST. For the composites, the grain sizes lie in between BST and HAP. The $Ca/P$ ratio in the specimens is 1.66, 1.64, 1.62, 1.60, and 1.59 for HAP, $80H-20B$, $60H-40B$, $40H-60B$, and $20H-80B$.

### 5.3.3 Bioactivity and Cell viability

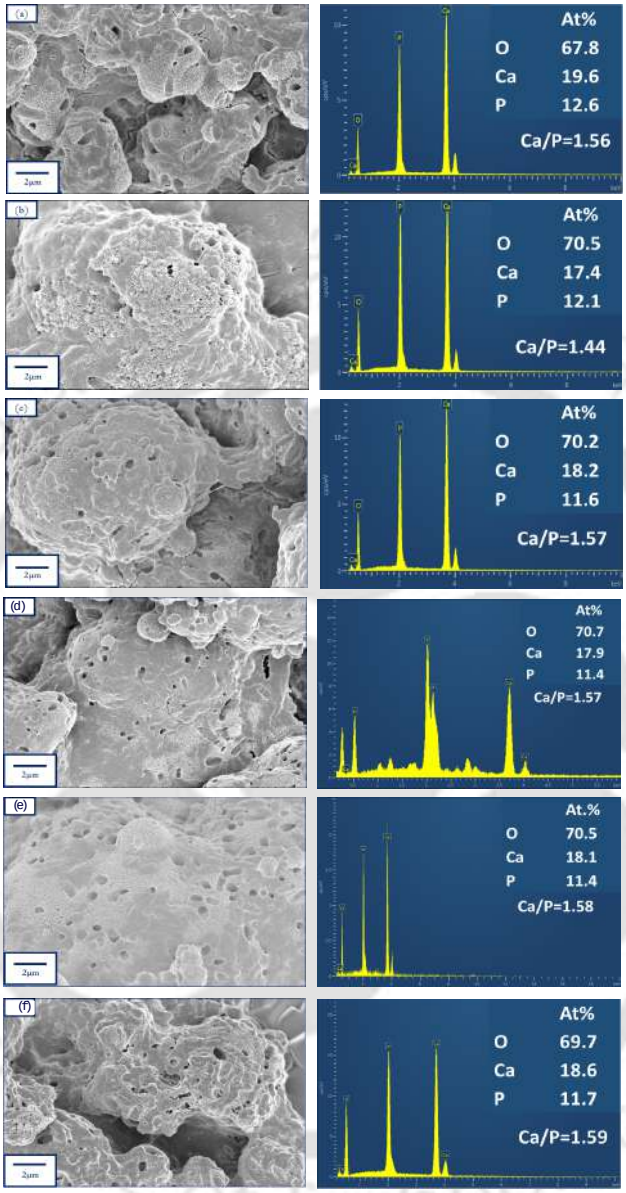


**Figure 5.4:** The FESEM micrographs showing clearly the nucleation of dense bone-like apatite structures along with micron-sized pores on the surface of (a) HAP, (b) BST, (c) $80H - 20B$, (d) $60H - 40B$, (e) $40H - 60B$, and (f) $20H - 80B$. The corresponding EDS of the bone-like apatite is also shown which is highest for $20H - 80B$, implying that the synergistic effect of the $Sr$, $Ba$, $Ti$, $(PO_4)^{3-}$ and $Ca$, enhances the biomineralization ability in the composite. The rectangles in (a), shows the position from which the EDS signals have been acquired.

The bioactivity of the specimens is determined by considering the ability of the discs to induce the growth of bone-like apatite on its surface when incubated in SBF

[90]. The SBF tests are pretty successful in predicting the *in-vivo* performance of biomaterials as they can successfully create an environment that mimics the actual physiological conditions inside the host body [123]. The FESEM images of the bone-like apatite nucleated on the surfaces of the compact discs are shown in Figure 5.4 for selected specimens. In all the specimens, a dense growth of the apatite layer is observed from the micrographs. Naturally occurring bone apatite is characterized by a flowery structure with plate-like petals and numerous pores [123, 123]. The apatite nucleated on the surfaces of the discs shows the mesoporous apatite layer formation with pore size in the range of microns. Such pores can help in the biointerfacial interactions of these structures when planted *in-vivo* as the pores are known to promote the ingrowth of bones [123, 123].

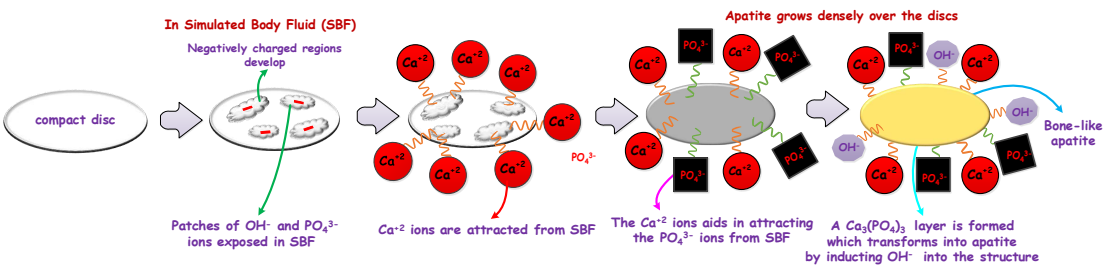


**Figure 5.5:** A schematic diagram of the probable mechanism of apatite nucleation in SBF over the surfaces of the discs. The nucleation mechanism is mainly related to the electrostatic forces that draw different ions from the SBF onto their surface. The illustration has been created using Visio 16 available at https://support.microsoft.com/en-us/office.

The mechanism of growth of apatite structures on compact discs can be understood by the chemistry and dynamics of the surface charges that build upon a surface when immersed in a fluid [240, 241]. In most of the cases, it has been seen that the apatite nucleation starts with $Ca^{+2}$ ions being nucleated on the surface resulting in the formation of $Ca$ rich surface, which is positively charged [215]. This positively charged surface forms the base layer for drawing the negatively charged $PO_4^{3-}$ ions by electrostatic interactions. Thus, an amorphous $Ca-P$ layer is generated, which has a high degree of solubility in water [242]. Therefore, from the point of thermodynamic stability, the amorphous $Ca-P$ layer would transform into a more stable bone-like apatite layer by incorporating $OH^-$ ions from the surrounding SBF. Reports have earlier demonstrated that among the variants of $Ca-P$ ceramics, the apatite is the thermodynamically most stable form and its solubility in *in-vivo* or *in-vitro* surroundings is the least at physiological pH [90]. A graphical view of the probable mechanism of apatite growth is depicted in Figure 5.5. Once

nucleation of the apatite layer starts over the surface of the compact discs, a further increase in the apatite layer takes place by consuming the ions present in the SBF, which is supersaturated with respect to apatite crystals. It is to be understood that the most crucial step in the nucleation of the apatite layer on the surface of the discs is the drawing of $Ca^{+2}$ ions from the SBF. The force of attraction must be electrostatic, and as the $Ca^{+2}$ ions are attracted towards the surface of the discs, it implies that the surfaces must be negatively charged. The zeta potential measurement is carried out to verify the proposition, and the results reveal that the surfaces are indeed negatively charged. The numerically obtained values of zeta potentials for selected specimens are measured, and it is found to be -21.97 mV, -16.32 mV, -35.64 mV, and -13.42 mV for $20H-80B$, $80H-20B$, BST, and HAP, respectively. The negative zeta potential values confirm the probable mechanism stated earlier, by which apatite growth must have taken place over the surface of the discs. The negative zeta potential of the surfaces are in fact useful for inducing bone growth under *in-vivo* environments [243].

In the case of the composites, the presence of $Sr$, $Ba$, $Ti$, and $Ca$ are reported to delay the release of ions into SBF, which are later exchanged with $H^+$ in the solution [243, 244]. The slow dissolution leads to continuous apatite nucleation on the interface of the discs. In the composites containing $Ba^{+2}$, $Sr^{+2}$, $Ti^{+4}$, and $Ca^{+2}$, the biomineralization proceeds longer due to the additional $Ca^{+2}$ ions. This reflects a higher $Ca/P$ ratio of the composites compared to the monoliths [243, 244]. In the case of the monoliths that contain lesser positive ions, reflected a lesser $Ca/P$ ratio. Amongst BST and HAP monoliths, the HAP surfaces offer thermodynamically favorable surfaces for apatite (Calcium Phosphate) formation due to similar nucleation centers that supports the growth of apatite layers [123]. It highly improves the $Ca/P$ ratio of HAP compared to BST. The FESEM images in Figure 5.4 shows that in the composites, the growth of the bone apatite layer is denser, which support the proposition. In BST, the growth is scattered, and the plate-like structures are seen only in patches. The composites contain layers of apatite structures over which multiple other layers of apatite have been deposited. Such dense bone apatite growth *in-vivo* would be very much suitable for the integration of any biomedical devices designed from the composites. The $Ca/P$ ratio of the deposited bone-apatite layer is highest for $20H-80B$ (1.59) and lowest for BST (1.44). Similar values of $Ca/P$ ratio for bone-apatite are also reported by Sarma *et al.* [123]. The theoretical $Ca/P$ ratio of HAP, an inorganic component of bone, is 1.67. The higher $Ca/P$ ratio in the presence of composites ($20H-80B$ and $80H-20B$) reflected their bioactivity.

The improvement in the $Ca/P$ ratio of bone-apatite in composites containing HAP dictates the prominent role of surface charge and different ions in the nucleation of apatite from SBF, as shown in Figure 5.4.

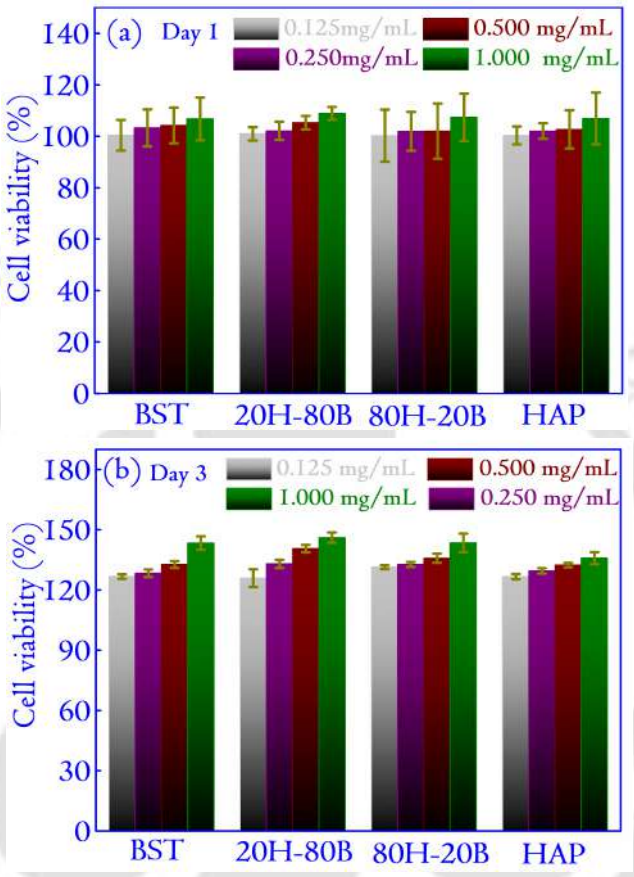


**Figure 5.6:** The cell viability studies of different specimens were studied with MG-63 cell lines for Day 1 and Day 3. All the specimens showed excellent viability amounting to values greater than 100% for all the concentrations. The higher cell viability of $20H-80B$ is mainly related to the presence of $Ba$ and $Sr$ ions, which have favored the proliferation of cells over the specimens.

The cytocompatibility analysis of the specimens is carried out using MTT assay on bone-like MG63 cell lines after incubating $1 \times 10^4$ cells/well for 1 and 3 days. Varying concentrations of the specimens amounting to 0.125, 0.250, 0.500, and 1.000 mg/mL are considered, and cell viability data are shown in Figure 5.6. The specimens showed excellent cytocompatibility, and the cell viability was more than 100 % compared to the control cells. Rather, the cell viability in the presence of material is higher than that of the control cells. In brief, the cell viabilities as compared to the controls are found to be 108.89, 107.39, 106.75, and 106.90 % for $20H-80B$, $80H-20B$, BST, and HAP, respectively at 1 mg/mL for Day 1. The cell viability

increases to 146.08, 143.47, 143.34 and 135.85 % for $20H-80B$, $80H-20B$, BST, and HAP, respectively at 1.000 mg/mL for Day 3. These observations indicate a better cellular response in the presence of $20H-80B$ than other studied samples. Additionally, the cell viability is higher at a higher material concentration *i.e.* 1.000 mg/mL due to more concentration of ions. Comparatively high cell viability is observed on $20H-80B$ suggesting the presence of $Ba$ and $Sr$ have favored the growth of cells over such specimens [245]. It is observed that the presence of $Sr$ and $Ba$ along with HAP encourages the new bone formation and enhances cell viability [246]. In a similar study on BST-based scaffolds, it is established that BST has no negative effect on the viability of mammalian cells [238]. The presence of $Sr$ is responsible for pre-osteoblastic cell differentiation, proliferation and also aids in suppressing osteoclastic differentiation. The overall high cell viability in the investigated ceramic composites and their monoliths demonstrates their cell proliferation ability and suitability in bone tissue regeneration applications.

### 5.3.4 Dielectric properties

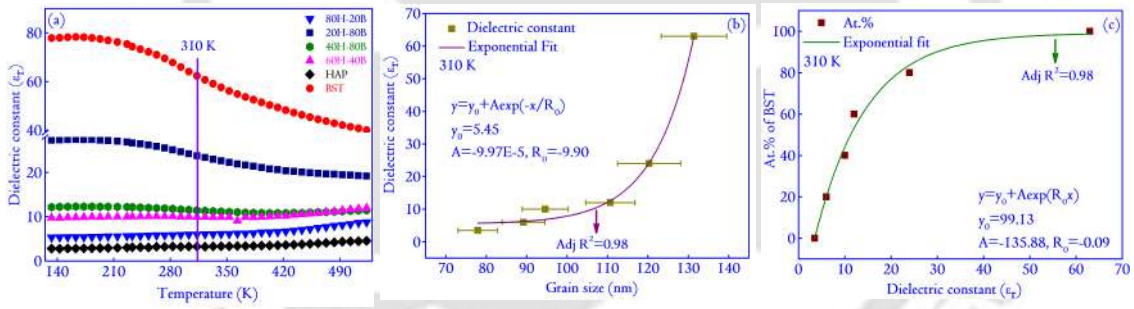


**Figure 5.7:** (a) The variation in the dielectric properties of the composites with the temperature at 1 MHz. The significant spike in the values is due to a probable phase transition of BST, and (b) shows the dependence of the $\epsilon_r$ (at 310 K) on the grain size of the composites. The relationship is found to be exponential with the adjusted R square value of 0.98. Similarly, in (c), the variation of $\epsilon_r$ with respect to the At.% of BST in the composites is considered. The variation is again exponential, with the R square value of the fit at 0.98.

The variation in the dielectric properties as a function of the temperature of the composites and the monoliths are shown in Figure 5.7(a). The variation of dielectric properties versus temperature can reveal a plethora of information regarding the dipole dynamics that determine the electrical properties of ceramics [86]. For instance, the ceramic BST has a phase transition temperature of 230 K [143, 247]. It causes an initial increase in the value of $\epsilon_r$ at a lower temperature, which gradually

decreases with a temperature rise in the dielectric spectra (measured at 1 MHz) shown in Figure 5.7(a). This can be explained due to the phase transition of BST near 230 K, at which the $\epsilon_r$ shows a spike [143]. However, in the present scenario, the phase transition is incomplete and requires probing lower temperature for the transition to complete. The dielectric properties of ceramics are largely dependent on the physical properties such as grain size and, most importantly, the density [90, 248, 249]. To quantify the relationship between the $\epsilon_r$ and grain size, a plot between the same is shown in Figure 5.7(b). An exponential dependence is evident from the plot and similar dependence of the $\epsilon_r$ with the At.% of BST is also considered, and it is observed that the dependence is exponential (shown in Figure 5.7(c)). As no densification method has been adopted in this study, the density of the ceramics is expected to be very low (a large fraction of voids are observed in the FESEM micrographs of BST). Also, the temperature at which the ceramics are sintered is very low compared to the conventional ceramics that are fired above 1273 K for enhanced densification [250, 251]. This might also reflect in the low value of $\epsilon_r$ in the case of BST, in contrast to the reports in the literature where BST is reported to have $\epsilon_r$ >1000 at 310 K [252, 253]. A similar value of $\epsilon_r$ (∼70) is also reported for composites made of BST and poly(vinylidene fluoride–chlorotrifluoroethylene) when the BST concentration in the ceramic is varied from 0 to 50 vol. % [249]. Interestingly, with the increasing content of HAP, the transition is completely suppressed, and the value of $\epsilon_r$ remains constant for the entire temperature range probed in the experiment. The losses occurring in the composites and monoliths expressed by the term ($tan\delta$) at selected temperatures have been included in Table C.1 (Appendix C). The values of $tan\delta$ are observed to rise with temperature, and it may be attributed to the kinetic energy of the mobile charge carriers responsible for losses within the composites and monoliths.

The BST content in the ceramic plays a dominant role in determining of electrical properties of ceramic composites. Mathematical modeling of $\epsilon_r$ reveals an exponential dependence on the At.% of BST ceramic, and the variation is shown in Figure 5.7(b). The dielectric properties are influenced by factors like grain size and crystallinity of the ceramic. It has been observed that for coarser grains (BST), the $\epsilon_r$ is highly sensitive to temperature. For nano-crystalline ceramics (HAP), the grains display a fine and uniform distribution, and therefore its dependence on the temperature is minimal. The presence of porosity in the ceramics with a higher content of BST (due to the lower sintering temperature of the ceramics) is a factor that controls the dielectric properties of the composites. The dependence of $\epsilon_r$ on

the grain size of the ceramic composites is shown in Figure 5.7(b). It is evident that with increasing BST content, the grain size enhances and leads to improvement of the $\epsilon_r$. Uniformly arranged grain sizes are essential in achieving greater $\epsilon_r$ [254]. In this study, it has been observed that in the case of BST, the grains are non-uniform. Moreover, there are large voids, which points towards insufficient densification of the ceramics resulting in lower $\epsilon_r$. It is discussed earlier that the sintering temperature for the ceramic composite is fixed at 1073 K, which is very low in comparison to the traditional ceramics firing temperature (>1273K) [255]. Such a lower sintering temperature and soaking time do not provide sufficient grain growth. However, the choice of sintering temperature is not arbitrary. The aim is to synthesize a composite with sufficiently good electrical properties to augment the biological properties. Bio-ceramics such as HAP are inherently brittle and efforts to densify, by application of high temperature without altering their phase composition, is a difficult task at bay [256]. A high sintering temperature pushes materials to the open spaces between particles, highly reducing porosity (see Figure 5.8). Such improved density is beneficial for achieving better electrical properties of composite ceramics.

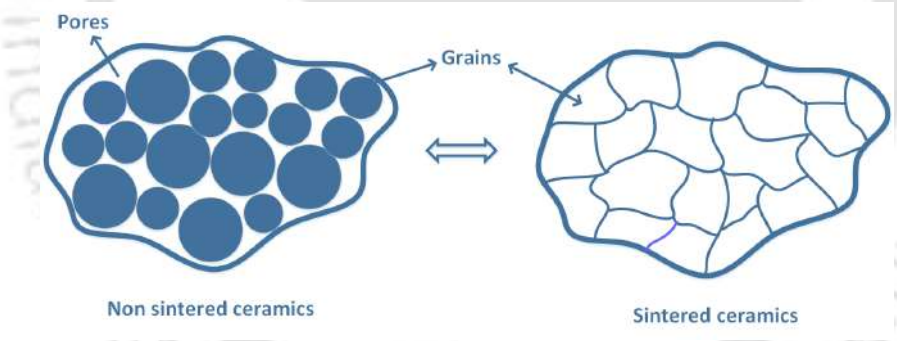


**Figure 5.8:** An illustration of the porosity in non-sintered ceramics and how the process of sintering leads to compactness in ceramics. In non-sintered ceramics (left), the point-like contacts between the individual grains leaves minimal space for interaction with the neighboring grains. This drastically reduces the contact in ceramics compared to highly dense ceramics (right), where the point contacts change over to elongated grain boundaries providing more room for conduction.

The exciting correlation of dielectric properties with biological applications stems out from the recent advances in medical science, where the treatment of bone fractures has seen the application of an electric field as bone growth stimulators [148]. In orthopedics, the treatment of fractures, non-unions, and delayed unions are classic examples of complex and challenging scenarios for Clinicians and patients alike.

The treatment of such complexities is accomplished by innovative techniques such as the applications of electrical fields [60]. The biology behind the healing mechanism of bone fractures in the presence of an electric field has not been understood (to a large extent) yet. Primarily, it is believed that the electric field applied at regular intervals accumulates ions such as $Ca^{+2}, PO_4^{3-}, OH^-$ locally near the fractured region, which leads to the initiation and further progress of the highly critical bone-forming process [148]. However, case studies of patients subjected to electric fields have shown that the process is quite tedious. The electric field needs to be administered for a period of (at least) three months with an exposure time of 10 hours (minimum) daily [148]. The duration is undoubtedly lesser than the average healing time (without stimulations); however, extensive research is being carried out to decrease the healing time further. In this regard, it is proposed that the scaffolds designed from electrically active materials such as the one considered in this article can decrease the healing time. In bone tissue engineering applications, scaffolds guide bone growth and regeneration. When the electrical stimulation is used in conjunction with the scaffolds, the stimulation can trigger polarization. The polarized field can continue generating the electric field internally, even when the external field is removed. Scaffolds generated from ceramics are inherently capable of undergoing polarization and can sustain the polarized field for a sufficiently long time [60]. It can be expected that the continuous generation of an electric field in the injured sites will lead to accelerated recovery by the patients. The composites which show modest $\epsilon_r$ in the range of 3-65 can be potential candidates associated with an innovative modality for rapid fracture healing. However, apart from $\epsilon_r$, biocompatibility and bioactivity are crucial factors that need to be addressed.

### 5.3.5 IS and Cole-Cole analysis

The Cole-Cole plots for the composite specimens are plotted using the Cole-Cole function described mathematically using the following equation

$$\epsilon(\omega) - \epsilon(\infty) \propto \frac{1}{(1 + i\omega\tau)^{1-\alpha}} \tag{5.3}$$

where $\epsilon(\omega)$ describes the permittivity at high frequencies, $\alpha$ represents the angle of deviation below the real axis of the Cole-Cole plot, and $\tau$ represents the characteristic relaxation time adequate to the system under investigation. To generate the Cole-Cole plot, the real and imaginary part of the impedance (Z) is used, and the plots are shown in Figure 5.9.

The Cole-Cole plots of the composites, along with the equivalent circuits that adequately represent the plots, are shown in Figure 5.9. It is observed that the impedance analysis brings out the direct correlation between the impedance of a real dielectric system and an idealized model circuit consisting of discrete electrical components [257]. Such models aid in understanding the complex overall behavior of the composite systems in terms of discrete electrical components like resistors, capacitors, and inductors [258]. The simplest of all circuits consists of an RC circuit, an elegant model to consider charge migration over a frequency range. A resistor can represent the dissipative contributions in a dielectric due to electrode polarization and dipole relaxations that occur at low and high frequencies, respectively [259]. The losses from migrating charges, extrinsic sources (ionic impurities), and intrinsic sources (transfer of proton along with ionic bonds) are also dissipative contributions that can be modeled through a resistor. The capacitor is used to model the storage capacity of dielectrics due to different polarization mechanisms. Another interesting parameter is the constant phase element, abbreviated as Q. The Q is commonly used to describe the behavior of a double layer, i.e., an imperfect capacitor in IS. The Q can behave either like a capacitor or a resistor depending upon the value of a parameter "n" taking the value of 1 or 0, respectively [257].

In Figure 5.9, it is observed that the simulated curve that fits the experimental data is not perfectly semi-circular. The fitted semi-circles are skewed, and such deviations from the ideal semi-circular behavior are attributed to the non-smoothness in the movement of the dipoles (to produce dipolar polarisation) in a non-idealized viscous environment [260]. The dipolar movements take place in the form of jumps or hops that are necessitated by the structure of the solid composite materials. To investigate further into the nature of the hopping polarization, the next section deals with the study of the $\sigma$ mechanism in the composites. The $\sigma$ mechanisms are crucial to understanding the nature of the hopping process in the specimens.

**Table 5.2:** The numerical values of the grain resistance and capacitance for the composites were obtained from the Cole-Cole plot. The value of Q in all the cases yielded $n\sim$ 0.9, and therefore the constant phase element for all practical purposes can be assumed to behave as a capacitor.

| Composite | Grain resistance (MΩ) | Grain capacitance (pF) |
|---|---|---|
| 20H-80B | 83.62 ± 0.26 | 16.01 ± 0.31 |
| 40H-60B | 26.45 ± 0.18 | 10.38 ± 0.15 |
| 60H-40B | 19.94 ± 0.13 | 4.28 ± 0.08 |
| 80H-20B | 7.68 ± 0.08 | 1.42 ± 0.02 |

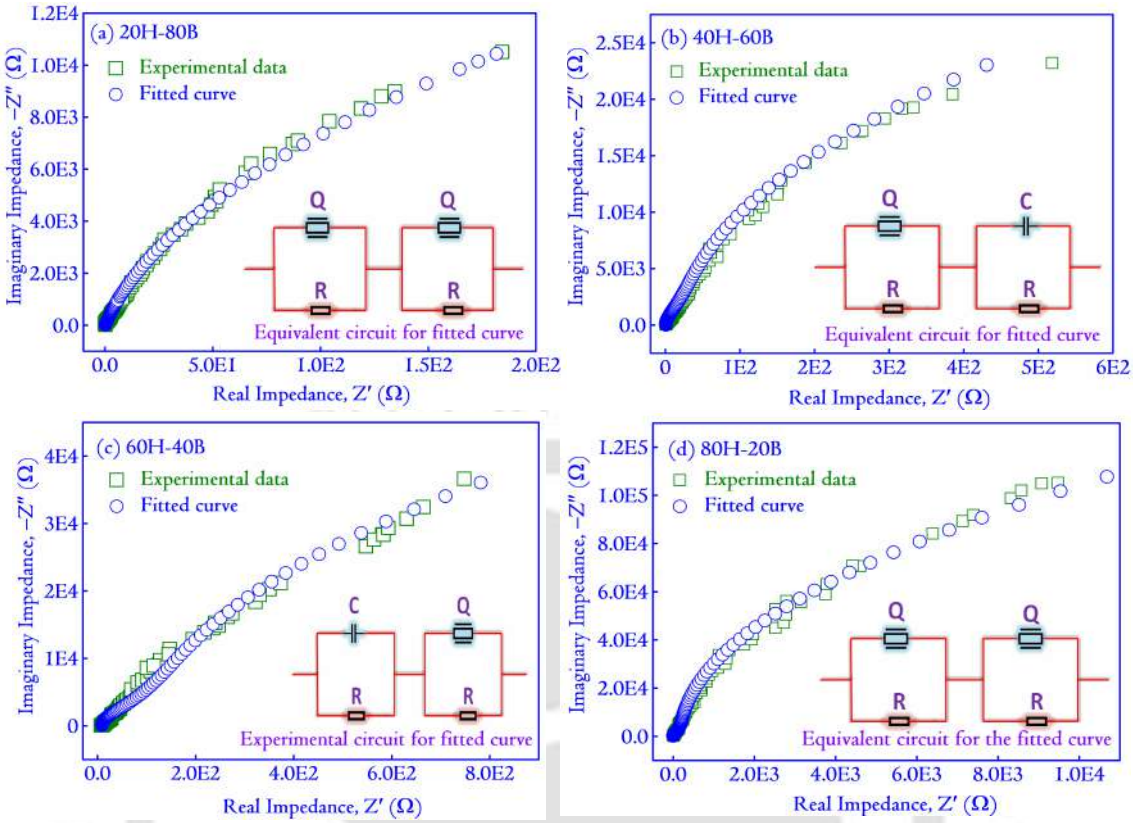


**Figure 5.9:** The diagram shows the fitting of the Cole-Cole function to the experimental data for the four variations of the composites. The plot is made between the real and imaginary parts of "Z" in the Argand plane. The electric circuit in each case describes the electrical model of the physical processes occurring inside the composite specimens. The equivalent circuit in each case is a series combination of a parallel combination of a capacitor and a resistor or a capacitor and a constant phase element. A ceramic composite is often a complex scenario of many conducting species, grains, and grain boundaries. The Cole-Cole formalism helps in mapping an equivalent circuit for the biomaterial. Such an equivalent circuit helps in the design of the biomedical devices that explicitly exploits the electrical properties of the biomaterial.

To understand the hopping process, one must start by understanding the relaxation phenomena in dielectrics. When an external electric field is applied to a dielectric material, the dipoles align themselves in the applied field's direction. A higher number of dipoles aligning to the applied field imply a higher $\epsilon_r$ (a high $\epsilon_r$ contributes to a higher amount of energy being stored in the dielectric). Relaxations in IS are related to the dipole's inability to follow the alterations in the externally applied ac field [33]. For instance, as the frequency of the externally applied ac field increases, the dipoles that can align themselves to the field at lower frequencies slowly start lagging [261]. As the ac field frequency changes faster, the dipoles relax

to the non-aligned positions, thus losing their ability to store energy. Dipoles composed of larger entities (for instance, atoms) tend to relax at lower frequencies (few Hz) due to the bulkiness of the structure, and those composed of smaller entities typically tend to relax at higher frequencies (kHz to MHz)[252]. Thus, the larger entities' relaxation times are in seconds, and the smaller entities have relaxation times in the range of milliseconds to microseconds [33]. The dipolar relaxation phenomena reportedly proceed through several processes, prominent among the hopping conduction [33]. The formalism of hopping conduction is very broad and elegant, and the analysis of the $\sigma$ mechanisms forms the platform for understanding the hopping process in composite ceramics. In Table 5.2, the values of the grain capacitance and grain resistance obtained from the simulated curve are displayed. The grain relaxation times were also obtained from the simulated curves, and these values are 1339.75 $\pm$ 60.16, 274.34 $\pm$ 11.67, 85.34 $\pm$ 4.30, 10.90 $\pm$ 0.53 for $20H - 80B$, $40H - 60B$, $60H - 40B$, and $80H - 20B$. Similar relaxation times for a composite of $MgTiO_3$ and $Ba_{0.5}Sr_{0.5}TiO_3$ were also obtained by Rabha *et al.* [257].

### 5.3.6 $\sigma$ analysis

The $\sigma$ of the composites at a frequency of 1 MHz studied with respect to temperature is shown in Figure 5.10. The $\sigma$ plots show a substantial temperature dependence after 300 K, when the $\sigma$ increases significantly compared to its dependence at low temperatures. It is stated earlier that a higher sintering temperature of the composites is responsible for pushing materials into the void open spaces as shown in Figure 5.8. Such a process leads to the growth of point contacts between the grains and grain boundaries. Lesser contact between the grains reduces the $\sigma$ of the charge-carrying species. In this case, the $\sigma$ of the ceramics is less than $10^{-7}$ S/cm. Such lesser value of $\sigma$ can be directly related to the lower value of sintering temperature and the porous nature of the sintered ceramics. The $\sigma$ for the monoliths has been included in Figure C.1 (Appendix C). A temperature range of 363 K to 483 K has been selected for the $\sigma$ analysis. The increasing research interest in the exploration of the biomaterials for electret generation in devices such as low powered electrostatic induction generator involves the generation of sufficiently high temperatures [203]. Thus, understanding the conduction mechanisms becomes markedly significant in these temperature ranges. The mechanisms can provide us insights into the working of the biomaterials in the temperature domain and is relevant for fabrication of device.

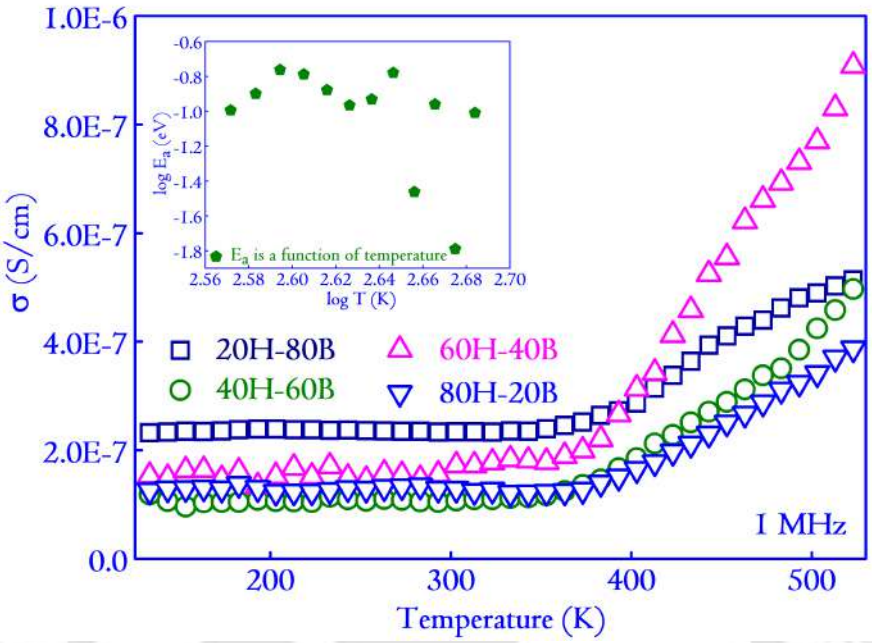


**Figure 5.10:** Variations in $\sigma$ with temperature for a wide range of temperatures. The $\sigma$ plots are made at a frequency of 1 MHz. The inset of the figure shows a variation in $E_a$ with temperature (in the log scale) to demonstrate the variation in the $E_a$ with temperature, unlike the thermally activated conduction mechanisms or NNH models where the $E_a$ remains constant over a specified range of temperature (for $20H - 80B$). The variation points towards the VRH conduction mechanism within the specimens. The variations are considered in the temperature range of 363 K to 483 K, which forms the basis of this report. The plot of $log(E_a)$ versus $logT$ for the other specimens are included in Appendix C (Figure C.2).

The explored temperature range is usually identified with the thermally activated band conduction mechanism that has the following temperature dependence [203]

$$\sigma = \sigma_0 exp(\frac{-E_a}{k_B T}) \tag{5.4}$$

where $\sigma_0$ is the pre-exponential factor (a constant), $K_B$ is the Boltzmann constant, $T$ is the temperature and $E_a$ is the activation energy of bulk conduction specific to the process and can be determined from the following expression [202]

$$E_a = -\frac{d[\ln \sigma]}{d[\frac{1}{k_B T}]} \tag{5.5}$$

Equation (5.6) enables us to determine the $E_a$ of the conduction process, independent of the conduction mechanism active within the specimens. From equation 5.5, it becomes increasingly evident that for thermally activated band conduction,

$E_a$ must have a constant value for a particular temperature range. However, from the inset of Figure 5.10, where $E_a$ is plotted as a function of temperature, it is evident that $E_a$ is a temperature-dependent function. This reveals that thermally activated band conduction is not the dominant conduction mechanism in the composites, in the selected temperature range [202]. The temperature dependence of $E_a$ also negates the possibility of nearest-neighbor hopping conduction (NNH), which has similar mathematical dependence as equation 5.5. The only conduction mechanism that appropriately describe the set of events is the variable hopping conduction (VRH). VRH is characterized by the hopping of charge carriers between levels close to the Fermi level irrespective of the spatial distribution of the charge carriers [205]. VRH conduction process is also characterized by the variable hopping distance that distinguishes it from NNH, where the hopping takes place only to the nearest neighbor empty site [203].

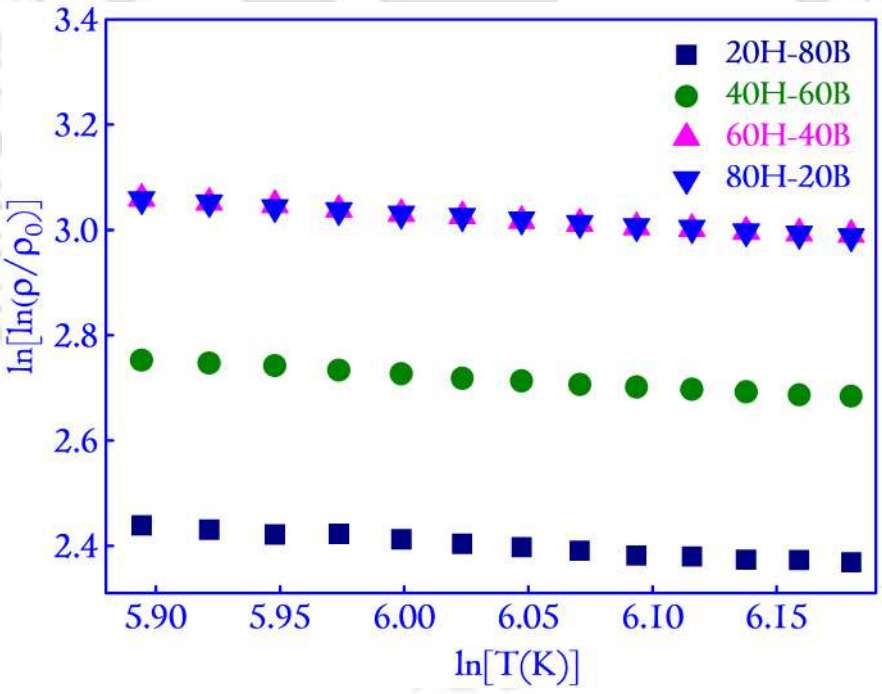


**Figure 5.11:** The figure shows the plot of $\ln[\ln(\rho/\rho_0)]$ versus $lnT$ that helps to identify the VRH mechanism in the composite in the temperature range of 303 K to 523 K.

Analyzing the VRH mechanism from the perspective of resistivity ($\rho = (1/\sigma)$) can reveal a plethora of information about the conduction mechanisms in the specimens. There is no particular preference for choosing $\rho$, and the conclusions equally apply even if $\sigma$ instead of $\rho$ is chosen for analysis. A number of VRH mechanisms have been specified in the literature. A generalized understanding of such mecha-

nism can be had from the following equation [206]

$$\rho = \rho_0 exp(\frac{T_0}{T})^p \tag{5.6}$$

where $\rho_0$ is the pre-exponential factor ($\rho_0 = 1/\sigma_0$, a constant), $T_0$ is the characteristic temperature relevant to the prevalent conduction mechanism, and $p = 1/2, 1/3, 1/4$ or 1, respectively, depending on the form of density of states at the Fermi level. In disordered systems without Coulomb interactions, $p = 1/4$, lead to Mott's VRH mechanism that assumes that the density of states (DOS) remains constant near the Fermi level [206].

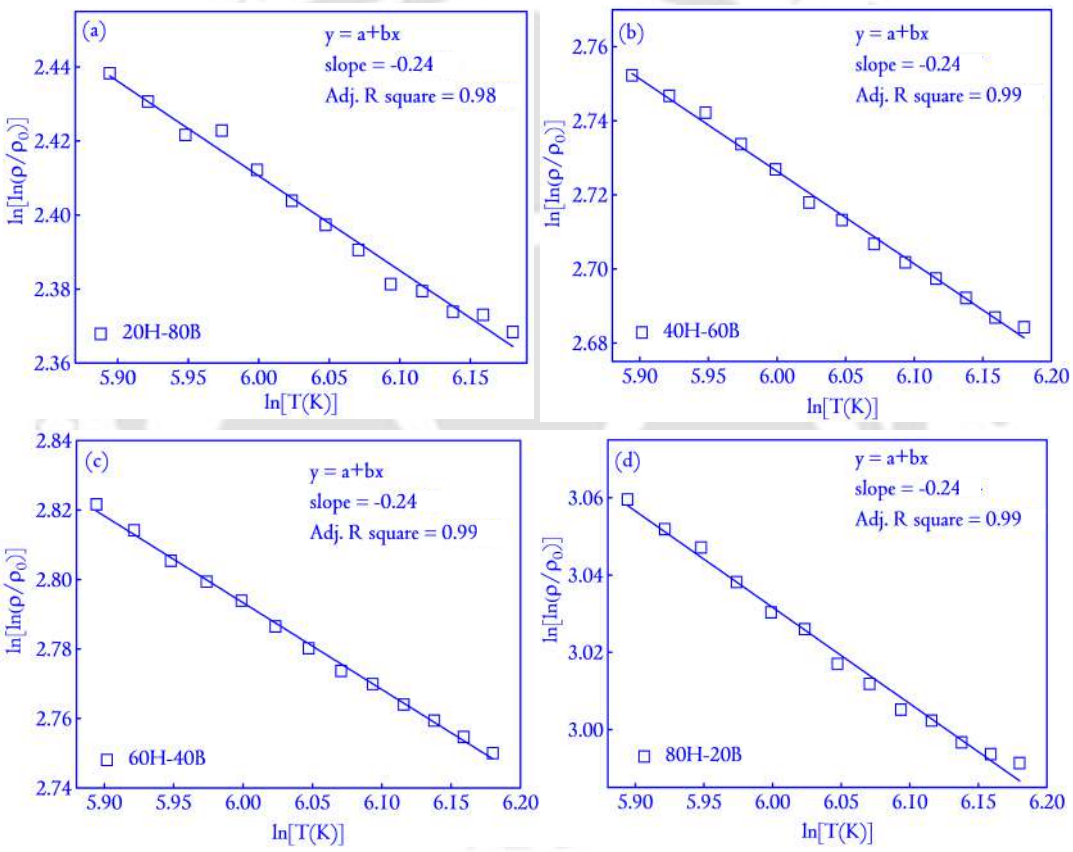


**Figure 5.12:** The figure shows the plot of the linear fit of $\ln[\ln(\rho/\rho_0)]$ versus $lnT$ that shows that the slope of the linear fit is ∼0.25, and this value identifies Mott's VRH mechanism to be the dominant conduction mechanism in the ceramic composites'.

An assumption that justifies the existence of Coulomb interaction between the initial and the final hopping states for the long-range electron hopping leads to $p = 1/2$ and generates the Efros-Shklovskii VRH model [207]. In this model, the DOS vanishes quadratically near the Fermi level. For 2D systems, Somoza and co-workers

suggested $p = 1/3$ as the index [208]. The $p = 1$ mode was also introduced for certain systems with a many-electron excitation effect that could lead to a hard gap in the DOS near the Fermi level. Identifying the dominant conduction mechanism from a diverse set of available models largely depends upon fitting the appropriate model to the $\sigma/\rho$ data. From a mathematical perspective, by a slight modification of equation 5.6, the following equation can be derived,

$$\ln[\ln(\rho) - \ln(\rho_0)] = p[\ln(T_0) - \ln(T)] \tag{5.7}$$

which is an equation of the form $y = mx + c$, with $m = -p$, $y = \ln[\ln(\rho/\rho_0)]$ and $x = \ln(T)$. The advantage of the mathematical manipulation in equation 5.7, provides us with the option to use the slope of straight line to determine the nature of conduction mechanism active within the specimens. These variations are shown in Figure 5.11. In all the composites, the slopes are close to 1/4 suggesting Mott's VRH to be the dominant mechanism in the specimens' as shown in Figure 5.12. With $p = 1/4$ , the equation 5.7 modifies to the form,

$$\rho = \rho_0 exp(\frac{T_0}{T})^{1/4} \tag{5.8}$$

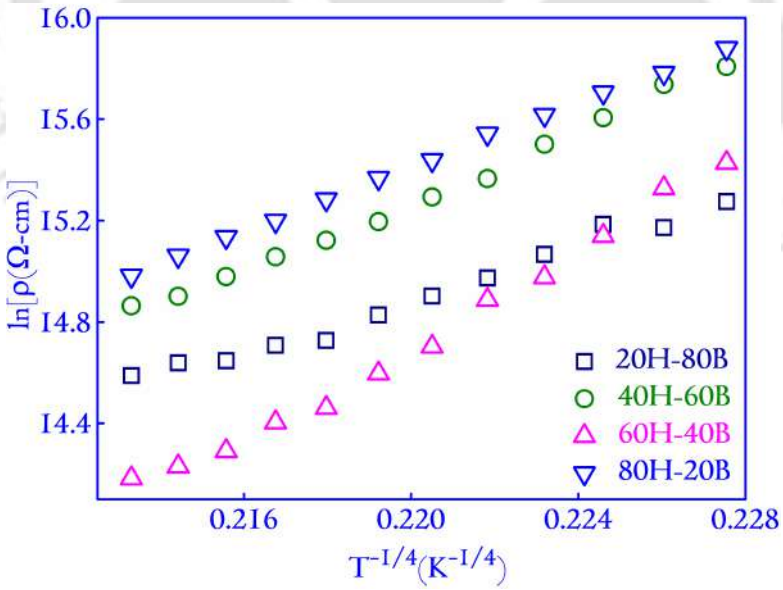


**Figure 5.13:** The plot of $\ln[\rho]$ versus $T^{-1/4}$ characteristic to Mott's VRH mechanism. The slope of the fitted straight line can be used to calculate the DOS, which is inversely related to the characteristic temperature of $T_0$.

It is stated earlier that $T_0$ in equation 5.8, and hence equation 5.9 is the character-

istic temperature dependent upon the active conduction mechanism in the specimen (see Figure 5.13 and Figure 5.14). Incidentally, the parameter $T_0$ is inversely related to the DOS near the Fermi level, $N(E_F)$ [205]. The values of the DOS have been included in Table 5.3. The mathematical relationship for determining the DOS near Fermi level is represented as [206]

$$N(E_F) = \frac{16}{T_0 k_B \zeta^3} \tag{5.9}$$

where $\zeta(= \alpha^{-1})$ is the decay length of the localized wave function, and signifies the spatial extension of the wave function $\exp^{-\alpha R}$ associated to the localized states ($R$ denoting the hopping length). There is no report on the value of $\zeta$ for the chosen ceramic composite. In case of $BaTiO_3$, Han *et al.* [202] considered $\zeta$ to be approximately 0.40 nm and this value is chosen for calculation of $N(E_F)$ using equation 5.9. The calculated values are listed in Table 5.3.

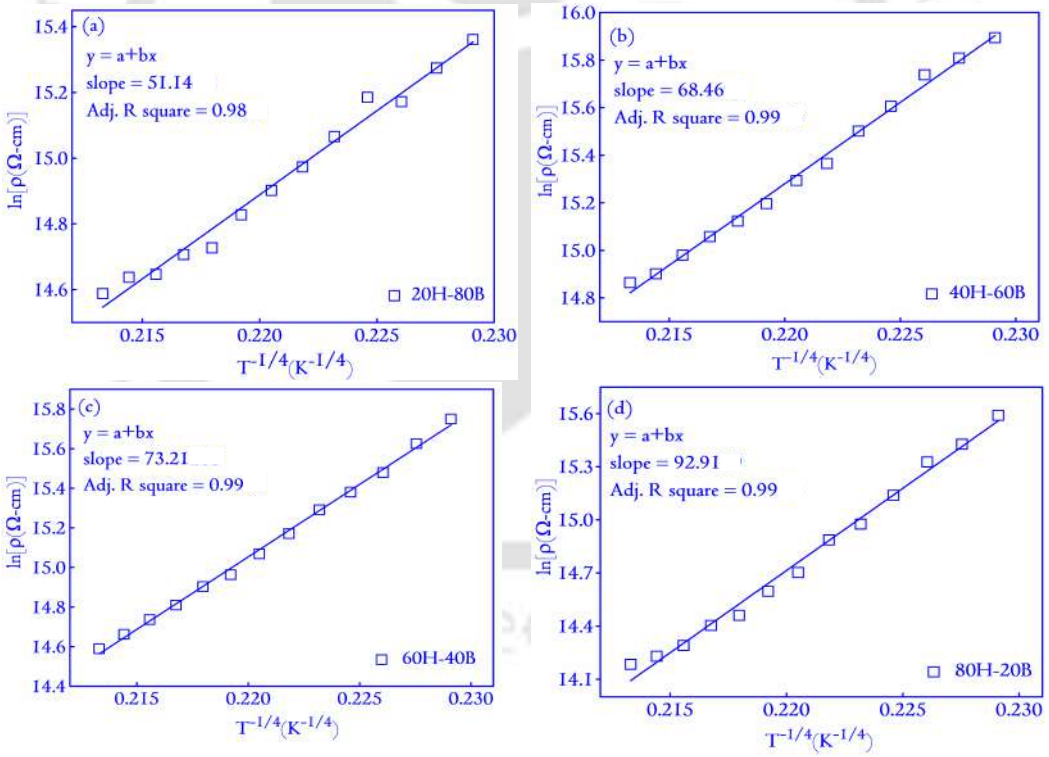


**Figure 5.14:** The fitted straight line in the plot of $\ln[\rho]$ versus $T^{-1/4}$. The slope of the fitted straight line can be used to calculate the DOS, which is inversely related to the characteristic temperature of $T_0$. The DOS are included in Table 5.3.

To complete the discussion, two important parameters viz. the hopping length ($R$) and the hopping energy ($W$) is determined from the Mott's VRH model using

the following equations [205]

$$R = \frac{3}{4}[\frac{3\zeta}{2\pi N(E_F)k_BT}]^{1/4} \; and \; W = [\frac{3}{4\pi R^3 N(E_F)}] \tag{5.10}$$

**Table 5.3:** Variation of the characteristic temperature and DOS for various specimens.

| Sample | $\mathbf{N(E_F)(eV^{-1})(cm^{-3})}$ |
|---|---|
| 20H-80B | $4.24 \times 10^{20}$ |
| 40H-60B | $1.32 \times 10^{20}$ |
| 60H-40B | $1.00 \times 10^{20}$ |
| 80H-20B | $3.89 \times 10^{19}$ |

The values calculated for $R$ and $W$ are shown as a function of temperature $T$ in Figure 5.15. For all the composites, the value of $R$ and $W$ shows a linear variation with temperature $T$. Moreover, the essential conditions $W \geq k_BT$ and $R/\zeta \geq 1$ is satisfied in all cases by the ceramic composites that confirms the validity of the approach [205].

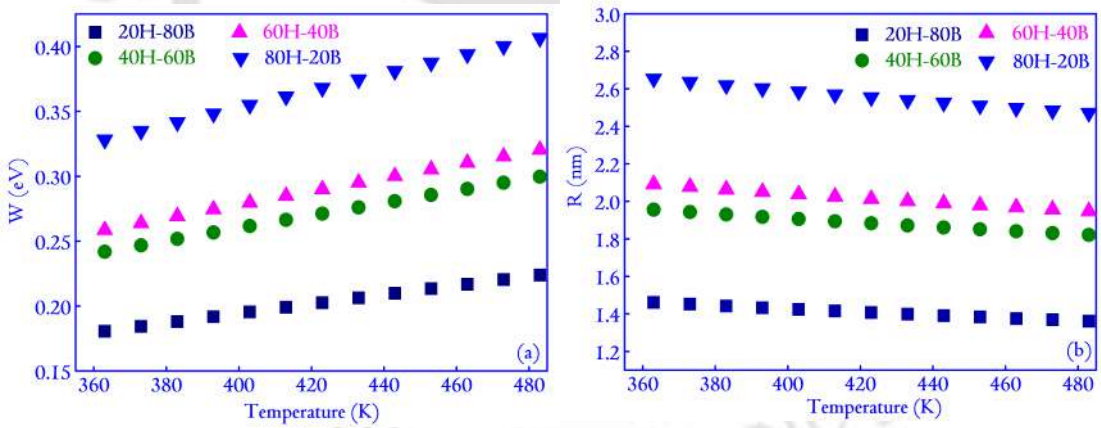


**Figure 5.15:** The variation of the (a) hopping energy $W$ and (b) hopping length $R$ as a function of temperature. $R$ and $W$ show a linear variation with temperature, $W$ increases linearly as a function of temperature, and $R$ decreases linearly.

Pattipaka *et al.* [210], considered a ceramic composite of $Bi_{0.5}Na_{0.5}TiO_3 - K_{0.5}Na_{0.5}NbO_3$ and in the temperature range of 300-419 K and 562-589 K, Mott's VRH mechanism was applied. The values of $W$ and $R$ were found to be similar to the present case. Interestingly, Kasamatsu *et al.* [262] pointed out that the polarization mechanisms active within HAP specimens, especially in the activation energy domain of 0.2- 0.8 eV is consistent with the range of hopping energy in the

case of ceramics. Tanaka *et al.* [260] reported that in HAP, the dipolar relaxation occurs with an activation energy of 0.6 eV. Such relaxations might proceed by the variable range hopping of charge carriers. It points to a close correlation between the active conduction mechanisms and the polarization mechanisms in ceramics. However, in the present scenario, there would be a contribution from BST, which makes the process all the more complex.

### 5.3.7 Protein adsorption and evolution of secondary structure

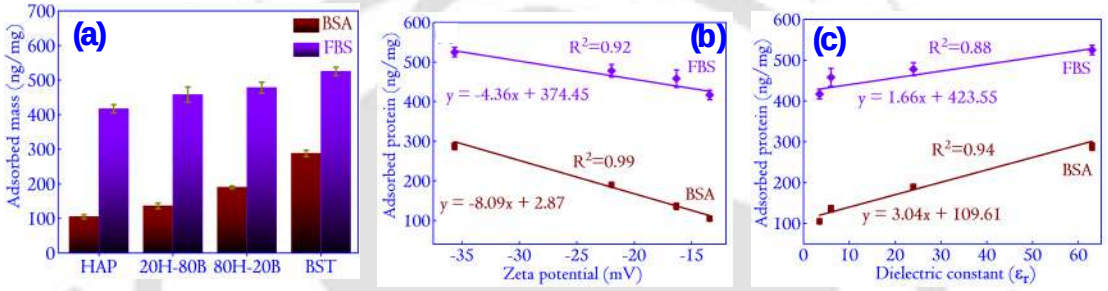


**Figure 5.16:** (a) The adsorbed mass of BSA and FBS on selected ceramic composites. The mathematical modeling of the behavior of the adsorbed proteins with respect to the zeta potential for (b) BSA and FBS follows a linear relation $y = mx + c$, with the parameters specified appropriately in the diagram. In (c), the variation of adsorbed proteins with $\epsilon_r$ is plotted. Similar to zeta potential, the variation with $\epsilon_r$ is also linear.

Protein adsorption is the first interaction at the interface of an implant in the host body. HAP is inherently adsorptive, and any implants into the host body that contains HAP would adsorb proteins from the physiological micro-environment [16]. These physiological proteins later support the binding of the cells [263]. The protein adsorption data on the monoliths and selected ceramic composites are shown in Figure 5.16. The normalized concentration (by weight) of the adsorbed BSA is the highest on BST (amounting to 288 ± 9 ng/mg) and least on HAP specimens (amounting to 105 ± 6 ng/mg). The adsorbed FBS on the ceramic surfaces shows the same trend, with the highest value on BST amounting to 525 ± 12 ng/mg and least on the HAP specimens amounting to 417 ± 12 ng/mg. The more adsorbed amounts of FBS than BSA on the individual specimens are due to higher initial protein concentration in the case of FBS. The protein adsorption behavior on the ceramic surfaces is highly modulated by the surface properties such as the zeta potential. The zeta potential of the surfaces provides information about the surface

charge properties in solution [264]. The $Ca$ ions present in the HAP readily interacts with the BSA that has active $Ca$ binding sites [265], favoring the BSA-$Ca$ interactions on the specimens interface. Furthermore, these interactions affect the protein structure and result in conformation changes upon adsorption [266]. Low conformational change leads to reversible protein adsorption and might be due to lesser protein adsorption. It causes less BSA to be adsorbed on the specimens containing $Ca$ (usually depending on the relative (homogeneous) distribution of HAP in the composites). BST, on the other hand, consists of $Ba^{+2}$, $Sr^{+2}$ and $Ti^{+4}$ positively charged ions. Thus the enhanced electrostatic interactions with negatively charged BSA molecules [267–269] resulted in a higher adsorbed amount on BSA. The XRD analysis Structural analysis reveals the formation of SAP in the case of the composites. The presence of $Sr$ in SAP is also responsible for BSA adsorption. Since all the surfaces in this investigation have shown preferentially reasonable amounts of adsorbed proteins (BSA and FBS), it is expected that these surfaces will induce faster bone-apatite growth on their surface, which is an essential condition for bonding the implants to the host site.

The mathematical dependence of the adsorbed protein with the electrostatic interaction properties of the ceramic surfaces (specifically the zeta potential) is vital for understanding the adsorption dynamics. In the inception, the adsorption of a specific protein on a surface increases if some or all of the following criteria are fulfilled: (a) the concentration is very high, (b) the protein is structurally flexible, (c) quick diffusion due to low molecular weight, and (d) the repulsion between the surfaces and the incoming proteins is very low [163]. Figure 5.16(b) reflects a linear relationship between the zeta potential and the adsorbed mass of BSA and FBS. A linear increase in the BSA adsorption with a decrease in the zeta potential indicates that a negative zeta potential favors the adsorption of globular proteins. BSA is also a major component in the FBS ($\simeq$ 70-80%). Thus the adsorption of FBS followed the same trend as BSA adsorption [268, 269]. As the electrical properties (specifically the $\epsilon_r$) is an intrinsic property related to the charge holding capacity of the material, the relationship between the adsorption and $\epsilon_r$ can be interesting to probe. The plots in Figure 5.16(b) and (c) reflects a linear relationship as depicted by the zeta potential. Thus it can be concluded that the $\epsilon_r$ of a surface might positively correlate with its zeta potential and is also related to the protein adsorption behavior of the surfaces. Such investigations are rare and would be an interesting field of research to explore in the future. We must note that protein adsorption in biomaterials is a complex scenario, and apart from zeta potential and $\epsilon_r$, factors like wettability and surface

energy also have an important role [270, 271].

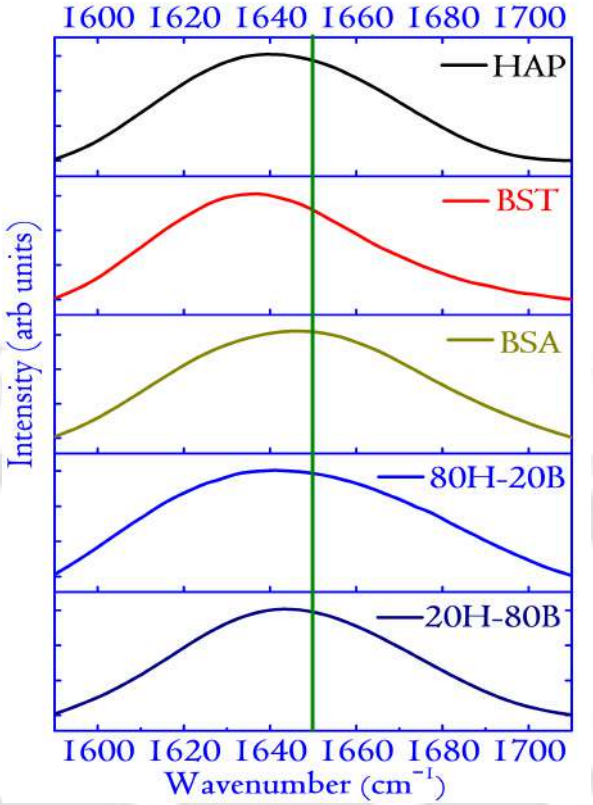


**Figure 5.17:** The FTIR spectra of BSA adsorbed surfaces in the Amide-I region (1580-1710 $cm^{-1}$). The BSA concentration is fixed at 1.000 mg/mL for the adsorption experiments. The vertical line at 1650 $cm^{-1}$ determines the shift in the maxima of the peak of BSA on adsorption to various surfaces. The shift is related to the conformational changes in the protein structure upon adsorption onto the surfaces of the compact discs.

For further in-depth analysis of the protein interactions with the synthesized ceramics, BSA is considered. The analysis of the secondary structure of the BSA reveals insight into adsorption behavior on the surfaces. Simultaneous with the surface adsorption of protein, conformational change and structural rearrangement of the protein occurs. Hence, deconvolution of the Amide-I region as obtained from FTIR analysis (Figure 5.17) is shown in Figure C.3 (Appendix C). Native BSA contains primarily $\alpha$ helical structure along with random ($\sim$45 %), $\beta$ sheet ($\sim$30 %), $\beta$ turns ($\sim$17 %), and side-chain ($\sim$ 8 %) [98]. The range for the appearance of different secondary structures in the FTIR spectra of BSA is $\alpha$-helix $\sim$ 1650 $cm^{-1}$, $\beta$ sheet $\sim$ 1620-1636 $cm^{-1}$, $\beta$ turns $\sim$ 1662-1688 $cm^{-1}$ and a random peak is found $\sim$ 1645 $cm^{-1}$ [98]. The variations in the secondary structures for different surfaces are plotted in Figure 5.18. Interestingly, it is observed that BST, which

adsorbed the highest amount of BSA on its surface, displayed the least content of $\alpha$ helicity. The trend is evident in all the specimens, and HAP, which adsorbed the least amount of BSA, displayed the highest content of $\alpha$-helicity. Consequently, the content of the $\beta$ sheet increased with the amount of adsorbed protein on its surface. The adsorbed protein on composite specimens resulted in higher helicity and lesser $\beta$ sheet contents than on BST specimens. The secondary structures of the adsorbed protein on the composite specimens are comparable to those on the HAP surface. However, the adsorbed amounts of proteins on the composite surfaces are enhanced up to 1.8 times compared to the HAP surface. These observations indicate better protein-surface interactions in the presence of composite specimens.

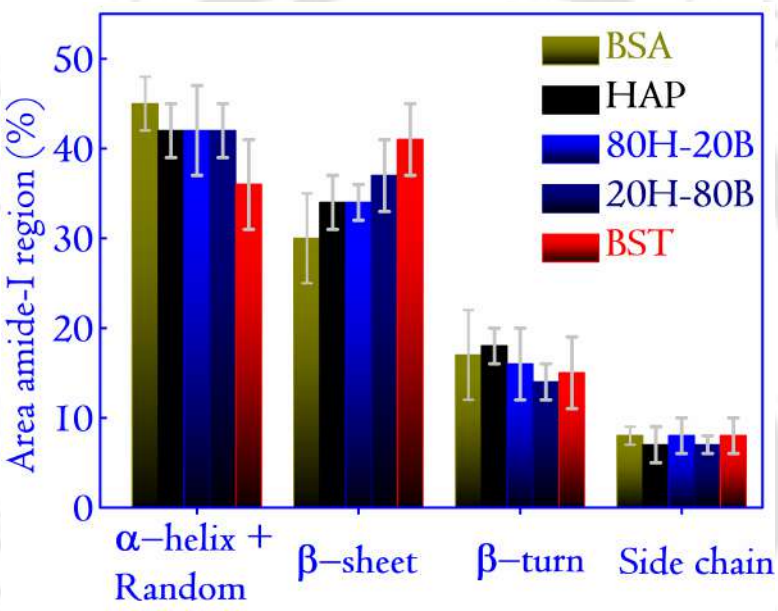


**Figure 5.18:** The variation in the content of secondary structures of BSA (in %) for various surfaces is considered for protein adsorption. The content of secondary structures are obtained by deconvoluting each of the FTIR spectra in Figure 6.17, and the deconvoluted graphs are shown in Appendix C (Figure C.3).

### 5.3.8 TEM analysis

Amongst the composites, $20H-80B$ exhibited the best dielectric properties. The $\epsilon_r$ of a composite directly demonstrates its ability to store electrical charges in it [86]. The higher value of $\epsilon_r$ usually implies a higher amount of charge storage capacity in the composite [65, 247]. Such a biocompatible composite that has charge storage capacity can be highly useful in designing electrets for biological applications [148]. Electrets are highly used in biological experiments for electrical mediation in tissue

growth, and anti-thrombogenic surfaces [152]. Moreover, the dielectric properties of a material measure its ability to interact with electrical fields. Since the role of the electric field is instrumental in mediating the growth of bone cells, under *in-vivo* environments, electrically active scaffolds could play a prominent role [230]. The composite with higher $\epsilon_r$ also undergoes high degree of polarization on exposure to external electric stimulation, as discussed previously. Additionally, the growth of bone apatite over any prospective implants is necessary for osseointegration, and as shown in Figure 5.4, the necessary apatite formation is obtained in the composites. However, the $20H - 80B$ composite that blends the properties of HAP and BST shows the $Ca/P$ ratio (1.59) of the bone apatite closest to the stoichiometric apatite (1.67). A higher degree of bioactivity is beneficial for our study as it would directly imply the superior bonding ability of the material with the tissue, thereby increasing the interfacial strength [246]. Based on the dielectric properties and bioactivity, the composite $20H - 80B$ is endowed with superior biological and physical properties and considered for further investigations. The choice of $20H-80B$ is also supported by the cell viability (highest for $20H - 80B$) and protein adsorption studies that display significantly high values for the specimen.

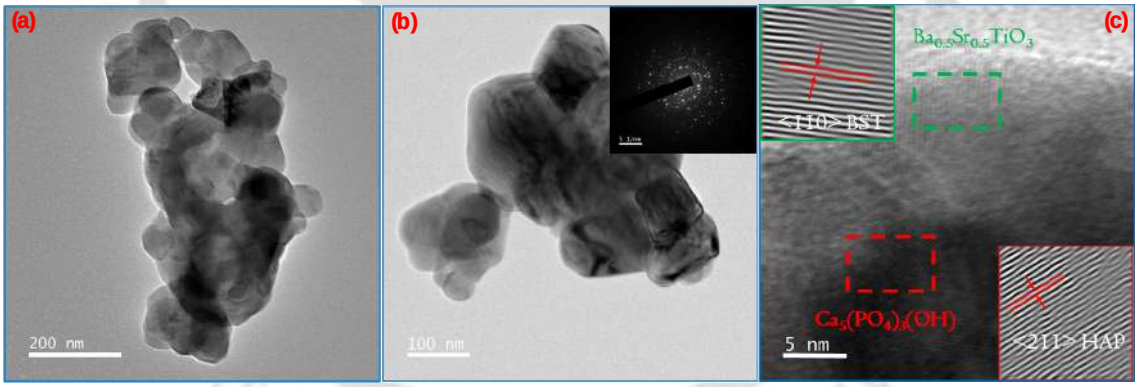


**Figure 5.19:** (a) The FETEM image of a selected region of $20H - 80B$ showing the morphology of monoliths (b) the images of a different region at higher magnification as well as the SAED pattern of the region (inset) and (c) the HRTEM images of a different region along with their IFFT images in the inset. The lattice planes from the monoliths can be identified from the HRTEM images, as shown in Figure 5.19(c).

Accordingly, to better understand the crystal structure, the FETEM analysis is carried out. In Figure 5.19(a and b), the images in two specific areas at two different magnifications have been shown along with the selected area electron diffraction (SAED) pattern of the composite in Figure 5.19(b). In Figure 5.19(c), the HRTEM images of the composite are displayed, and lattice fringes corresponding to both the precursors are seen corresponding to the (110) plane of BST and (211) plane

of HAP. The lattice fringes are generated by inverse fast Fourier transform (IFFT) of the regions indicated by the dotted rectangle, and the corresponding inter-planar spacing has been compared to the standard ICDD files of HAP and BST to identify the corresponding (hkl) planes. The planes also appear in the XRD analysis shown in Figure 5.2 and thus complements the XRD analysis. The high-resolution surface features of the composite are studied by scanning transmission electron microscope (STEM) mapping, which gives the distribution of various elements and has been included in Figure 5.20(a-g). The area selected for mapping analysis is chosen from Figure 5.19(b) that contained BST and HAP.

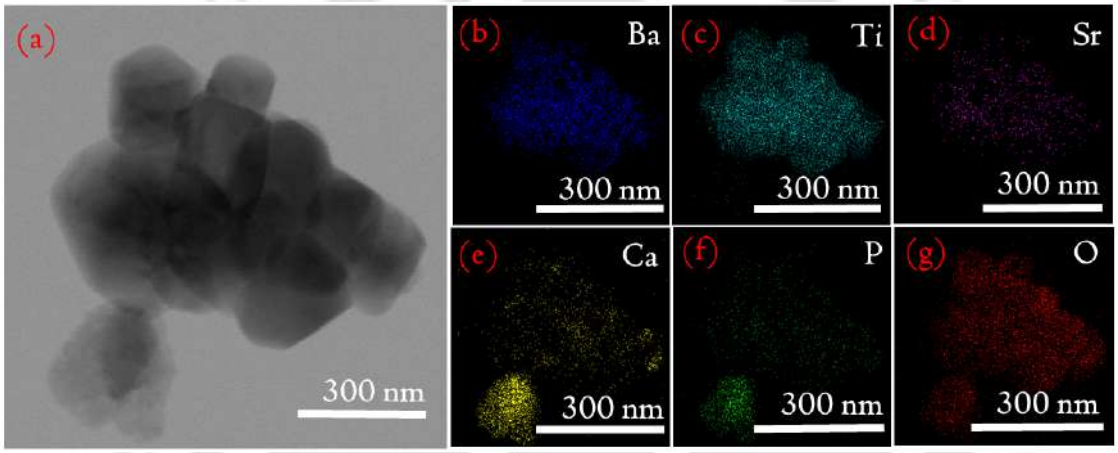


**Figure 5.20:** The STEM mapping of the region in Figure 5.19(b). The images show the distribution of different elements in the region. The distribution of the elements is shown in different colors, which helps to understand the presence of the elements in a different region of the STEM image. O being common to BST as well as HAP is distributed symmetrically.

In Figure 5.20(a-g), larger grains that are visible in the STEM image correspond to the BST grains. The HAP grains are distributed evenly, which can be confirmed from the distribution of $Ca$ and $P$ (Figure 5.20(e) and (f)). However, the presence of HAP is more prominent in the lower part, where the distribution is denser. The distribution proves that the HAP agglomerates in this region are quite expected as the grain sizes of HAP are in the nano-domain. The surface-to-volume ratio of the nanoparticles is usually large, leading to an increased level of surface energy. So, by agglomeration, an interface with lower energy is formed to reduce the surface energy, thereby stabilizing its present form.

## 5.4 Conclusions

In summary, a series of composites with varying concentrations of BST and HAP is synthesized successfully, and the composite with enhanced biophysical property is identified. Microstructural analysis of the composites and monoliths using XRD reveals details of the composite structures. An interesting observation is apparent: the formation of SAP in the composites due to the substitution of a small fraction of $Ca$ by $Sr$. The FESEM reveals numerous pores in the synthesized composites and monoliths, and the grain size derived from it is found to increase with the concentration of BST. All the specimens could induce bone apatite from SBF, which is desirable for biomedical applications. The capacity to nucleate bone apatite from SBF directly points at a high degree of bioactivity. The presence of more cationic and anionic sites in the composites favored biomineralization of bone apatite compared to pristine BST and HAP. This resulted in dense apatite growth in the composites compared to the monoliths.

The dielectric spectra of the specimens show the $\epsilon_r$ to lie in the range of 3-65, and low density of the specimens was identified as the significant factor in lowering the $\epsilon_r$. The modest values of $\epsilon_r$ can be harnessed to generate a polarized electric field, contributing to the expedited healing process of bone injury. The Cole-Cole formalism is adopted to model the response of the ceramic composites. The equivalent models predicted by the formalism adequately described the role of grain and grain boundaries in the electrical response of the composite to ac fields. It shows that the specimen $20H-80B$ had the highest value of grain capacitance in conjunction with the highest value of $\epsilon_r$ displayed previously, demonstrating the capability of storing the externally applied field by undergoing a high degree of polarization. This phenomenon is highly suited for scaffolds, which would retent the electrical stimulation (as Polarized fields), leading to faster bone regeneration. The Cole-Cole plots further revealed that the dipoles in the composites do not display a smooth movement under applied electrical fields but revealed the possibility of "jumps" or "hops". This is further verified by analyzing the conduction mechanism in the specimens. The conduction mechanisms active in the specimens helped gain a deeper understanding of the Mott's VRH active within the composites. Hopping of the active conducting species revealed that the jumps did not have a fixed range but varied with temperature. The $E_a$ associated jumps are also a varying function of temperature. Mathematical modeling of the dependence of $R$ and $W$ with temperature revealed a linear dependence. The range of hopping energy calculated for the

experiments related closely to theoretical studies on polarization mechanism that associated $OH$ flipping in the energy domain of 0.2-0.8 eV.

Protein adsorption studies on the specimens show the highest concentration of BSA adsorption on BST. The surface charges (zeta potential) on the ceramics dictate the composites' adsorption behavior, revealing a linear dependence (versus adsorbed mass for BSA). FBS adsorption showed a similar trend to BSA and is attributed to the major component (BSA) in FBS. The variation in the content of the secondary structures of BSA adsorbed on the ceramic surfaces is studied by the FTIR. The deconvolution results pointed at the presence of $\beta$-sheets, $\alpha$-helix, and $\beta$-turn in line with several studies conducted earlier. Based on the protein adsorption studies, we conclude that under *in-vivo* environments, the composite properties will be modulated by the collective behavior of the two monoliths. The exploration of the relationship between adsorbed proteins with $\epsilon_r$ and zeta potential generated a linear mathematical model into the complex interactions of proteins with biomaterials surfaces. Furthermore, the MTT studies revealed that specimens under investigation had cell viability above 100 %, a factor crucial for the cell proliferation ability of the composites. In this context, $Ba$, $Sr$, $Ti$ alongside HAP is also instrumental in new bone formation and enhancing cellular proliferation. Inspired by the results presented, we conclude the suitability of $20H - 80B$ for designing bioelectrets and electrically active scaffolds.

# Chapter 6

# Electroactive Scaffolds, Thin films of 20H – 80S, and bilayers of BST-HAP

This chapter discusses electroactive scaffolds made from 20 At.% $Ca_{10}(PO_4)_6(OH)_2$ (HAP) and 80 At.% $Ba_{0.5}Sr_{0.5}TiO_3$ (BST) ($20H-80B$), and 20 At.% HAP and 80 At.% $SrTiO_3$ (ST) ($20H-80S$), thin films of $20H-80S$, and BST-HAP bilayers' based on previous discussions. By analyzing the electrical and biological microstructural analysis, the suitability of the scaffolds and thin films is discussed for potential use in biomedical applications.

## 6.1 Introduction

The domain of "tissue engineering" encompasses life sciences and engineering methods to understand the structure-function relationship in mammalian tissues [272]. It advocates the role of 3D porous scaffolds for providing a suitable micro-environment for tissue and organ regeneration [273]. In this direction, scaffolds synthesized from electrically active ceramic composites have received significantly less attention in biomedical applications. Electrical properties like the $\epsilon_r$ of the bioceramics surface can help generate an electric field (internally by undergoing polarization, in which the dipoles align along the direction of the applied field by various mechanisms) on the application of an external electric field [86]. In clinical practice, the periodic

Parts of this chapter are published in A. Das, E. Barua, S. Mushahary, A. Bhardwaj, V. Saxena, P. Deoghare, and P. Dobbidi, Materials Letters **304**, 130668 (2021). The second part of the chapter is accepted in A. Das, S. Rabha, V. Saxena, A. Bhardwaj, L. M. Pandey, K. A. Emmanuel, and P. Dobbidi, *The role of electrical property in determining the response of 20H-80S composite thin films fabricated for biological applications* in Journal of Materials Science. The third part of the chapter is published as A. Das, V. Saxena, A. Bhardwaj, S. Rabha, L. M. Pandey, and P. Dobbidi, Surfaces and Interfaces **31, 102063 (2022)**

application of external (radio frequency) electric fields has proved to be an effective course of treatment in healing fractures, enabling faster bone regeneration [200]. Although the mechanism is not fully understood, it is believed that the application of electric fields can help in the biomineralization process by drawing the essential $Ca^{+2}$ and $PO_4^{3-}$ ions (which is the prime step towards the formation of new bones) from the *in-vivo* surroundings [200].

Using scaffolds designed from materials capable of generating an internal field in clinical settings (when the external field is not present) provides an advantage over other materials used in scaffolds generation. This expedited healing process will enable the patient to undergo faster recovery, significantly reducing the trauma associated with the complex medical procedures during recovery [90]. Inspired by the developments, this study explores scaffolds designed from electrically active bioceramics for bone tissue engineering applications. Scaffolds designed from composite bioceramics have been the main focus of the first part of this chapter. The scaffolds are designed from the composition, which is identified to provide superior properties as established in our earlier chapters 4 and 5 [88, 97, 274]. It was established previously that from the composites prepared out of ST/BST and HAP, the composite $20H - 80S$/or $20H - 80B$ as the specimen blended with superior biological and electrical properties. This chapter explores the composite scaffolds' fabrication and performance based on their biological properties prepared from the two specimens. To the best of our knowledge, the composite materials chosen for scaffold generation are relatively new, and it establishes the suitability of electrically active materials for scaffolds generation.

The second half of the chapter deals with composite thin films deposited over $Ti$ as implants in biomedical coatings. The coatings are developed from the composition identified as the one blended with superior electrical and biological properties (of ST and HAP). It is believed that Ti chosen for the coating process can provide stable fixation with reduced risk of implant loosening [275]. The biomechanical properties of $Ti$ are commensurate to natural bones. Further, the coating of bioceramic like HAP over the implants ensures the long-term clinical success of the implanted biomedical devices by providing an osseointegration interface between the implanted device and the bone tissue [276]. Such coatings on implants facilitate specific bonding to the host tissue [277]. The bonding occurs through a bone-like apatite layer formed over the surface of the implants in the living body [278]. The recent advances in biomedical research advocate electrically active coatings in implants that would lead to superior performance *in-vivo* [279, 280]. The interest in the exploration of

electrical properties for biological applications derives its root from natural systems (such as the human body) that uses exquisite properties like piezoelectricity and ferroelectricity to perform several metabolic functions [29, 143, 279]. Interestingly, the interaction mechanism of the electromagnetic field (EMF) in bone repair (or, for that matter, the role of electrical properties in natural systems) is yet to be understood fully by clinicians [281]. It leads to a random selection of the exposure parameters (relating to the EMF stimulation applied to the fractured regions), and as a result, the parameters such as the stimulated field magnitude, cell medium, and fracture gap are not properly optimized [200, 282].

To this extent, for a proper understanding of the interaction of the EMF with the implanted device, it is of prime importance to study the electrical properties of the coated electrically active layer. As the interaction between the EMF and the coated layer will be mediated by the electrical properties such as the leakage current and $\epsilon_r$, a thorough examination of such properties is essential to expedite the fracture healing process in bones. The interaction of the electric field with the coated layer would lead to dipolar polarization, which after removal of the externally applied field, would continue to generate polarized electric fields [33]. The larger the $\epsilon_r$, the higher the induced fields' magnitude after removing the external field. A similar concept is used in electrets made of biocompatible and bioactive materials used in self-healing bandages for wound healing [37, 144]. However, the polarized electric field is a non-permanent entity and decays with time. The decay of the dipolar electric field proceeds through the various conduction process active in the material. Therefore, the conduction mechanisms are essential to the service life of the polarized fields (indirectly) and possibly serve as a parameter that can help us estimate the subsequent exposure to EMF stimulation. Using the versatile radio frequency (RF) magnetron sputtering, we report thin films of $20H-80S$ be developing our sputtering target indigenously in our laboratory. Using $Ti$ and n-type $Si$ substrate to deposit the films, coatings of varying thickness to understand the fabricated thin films' microstructural, electrical, and biological properties were developed. The study is expected to help determine the future direction of biomedical implants (containing coatings of electroactive materials), which is currently limited to HAP coatings over commercial $Ti$.

In the last part of this chapter, we study bilayered thin films developed from BST and HAP. Traditionally, $Ti$ or $Ti$-based alloys ($Ti-6Al-4V$) have been the material of choice for implants [283]. However, the risk of implant loosening due to the generation of wear debris at the implant-bone interface has gradually declined the

use of such orthopedic implants [284]. Surface modifications have been suggested to diverge the complexities, and it has been found to yield satisfactory results. Thermal oxidation, carbon-based coatings, $TiN$ coating, and ion implantation techniques are frequently used surface modifications to tune the implant properties for effective functioning [285]. Plasma spraying has emerged as the industrially most favored process for coating biocompatible layers with the added advantage of being Food and Drug Administration (FDA) compliant [286]. However, the hurdles associated with the phase intactness have compelled researchers to constantly lookout for superior quality smart coatings to enhance the performances of implantable devices. Focus has driven towards electrically active layers that can augment the biological performances of the coatings *in vivo*. These smart coatings rely on electrical properties such as the $\epsilon_r$, loss mechanisms, and non-linear electrical properties like piezoelectricity and ferroelectricity to induce the growth of bone cells [279]. The electrically active layers are also developed for assisting electrical cell stimulations in provoking specific cellular responses, which in the case of bone implants involves the growth of osteoblasts [287].

Bilayered coatings on $Ti/Ti$ alloys have received significant attention due to their superior ability to generate high-quality medical coatings that, on the lab scale, have produced quite conducive responses [83]. In this regard, $BaTiO_3$ based bilayer coatings have been reported in quite a few articles, and these coatings are exceptionally bioactive and non-cytotoxic [84]. Other advantages of using bilayers over implants lie in the decreased material consumption of costly components like $Ba_xSr_{1-x}TiO_3$ or $BaTiO_3$, which are necessary for inducing electrical properties in the coatings. Using bilayers provides additional leverage of tuning the material properties by collectively incorporating the behavior of both the layers, thereby making the coatings suitable for *in vivo* environments [85].

In the case of bone implants, one component which has better bone regeneration ability will help in bonding with the surrounding tissues, and the other layer with superior electrical properties will aid in faster healing of the fractured region [85]. Thus bilayers are imperative for avoiding component failures and faster bone healing. In this context, the coating technology adopted for obtaining bilayers is vital to developing economically viable implants and has superior electrical and biological properties. A versatile method for obtaining such coating is the RF magnetron sputtering, which can produce high-quality uniform coatings over implants [86]. RF sputtering has the reputation of successfully coating complex layers with specific electrical properties for fabricating devices [86]. Therefore, in this chapter, using

RF sputtering, we report the fabrication of bilayers of BST and HAP over $Ti$ by maintaining a thickness ratio of 1:1. Incorporating $Sr$ into $BaTiO_3$ provides substantial advantages specifically in terms of $Sr$ ions, which have been recognized as an inorganic bioactive element capable of promoting proliferation, differentiation, and biomineralization of the osteoblasts [90]. The idea stems from our previous work on HAP and BST bulk composites for generating scaffolds [90]. BST has a high $\epsilon_r$ and its bilayer with HAP leads to an overall improvement of the resultant $\epsilon_r$. The enhancement in dielectric properties can tune the coated layers for undergoing polarization during electrical stimulations applied for healing fractures. Once polarized, such coatings can continue generating an internal electric field, thereby leading to rapid fracture healing [236]. The only factor determining the effectiveness of polarized layers is the "leakage current" that can disrupt the polarization leading to degradation of the internal field. This report measures the "leakage" in the bilayers and accordingly determines the conditions for maximizing the effect of the polarized field. In addition, the effect of stacking order was considered for understanding the variations in the physical properties of the deposited films. Such aspects of biomedical coatings are an emerging area of research and are presented for the first time that might lead to the design of advanced biomedical devices. We believe that the studies will incite further research into the application of bilayers in biomedical science.

## 6.2 Experimental Details

### 6.2.1 Preparation of Scaffolds

The composite scaffold is developed using $20H-80S/20H-80B$ and poly (methyl methacrylate) (PMMA) in 70:30 (W/W) ratio using the gas foaming technique. For the development of scaffolds, 70 wt.% of $20H-80S/20H-80B$ is dispersed in ethanol by stirring for 12 hours in a magnetic stirrer, with the simultaneous dissolving of 30 wt.% PMMA in acetone in a separate container. The PMMA solution is stirred vigorously for about 11 hours at room temperature to ensure the complete mixing of the PMMA. Thereafter, ammonium bicarbonate ($NH_4HCO_3$) is added to PMMA solution such that its concentration is maintained at 1:1 (W/W) ratio with $20H-80S/20H-80B$. The $NH_4HCO_3$ serves as the foaming agent. Finally, the PMMA solution containing $NH_4HCO_3$ is mixed with the $20H-80S/20H-80B$ solution, and the mixture is vigorously stirred for 24 hours followed by ultra-sonication of

2h to obtain a homogeneous viscous slurry. This viscous slurry is transferred into silicon rubber molds, oven-dried in a vacuum at 343 K for about 48 hours. During the process, heat liberates $CO_2$ from the scaffolds that introduce porosity to the scaffolds. The scaffolds are then carefully removed from the molds and sintered at 473 K for about 2 hours to densify the composite. The samples are allowed to cool inside the furnace for about 12 hours before taking them out. The resultant is a composite scaffold made out of $20H-80S/20H-80B$ and PMMA.

### 6.2.2 Thin films of 20H – 80S

#### 6.2.2.1 Fabrication of sputtering target and deposition of thin films

The starting reagents for the fabrication of the sputtering target, such as HAP and ST, are synthesized by the sol-gel and solid-state reaction processes. The details of the process are described in Chapter 2. The synthesized powders are then mixed in appropriate concentration ($20H-80S$) in a ball mill (Pulverisette 6, Fritsch, Germany) using acetone as the grinding media. Next, the powders are ground, dried, mixed with polyvinyl alcohol (PVA, Loba Chemie, India), and pressed in a hydraulic press (pressure applied: 25 $kg/cm^2$) of diameter 2 inches to obtain the sputtering target. The target is later sintered in a furnace at 1273 K for 3 h to achieve compaction.

The deposition of the thin films is done in an RF magnetron sputtering unit under $Ar$ ambiance at a deposition pressure of $3.5 \times 10^{-2}$ mbar. The deposition chamber loaded with the $20H-80S$ sputtering target is initially evacuated to a base pressure of $6 \times 10^{-6}$ mbar using the rotary and turbo molecular pump. $Ar$ is then introduced into the chamber, raising the pressure level to $3 \times 10^{-2}$ mbar (30 standard cubic centimeters per minute (SCCM)). At an RF power of 50 watts, the deposition starts, and three-thickness variation of films are deposited and considered for the study. The deposition is carried out in $Ti$ and $n$-type $Si$ substrates and analyzed for further characterization.

#### 6.2.2.2 Characterization and extraction of the properties of the sputtered films

The microstructural analysis of the thin films was carried out by analyzing the X-ray diffraction (XRD) patterns recorded in an X-ray diffractometer (TTRAX III, Rigaku, Japan). The XRD patterns were then matched to the standard International Center for Diffraction Data (ICDD) files. The thickness of the deposited

films was determined using a surface profilometer (Dektak 150, Vecco, USA). The morphology of the deposited films was viewed using field emission scanning electron microscopy (FESEM) (Sigma 300, Zeiss, Germany), and the composition of the deposited films was analyzed using the elementary dispersive X-ray spectroscopy (EDS) (Oxford, UK). The cytocompatibility analysis of the thin films was carried out using bone-like MG63 cell lines by following the protocol previously described by our group [288]. In brief, $5 \times 10^3$ cells/well were seeded in each of the wells, and they were incubated for 24 hours. Pre-incubation, cells underwent incubation in Dulbecco's modified eagle medium (DMEM), which was supplemented with 10 % fetal bovine serum (FBS) and 1 % penstrap. The entire process was carried out in a $CO_2$ incubator at 5 % $CO_2$ and 310 K, following which the thin films were introduced into the wells. The absorbance was then measured at 570 nm, and the cell viability was calculated by comparing it with control wells, for which the viability was considered 100 %. The dielectric properties of the thin films were analyzed in an LCR meter (1J43100, Wayne Kerr, UK). For extracting the dielectric properties, the thin films were deposited over platinized $Si$ substrates, fabricating a capacitor configuration (Metal-Oxide-Semiconductor (MOS) capacitor configuration) by depositing electrodes over the thin films. The surface topography of the deposited sputtered films was analyzed using the atomic force microscopy (AFM) (Cypher, Oxford Instruments, UK). Finally, the current density analysis was carried out using a Keithley parameter analyzer (4200A, Tektronix, USA).

The bioactivity of the specimens was analyzed with the simulated body fluid (SBF) experiments. The SBF was prepared following the protocol prescribed by Kokubo *et al.* [96] and the sputtered $Ti$ substrates were incubated in SBF for 12 days at 310 K. The SBF was refreshed every alternate day, and at the end of the incubation period (12 days), the substrates were washed in deionized water to remove any undissolved salt. Finally, the discs were dried at 333 K overnight and stored in a vacuum desiccator.

### 6.2.3 Deposition of bilayers of BST and HAP

The thin films were developed over the $Ti$ and $n$-type $Si$ substrates by RF sputtering. In this process, the sputtering chamber was initially pumped down to a pressure of $6 \times 10^{-6}$ mbar using a combination of rotary and turbo molecular pump [276]. Once the pressure levels were reached, $Ar$ and $O_2$ gas were introduced into the chamber to bring up the pressure levels to $3.5 \times 10^{-2}$ mbar. This was accomplished by purging

$O_2$ and $Ar$ using a mass flow controller (MFC) at 5 and 25 SCCM, respectively. The deposition pressure of $3.5 \times 10^{-2}$ mbar was maintained throughout the deposition period [276]. The depositions were carried out using RF sputtering (13.56 MHz) capable of accommodating two sputtering targets simultaneously. HAP and BST sputtering targets were used for the deposition. As detailed in the manuscript, two stacking orders were considered along with the corresponding monolayers for deposition. The monolayered HAP and BST films were deposited using an RF power of 50 and 40 watts, respectively, under the conditions described previously. For the bilayered films, the same deposition conditions was used, except for the deposition time. The schematic diagram of the deposition conditions is illustrated in Figure 6.1. For the BHBF film, the BST layer was first developed, and then the power to the BST cathode was turned off. Simultaneously, the RF power to the HAP cathode was switched on to continue the deposition of the HAP top layer. A precisely similar process was followed for the deposition of HBBF films with the bottom layer HAP developed over the substrates, first followed by the BST top layer. The films were subjected to an annealing treatment at 973 K following deposition.

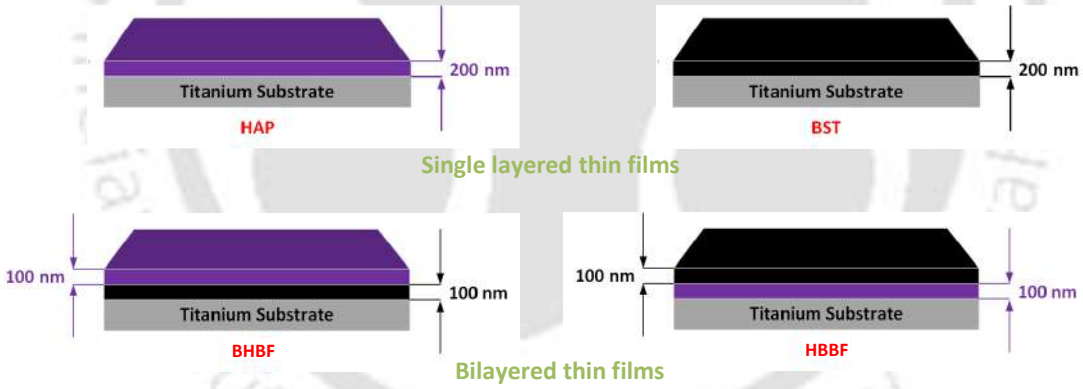


**Figure 6.1:** Illustration showing the monolayered thin films of HAP and BST of thickness 100 nm each. The films are deposited by maintaining a stacking order and thickness ratio of 1:1. The row in the bottom shows the bilayered films of HAP and BST, with their nomenclatures and respective thicknesses. The transmittance of the films is shown in Appendix D (Figure D.1), which helps determine the approximate thickness of the deposited films. BST stacked at the bottom with HAP at the top is named BHBF, and the reverse stacking order is named HBBF. In the acronym, the first two letters B and H stand for BST and HAP, and the last two letters B and F stand for bottom and front, respectively.

The $n$-type $Si$ substrates used in the deposition were specifically used for extracting the electrical properties. The $n$-type $Si$ substrates are conducting and facilitate the development of MOS configurations necessary for the electrical properties. The

microstructural, interfacial, and biological properties are extracted from the films deposited over $Ti$.

#### 6.2.3.1 Preparation of Sputtering targets

The development of sputtering targets, specifically BST and HAP, are detailed below. BST ceramic powders are initially developed for generating the sputtering target using the solid-state reaction methodology. The powder BST, is developed from $BaCO_3$, $SrCO_3$ and $TiO_2$ powders using the following reaction

$$BaCO_3 + SrCO_3 + 2TiO_2 \rightarrow 2Ba_{0.5}Sr_{0.5}TiO_3 + 2CO_2 \uparrow \tag{6.1}$$

A similar technique was followed for fabricating the HAP sputtering target. However, in this case, the powder was generated by sol-gel process using $Ca(NO_3)_2.4H_2O$ (Sigma Aldrich, USA) and $P_2O_5$ (Sigma Aldrich, USA) as the precursors. The starting powders are weighed in order to maintain the $Ca/P$ ratio 10:6. The measured powders are added separately in two 25 mL Ethanol (Merck, India) containing beakers and stirred vigorously using magnetic stirrers (Tarsons, India). The stirring is continued for 30 minutes, following which the two solutions are mixed, slowly adding one component to the other dropwise. This is done to ensure that there is no precipitation of the components. After completing the addition, the beaker is stirred continuously for 24 hours, following which the stirring is stopped, and the beaker is left undisturbed for another 24 hours. The contents of the beaker are then dried in a hot air oven at 363 K overnight, during which the gel transforms into powder. The powder is finally calcined at 773 K for 2h to ensure phase formation. The process of transforming the powders to sputtering targets is the same as discussed previously.

#### 6.2.3.2 Characterization of the fabricated surfaces

The fabricated thin films were subjected to XRD (SmartLab, Rigaku, Japan). The X-ray used a wavelength of 1.5406 $\mathring{A}$ to generate the diffraction spectra. The X-rays were made incident on the thin film substrates at an incident angle of 0.5°, scanning the specimens at 5°/min and collecting the photons at a step size of 0.03°. The FESEM (Sigma 300, Zeiss, Germany) were obtained over specimens deposited on n-type substrates, and the FESEM images were also used to determine the grain size of the specimens using ImageJ. The EDS was recorded in an attachment associated with the FESEM (Oxford, UK). The current-voltage characteristics were measured in Keithley Parametric analyzer (4200A, Tektronix, USA). The dielectric

spectra were recorded in an LCR meter that facilitates the temperature as well as frequency variation simultaneously in the range of 298-673 K and $10 - 10^6$ Hz, respectively. The contact angle (CA) measurements (HO-ED-M-01, Holmarc, India) were carried out using the sessile drop method in which deionized water (DI water) and diiodomethane (DIM) were used for recording the CA. The CA was recorded at room temperature (298 K), and the surface energy calculations were carried out as described in the text.

For the bioactivity analysis of the specimens, the specimens were incubated in SBF for 12 days at 310 K. To ensure that the ionic concentration of the SBF was maintained at a constant level, the solution was refreshed every alternate day. On the 12th day, the specimen was lifted from the SBF solution, rinsed in deionized water to remove the salts, and finally dried in a hot air oven at 333 K for 24h. The FESEM micrographs were then recorded to analyze the growth of the apatite structure.

The cytocompatibility analysis was carried out using bone-like MG63 cell lines. $5 \times 10^3$ cells were incubated in each well for 24 hours. Prior to incubation, they were considered for another incubation process in DMEM, where it was supplemented with 10% FBS and 1% penstrap. The process was accomplished in a $CO_2$ incubator at 5% $CO_2$ and 310 K, following which the thin films were introduced into the wells. Finally, the absorbance was recorded at 570 nm, and the cell viability was measured by comparing it with control wells, for which the cell viability is considered 100% [289].

## 6.3 Results and Discussions

### 6.3.1 Scaffolds

#### 6.3.1.1 Microstructural and Biomineralization properties

The XRD of the synthesized monoliths and the composites are shown in Figure 6.2. The phase identification of the (hkl) planes is explained using the ICDD files 39-135 (for BST), 009-0432 (for HAP), and 073-0661 (for ST). All the reflections in the composites correspond to the different (hkl) planes of the monoliths, and selected (hkl) planes are shown indexed in Figure 6.2(a). There is no reflection corresponding to any phase that the reaction between the monoliths might form. The reflections are sharp and intense that are indicators of high crystallinity of the starting powders. Additionally, all the (hkl) planes seen in case of $20H - 80S$ in

Chapter 3, and $20H - 80B$ in Chapter 4 are also evident in the present scenario.

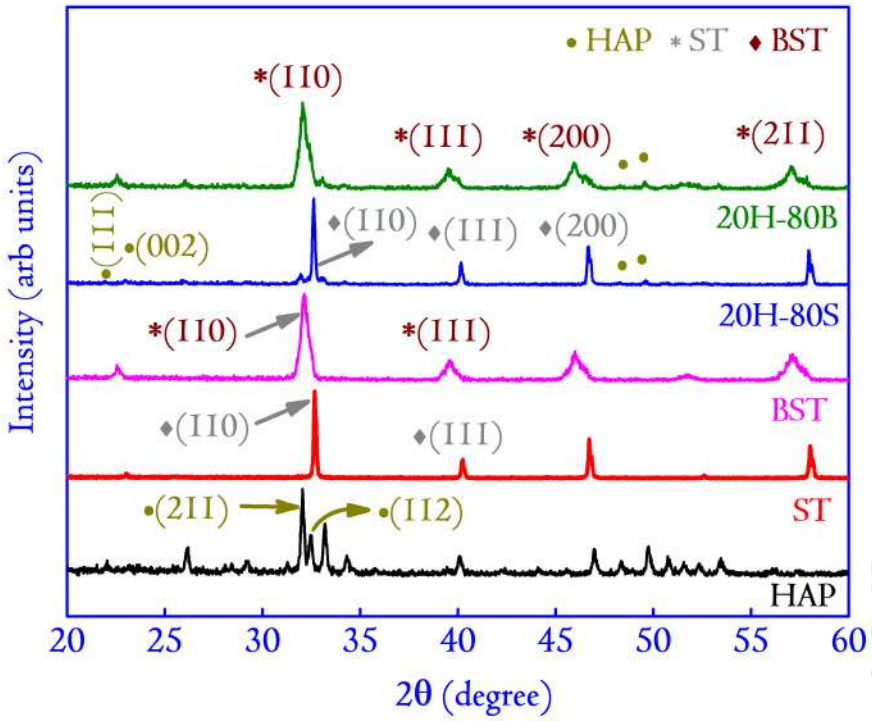


**Figure 6.2:** The XRD pattern of the composites and their monoliths. The (hkl) planes are sharp and highly intense, indicating the high crystallinity of the synthesized specimens.

The microstructure of the starting powders is shown in Figure 6.3. The grain sizes are calculated to be 110.3 ± 5.1 nm and 92.2 ± 4.5 nm for $20H - 80B$ and $20H - 80S$, respectively. The porosity in $20H - 80B$ from Figure 6.3(a) is seen to be slightly higher than the $20H - 80S$. The larger sized grains in $20H - 80B$ contribute to the composite scaffold's higher porosity, which is calculated to be 79.4 ± 0.8% and 86.1 ± 1.1% for $20H - 80S$ and $20H - 80B$ scaffolds, respectively (Table 6.1). The presence of adequate porosity in the scaffold is paramount for successful osteogenesis and apatite nucleation ability, and in this case, it satisfies the minimum value of 60-80% necessary for cell growth, and adhesion [273, 290]. The apatite deposited over the surface of the scaffolds is shown in Figure 6.3(a) and (b) to support the proposition. The apatite growth is dense in both cases and contains micropores that are characteristic of the bone apatite. The apatite layer's EDS shows that in $20H - 80B$, it is 1.64, close to 1.67 for stoichiometric HAP. This points to the superior biomineralization capability of the $20H - 80B$ composite scaffolds. The superior biomineralization capability projects $20H - 80B$ as the scaffold with better properties for clinical applications. For further verification of the proposition, we

present the biological properties of the scaffolds in the following section.

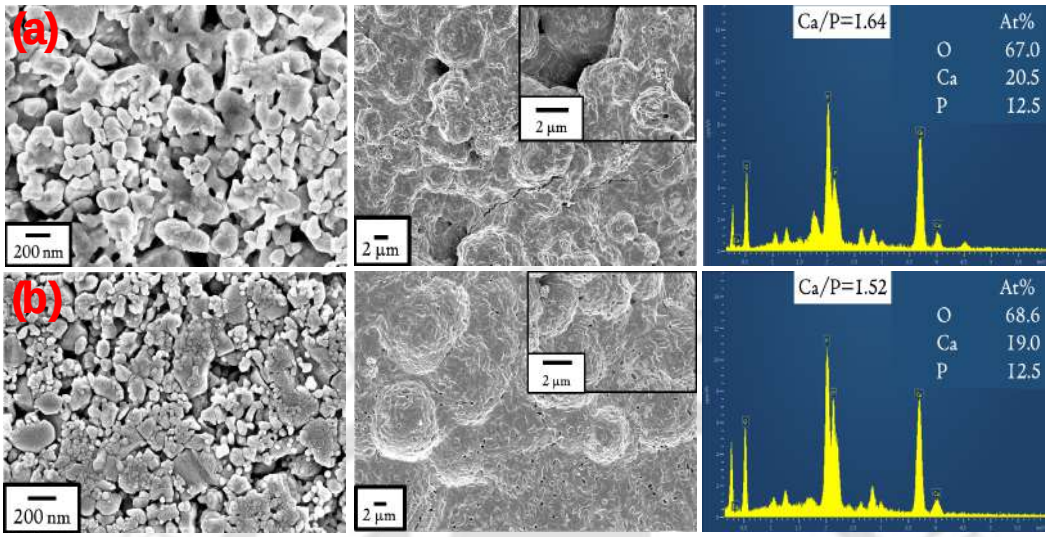


**Figure 6.3:** In (a), the FESEM of $20H-80B$ and the growth of bone apatite in SBF over the scaffolds are shown. The EDS in the first row corresponds to the apatite deposited over $20H-80B$. In 3(b), the micrograph of $20H-80S$ is shown. The bone apatite growth and its EDS are shown in the same row. In (a) and (b), the FESEM images correspond to the starting powders following calcination at 773 K for 2 h.

**Table 6.1:** The variation in the grain size and porosity in the scaffolds.

| Specimen | Grain size | Porosity (%) |
|---|---|---|
| 20H-80B | 110.3 ± 5.1 | 86.10 ± 1.10 |
| 20H-80S | 92.2 ± 4.2 | 79.4 ± 0.80 |

#### 6.3.1.2 Protein adsorption and Cyto-compatibility analysis

Proteins are the key mediators in the interaction of the biomaterial in the physiological microenvironment [100]. In this direction, BSA adsorption (500 $\mu$g/ml) is carried out at 298 K for 1 hour at static conditions. The protein adsorption of the scaffolds are shown in Figure 6.4(a). It is found that the $20H-80B$ scaffolds show higher adsorption concentration (46.3 ± 5.56 $\mu$g/ml) and mass (595.9 ± 71.5 ng/mg) compared to the $20H-80S$. This is attributed to a higher porosity in $20H-80B$. A higher porosity leads to a larger specific surface area and improves scaffolds' permeability, leading to higher protein adsorption [291, 292]. Also, the cytocompatibility analysis of the prepared scaffolds is performed, and the results are

shown in Figure 6.4(b). MG63 cell lines chosen for the cytocompatibility analysis share characteristics such as expression of most integrin subunits, an organization similar to internal cellular structures, and adhesion to physio-chemically modified surfaces similar to primary human osteoblasts [293–295]. The MG63 cell lines also provide information about the scaffold-bone cell interactions and bone regeneration ability. Additionally, the capacity to retain their differentiated phenotype and bio-functionality over numerous passages under in-vitro culturing environments along with faster cell division time (30-36 hours) makes it a primary candidate amongst the researchers for analysis of novel biomaterials [296, 297]. However, the major drawback of using MG63 cell lines remains its faster proliferation rate than osteoblasts, and hence, the results differ slightly in *in-vivo* investigations [297]. However, the advantages outweigh the drawbacks and have become a preferred choice for short and long-term analysis in bone tissue engineering applications. The cells reflected 94% and 98% excellent cell viability for day 1 for $20H-80S$ and $20H-80B$ scaffolds, respectively. The cell viability is found to increase with time, and the cell viability is 96 and 98% after three days of incubation. No further change in the cell viability is observed after day 5. The increased cell viability reflected no toxicity by the scaffolds compared to the control cells. In conclusion, cell viability >90% elucidates the high cytocompatibility of the scaffolds for biomedical applications.

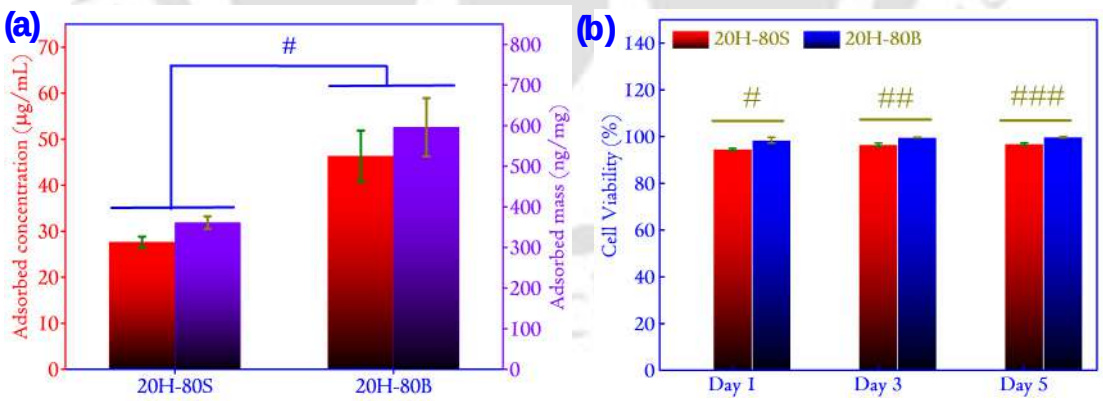


**Figure 6.4:** (a) Protein adsorption data of the $20H-80S$ & $20H-80B$ scaffolds. The statistical significance of the specimens is denoted by # that signifies p<0.0001.(b) Cyto-compatibility analysis of the scaffolds for different periods. The cytocompatibility is compared with the control that has cell viability of 100 %. The statistical significance denoted by # represents p<0.01, ## represents p<0.005, and ### represents p<0.001.

### 6.3.2 Thin films of 20H – 80S

#### 6.3.2.1 XRD analysis

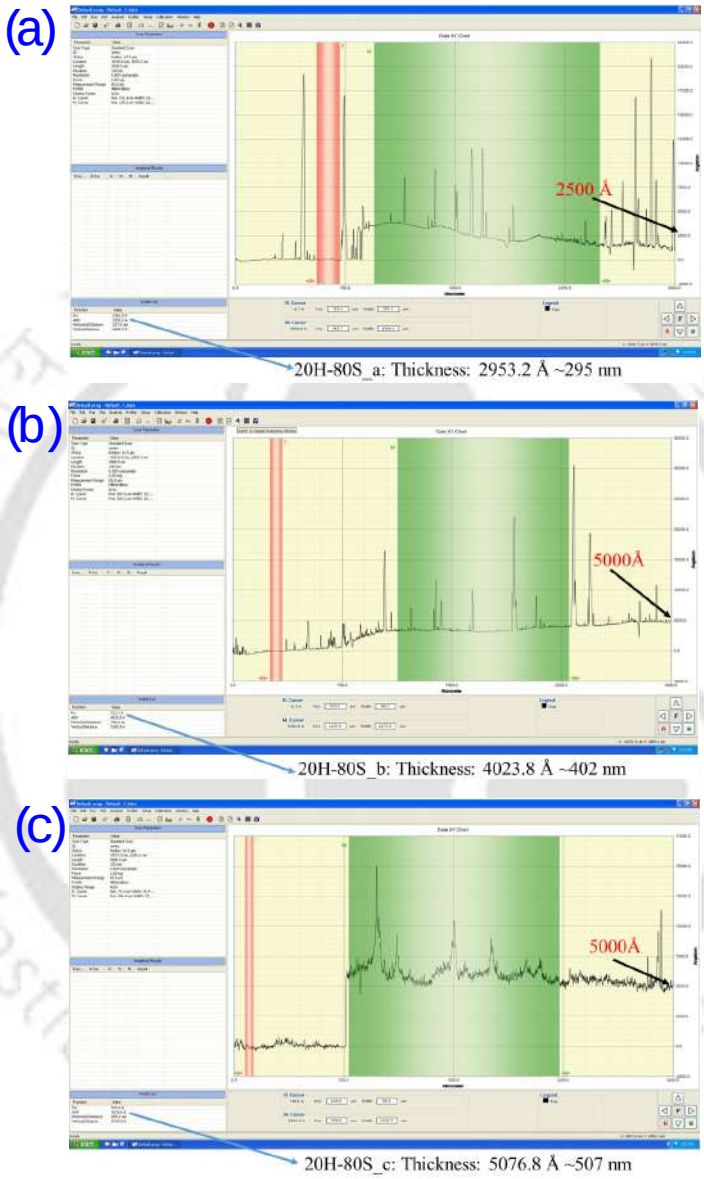


**Figure 6.5:** The variation in thickness of the thin films (a) $20H-80S\_a$, (b) $20H-80S\_b$ and (c) $20H-80S\_c$. The thickness measured by the surface profilometer is 295 ± 15 nm ($20H-80S\_a$), 402 ± 20 nm ($20H-80S\_b$), and 507 ± 23 nm ($20H-80S\_c$).

We consider three variations of the thin film thickness for this study. The thickness are varied as 295 ± 15 nm ($20H-80S\_a$), 402 ± 20 nm ($20H-80S\_b$), and 507 ± 23 nm ($20H-80S\_c$) and their properties are analyzed (shown in Figure 6.5). In this direction, the XRD spectrum of the sputtered composite films is presented in

Figure 6.6. The post-deposition annealing treatment at 973 K for 2 h induced crystallinity in the deposited thin films, which are, however, nanocrystalline indicated by the appearance of broad peaks [288]. In all the films, the (hkl) planes corresponding to ST and HAP phases are observed. The most intense XRD corresponding to the (110) plane belongs to the ST due to the larger concentration of ST in the composition. This highly illustrates the role of RF sputtering in depositing stoichiometric thin films similar to the composition present in the sputtering target [92]. Also, with increasing deposition time, there are an enhancement in the crystallinity of the observed (hkl) planes, which can be attributed to an increase in the number of lattice planes in the deposited thin films. It is observed that with increasing deposition times, a large number of atoms from the target disembark upon the nucleation sites created by the incoming atoms deposited previously. These developed nucleation sites are thermodynamically favorable sites for the incoming atoms to settle down, thereby contributing to an increase in thickness with time [276, 288].

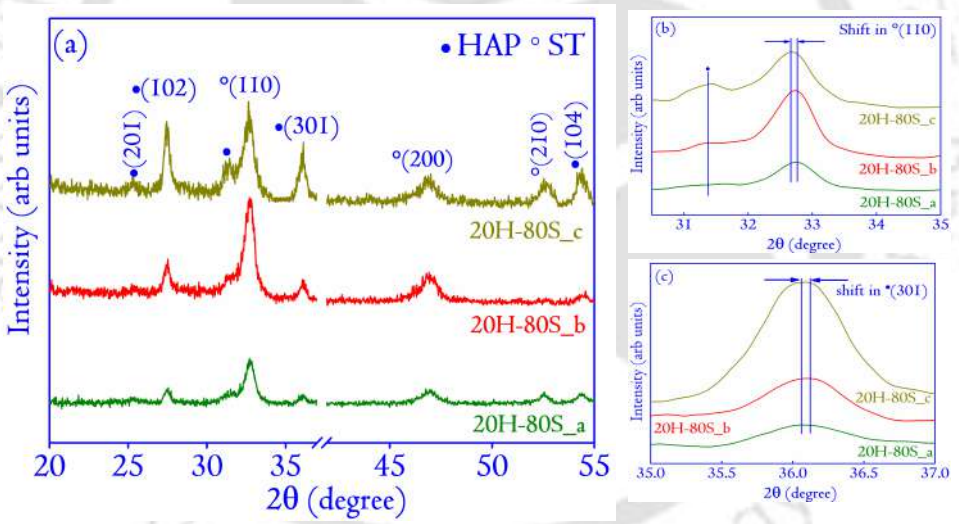


**Figure 6.6:** (a) presents the XRD pattern of the deposited thin films corresponding to $20H-80S\_a$, $20H-80S\_b$, and $20H-80S\_c$. The XRD films are annealed at 973 K for 2 h to induce crystallinity. The break in the XRD patterns masks the reflections from the $Ti$ substrates. (b) and (c) represents the shift in the XRD patterns corresponding to (110) plane of ST and (301) plane of HAP. The shift is systematic and is towards the lower Bragg angles with increasing thickness. The systematic shift towards the lower Bragg angles is due to the release of strain in the thin films with increasing thickness, as described elaborately in the text.

The XRD patterns are indexed to the hexagonal HAP and cubic ST according to the International Centre for Diffraction Data (ICDD) card no. 00-009-0432, and 073-0661, respectively. In Figure 6.6(b) and Figure 6.6(c), significant shifts in the

(hkl) planes of the thin films are seen. The shifts are attributed mostly to the lattice mismatch between the substrate and the deposited thin films (a=2.95 $\mathring{A}$, c=4.68 $\mathring{A}$, as compared to a=9.41 $\mathring{A}$, c=6.88 $\mathring{A}$ for HAP, and a=3.90 $\mathring{A}$) that creates a residual strain [276]. The strain analysis in the deposited films is done using the Williamson-Hall (WH) plots, and the crystallite sizes of the deposited films are also extracted from the same [132]. The mathematical form of the WH plot can be derived assuming that the broadening in the XRD peaks is due to the independent contributions of the crystallite size and the strain

$$\beta = \beta_{size} + \beta_{strain} \tag{6.2}$$

where, $\beta_{size} = \frac{k\lambda}{D\cos\theta}$ is the Scherrer equation (with $D$ representing the crystallite size and $k$ is the Scherrer constant (0.94) assuming nearly spherical crystallites are formed) and $\beta_{strain} = 4\epsilon\tan\theta$ (with $\epsilon(= \frac{\delta l}{l})$ representing the strain predominantly due to the lattice mismatch). By a slight modification, we obtain

$$\beta = \frac{k\lambda}{D\cos\theta} + 4\epsilon\tan\theta \tag{6.3}$$

$$\beta\cos\theta = \frac{k\lambda}{D} + 4\epsilon\sin\theta \tag{6.4}$$

which is an equation of a straight line, the slope ($\epsilon$) denoting the strain and intercept ($\frac{k\lambda}{D}$) representing the crystallite size of the thin films. A plot of $\beta\cos\theta$ versus $4\sin\theta$ for all the specimens are shown in Figure 6.7. The strain is highest for $20H-80S\_a$ and decreases with the increasing thickness of the deposited films. It is mentioned previously that the lattice parameters for the substrate ($Ti$) is comparatively smaller than HAP and ST present in the target. Thus, at the onset of the deposition, the incoming atoms from the sputtering target would grow according to the substrates' lattice parameters, which leads to a significant strain in the initial layers of the deposited films. With increasing thickness, the films release this strain by growing according to their lattice parameters, and a monotonic drop in the strain is observed. Das *et al.* [276] and Pattipaka *et al.* [298] also observed such behavior of thin films and is common in films deposited by sputtering. The calculated crystallite size in the films are from $21.3 \pm 3.2$ nm and gradually increases to $23.9 \pm 3.2$ nm and $26.3 \pm 3.6$ nm for $20H-80S\_b$ and $20H-80S\_c$. Such increases in crystallite size with increasing thickness are in conjunction with results reported previously in thin films deposited by the same technique [132]. For lower deposition times, the substrate temperature produced due to the bombardment of the sputtered species

is low due to lesser deposition times. This leads to small and discontinuous islands with lesser mobility of the sputtered species causing less crystallinity (and hence small crystallite size). However, increasing the deposition times, the temperature of the substrates becomes higher due to continuous bombardment leading to significant diffusion of the sputtered species, improving the crystallinity (crystallite size) along with the thickness of the sputtered films [91]. The WH plots, along with the crystallite sizes, are shown in Figure 6.7 for the thin film of different thicknesses.

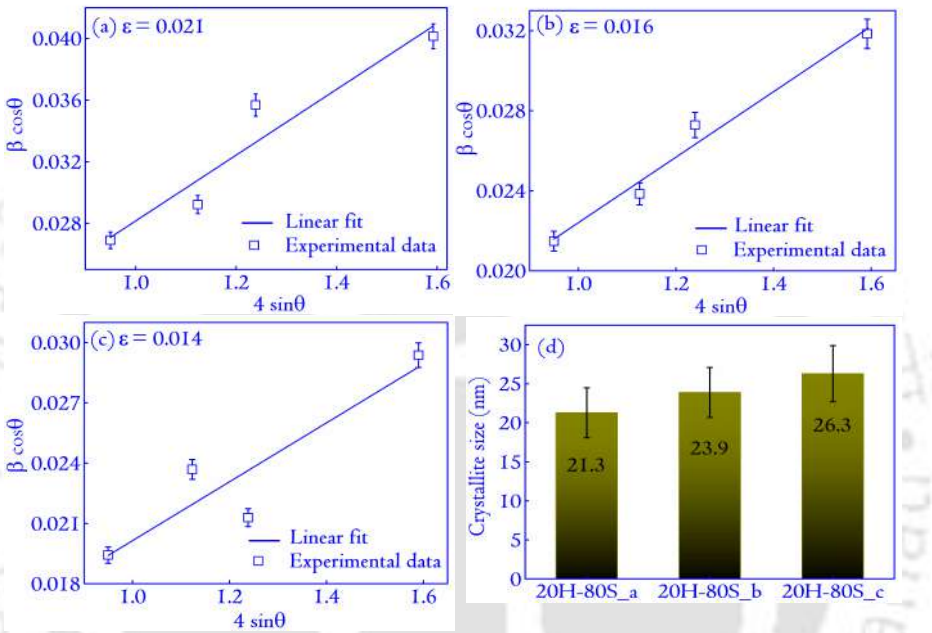


**Figure 6.7:** (a) The variation in the strain of the thin films deposited for (a) $20H-80S\_a$, (b) $20H-80S\_b$, and (c) $20H-80S\_c$. The strain is lowest for the film of the highest thickness. The existence of strain in the thin films is attributed to the lattice mismatch between the substrate and the deposited films. In (d), the variation in the crystallite size of the specimens is plotted. The smallest crystallite size is obtained for the film of lowest thickness $20H-80S\_a$, and it is related to the highest strain present in the thin film.

#### 6.3.2.2 Surface Morphology and AFM analysis

The FESEM images of the deposited films are shown in Figure 6.8. The micrographs show elongated grain-like morphology in all the films, with the grains distributed homogeneously throughout the substrates. The grain-like morphology is in agreement with previous reports using the same deposition technique [288]. The uniformly distributed grains over the substrates are helpful for improved electrical properties of the thin films, and the uniformity can be partially attributed to the post-deposition annealing conditions.

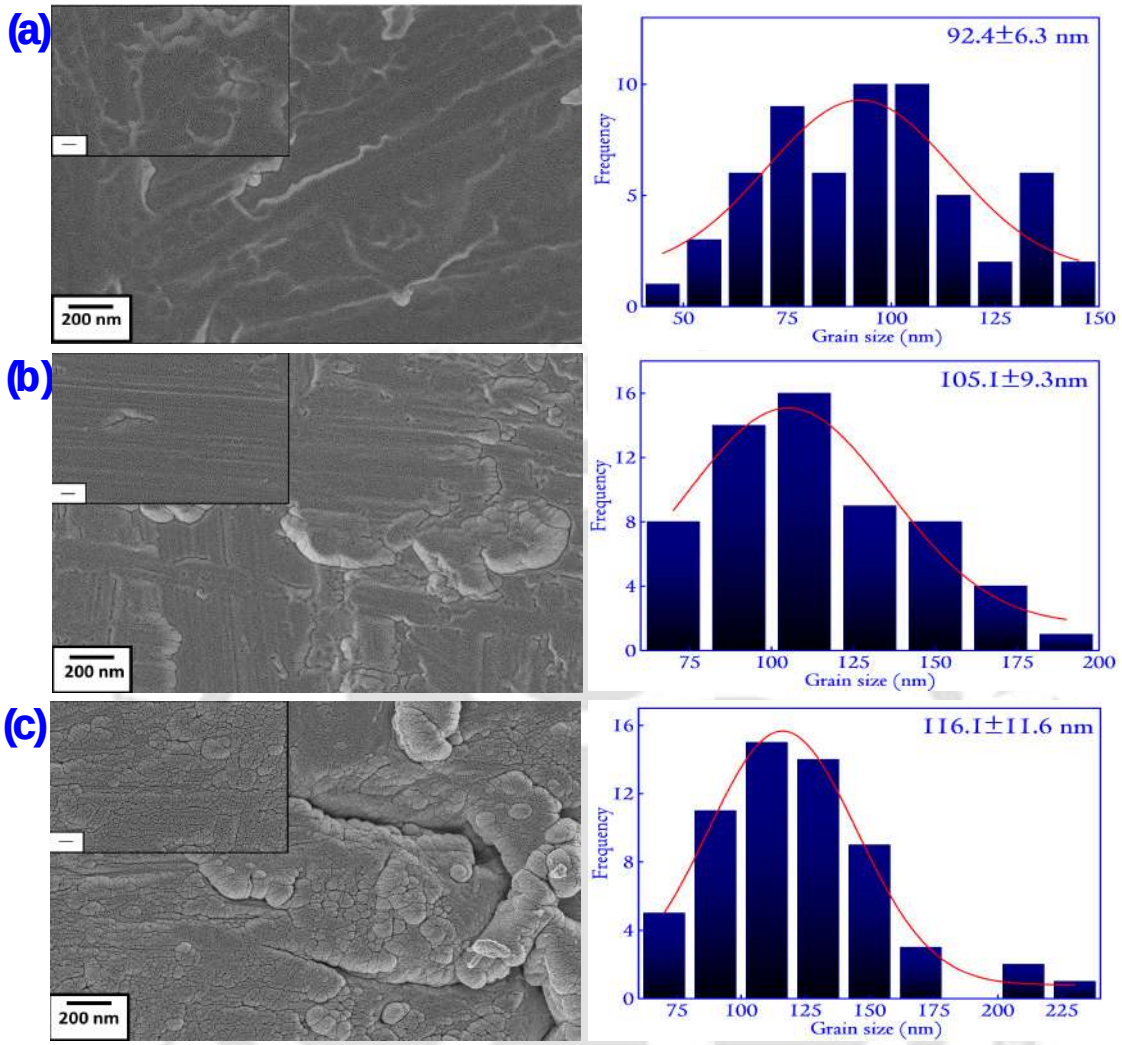


**Figure 6.8:** (a) The FESEM images of the deposited films are shown that corresponds to (a) $20H - 80S\_a$, (b)$20H - 80S\_b$, and (c) $20H - 80S\_c$ and their grain histograms. The grains are elongated with a grain-like morphology and are homogeneously distributed over the substrates. The most petite grain sizes are observed for $20H - 80S\_a$ (92.4 ± 6.3 nm) and the largest grain size for $20H - 80\_c$ (116.1 ± 11.6 nm), which also has the highest thickness implying a direct relationship between the thickness of the films and grain growth. For $20H - 80S\_b$, the grain size is 105.1 ± 9.3 nm. The scale bar in the inset of each figure corresponds to 200 nm.

The grain size of the particles is evaluated and is found to be following the same trend as the crystallite size. The increasing grain size with thickness also complements the XRD patterns, where an enhancement in the intensity of the (hkl) planes is observed. Increasing deposition times allows sufficient atoms to deposit over the nuclei, which leads to grain growth [299]. It has been mentioned previously that the films are annealed at 973 K for inducing crystallinity. As the amorphous

films tend to have more significant dissolution rates, they can have adverse effects on coatings intended to be used in implants [300]. This aptly justifies the role of annealing in thin films proposed to be used for biomedical applications. Additionally, the sputtered thin films reportedly achieve crystallinity only after annealing at 773 K, and our group has reported previously that 973 K is the temperature appropriate for the intended applications [276].

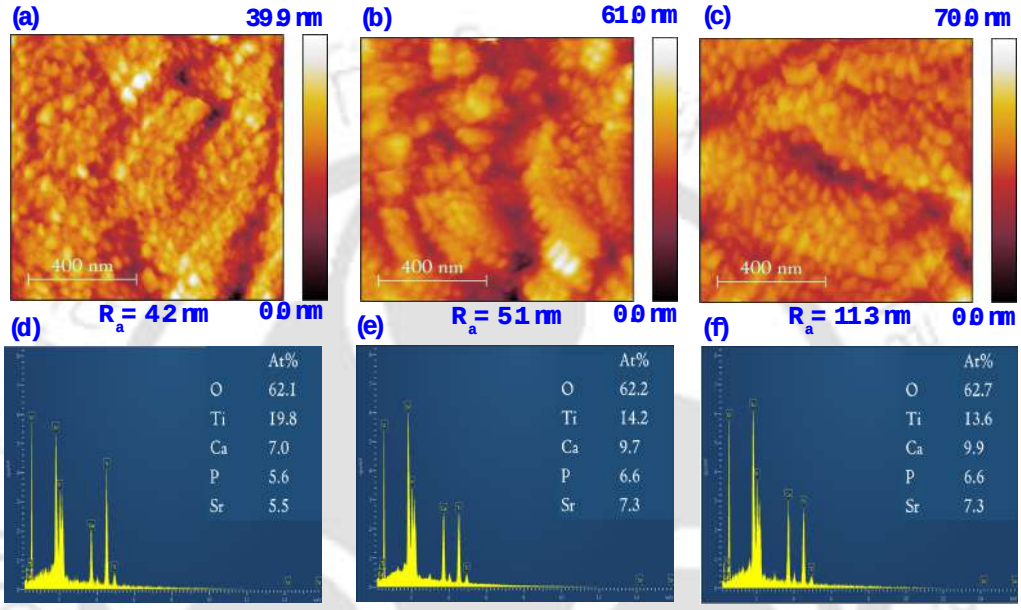


**Figure 6.9:** (a) The AFM images of the sputtered thin films of different thicknesses are shown that corresponds to (a) $20H - 80S\_a$, (b) $20H - 80S\_b$, and (c) $20H - 80S\_c$. The roughness parameter $R_a$ is seen to increase with the thickness of the thin films. The elongated grain-like morphology evident from the FESEM images is also seen to be homogeneously distributed over the surface of the sputtered thin films. The EDS spectra of the thin films corresponding to $20H-80S\_a$, $20H-80S\_b$, and $20H-80S\_c$ are shown in (d), (e), and (f), respectively. From the EDS spectrum, it is observed that with increasing deposition times, the At.% of $Ti$ decreases, and it might be related to the weak substrate effect, which is minimized at higher thickness.

The FESEM micrographs are complemented by the AFM images of the specimens for a scan area of 1 $\mu$m $\times$ 1 $\mu$m for the three thicknesses as shown in Figure 6.9. The $R_a$ parameter of the films is found to increase with the thickness of the thin films. The increase in $R_a$ factor of the thin films with thickness is characteristic of RF magnetron sputtered thin films and is in line with reports reported previously by several groups [299]. The elongated grain-like morphology obtained from the FESEM micrographs is also seen in the AFM images. In similar lines to the FE-SEM, the increase in grain size with thickness is also apparent from the AFM images where, with increasing thickness, bigger-sized grains are observed. The EDS of the

deposited films is also shown along with the AFM images. Regarding the $Ca/P$ ratio of the thin films, it is observed that for $20H-80S\_a$, the ratio is 1.2, which improves to 1.4 for $20H-80S\_b$, finally reaching 1.5 for $20H-80S\_c$. This improvement in thickness can be attributed to an increasing amount of $Ca$ and $PO_4$ with an increased thickness. A similar improvement in the $Ca/P$ ratio of the thin films was earlier reported by Behera *et al.*[288]. At lower thickness, the substrate ($Ti$) also contributes to the At.% and gradually decreases with an enhancement of the thickness. This results in lowering the $Ti$ concentration in the EDS and detection of more elements from the coating, as shown in Figure 6.9.

#### 6.3.2.3 Bioactivity analysis

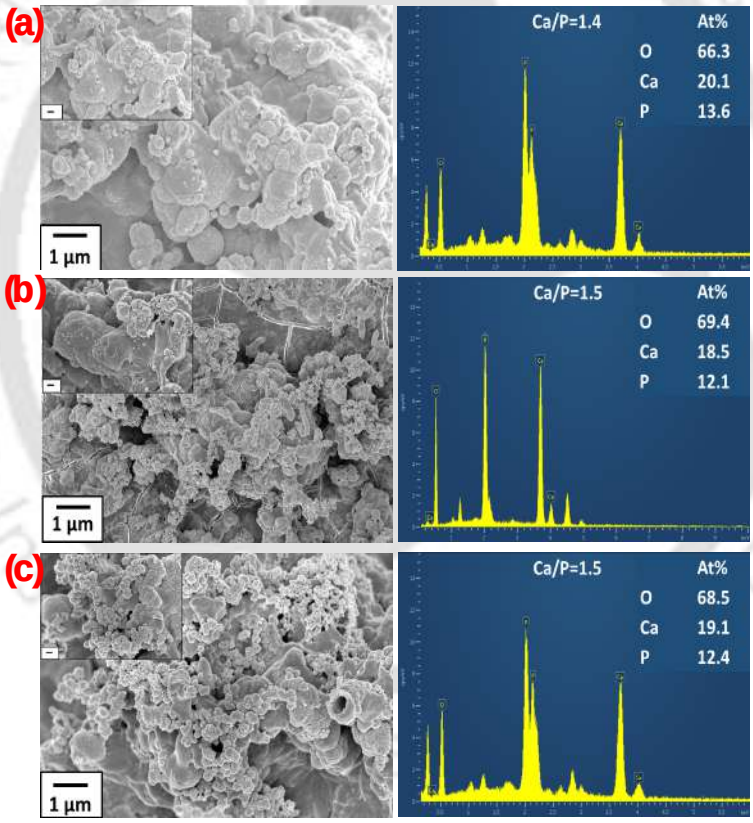


**Figure 6.10:** The demonstration of the globular bone-like apatite layers over the surface of the sputtered thin film of different thicknesses *viz,* (a) $20H-80S\_a$, (b) $20H-80S\_b$ and, (c) $20H-80S\_c$. A dense apatite layer growth is observed in all the films and numerous pores characteristic of the bone-like apatite layer. Corresponding to the FESEM images, the EDS of the apatite layers is also presented, showing a substantial improvement of the $Ca/P$ ratio with increasing thickness. The deviation of the $Ca/P$ ratio in bone-like apatite layers is attributed to trace amounts of alkaline earth ions ($Mg$, for instance) in $Ca$ sites.


**Figure 6.11:** The mechanism of the growth of bone-apatite over the sputtered films deposited over $Ti$ substrate. On incubation in SBF, the films develop a negative surface charge. This negative surface charge are responsible for attracting the $Ca^{+2}$ charges from SBF. The $Ca^{+2}$ further attracts the negatively charged $(PO_4)^{3-}$ ions that undergo hydrolysis to form a bone apatite layer.

The capability of the sputtered films to induce bone-like apatite is indicative of the superior bioactivity of the films [123]. Globular apatite layers are formed upon 12 days of incubation with constant refreshing of the SBF solution every alternate day in all three variants. The FESEM micrographs depicting the growth of apatite layers are demonstrated in Figure 6.10. Dense apatite layers are observed in all the films with numerous pores characteristic of bone-like apatite structures [301]. The EDS analysis of the globular apatite structures has shown that the $Ca/P$ ratio in all the thin films is less than 1.6, which characterizes the bone-like apatite layers. The bone-apatite layers also contain trace amounts of alkaline earth metal ions other than $Ca$ essential for various metabolic processes inside the living body. These trace ions occupying the $Ca$ sites reduce the $Ca/P$ ratio from the stoichiometric 1.67 [302]. However, the $20H-80S\_b$ and $20H-80S\_c$ show an improved $Ca/P$ ratio closer to the stoichiometric HAP, pointing at the superior nucleation ability of bone-like apatite under *in-vitro* conditions. The mechanism of the nucleation of bone-like apatite has been demonstrated appropriately in our previous study [288]. However, in brief, the HAP sites in the composite films on coming in contact with SBF expose the negatively charged $OH^-$ and $(PO_4^{3-}$ ions, rendering the surface negatively charged. In addition, at a pH of 7.4, the ST sites develop a negative charge, and this development (of negative charge) is crucial for the nucleation of apatite in SBF. Once the surface is at an overall negative potential, it draws the $Ca^{+2}$ ions from the solution, rendering a $Ca$-rich surface, which later on attracts the negatively charged $(PO_4)^{3-}$ ions leading to an amorphous $Ca-P$ layer over

the sputtered films. The amorphous layer is highly soluble, and for thermodynamic stability, it transforms into a bone-like apatite layer by consuming $OH^-$ ions from the SBF [217]. The demonstration of the mechanism of bone-like apatite growth over the sputtered surfaces is shown in Figure 6.11.

#### 6.3.2.4 Cell viability

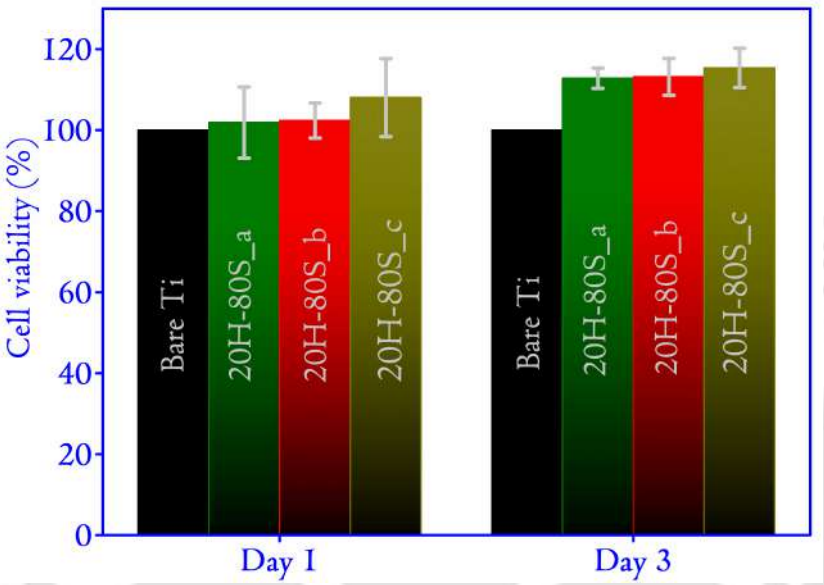


**Figure 6.12:** The cytocompatibility analysis of the sputtered thin films was analyzed with MG63 cell lines for Day1 and Day 3. In all the cases, the cell viability is more than 100% for Day 1 and increased subsequently on Day 3. This indicates excellent cytocompatibility of the thin films. Day 1 and Day 3 display better cell viability by $20H-80S\_c$, implying a positive correlation between thickness and cell viability.

Biological reactions on implant surfaces are modulated by topography, wettability, surface energy, and surface chemistry [303, 304]. Cells have the inherent capability to sense the surface on which they are seeded; therefore, surface topography can be a dominating factor in determining the biological response of the surface of a biomaterial [305]. Micro-scale roughness undoubtedly improves cellular proliferation; however, the impact of nano-scale roughness is yet to be unambiguously defined [305]. For MG63 cell lines, reports by Molina *et al.* [306] on the effects of nanoroughness on the behavior of osteoblasts showed that the proliferation rate increased with $R_a$ up to 6 nm, and after that, it saturated. In the present study, we observe that with increasing thickness, there is an improvement in $R_a$, and this is reflected in the cell viability shown in Figure 6.12. It has been previously found in our studies with the composites that the presence of ST can be a boon in enhancing

the cytocompatibility of the specimens [88]. Our studies were supported by several other studies, in which it was reported that $Sr$ coated implants have tremendous potential for healing bone defects, improved osseointegration abilities, and bone remodeling. $Sr$ containing drugs have also been used to reverse osteoporosis, thereby stimulating osteoblasts for new bone regeneration. In another report by Sahoo *et al.* [67], laser-assisted ST reinforced $Ti$ matrix coatings showed release of $Sr$ ions in a sustained manner which enhanced the cell viability of surface modified $Ti$ surface multiple times. Xin *et al.* [307] also reported enhanced cell viability and bioactivity in the presence of $Sr$ in the ST nanotube array. We find similar results on the cell viability with MG63 cells, which shows improvement with thickness and time. On Day 1, the $20H-80S\_c$ shows the highest value of cell viability (108.06%) and even on Day 3, the same specimen shows the highest value of cell viability (115.40%). It tells us that with increasing thickness, when the content of ST in the composite films increases, the cell viability also increases. It implies a positive correlation between film thickness, composition, and cell viability.

### 6.3.3 Electrical properties

#### 6.3.3.1 Dielectric properties

From a biomedical perspective, the dielectric properties are essential to understand the capacity of the thin films to store charges under an alternating electric field. The increasing application of alternating electric fields for faster wound healing can be utilized to a maximum capacity by introducing a biocompatible ceramic coating over bone implants. Since the ceramics undergo polarization under applied electric field, the polarization can be a source of the electric field after removing the external electric field [33]. This polarization of the ceramic layer can continue generating the electric field internally and augment the faster healing of wounds. The larger the $\epsilon_r$, the stronger the generated field, and hence implants coated with a biocompatible material of higher $\epsilon_r$ can be helpful in clinical applications [86]. With this motivation, the variation in $\epsilon_r$ with frequency and temperature is plotted and shown in Figure 6.13. In Figure 6.13(a), (b), and (c), the initial dispersion in the $\epsilon_r$ in the probed frequency regime is attributed to the activation of various polarization mechanisms. The frequency dispersion of $\epsilon_r$ is understood by Koop's phenomenological theory that assigns the initial exponentially high value of $\epsilon_r$ to the accumulation of space charges at the interface of the thin film and the electrodes [92]. With an increase in frequency, the polarization mechanisms that can easily follow the applied field at

low frequency slowly starts lagging and causes a drop in the value of the $\epsilon_r$. Such variations in $\epsilon_r$ are observed in thin films deposited by RF magnetron sputtering [298]. In addition to frequency, the dielectric response of a bio-ceramic coating is also governed by factors like the grain size, the orientation of the films along particular (hkl) directions, presence of secondary phases, mechanical stress, etc. to name a few [307]. A plot showing variation in $\epsilon_r$ with the grain size of the composites is shown in the inset of Figure 6.13(a). In thin films, the grain boundary region contains defects known to introduce defect states in the bandgap region and facilitates the hopping conduction process [308].

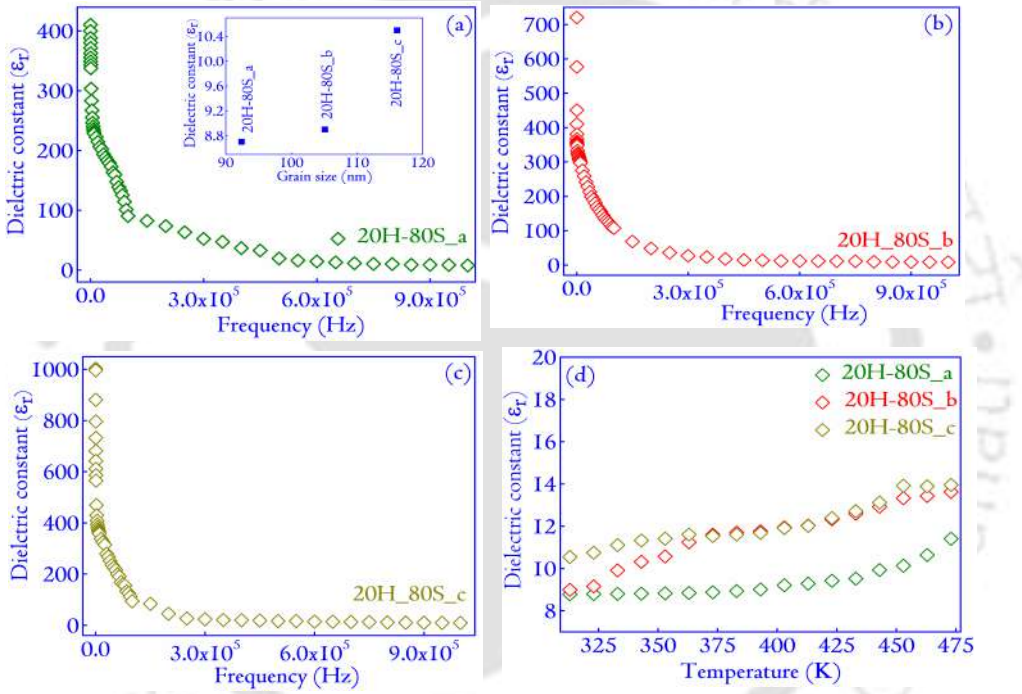


**Figure 6.13:** The variation in the $\epsilon_r$ of the sputtered films with frequency is plotted in (a), (b), and (c). The frequency variation is considered at a temperature of 313 K, owing to its closeness to the physiological temperature of 310 K. In (d,) the temperature variation of the $\epsilon_r$ with temperature is shown at a frequency of 1 MHz. The inset of (a) show the variation in the $\epsilon_r$ with the grain size of the films. The $\epsilon_r$ increases monotonically with the grain size and directly correlates with the crystallinity of the thin films that is observed to increase with the deposition time.

At lower frequencies, the mobile charges accumulate quickly near the grain-grain boundary interface. As the frequency is low, the instantaneous field keeps them accumulated for a somewhat longer duration (compared to the higher frequencies), before which the charges reverse to the other end of the grain boundary under the effect of the alternating field. This behavior is equivalent to a small capacitor of a

thickness equivalent to the grain boundary thickness. As grain boundary thickness is minimal (as observed from the FESEM micrographs in Figure 6.8), the capacitance of the grain boundary is very high. Such contributions from the grain boundary also contribute to raising the $\epsilon_r$ of the thin films at lower frequencies [308]. At higher frequencies, as the instantaneous fields act only for a brief period before reversing their direction, the mobile charge accumulation at the grain-grain boundary interface decreases rapidly. It leads to the decrease in the contribution of the grain boundaries to the $\epsilon_r$ [308]. The increasing crystallinity of the thin films is also found to positively correlate with the thin films' dielectric properties. This explains the enhancement in the value of $\epsilon_r$ with increasing thickness of the thin films [307]. In addition, with improvement in thickness, more dipoles are available for responding to the applied field, contributing positively to the $\epsilon_r$. In Figure 6.13(d), an increase in the value of $\epsilon_r$ with temperature is observed. Such variations are due to the thermally activated orientation motion of the dipoles along the field direction [86]. The application of temperature provides rotational energy to accompany the alignment of the dipoles along the field direction (thereby contributing to the increase in the polarization), which otherwise remain frozen at lower temperatures [33].

#### 6.3.3.2 Leakage current density

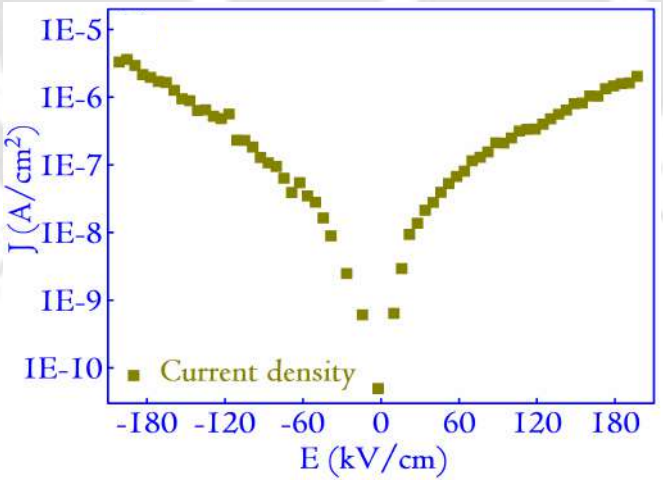


**Figure 6.14:** (a) The variation in the current density versus applied electric field measured at room temperature for the sputtered thin film $20H-80S\_c$. The room temperature measurements are carried out, as it is closest to the physiological temperature (310 K) at which most of the metabolic reactions occur in the human body.

The properties investigated for the sputtered films have displayed enhanced dielectric properties for $20H-80S\_c$. Furthermore, the investigation of the bioactivity

of the films shows that the bone-like apatite nucleating capability of $20H-80S\_c$ is formidable, with the $Ca/P$ ratio of bone-like apatite highest amongst the investigated films. All such properties point towards the possibility of the superior performance of $20H-80S\_c$ under *in-vivo* settings. It was also pointed out earlier that the implanted sputtered films with superior $\epsilon_r$ will show improved fracture healing capabilities due to their capacity of undergoing enhanced polarization on the application of the external electric stimulation. It would lead to the generation of a stronger polarized field (higher $\epsilon_r$ will lead to the superior polarized electric field) at the injured site (internally), leading to a faster bone healing response. Although the clinical evidence supporting the use of electrical stimulations in fracture healing is inconclusive, it has proven to be an effective course of treatment that has prevented severe morbidities such as increased pain and secondary procedures, medically prescribed for bone healing [201]. Moreover, the application of electrical stimulations is believed to support the healing process by stimulation of the calcium-calmodulin pathway necessary for the enhanced regulation of bone morphogenic proteins [309]. Therefore, based on the above discussions, $20H-80S\_c$ can suit coatings in bone implants ($Ti$ or $Ti-6Al-4V$). Furthermore, the cytocompatibility results also support the proposition, as amongst the investigated films, $20H-80S\_c$ displayed the highest cell viability value that directly points at its superior biological properties. From the prospect of applications of such biocompatible films in bioelectronics gadgets, it is of prime importance to understand electrical behavior from a broader perspective. Dielectric properties are undoubtedly the starting point of such analysis. However, it is imperative that we understand the loss mechanisms as well. Such information is handy in an indirect estimation of the time up to which the polarized electric field shall continue to function without decaying.

The mechanism responsible for such decay of polarization is primarily related to the leakage currents in the specimens, which can be elegantly investigated by considering the current-voltage ($J-E$) relationship of the fabricated thin-film capacitor. Ideally, a dielectric is an insulator with infinite resistance, and no current can flow through it under ordinary circumstances [33]. In reality, dielectrics are never perfect, and on the application of electric fields, nominal current flows through them. This disrupts the polarization and leads to a decrease in the magnitude of the dipolar electric field, which directly affects the time limit up to which the dielectric can retain the polarized electric field. Therefore, the leakage current measurements are considered an important tool to accurately study the conduction process by which it can be tuned for various electronic applications. It is described earlier that for ex-

pedited bone healing, electrical stimulation to the injured site forms the best course of treatment. There are different methods of administering the electric field to the injured sites. In brief, a method known as capacitive coupling involves electrodes on the opposite side of the fractured bones to be stimulated. By a power source attached to the patient's cast, the electrical field is generated within the injured site [201]. The standard course of treatment requires applying a voltage of about 1-10 V at a frequency of 20-200 kHz that accounts for an electric field of 1-100 mV/cm in between the electrodes [201]. To estimate the leakage current under such environments and provide a comprehensive understanding of the broader limit, we present the plot of $J$ versus $E$ for electric fields varying between -200 to 200 kV/cm in Figure 6.14. The measurements show that the leakage current density typically lies between $-3 \times 10^{-11}$ A/$cm^2$ to $3 \times 10^{11}$ A/$cm^2$ in the range of 1-100 mV/cm. With increasing field, the current expectedly shows an exponential rise, characteristic of insulating thin films [310]. This magnitude of leakage current is low, and the dipolar polarization in the deposited films is likely to maintain its magnitude without significant decay. From a physical perspective, the enhanced crystallinity, grain size, and roughness factor $R_a$ are the factors that contribute directly to the lessening of the leakage in $20H - 80S\_c$. Similar variations in the magnitude of leakage current are also reported for composite thin films of $MgTiO_3 - Ba_5Nb_4O_{15}$ and establish the effectiveness of $20H - 80S\_c$ thin films for energy storage applications apart from implant coatings in biomedical applications [132].

#### 6.3.3.3 Nyquist plots and electrical modelling using Cole-Cole analysis

The complex nature of the composite thin films under the application of an electrical field can be modeled to an idealized electric circuit consisting of discrete electric components by the Nyquist plots of the film. Such models help in the understanding of the electrical behavior of the thin films by establishing a direct correlation with the intrinsic properties like microstructure, grain, and grain boundaries [311]. The simplest models consists of an $R - C$ circuit, with R denoting the system's resistance to map the dissipative contributions such as electrode polarization, dipolar relaxation, and losses occurring due to migrating charge carriers. The capacitance denoted by $C$ is used to model the charge storing capacity of the dielectric due to different polarizations. Another most commonly used parameter in modeling is the constant phase element $Q$ associated with a parameter $n$. It models an imperfect capacitor and based on the value of $n$ taking the value of 1 or 0; it can behave as a capacitor or resistor, respectively [257].

The Nyquist plot of $20H - 80S\_c$ at different temperatures is shown in Figure 6.15. At lower temperature, a semi-circular arc is observed, which are skewed. The skewed nature of the arc is related to the non-smoothness in the movement of the dipoles in a non-ideal viscous environment [312]. The nature of the semi-circular arc corresponds to the Cole-Cole phenomenon that indicated the presence of non-Debye conduction in the sputtered films. In addition, the semi-circular arc in Cole-Cole plots are signatures of the relaxation of bound charges like the dipoles in the specimens [33]. The origin of relaxations is related to the inability of the dipoles to follow the variations in the frequency of the applied signal. Since only one semicircle is required to fit the arc, it is evident that the contributions are primarily due to bound diploes in the grain and the grain relaxation frequencies along with the different parameters that describe the equivalent circuit are listed in Table 6.2.

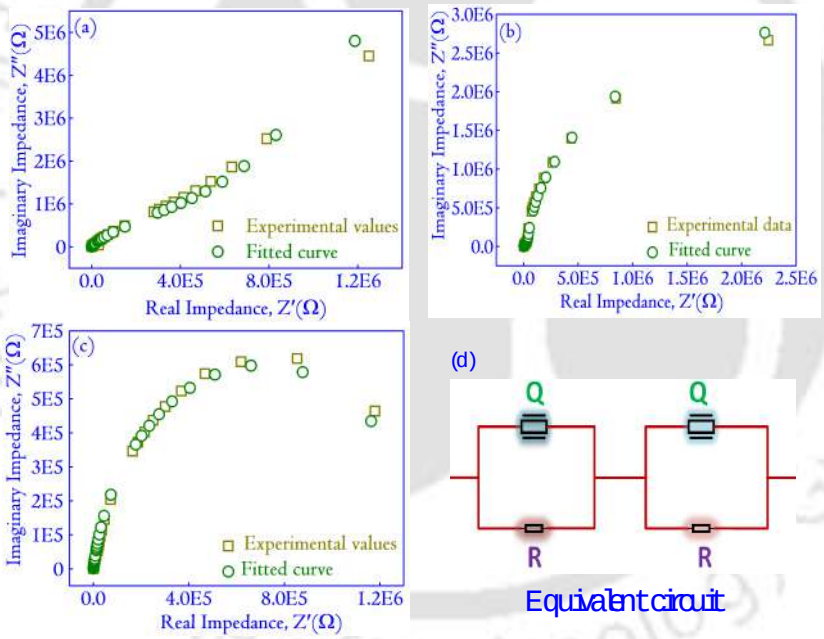


**Figure 6.15:** The fitting of the Cole-Cole function to the thin film $20H - 80S\_c$ at three different temperatures (a) 313 K, (b) 373 K, and (c) 473 K. (d) shows the equivalent circuit corresponding to the three temperatures considered in (a), (b) and (c). The circuit model consists of two parallel $QR$ circuits connected in series. The circuit element Q represents the constant phase element associated with a parameter $n$ that is considered a capacitor for $n = 1$ or a resistor for $n = 0$. The circuit presents the electrical modeling of the different physical processes occurring in the composite thin films.

Finally, the origin for a complete semi-circular arc at higher temperatures can be understood from the reasoning put forward by Khopkar *et al.* [311] in the case

of Cole-Cole plots observed in barium iron niobate ceramics. It is proposed that at higher temperatures, there are accumulations of the free charge carriers, electrons, or ions at the grain boundary regions due to Maxwell-Wagner polarization [308]. At lower temperatures, the motions of these mobile charge carriers are inhibited by the absence of sufficient thermal energy, resulting in the incompleteness of the semi-circular arc towards the low-frequency end of the Cole-Cole plot. To conclude, the successful modeling of the electrical blueprint of the $20H-80S\_c$ thin film would be help design the electrical component using these thin films in bio-electronic gadgets.

**Table 6.2:** The variation in the grain resistance, grain capacitance, and the corresponding relaxation time for $20H-80S\_c$. The value of n associated with Q in all the cases is either 0.8 or 0.9; the constant phase element is assumed to behave as a capacitor for all practical purposes.

| Temperature (K) | Resistance (MΩ) | Capacitance (pF) | Relaxation time ($\mu$S) |
|---|---|---|---|
| 313 | 1.41 ± 0.21 | 3.68 ± 0.02 | 5.18 ± 0.41 |
| 373 | 5.92 ± 0.40 | 4.05 ± 0.03 | 23.98 ± 1.22 |
| 413 | 8.95 ± 0.62 | 8.06 ± 0.09 | 79.56 ± 5.56 |

## 6.3.4 Bilayers of BST and HAP

### 6.3.4.1 X-ray Diffraction

Figure 6.16(a) shows the X-ray diffraction patterns of the bilayers developed over $Ti$ along with the monolayered coatings. The reflection planes were identified individually to BST (ICDD card no. 39-1395) and HAP (ICDD card no. 009-0432), with no trace of any additional phase. Interestingly, the stacking order led to significant variation in the diffraction intensities, with the top layer of the bilayered films having a significantly high contribution to the diffraction spectra of the films (as the reflections from the top layer are most apparent in the XRD spectra). The crystallite size associated with the diffraction patterns (included in Figure 6.16(b)) show a slight difference for the bilayered films, their magnitude solely lying between the fabricated monolayered films (∼17.7–22.4 nm). The microstructure of the bilayers shows exciting features, as portrayed in the FESEM micrographs adjacent to the diffraction spectra in Figure 6.16. The BHBF specimens show elongated grain-like morphology that is homogeneous and uniformly distributed over the surface. The HBBF, on the other hand, forms island-like regions containing the elongated grains that are distributed throughout the film. The region between the islands is distributed with polyhedral grains of different sizes. The EDS of BHBF and HBBF in

the region marked by the dotted rectangle shows the elementary compositions with the $Ca/P$ ratio of HAP, 1.54 and 1.52 for BHBF, and HBBF, respectively. However, the content of $Ca$ in BHBF is 2.5 times higher than HBBF due to the upper HAP layer. The grain size of HBBF and BHBF is also estimated, and it is 85 ± 5 nm for HBBF and 90 ± 8 nm for BHBF. Both the bilayers have a dense coverage of grains over the surface. Such dense microstructures are favorable for improved interfacial and electrical properties of the fabricated films, as will be evident from the following discussions.

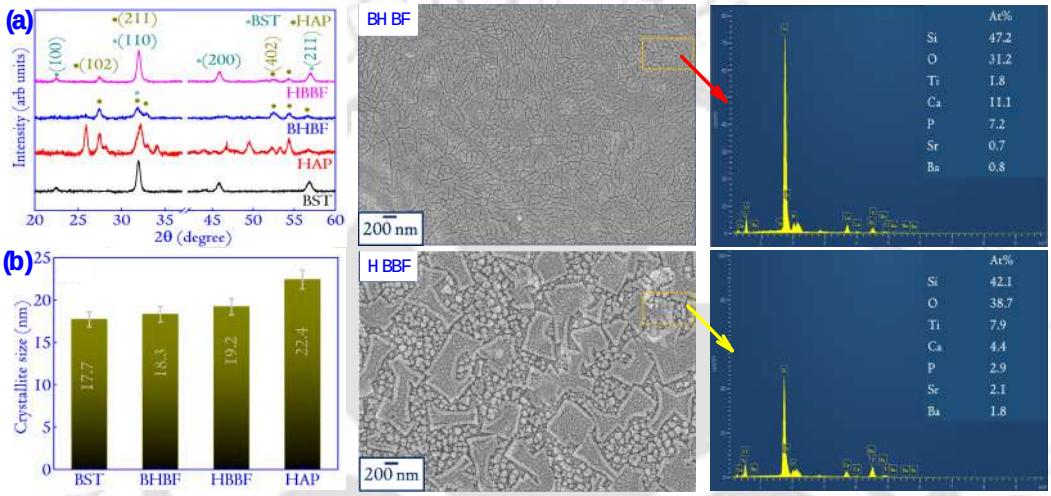


**Figure 6.16:** (a) The XRD pattern of the bilayers and the monolayers. The XRD spectra contain reflections from both the monolayers and no intermediate reflections peaks could be identified that might have been formed due to the reaction between the monolayers. The crystallite size shown in (b) is highest for the HAP and lowest for BST. For the bilayers, the crystallite size is very close to one another. In addition, the reflections in the diffraction spectra are broad and are of low intensity. It implies that the films are nanocrystalline, which may be due to the limited (hkl) planes in the films. The corresponding microstructure, and EDS spectra, of the bilayered films are also shown such that the first row corresponds to the BHBF and the second row to the HBBF. The grain size of the films are 90 ± 8 nm and 85 ± 5 for BHBF and HBBF, and the size is lesser than 100 nm, indicating that size-related effects are probably dominant in the fabricated bilayered films. The XRD pattern of the sputtering targets is included in Appendix D (Figure D.2).

#### 6.3.4.2 Wettability, bioactivity and cytocompatibility

The wettability, bioactivity, and cytocompatibility data of the bilayered films are compiled together in Figure 6.17. The bioactivity of the films was studied by incubating the films deposited on $Ti$ in SBF for 12 days [236]. The SBF is a supersaturated solution with respect to apatite, and bioactive surfaces induce dense growth

of bone-like apatite structures of flowery shape [236]. As shown in Figure 6.17(a) and (b), dense globular apatite structures are seen in both cases, implying a high degree of bioactivity in both specimens. Materials with bioactive properties (bone-bonding abilities) can form a bone-like apatite layer on their surfaces in biological environments and are expected to bond to the living bones through this layer. The mechanism for the nucleation of bone-apatite from SBF in the case of bilayers has been schematically illustrated in Figure 6.18. Usually, when the bilayer coated $Ti$ substrates are incubated in SBF, $Ca^{+2}$ ions nucleate on the coated layer, resulting in a $Ca$ rich positively charged surface. The $Ca$ rich layer leads to the generation of an electrostatic force field that attracts the $(PO_4)^{3-}$ ions towards the interface. An amorphous $Ca-P$ layer is thus generated, which undergoes hydrolysis to form a thermodynamically stable bone-like apatite layer. It must be realized that the most crucial step for successful generation of bone-apatite structures involve the nucleation of $Ca^{+2}$ ions over the $Ti$ substrates that is related to the zeta-potential of the bilayers. The zeta-potential must be negative in order to draw the $Ca^{+2}$ ions, and from our earlier reports, it is indeed found negative for both HAP and BST.

The surface wettability of monolayer and bilayer films is shown in Figure 6.17(c). HAP coated monolayer film is hydrophilic ($81\pm2^{\circ}$) [84], while BST coated monolayer film is hydrophobic ($110\pm5^{\circ}$). For the bilayered films, intermediate contact angles are observed. The fractions of individual constituents contributing to the surface wettability are estimated using the Cassie equation [99]. The contents of HAP and BST in BHBF are 38 and 62 %, respectively, while the same in HBBF are 26 and 74 %, respectively. The surface energy of deposited thin films is calculated using the Young–Dupré equation [289]. The surface energy ($mJ/m^2$) follows the order of HAP (33.85) > BHBF (29.57) > HBBF (26.82) > BST (23.95). It is important to understand that hydrophobic coatings over $Ti$ implants can be good for platelet adhesion [313]. Obtaining hydrophobic coatings over implants is a difficult task, and the technique adopted in the present article is an easy way to enhance the corrosion resistance of the implants along with their biological properties [287]. As hydrophobicity is known to enhance the resistance of the coatings towards harsh *in-vivo* environments, it can lead to slower degradation adding to the lifetime of the implants. We believe that the lower surface energy of BST and HAP thickness are the major factors behind its hydrophobicity. One of the basic approaches to inducing hydrophobicity in thin films is to reduce the surface energy by modifying the coated layers' surface chemistry. In the present approach, since oxide films over metallic substrates are involved, these films are known to be thermodynamically stable as

demonstrated by Jeurgens *et al.* [314]. This certainly decreases the surface energy of the deposited films, making them hydrophobic. Such surfaces essentially promote protein adherence due to hydrophobic interactions, and adherence of proteins upon the biomaterials surfaces are considered the primary event that occurs when it is inserted in a biological environment [313]. Subsequently, the adhered proteins determine the interaction of the materials with cells, thereby determining the fate of the implants in the biological environment. Thus, protein adsorption is an initial marker of biocompatibility of a surface [313]. Hydrophobic surfaces that promote adherence of proteins can therefore be essential for the integrity of implants.

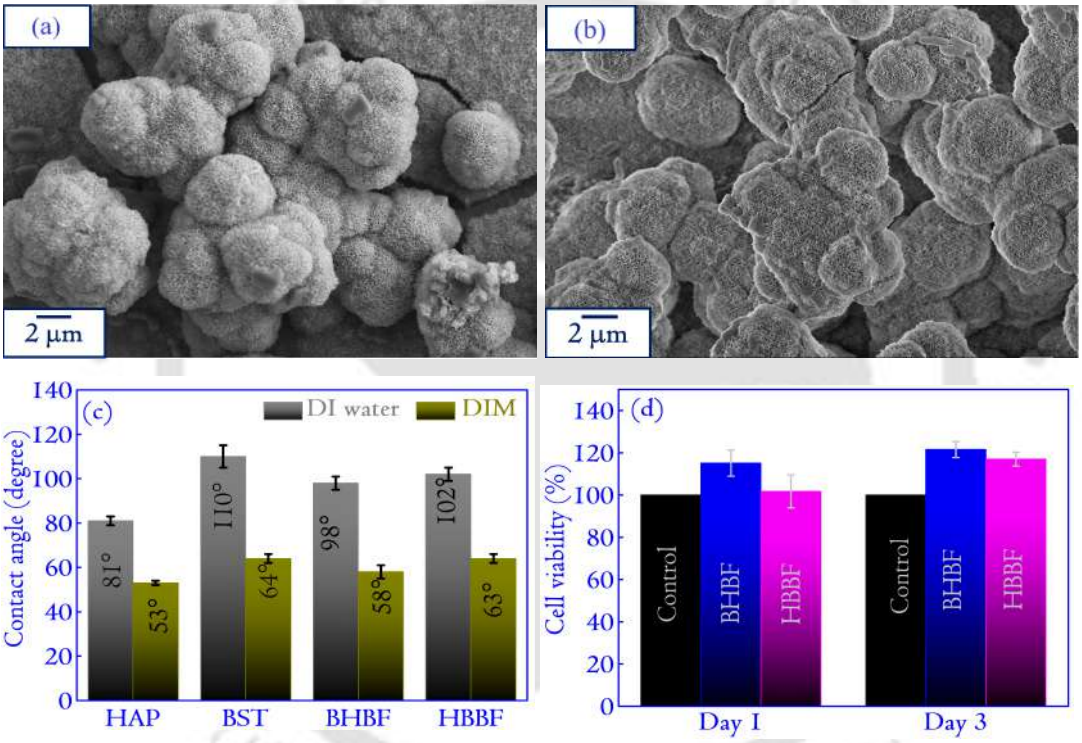


**Figure 6.17:** The growth of bone-like apatite from SBF, showing the bioactivity of the bilayered films for (a) BHBF and (b) HBBF. In (c), the variation of the contact angle measured with deionized water (DI) and diiodomethane (DIM) is shown. The corresponding surface energy calculated from the contact angles of DI water and DIM is shown. The surface energy of the films has an intrinsic relationship with hydrophobicity. Highly hydrophobic films have shallow surface energy and are considered thermodynamically stable. In (d), the cytocompatibility using bone-like MG63 cell lines is shown in comparison to the control, for which the viability is taken as 100%. The images of the contact angles are included in Appendix D (Figure D.3-D.6).

In view of the previous conclusion that hydrophobic films are cytocompatible, the assessment with bone-like MG63 cell lines show that the bilayered films have excellent cell viability (>100%) after Day 1 and Day 3. BHBF films show the highest

value of cell viability due to the HAP layer on top, which favors the proliferation of osteoblasts. In a previous study, it was revealed that the presence of ions like $Ba$ and $Sr$ along with HAP had a positive impact on the cell viability as it encourages the growth of bone-like MG63 cells over the interface of the films [244]. Additionally, the surfaces with lower hydrophobicity resulted in more significant cell proliferation, thus indicating a relationship between cytocompatibility and the associated hydrophobicity of the films. It has been revealed that surface properties have an essential role in determining the cell viability of the surface. Studies have shown that the surfaces exhibiting lower water contact angle display poor cell attachment and proliferation [315]. Additionally, cell membranes with hydrophobic properties have an affinity for hydrophobic surfaces due to the relevant hydrophobic interactions [315]. It probably affects the cytocompatibility of the surfaces as well. Since the surfaces displayed substantially good cytocompatibility, it is clear that the hydrophobicity of the surfaces has aided the cell viability.

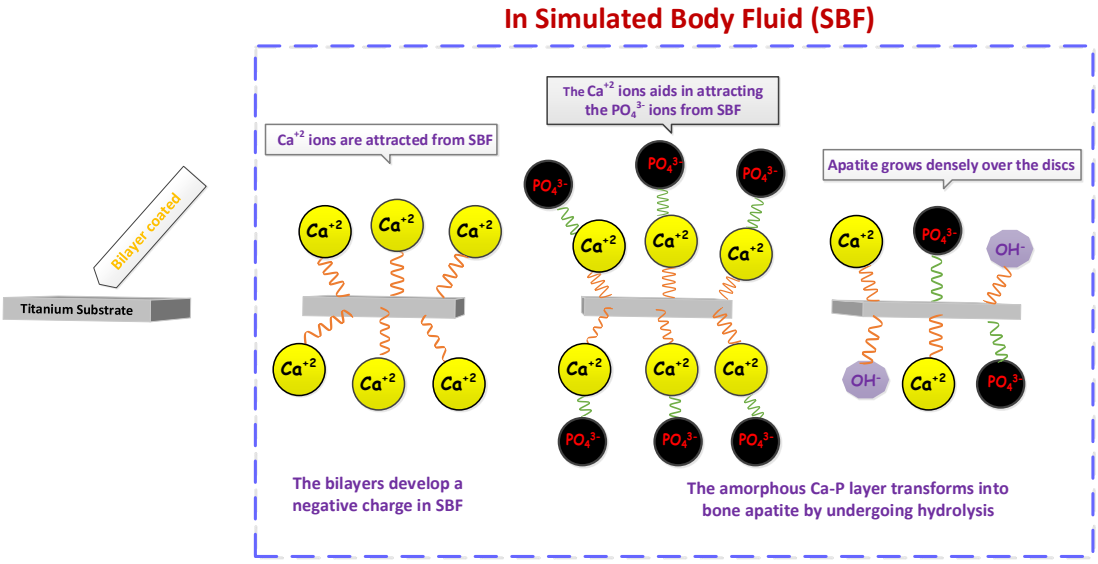


**Figure 6.18:** The illustration of bone-like apatite growth mechanism over bilayered $Ti$ substrates. In the figure, the reaction proceeds from left to right. The reaction mechanism relies on the $Ti$ substrates acquiring negative charges on incubation in SBF at physiological pH. This negative charge helps in drawing the $Ca^{+2}$ charges, which later attracts the $(PO_4)^{3-}$ ions forming an amorphous $Ca-P$ layer that transforms to bone-apatite by undergoing hydrolysis. The process of transformation occurs as hydrolysis leads to the formation of a more stable bone-apatite phase rather than the amorphous $Ca-P$ layer.

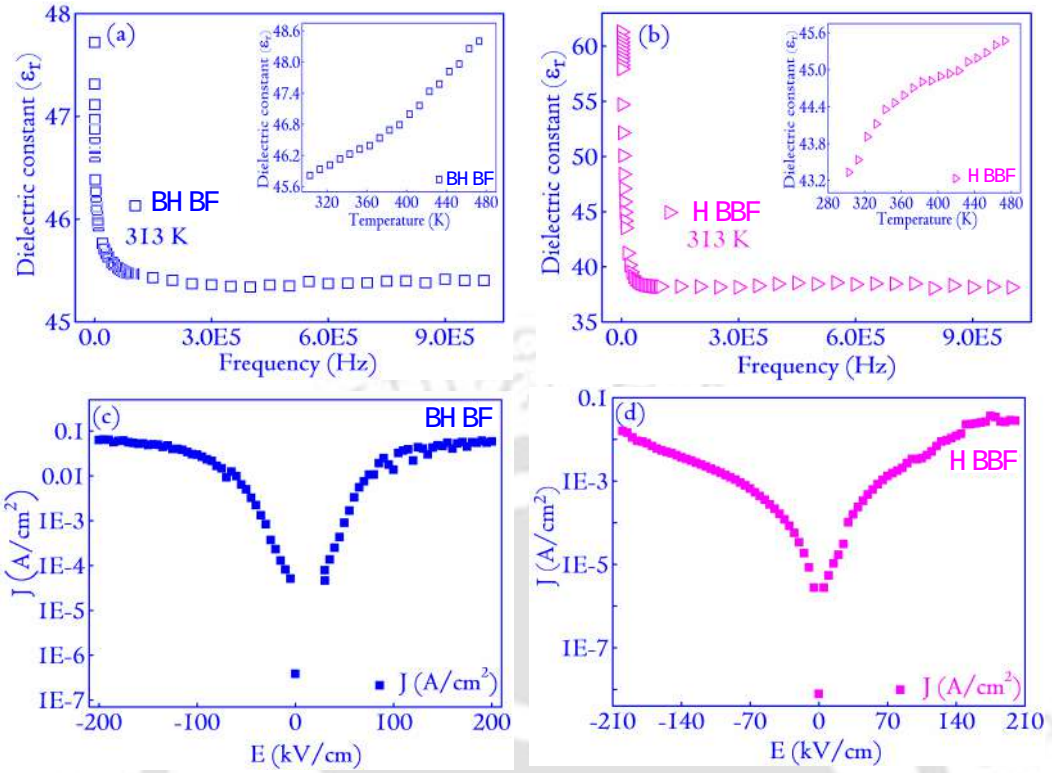


**Figure 6.19:** The variation of $\epsilon_r$ with frequency and temperature (see inset) for (a) BHBF and (b) HBBF films. The frequency variation of $\epsilon_r$ displays substantial dispersion due to the several active polarization mechanisms freezing at higher frequencies. The temperature variation shows a steady rise in $\epsilon_r$ with the temperature. The leakage current variations are shown in (c) and (d).

#### 6.3.4.3 Electrical properties

The dielectric properties of biomaterials garner high research interest due to their ability to assist the biological properties in achieving superior host response. In Figures 6.19(a) and (b), the frequency variation of dielectric properties are shown along with the temperature changes (see inset of Figure 6.19(a) and (b)). The $\epsilon_r$ of BHBF and HBBF are 45 and 38, respectively, at 1 MHz. Unlike the biological properties determined mainly by the surface properties, the $\epsilon_r$ is related to the properties such as density and grain size. Figure 6.16 (FESEM) shows that BHBF represents a more compact microstructure than HBBF, which shows open spaces between the larger polyhedral grains. This variation in compactness of the microstructural arrangement leads to a difference in the density and manifests as a minor change in $\epsilon_r$ of the bilayered thin films [316]. The frequency dependence of $\epsilon_r$ shows a high dispersion in bilayered films and is a common phenomenon observed in dielectrics [33]. The dependence of the $\epsilon_r$ with temperature shows a rise with increasing tempera-

ture, and it may be attributed to the thermal energy that facilitates the rotation of the dipoles in the direction of the applied field [90]. From a biomedical perspective, the $\epsilon_r$ of coatings in implants can serve as a parameter determining the recovery rate of the fractures. The healing rate is related to exposure to electromagnetic stimulations, which emerged as the preferred treatment course for expedited bone trauma recovery. In fact, the higher value of $\epsilon_r$ for BHBF corresponds to the greater cell proliferation (Figure 6.17(d)). Using a dielectric coating over such implants can lead to polarization of the insulating layer (during stimulations) that can produce an internal electric field even after removing the external stimulations, thereby leading to a faster healing process [90].

Identifying the polarization disruption mechanism in paraelectric thin films are essential as it can affect the internal field [317]. The leakage current in dielectrics forms a vital parameter to quantify the disruption mechanisms and provides a way of determining the exposure parameters (of the external stimulations) in a range where the leakage is minimum. The leakage current measurements of the films are shown in Figures 6.19(c) and (d). Considering a case study on the use of electrical stimulation (for treating non-union of bones and fractures) reveals the technique of capacitive coupling, in which skin electrodes are used on opposite sides of the fractured bones to generate the electric field. Using these electrodes and setting potentials between 1-10 V at 20-200 kHz, fields of magnitude up to 1-100 mV/cm are generated [318]. Additionally, clinical data show that these treatments are to be administered for a minimum of 3 months or ten weeks with at least 10 hours of exposure daily [201]. Instead, exploring the concept of the polarized electric field to generate internal fields and choosing the applied field within limits 1-30 kV/cm when the leakage is $\sim 1\ \mu A/cm^2$ for both the bilayered films, these films present a superior alternative. Since the dielectric films would be continuously generating the electric field *in-vivo* (after removal of the external stimulations), these are expected to lead to a faster healing, extra cost-cutting, and most importantly, lessens the unimaginable trauma associated with the recovery process of severe bone fractures [97].

## 6.4 Conclusions

In the chapter, a comparative study of scaffolds synthesized from $20H - 80S$ and $20H - 80B$, is presented. Following the preliminary microstructural analysis, the bioactivity, protein adsorption, and cytocompatibility studies are performed. $20H -$

$80B$ displays better biomineralization with its $Ca/P$ ratio (1.64) closer to stoichiometric HAP ($Ca/P$-1.67). The protein adsorption (BSA) is highest on $20H-80B$ due to more significant porosity in the scaffolds. Finally, the scaffolds' cytocompatibility analysis revealed that cell viability is greater than 90% and higher in $20H-80B$, thus making it suitable for clinical applications.

In the second part of the chapter, we also reported the fabrication of sputtered thin films of $20H-80S$ of varying thicknesses. The microstructural properties of the thin films are studied, and the XRD analysis reveals the presence of (hkl) planes corresponding to $P63/m$ of HAP (hexagonal) and $Pm3m$ (cubic) of ST. Systematic shifts in the XRD plots are obtained, and WH analysis revealed the presence of strain that decreases systematically with increasing thickness of the thin films. The crystallite sizes of the thin films are also estimated using the WH plots, and the largest crystallite sizes are obtained for the film $20H-80S\_c$, which incidentally also have the highest intensity XRD peaks amongst the three variants considered for the study. The FESEM micrographs reveal a dense coverage of the sputtered thin films for all the thin films, and the largest grain size is obtained for $20H-80S\_c$, similar to the behavior predicted by the crystallite size. The AFM analysis is also performed on the thin films to see the variations in the topography of the sputtered films, and the roughness parameter derived from the AFM analysis revealed a systematic increase with the thickness.

Further, to determine the bone nucleation ability of the thin films, the SBF immersion tests are conducted, and it is observed that the $Ca/P$ ratio of $20H-80S\_c$ is also the highest amongst the specimens indicating the superior ability of the specimen to nucleate bone-like apatite. The cytocompatibility analysis (with MG-63) revealed that the cell viability exceeds 100 % in all the specimens, indicating that the fabricated thin films are suitable as implants for biomedical applications. The electrical properties are also investigated to determine the correlation between electrical and biological properties. The $\epsilon_r$ is highest for $20H-80S\_c$, and such a film would produce a larger polarized field (under *in-vivo* settings) that will supplement the rapid healing process of the fractured regions. Based on the properties discussed above, $20H-80S\_c$ displays superior properties amongst the sputtered specimens, and to further understand the dynamics of charge carriers inside the films; the $J-E$ analysis is carried out. Such analyses help understand the decay process of the polarized field in the implanted site. In the region of interest that matches with the clinical applications, the $J$ is very low ($< 10^{-8}$ A/$cm^2$), which is a direct indication of the fact that the polarized electric field can be retained for very long

durations, and the film would be suitable for clinical applications. Finally, the bio-ceramic thin film ($20H - 80S\_c$) is modeled to an electric circuit consisting of two parallel circuits constituting a resistor and a constant phase element that behaves as a capacitor for all practical purposes. The modeling allows a simplistic understanding of the aspects of the thin film from an electrical perspective that will help design bio-electronic gadgets for future use.

In the third part, we successfully demonstrate bilayered thin films developed using RF magnetron sputtering by considering a thickness ratio of 1:1 for the individual layers and a variation in their stacking order. The preliminary investigations revealed the presence of BST and HAP in the bilayered films, with the top layer showing dominance in the XRD pattern and interfacial properties. The bioactivity, wettability, and cytocompatibility analysis preceded the microstructural analysis, and the films displayed excellent bone-like apatite nucleation capability and hydrophobicity, which are crucial to biomedical applications. A plausible mechanism for the growth of bone-like apatite is modeled that relies on the coatings developing a negative charge on their surface on incubation in SBF. This negative charge further takes care of the subsequent reactions on the interface that leads to the formation of dense bone-like apatite, an indicator of superior bioactivity of the thin films.

The films showed a high degree of cell viability (>100%) for Day 1, steadily increasing on Day 3. The superior biocompatibility of the thin films is related to the presence of $Ba$ and $Sr$ ions and the HAP layer that traditionally favors the osteoblasts' growth. It was also observed that high values of water contact angle (hydrophobicity) favored the cell growth over the thin films, improving the cell viability of the surfaces. However, the prime point of this report was the analysis of the electrical properties and their correlation to biological performances. Cell proliferation is found to be related to the dielectric properties of the surfaces. The films displayed modest $\epsilon_r$ ($\sim$ 35-45 at 1 MHz) to create an *in-vivo* internal field. The leakage current analysis was carried out to complement the dielectric properties, which revealed leakage of ($<$ or $=$) 1 $\mu A/cm^2$ within 1-30 kV/cm. The magnitudes are deemed suitable for assisting the generation of polarized electric fields without the possibility of their significant decay (within a short period). Such applications of bilayered films can be novel for biomedical implants in which cytocompatibility and bioactivity are primary concerns.

# Chapter 7

# Conclusions & future scopes

This chapter presents the concluding remarks of the thesis work and discusses the possibilities of further work that can be carried out in the area.

## 7.1 Conclusions

In this thesis, we studied two composites in terms of their micro-structural, electrical, and biological properties. The idea is to consider their applications in designing scaffolds and thin-film coatings for biomedical devices in general. In particular, we focussed on identifying the composite with superior electrical and biological properties to design the scaffolds and coatings. However, before moving into the composites directly, we made efforts to probe some preliminary properties of HAP. This gave us a platform to re-establish the versatility of HAP and unearth some crucial properties of HAP, which we found could be helpful in biomedical imaging. The brief journey for developing the scaffolds and coatings is embedded in the following chapters.

Chapter 1 presents an introduction to the work presented in the thesis. Based on a careful literature survey, various research work on biomaterials, primarily focussing on the electrical properties of biomaterials, is discussed. The interconnection between the biological and electrical properties of biomaterials is discussed elaborately which forms the basis of the thesis work. The literature survey considers all the relevant work done with bulk HAP and its ceramic composites along with the thin films. Towards the end of the chapter, the objectives of the thesis work and the motivation for the thesis are presented. The chapter concludes by briefly presenting a snap short of the work presented in various chapters. Chapter 2 is an extension of chapter 1, where the materials and methods adopted for conducting the research work are discussed. Comprehensively, the processing conditions of bulk

and thin films specimens and the characterization techniques adopted to complete the research work have been discussed. This chapter provides the deciding platform for understanding the research work presented in the following chapters.

Chapter 3, presented the results related to the temperature-induced changes in synthetically prepared HAP. The results showed that the $OH$ ion dynamics dominate the behavior of HAP.. Exploring the $OH$ ion reorientation with the high polarizability from the micro-Raman spectroscopy in conjunction with dielectric spectroscopy ($OH$ being a dipole) displays the temperature-dependent volume fraction change to the polymorph HAP. The micro-Raman spectroscopy further revealed the reorientation motion of the $OH$ group, and dielectric spectroscopy established that the reorientation is purely rotational transformation due to the temperature aided activation energy. It is further understood that the rotation is not a collective motion but occurs monotonically, with the temperature reaching a maximum near 523 K. The evidence of these results were apparent from the temperature-dependent XRD studies, which showed shifts in the diffraction patterns of the (hkl) planes. We observed from the XRD studies that certain crucial aspects relating to the reorientation motion of the $OH$ dipoles were not evident from the XRD spectra. Precisely, due to the low scattering power of the $O$ atoms, the detection of the reorientation is challenging in the diffraction pattern. Raman spectroscopy analysis remains highly sensitive to structural displacements of ions/atoms. This aspect makes Raman spectroscopy a handy tool in analyzing the temperature-induced rotational motions in HAP. Further, the defect dynamics in HAP have recently gained much attention due to its possible implications in photoluminescence, which has direct biological application. The display of PL by HAP is related to the defect structures. It is proposed that the PL in HAP is due to an oxygen vacancy from $PO_4$ and/or an entire group of $OH$. An interesting consequence of the presence of defects emerged in the bandgap study that pointed at the possibility of the photo-catalysis ability of HAP under UV light. This phenomenon also arise due to the vacancy in the $PO_4$ group that produces energy levels in the forbidden gap (towards the lower half, near the valence band). The dynamics of the defects in the HAP structure are further probed with TRPL, and it revealed an average lifetime of 7.95 ns for the excitation. Such inputs help in mapping the fundamental properties of HAP and hold the possibility of opening new avenues of its application in areas related to bioimaging. The upsurge of research in biomedical imaging, where there is a continuous search for biocompatible materials (such as HAP), would be beneficial for in-situ investigations in surgery and the detection and imaging of cancer cells.

Chapter 4, proceeds with fabricating ceramic composites of HAP and $SrTiO_3$ and report their biological, microstructural, and electrical properties. We discuss in detail the production of a series of composites, from which we aim to identify the composite with the best properties. Several properties were probed in the studies. The focus was primarily on the electrical properties and their intrinsic connection to the biological response of the composites. The Impedance spectra of the specimens that determine the dielectric behavior show the $\epsilon_r$ to lie in the range of 5 - 35. The Bode plots further reveal that the specimens have a capacitive behavior for most of the frequency range probed in the experiment. The study points at an interesting association of the service life of electrets and the active conduction mechanisms. We remark that the lower conductivity($\simeq 10^{-8}$S/cm) can serve as an indirect way for estimation of the service life. Also, the lower conductivity is correlated with the inherently porous nature of the specimens, which reduces the effective contact area between the grains, reducing the conductivity drastically. Theoretical advances in the study of electrical properties (specifically in the field of conductivity mechanisms) are yet to be rigorously considered in the design of bio-electrets. The chapter will serve to bridge the gap between theory and industry. A ceramic composite of HAP and ST, specifically for electrets, can be a strong starting point in this direction. The results established in the study can be beneficial for designing prototype electrets and scaffolds in biomedical applications. We then analyze the bioactivity, protein adsorption, and cytocompatibility of the specimens. These studies pointed out that the composite $20H - 80S$ had superior microstructural, dielectric properties, and high bioactivity. Better dielectric properties are essential for the composites to augment the biological responses. It was indeed found that $20H - 80S$ displayed higher BSA adsorption and higher cell viability. The experiments led us to successfully identify the composite with the better biological and electrical response, which we interpreted that it would be a suitable candidate for designing scaffolds and bio-electrets.

Proceeding to chapter 5, we introduce the $Ba$ component in $SrTiO_3$ to fabricate $Ba_{0.5}Sr_{0.5}TiO_3$, which following the roadmap of the previous chapter is considered for developing composites of $BST$ and HAP. These composites are tested for their microstructural, biological, and electrical properties to identify a suitable composite that blends the best biological and electrical properties. The introduction of $Ba$ is fascinating as the $\epsilon_r$, protein adsorption, and cell viability increased considerably. The introduction of $Ba$ (in the form of $BaTiO_3$ nanoparticles) have been extensively investigated, and the properties such as viability and cell proliferation have enhanced

as reported in several investigations. Similar to the previous chapter, we found that $20H - 80B$ displayed considerably better $\epsilon_r$, cell viability, and protein adsorption behavior (with BSA and FBS). We were able to establish that a higher $\epsilon_r$ of the ceramic composites will be helpful in better retention of the polarization in ceramics, which will lead to its electric field when such composites are used for designing scaffolds for bone tissue engineering applications. The idea originated from the fact that clinicians frequently resort to applying electric fields externally in the regions of the fractured bones for a quick healing response. Similar to the procedure adopted, when we use scaffolds designed from the composites as a template for bone healing, the periodic application of these external fields will lead to better and rapid healing. Along with that, the presence of $Sr$ and $Ba$ in the scaffolds is expected to augment the fracture healing process. These possibilities make $20H - 80B$ an exciting candidate for biomedical applications.

Chapter 6, focusses on assimilating the preliminary knowledge gained from the previous chapters to design scaffolds and thin films that have direct applications in the biomedical industry. To start, we consider the first part, where we present a comparative study of scaffolds prepared from $20H - 80S$ and $20H - 80B$. We begin by describing the processing method for scaffolds of $20H - 80S$ and $20H - 80B$, following which we consider their microstructure and preliminary biological properties. From the analysis, we established that $20H - 80B$ is a better blend of biological and microstructural properties that can be considered a suitable candidate for the generation of scaffolds. Following the preliminary analysis, we move to discuss the thin films generated from $20H - 80S$ of three thickness variations to understand the suitability of such thin films as coatings for $Ti/Ti$-based alloy implants. The film with the largest thickness ($507 \pm 23$ nm deposited over $Ti$ substrate) showed prominence for the microstructural, electrical, and biological properties. It has been observed that clinicians do not fully understand the interaction mechanisms of the electromagnetic field in bone repair. This leads to a random selection of the parameters related to the electrical stimulation, and as a result, parameters like the magnitude of the electric field, fracture gap, etc., are not correctly optimized. It led us to a careful analysis of the loss mechanisms by studying the variations in $J$ of the films with respect to $E$. There are several advantages of understanding the electrical properties of thin films. The determination of current density, which must be low for ceramic thin films, is a direct estimation of the loss mechanism. A low current density usually implies that the polarization of the films can be retained for very long durations. Polarized films with longer retention times will help in the

healing process of bones. Furthermore, special efforts were put in to model the thin films by a suitable electric circuit using the Cole-Cole analysis. Such a model would help design bio-electronic gadgets, which primarily rely on the electrical properties of thin films.

In the last part of this chapter, we discuss the bi-layered thin films of BST and HAP. The thin films were deposited on $Ti$ substrates, and the stacking order was changed to obtain two variants of thin films. In one order, HAP was deposited as the bottom layer, and BST on top of it. On the other, HAP on top of the BST layer was considered. The thickness of each layer was maintained at 100 nm. The objective of depositing bilayers of HAP and BST was to ensure the longevity of bone implants that tend to dislodge or loosen up after specific time durations. Surface coating of the implants with a biocompatible layer has proven effectiveness by ensuring that the implants function smoothly under natural environments. Using bilayers with tunable materials properties by collectively incorporating the behavior of both the layers makes the coatings suitable for *in-vivo* environments. In the case of bone implants, one component with better bone regeneration ability will help in bonding with the surrounding tissues, and the other layer with superior electrical properties will aid in faster healing of the fractured region. The analysis of properties revealed the presence of BST and HAP in the bilayered films, with the top layer showing dominance in the XRD pattern and interfacial properties.

The bioactivity, wettability, and cytocompatibility analysis preceded the microstructural analysis, and the films displayed excellent bone-like apatite nucleation capability and hydrophobicity, which are crucial to biomedical applications. A plausible mechanism for the growth of bone-like apatite is modeled that relies on the coatings developing a negative charge on their surface on incubation in SBF. This negative charge further takes care of the subsequent reactions on the interface that leads to the formation of dense bone-like apatite, an indicator of superior bioactivity of the thin films. The films showed a high degree of cell viability (>100%) for Day 1, steadily increasing on Day 3. The superior biocompatibility of the thin films is related to the presence of $Ba$ and $Sr$ ions and the HAP layer that traditionally favors the osteoblasts' growth. Furthermore, hydrophobicity is intrinsically related to cell growth over the surfaces, and cell viability is found to improve.

The prime point of this report was the analysis of the electrical properties and their correlation to biological performances. Cell proliferation is found to be related to the dielectric properties of the surfaces. The films displayed modest $\epsilon_r$ ($\sim$ 35-45 at 1 MHz) to create an *in-vivo* internal field. The leakage current analysis was carried

out to complement the dielectric properties, revealing leakage of ($<$ or $=$) 1 $\mu A/cm^2$ within 1-30 kV/cm. The magnitudes are deemed suitable for assisting the generation of polarized electric fields without the possibility of their significant decay (within a short period). Such applications of bilayered films can be novel for biomedical implants in which cytocompatibility and bioactivity are primary concerns.

In chapter 7, a conclusion of the thesis is presented. This is followed by the presentation of the scope of future work.

## 7.2 Scopes for Future Work

In the thesis, we opened up many possibilities and frontiers to work in the future. Beginning from the optical properties of HAP, the study can be taken up further to enhance the optical properties by considering the scenario of doping various rare earth elements such as *Gd*. However, it must be kept in mind that doping rare earths can be possible only up to specific concentrations without making it cytotoxic. This can be tackled by controlling the defect structures in HAP that would be beneficial in keeping the doping concentration very low. In this direction, much emphasis needs to be put in, and we are confident that in the near future, several features of HAP will emerge, leading to the design of bio-imaging gadgets using HAP.

In chapter 3 and Chapter 4, while dealing with the biological properties, we concluded the results from *in vitro* tests. In the next level, the identified composite with the best properties has to be subjected to *in-vivo* tests, where they will be implanted into the rat/mice model for identifying any further complications (if at all it exists) in our specimens. These tests will be beneficial in further tuning the material properties to remove the drawbacks of animal experiments. We intended to design scaffolds from the identified best specimens. The results presented for the fabricated scaffolds are preliminary by nature. Since scaffolds are the products that will be directly applicable for biomedical applications, a technique for mass production of the scaffolds for the industry has to be devised. One such technique is the 3D printing technology, which can design customized scaffolds based on the shape and size of the defect, where the scaffolds are intended to be implanted. The 3D printing technology has certain features that will lead to scanning the area of the bone defect based on which an auto computer aided design (CAD) model shall be generated. This CAD model is used to design the final prototype of the scaffolds with optimized porosity. The prototype scaffolds shall be tested for mechanical properties, which are essential for load-bearing applications and would supplement the animal

experiments performed. Additionally, based on the critical area of application, the mechanical properties can be tuned by optimizing the level of porosity and density of the scaffolds. It would add to the versatility of the scaffolds for considering their commercial applications. We shall be taking up these projects as soon as possible.

We also considered the thin films of $20H - 80S$ and bilayers of BST and HAP as possible coatings for $Ti/Ti$-based alloys. At the next level of the research, we need to consider further *in-vitro* tests such as the protein adsorption using BSA and FBS along with the cell attachment studies and antibacterial tests. The mechanical strength of the coatings needs to be determined further for finding the effectiveness of our developed coatings under harsh *in-vivo* environments. This would help us pre-determine the characteristics of the coatings and lead to the identification of the limitations of the coatings to tune the properties to suit the need for biomedical applications. Following these studies, the animal experiments in a rat/mice/rabbit model need to be considered. For considering the animal experiments, the coatings are required to be developed over specially designed biomedical implants, and these implants are later on substituted in animals. Based on the inputs obtained, if further tuning of the properties is necessary, it has to be done as a part of our requirement for commercialization of the products. Hence, we will take up these projects as an extension of our thesis work in the future.

# Appendix A

# Appendix A

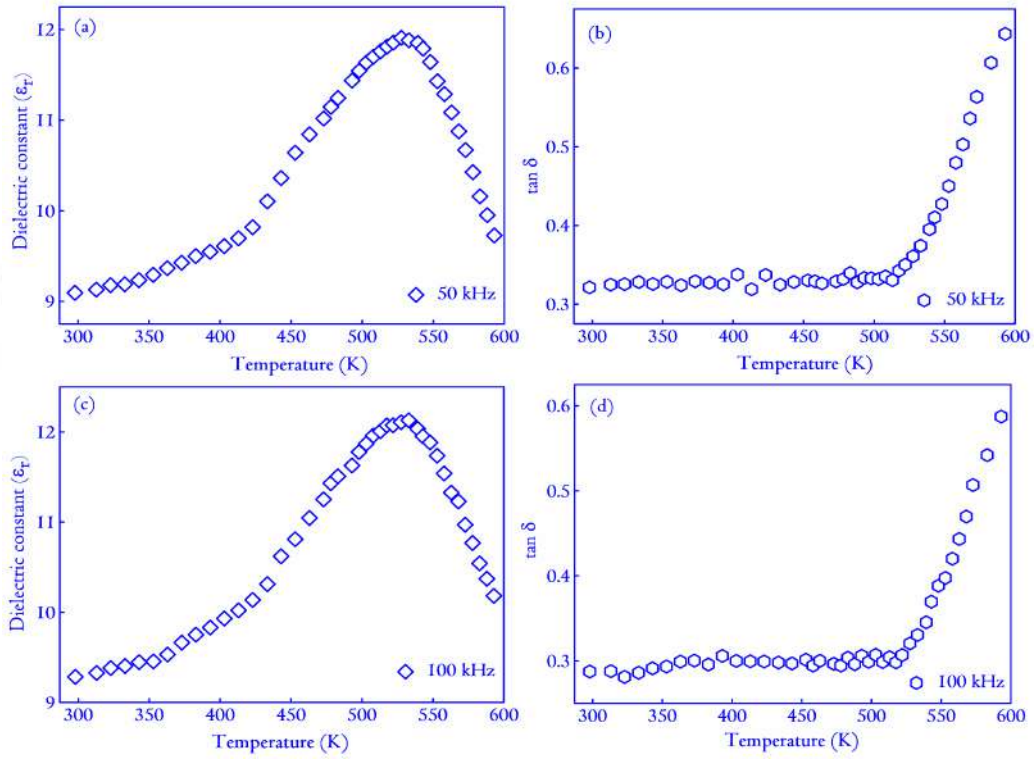


**Figure A.1:** The variation in (a, c) $\epsilon_r$ with temperature and (b, d) variation in tan$\delta$ with temperature. The variations are plotted at frequencies of 50 kHz and 100 kHz.

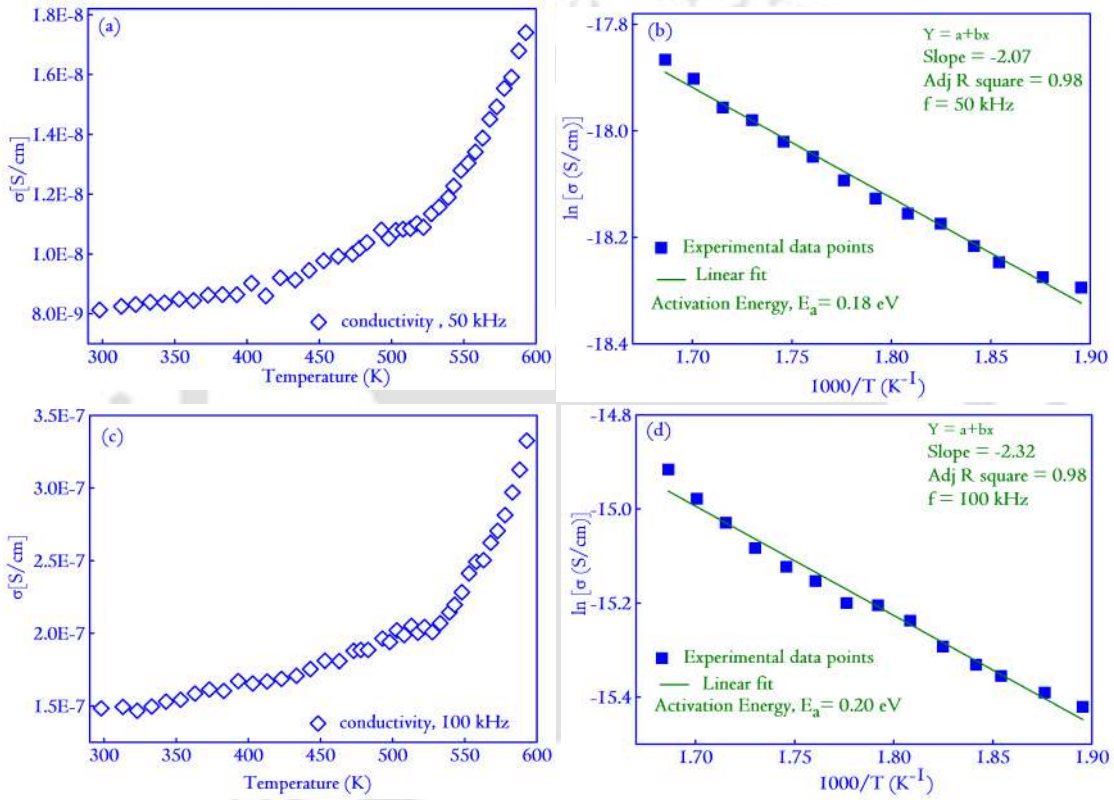


**Figure A.2:** The variation in (a, c) conductivity with temperature and (b, d) represents the Arrhenius plots for determination of the $E_a$. The variations are plotted at frequencies of 50 kHz and 100 kHz.

**Table A.1:** The parameters associated to the deconvolution of the PL spectra.

| Temperature (K) | FWHM | Peak position | Area (%) |
|---|---|---|---|
| 298 | 32.13 | 525.25 | 3.49 |
| | 64.78 | 568.49 | 13.68 |
| | 118.70 | 630.65 | 45.49 |
| | 124.09 | 712.07 | 34.98 |
| | 96.02 | 844.34 | 2.36 |
| 363 | 34.69 | 525.77 | 4.28 |
| | 63.84 | 569.97 | 15.05 |
| | 118.80 | 630.08 | 44.62 |
| | 122.50 | 713.06 | 34.26 |
| | 68..08 | 844.33 | 1.78 |
| 473 | 35.35 | 525.25 | 5.25 |
| | 63.91 | 568.49 | 16.75 |
| | 123.63 | 629.65 | 54.01 |
| | 96.67 | 712.06 | 22.54 |
| | 102.09 | 844.00 | 1.44 |
| 513 | 41.22 | 527.62 | 8.20 |
| | 59.17 | 572.20 | 15.63 |
| | 125.42 | 629.75 | 49.31 |
| | 125.54 | 710.05 | 24.92 |
| | 103.61 | 844.71 | 1.94 |

# Appendix B

# Appendix B

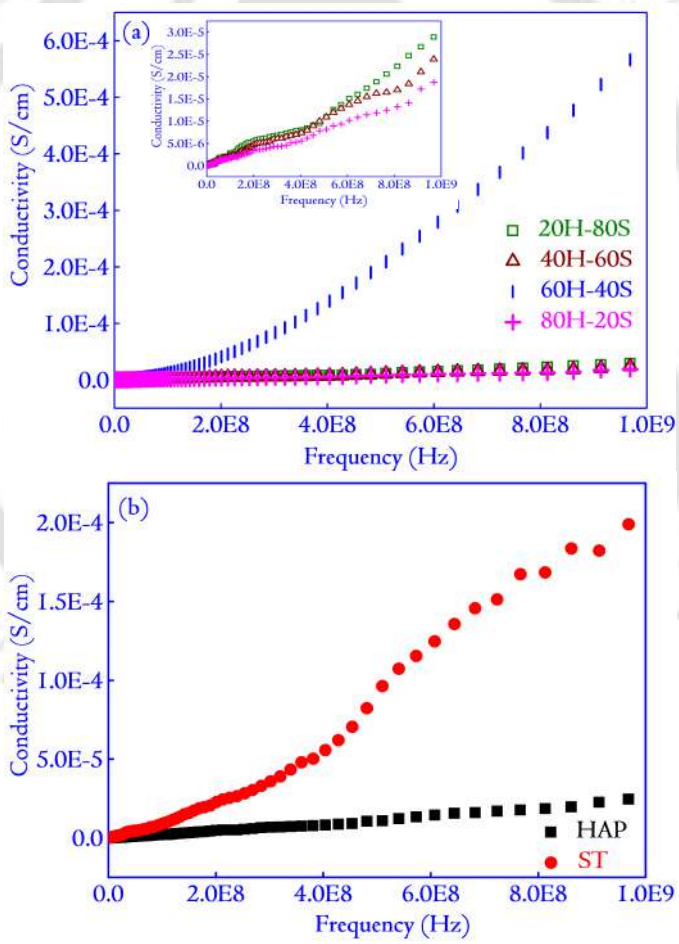


**Figure B.1:** (a) The variation in the conductivity of the specimens with respect to frequency (1 MHz-1 GHz) are shown. In the inset of Figure 3(a), a zoomed in view of the conductivity variation is shown for better viewing the $80H - 20S$, $40H - 60S$, and $20H - 80S$. (b) The variation of conductivity with respect to frequency for the monoliths HAP and ST.

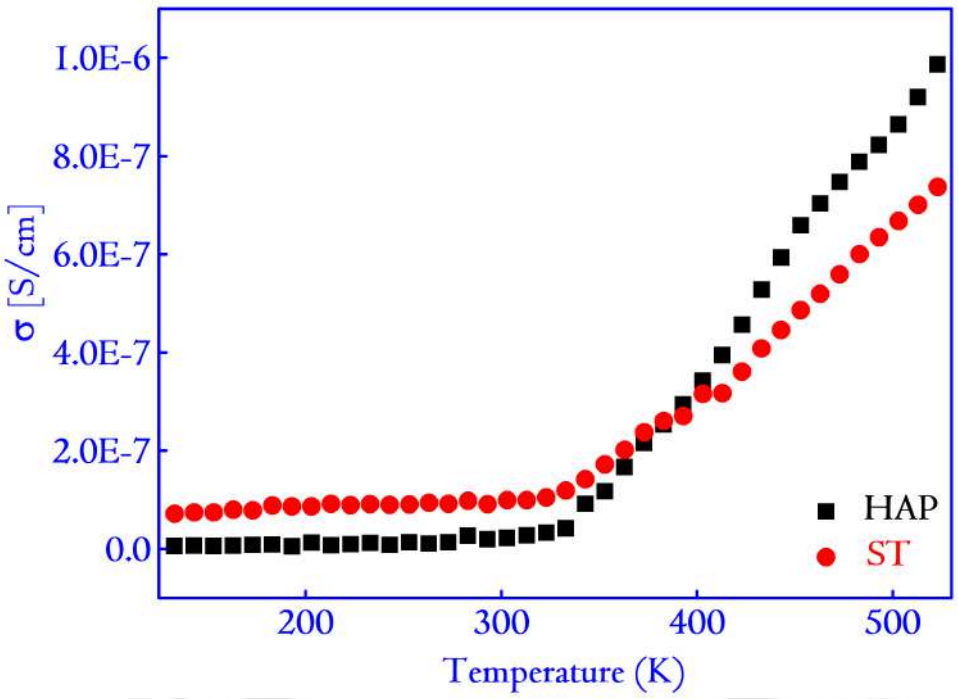


**Figure B.2:** The variation in the conductivity of the monoliths at 1 MHz with respect to temperature.

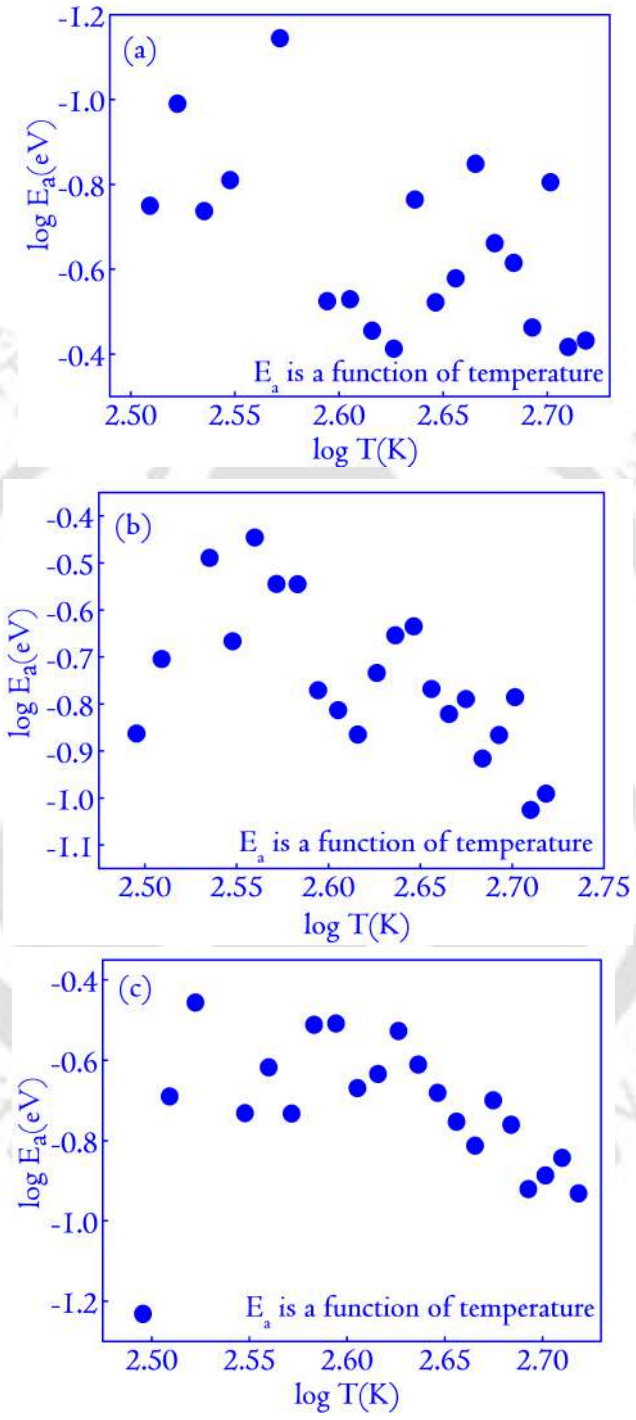


**Figure B.3:** (a), (b) and (c) denotes the variation in the values of $E_a$ with temperature. As there is no specific trend in the variation, it can be concluded that the thermally activated band conduction or the NNH hopping is not active within the specimens.

# Appendix C

# Appendix C

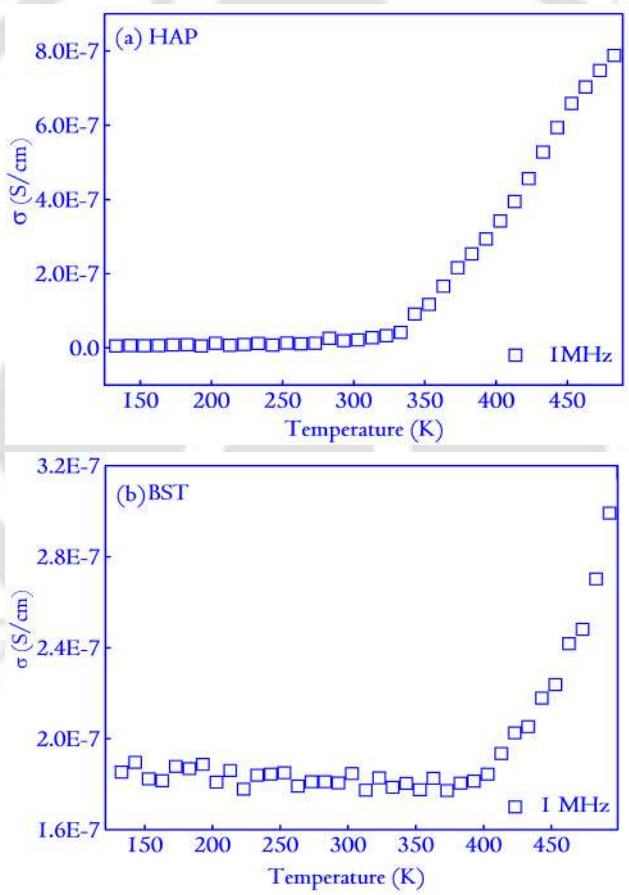


**Figure C.1:** (a), (b) shows the variation in the conductivity of HAP and BST.

**Table C.1:** The variation of $tan\delta$ with temperature for the specimens.

| | Temperature (K) | | | | |
|---|---|---|---|---|---|
| Specimens | 283 | 323 | 373 | 423 | 473 |
| BST | 0.36 | 0.45 | 0.41 | 0.41 | 0.46 |
| HAP | 0.20 | 0.24 | 0.27 | 0.63 | 1.03 |
| 20H-80B | 0.34 | 0.37 | 0.42 | 0.61 | 0.79 |
| 40H-60B | 0.25 | 0.21 | 0.27 | 0.28 | 0.35 |
| 60H-40B | 0.26 | 0.41 | 0.66 | 0.74 | 1.13 |
| 80H-20B | 0.21 | 0.22 | 0.24 | 0.45 | 0.57 |

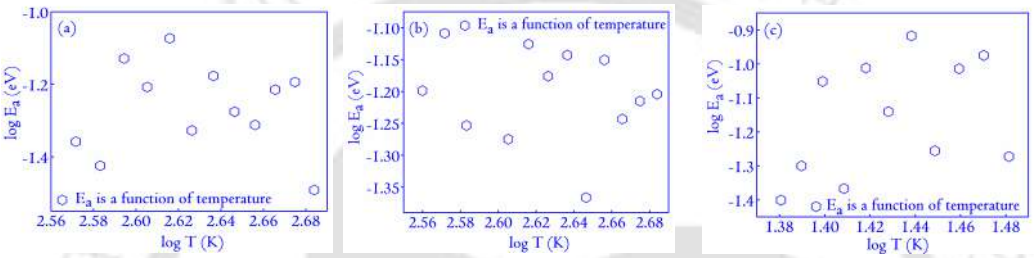


**Figure C.2:** Variation in the values of $E_a$ with temperature T for (a) $40H - 60B$, (b) $60H - 40B$, and (c) $80H - 20B$.

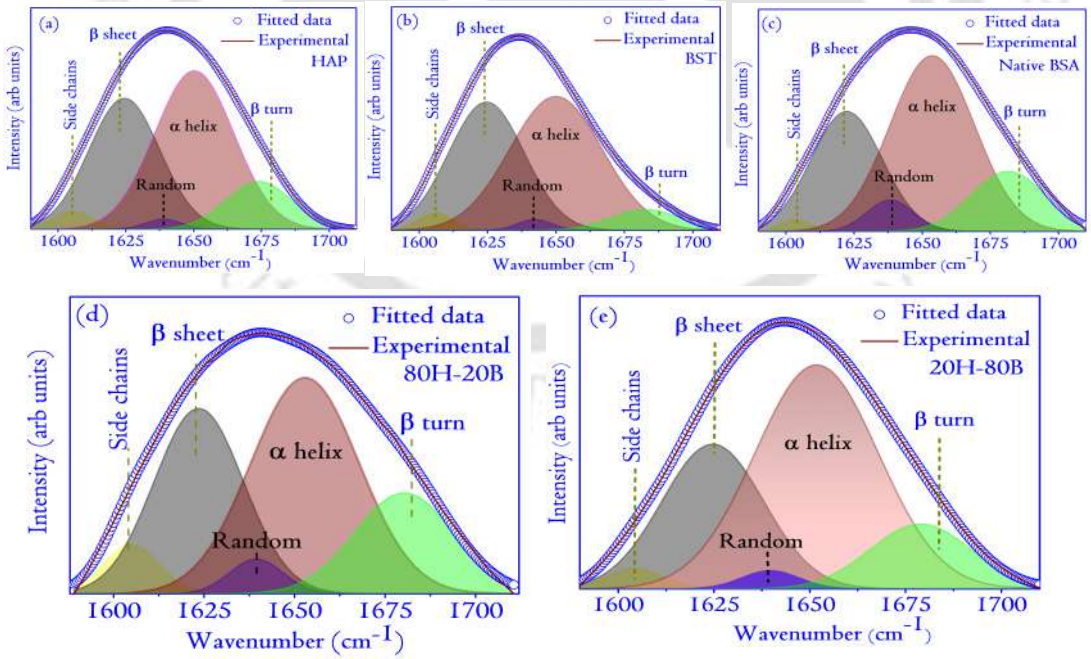


**Figure C.3:** Deconvoluted FTIR spectra (after protein adsorption) for different specimens.

# Appendix D

# Appendix D

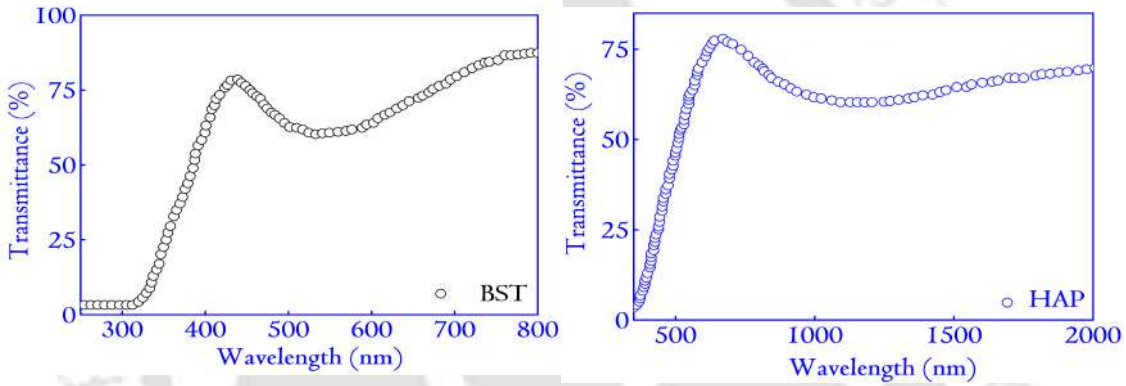


**Figure D.1:** The transmittance spectra of 100 nm BST and 100 nm HAP fabricated over quartz substrates.

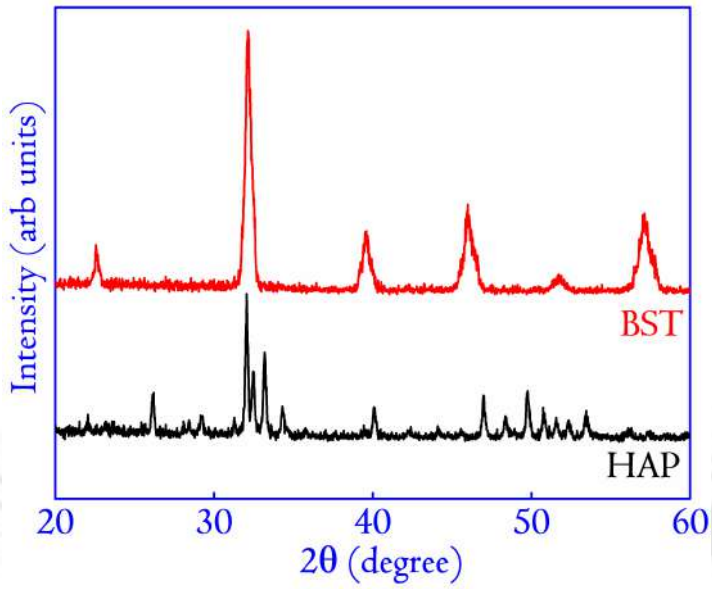


**Figure D.2:** The XRD pattern of the sputtering target fabricated using the technique mentioned in the experimental section.

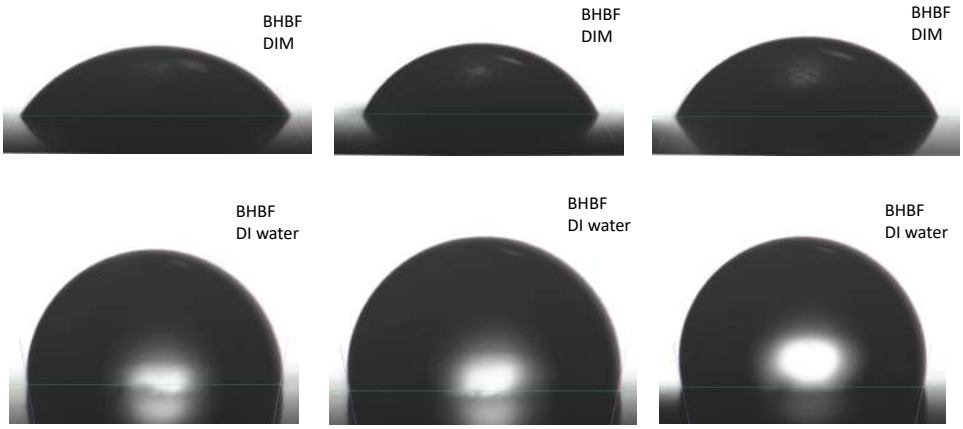


**Figure D.3:** The contact angle of the films measured using DIM and DI water for BHBF.

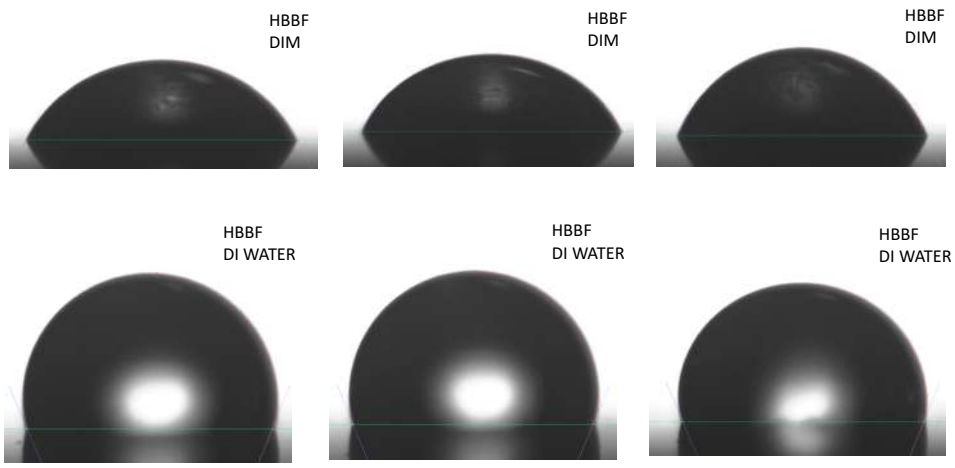


**Figure D.4:** The contact angle of the thin film HBBF using DI water and DIM.

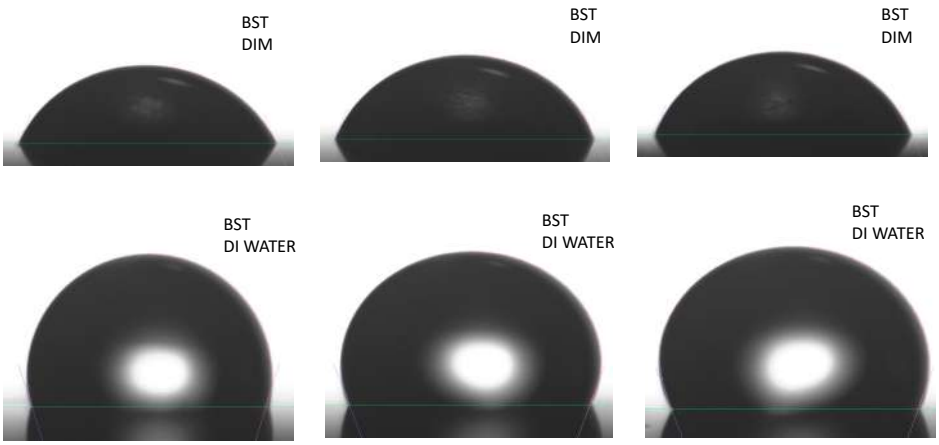


**Figure D.5:** The contact angle of BST thin films using DI water and DIM.

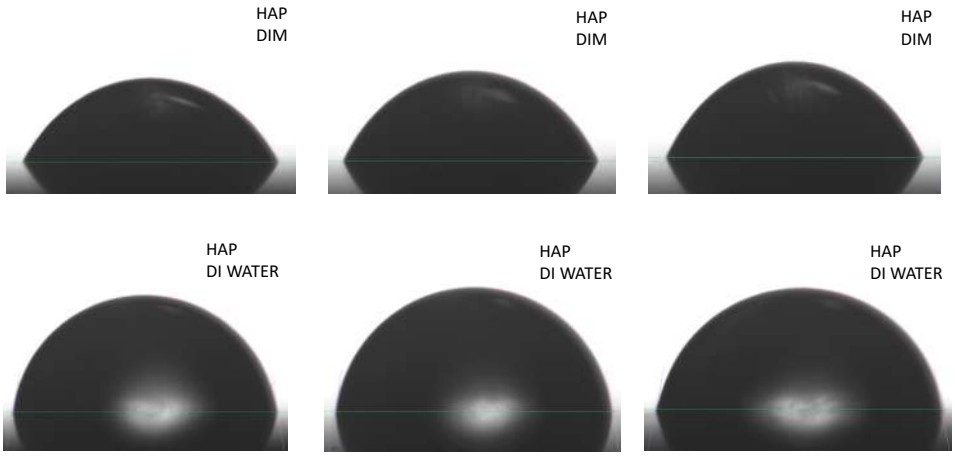


**Figure D.6:** The contact angle of HAP thin films using DI water and DIM.

# Bibliography


[1] D. F. Williams, *The Williams Dictionary of Biomaterials* (Liverpool University Press, 1999).

[2] D. F. Williams, Biomaterials **30**, 5897 (2009).

[3] L. L. Hench, Journal of the American Ceramic Society **74**, 1487 (1991).

[4] W. Cao and L. L. Hench, Ceramics International **22**, 493 (1996).

[5] W. Weng, G. Shen, and G. Han, Journal of Materials Science Letters **19**, 2187 (2000).

[6] K. Cheng, W. Weng, G. Han, P. Du, G. Shen, J. Yang, and J. M. Ferreira, Materials Chemistry and Physics **78**, 767 (2003).

[7] R. E. Riman, W. L. Suchanek, K. Byrappa, C.-W. Chen, P. Shuk, and C. S. Oakes, Solid State Ionics **151**, 393 (2002).

[8] L.-Y. Huang, K.-W. Xu, and J. Lu, Journal of Materials Science: Materials in Medicine **11**, 667 (2000).

[9] W. Weng, S. Zhang, K. Cheng, H. Qu, P. Du, G. Shen, J. Yuan, and G. Han, Surface and Coatings Technology **167**, 292 (2003).

[10] D. Choi, K. G. Marra, and P. N. Kumta, Materials Research Bulletin **39**, 417 (2004).

[11] W. Weng and J. Baptista, Biomaterials **19**, 125 (1998).

[12] K. Cheng, G. Han, W. Weng, H. Qu, P. Du, G. Shen, J. Yang, and J. Ferreira, Materials Research Bulletin **38**, 89 (2003).

[13] K. Cheng, G. Shen, W. Weng, G. Han, J. M. Ferreira, and J. Yang, Materials Letters **51**, 37 (2001).

[14] W. Weng, G. Han, P. Du, and G. Shen, Materials Chemistry and Physics **77**, 578 (2003).

[15] A. J. Salinas and M. Vallet-Regi, Zeitschrift für anorganische und allgemeine Chemie **633**, 1762 (2007).

[16] K. Tomoda, H. Ariizumi, T. Nakaji, and K. Makino, Colloids and Surfaces B: Biointerfaces **76**, 226 (2010).

[17] M. Kester, Y. Heakal, T. Fox, A. Sharma, G. P. Robertson, T. T. Morgan, E. I. Altinoglu, A. Tabakovic, M. R. Parette, S. M. Rouse, V. Ruiz-Velasco, and J. H Adair, Nano Letters **8**, 4116 (2008).

[18] S. Bose and S. Tarafder, Acta Biomaterialia **8**, 1401 (2012).

[19] N. Huebsch and D. J. Mooney, Nature **462**, 426 (2009).

[20] X. Bi, B. Liu, Z. Mao, C. Wang, N. Dunne, Y. Fan, and X. Li, Materials Science and Engineering: C , 111326 (2020).
[21] M. Alizadeh-Osgouei, Y. Li, and C. Wen, Bioactive Materials **4**, 22 (2019).
[22] W. Habraken, J. Wolke, and J. Jansen, Advanced Drug Delivery Reviews **59**, 234 (2007).
[23] W. Bonfield, M. Wang, and K. Tanner, Acta Materialia **46**, 2509 (1998).
[24] A. Vedadghavami, F. Minooei, M. H. Mohammadi, S. Khetani, A. R. Kolahchi, S. Mashayekhan, and A. Sanati-Nezhad, Acta Biomaterialia **62**, 42 (2017).
[25] L. Wang, C. Wang, S. Wu, Y. Fan, and X. Li, Biomaterials Science **8**, 2714 (2020).
[26] J. Oliver-De La Cruz, G. Nardone, J. Vrbsky, A. Pompeiano, A. R. Perestrelo, F. Capradossi, K. Melajová, P. Filipensky, and G. Forte, Biomaterials **205**, 64 (2019).
[27] A. Hasan, V. Saxena, and L. M. Pandey, Langmuir **34**, 3494 (2018).
[28] J. Lu, H. Yu, and C. Chen, RSC Advances **8**, 2015 (2018).
[29] D. Khare, B. Basu, and A. K. Dubey, Biomaterials **258**, 120280 (2020).
[30] J.-H. Chen, C. Liu, L. You, and C. A. Simmons, Journal of Biomechanics **43**, 108 (2010).
[31] P. Vaněk, Z. Kolská, T. Luxbacher, J. García, M. Lehocký, M. Vandrovcová, L. Bačáková, and J. Petzelt, Journal of Physics D: Applied Physics **49**, 175403 (2016).
[32] L. Cui, J. Zhang, J. Zou, X. Yang, H. Guo, H. Tian, P. Zhang, Y. Wang, N. Zhang, X. Zhuang, Z. Li, J. Ding, and X. Chen, Biomaterials **230**, 119617 (2020).
[33] K. C. Kao, *Dielectric Phenomena in Solids* (Elsevier, 2004).
[34] D. M. Ciombor and R. K. Aaron, Foot and Ankle Clinics **10**, 579 (2005).
[35] M. H. Shamos, L. S. Lavine, and M. I. Shamos, Nature **197**, 81 (1963).
[36] A. Blázquez-Castro, A. García-Cabañes, and M. Carrascosa, Applied Physics Reviews **5**, 041101 (2018).
[37] V. Bystrov, E. Seyedhosseini, S. Kopyl, I. Bdikin, and A. Kholkin, Journal of Applied Physics **116**, 066803 (2014).
[38] S. B. Lang, Nature **212**, 704 (1966).
[39] A. A. Gandhi, M. Wojtas, S. B. Lang, A. L. Kholkin, and S. A. Tofail, Journal of the American Ceramic Society **97**, 2867 (2014).
[40] S. Lang, S. Tofail, A. Gandhi, M. Gregor, C. Wolf-Brandstetter, J. Kost, S. Bauer, and M. Krause, Applied Physics Letters **98**, 123703 (2011).
[41] S. Joschek, B. Nies, R. Krotz, and A. Göpferich, Biomaterials **21**, 1645 (2000).
[42] M. Fabbri, G. Celotti, and A. Ravaglioli, Biomaterials **15**, 474 (1994).
[43] R. G. Carrodeguas and S. De Aza, Acta Biomaterialia **7**, 3536 (2011).
[44] B. Caruta, *Ceramics and Composite Materials: New Research* (Nova Publishers, 2006).
[45] C. Benaqqa, J. Chevalier, M. Saädaoui, and G. Fantozzi, Biomaterials **26**, 6106 (2005).

[46] L. J. Cummings, M. A. Snyder, and K. Brisack, Methods in Enzymology **463**, 387 (2009).
[47] K. E. Salyer and C. D. Hall, Plastic and Reconstructive Surgery **84**, 236 (1989).
[48] C. Van Blitterswijk, J. Grote, W. Kuypers, C. Blok-van Hoek, and W. T. Daems, Biomaterials **6**, 243 (1985).
[49] C. N. Trueman and N. Tuross, Reviews in Mineralogy and Geochemistry **48**, 489 (2002).
[50] H.-M. Kim, T. Himeno, T. Kokubo, and T. Nakamura, Biomaterials **26**, 4366 (2005).
[51] "Hydroxyapatite:global markets," `https://finance.yahoo.com/news/hydroxyapatite-global-markets-081200825.html` (2020).
[52] D. Haverty, S. A. Tofail, K. T. Stanton, and J. B. McMonagle, Physical Review B **71**, 094103 (2005).
[53] J. C. Elliott, P. Mackie, and R. Young, Science **180**, 1055 (1973).
[54] K. Matsunaga and A. Kuwabara, Physical Review B **75**, 014102 (2007).
[55] J. Suetsugu, Yasushi and, Journal of Materials Science: Materials in Medicine **13**, 767 (2002).
[56] S. Flores, A. G. Evans, F. W. Zok, M. Genet, B. Cox, D. Marshall, O. Sudre, and Q. Yang, Composites Part A: Applied Science and Manufacturing **41**, 222 (2010).
[57] M. A. Bakar, M. Cheng, S. Tang, S. Yu, K. Liao, C. Tan, K. Khor, and P. Cheang, Biomaterials **24**, 2245 (2003).
[58] L.-C. Zhang and L.-Y. Chen, Advanced Engineering Materials **21**, 1801215 (2019).
[59] J. Zhang, D. Huang, S. Liu, X. Dong, Y. Li, H. Zhang, Z. Yang, Q. Su, W. Huang, W. Zheng, and W. Zhou, Materials Science and Engineering: C **105**, 110054 (2019).
[60] C. Bowen, J. Gittings, I. Turner, F. Baxter, and J. Chaudhuri, Applied Physics Letters **89**, 132906 (2006).
[61] F. Jianqing, Y. Huipin, and Z. Xingdong, Biomaterials **18**, 1531 (1997).
[62] F. R. Baxter, I. G. Turner, C. R. Bowen, J. P. Gittings, and J. B. Chaudhuri, Journal of Materials Science: Materials in Medicine **20**, 1697 (2009).
[63] M. Nakamura, T. Soya, R. Hiratai, A. Nagai, K. Hashimoto, I. Morita, and K. Yamashita, Journal of Biomedical Materials Research Part A **100**, 969 (2012).
[64] H. Zhang, Y. Zhu, Z. Li, P. Fan, W. Ma, and B. Xie, Journal of Alloys and Compounds **744**, 116 (2018).
[65] S. Liu and J. Zhai, Journal of Materials Chemistry A **3**, 1511 (2015).
[66] Y. Xin, J. Jiang, K. Huo, T. Hu, and P. K. Chu, ACS Nano **3**, 3228 (2009).
[67] S. Sahoo, A. Sinha, and M. Das, Journal of the Mechanical Behavior of Biomedical Materials **102**, 103494 (2020).
[68] J. Zhang, J. H. Bang, C. Tang, and P. V. Kamat, ACS Nano **4**, 387 (2010).
[69] C. Wu, Y. Ramaswamy, D. Gale, W. Yang, K. Xiao, L. Zhang, Y. Yin, and H. Zreiqat, Acta Biomaterialia **4**, 569 (2008).
[70] P. Heinl, L. Müller, C. Körner, R. F. Singer, and F. A. Müller, Acta Biomaterialia

**4**, 1536 (2008).
[71] A. Pazo, E. Saiz, and A. Tomsia, Acta Materialia **46**, 2551 (1998).
[72] A. Kania, W. Pilarczyk, and M. M. Szindler, Thin Solid Films **701**, 137945 (2020).
[73] M. Qadir, Y. Li, and C. Wen, Acta Biomaterialia **89**, 14 (2019).
[74] E. Mohseni, E. Zalnezhad, and A. R. Bushroa, International Journal of Adhesion and Adhesives **48**, 238 (2014).
[75] D. A. Hamdi, Z.-T. Jiang, K. No, M. M. Rahman, P.-C. Lee, L. N. T. Truc, J. Kim, M. Altarawneh, L. Thair, T. A.-J. Jumaa, and B. Z. Dlugogorsk, Applied Surface Science **463**, 292 (2019).
[76] K. Prosolov, K. Popova, O. Belyavskaya, J. Rau, K. Gross, A. Ubelis, and Y. P. Sharkeev, Bioactive Materials **2**, 170 (2017).
[77] K. Wasa and S. Hayakawa, *Handbook of Sputter Deposition Technology* (Elsevier, 1992).
[78] K. S. TenHuisen and P. W. Brown, Biomaterials **19**, 2209 (1998).
[79] S.-J. Ding, Biomaterials **24**, 4233 (2003).
[80] S.-J. Ding, C.-P. Ju, and J.-H. C. Lin, Journal of Biomedical Materials Research Part A **44**, 266 (1999).
[81] V. Nelea, C. Morosanu, M. Iliescu, and I. Mihailescu, Surface and Coatings Technology **173**, 315 (2003).
[82] R. Snyders, D. Music, D. Sigumonrong, B. Schelnberger, J. Jensen, and J. Schneider, Applied Physics Letters **90**, 193902 (2007).
[83] B. Majkowska-Marzec, D. Rogala-Wielgus, M. Bartmański, B. Bartosewicz, and A. Zieliński, Coatings **9**, 643 (2019).
[84] V. Cannillo and A. Sola, Journal of the European Ceramic Society **30**, 2031 (2010).
[85] F. Khosravi, S. Nouri Khorasani, S. Khalili, R. Esmaeely Neisiany, E. Rezvani Ghomi, F. Ejeian, O. Das, and M. H. Nasr-Esfahani, Polymers **12**, 1022 (2020).
[86] A. Das and D. Pamu, Materials Science and Engineering: C **101**, 539 (2019).
[87] L. L. Hench and J. K. West, Chemical Reviews **90**, 33 (1990).
[88] A. Das, A. Bhardwaj, S. Rabha, L. M. Pandey, and P. Dobbidi, Journal of the American Ceramic Society **105**, 1790 (2022).
[89] A. K. Galwey, Reaction Kinetics, Mechanisms and Catalysis **114**, 1 (2015).
[90] A. Das and P. Dobbidi, ACS Biomaterials Science & Engineering **7**, 2296 (2021).
[91] K. Wasa, I. Kanno, and H. Kotera, *Handbook of Sputter Deposition Technology: Fundamentals and Applications for Functional Thin Films, Nano-materials and MEMS* (William Andrew, 2012).
[92] R. Behera, A. Das, D. Pamu, L. Pandey, and M. Sankar, Journal of the Mechanical Behavior of Biomedical Materials **86**, 143 (2018).
[93] D. A. Skoog, F. J. Holler, and S. R. Crouch, *Principles of Instrumental Analysis* (Cengage learning, 2017).
[94] H. H. Willard, L. L. Merritt Jr, J. A. Dean, and F. A. Settle Jr, *Instrumental Methods of Analysis* (Florence, KY (US); Wadsworth Publishing Company, 1988).

[95] R. Swanepoel, Journal of Physics E: Scientific Instruments **16**, 1214 (1983).
[96] T. Kokubo and H. Takadama, Biomaterials **27**, 2907 (2006).
[97] A. Das, P. Dobbidi, A. Bhardwaj, V. Saxena, and L. M. Pandey, Scientific Reports **11**, 22304 (2021).
[98] A. Hasan, G. Waibhaw, and L. M. Pandey, Langmuir **34**, 8178 (2018).
[99] A. Hasan and L. M. Pandey, Materials Science and Engineering: C **68**, 423 (2016).
[100] A. Hasan, G. Waibhaw, V. Saxena, and L. M. Pandey, International Journal of Biological Macromolecules **111**, 923 (2018).
[101] T. Mosmann, Journal of Immunological Methods **65**, 55 (1983).
[102] A. Billiau, V. Edy, H. Heremans, J. Van Damme, J. Desmyter, J. Georgiades, and P. De Somer, Antimicrobial Agents and Chemotherapy **12**, 11 (1977).
[103] J. Ryu, S. H. Ku, H. Lee, and C. B. Park, Advanced Functional Materials **20**, 2132 (2010).
[104] M. I. Kay, R. Young, and A. Posner, Nature **204**, 1050 (1964).
[105] A. Slepko and A. A. Demkov, Physical Review B **84**, 134108 (2011).
[106] H. Athenstaedt, H. Claussen, and D. Schaper, Science **216**, 1018 (1982).
[107] A. C. Ahn and A. J. Grodzinsky, Medical Engineering & Physics **31**, 733 (2009).
[108] W. S. Williams and L. Perletz, Nature New Biology **233**, 58 (1971).
[109] J. Elliott, Nature Physical Science **230**, 72 (1971).
[110] S. Hu, F. Jia, C. Marinescu, F. Cimpoesu, Y. Qi, Y. Tao, A. Stroppa, and W. Ren, RSC Advances **7**, 21375 (2017).
[111] L. Calderin, M. Stott, and A. Rubio, Physical Review B **67**, 134106 (2003).
[112] N. Horiuchi, N. Wada, K. Nozaki, M. Nakamura, A. Nagai, and K. Yamashita, Journal of Applied Physics **119**, 084903 (2016).
[113] N. Horiuchi, Y. I ki, K. Nozaki, M. Nakamura, K. Hashimoto, A. Nagai, and K. Yamashita, Journal of the American Ceramic Society **100**, 501 (2017).
[114] N. Horiuchi, K. Madokoro, K. Nozaki, M. Nakamura, K. Katayama, A. Nagai, and K. Yamashita, Solid State Ionics **315**, 19 (2018).
[115] K. Momma and F. Izumi, Journal of Applied Crystallography **44**, 1272 (2011).
[116] H. Suda, M. Yashima, M. Kakihana, and M. Yoshimura, The Journal of Physical Chemistry **99**, 6752 (1995).
[117] V. J. Huerta, P. Fernández, V. Gómez, O. A. Graeve, and M. Herrera, Applied Materials Today **21**, 100822 (2020).
[118] Y. Xie, W. He, F. Li, T. S. H. Perera, L. Gan, Y. Han, X. Wang, S. Li, and H. Dai, ACS Applied Materials & Interfaces **8**, 10212 (2016).
[119] J. M. Leger, P. Tomaszewski, A. Atouf, and A. S. Pereira, Physical Review B **47**, 14075 (1993).
[120] M. Yashima, H. Arashi, M. Kakihana, and M. Yoshimura, Journal of the American Ceramic Society **77**, 1067 (1994).
[121] A. Hadrich, A. Lautié, and T. Mhiri, Journal of Raman Spectroscopy **32**, 33 (2001).
[122] G. Penel, G. Leroy, C. Rey, and E. Bres, Calcified Tissue International **63**, 475 (1998).

[123] B. K. Sarma, A. Das, P. Barman, and A. R. Pal, Journal of Physics D: Applied Physics **49**, 145304 (2016).
[124] H. Tsuda and J. Arends, Journal of Dental Research **73**, 1703 (1994).
[125] A. Antonakos, E. Liarokapis, and T. Leventouri, Biomaterials **28**, 3043 (2007).
[126] A. Slepko and A. A. Demkov, Journal of Applied Physics **117**, 074701 (2015).
[127] M. A. Reshchikov, Journal of Applied Physics **115**, 012010 (2014).
[128] V. S. Bystrov, L. A. Avakyan, E. V. Paramonova, and J. Coutinho, The Journal of Physical Chemistry C **123**, 4856 (2019).
[129] R. Das, S. Parveen, A. Bora, and P. Giri, Carbon **160**, 273 (2020).
[130] T. R. Machado, J. C. Sczancoski, H. Beltran-Mir, M. S. Li, J. Andres, E. Cordoncillo, E. Leite, and E. Longo, Ceramics International **44**, 236 (2018).
[131] J. Soares da Silva, T. R. Machado, T. A. Martins, M. Assis, C. C. Foggi, N. G. Macedo, H. Beltran-Mir, E. Cordoncillo, J. Andres, and E. Longo, Inorganic Chemistry **58**, 5900 (2019).
[132] S. Rabha and P. Dobbidi, Applied Surface Science **489**, 831 (2019).
[133] G. Gonzalez, C. Costa-Vera, L. J. Borrero, D. Soto, L. Lozada, J. I. Chango, J. C. Diaz, and L. Lascano, Journal of Luminescence **195**, 385 (2018).
[134] V. Bystrov, C. Piccirillo, D. Tobaldi, P. Castro, J. Coutinho, S. Kopyl, and R. Pullar, Applied Catalysis B: Environmental **196**, 100 (2016).
[135] V. Bystrov, J. Coutinho, A. Bystrova, Y. D. Dekhtyar, R. Pullar, A. Poronin, E. Palcevskis, A. Dindune, B. Alkan, C. Durucan, and E. V. Paramanova, Journal of Physics D: Applied Physics **48**, 195302 (2015).
[136] T. Ikoma, A. Yamazaki, S. Nakamura, and M. Akao, Journal of Materials Science Letters **18**, 1225 (1999).
[137] H. Chen, X. Fu, Q. An, B. Tang, S. Zhang, H. Yang, Y. Long, M. Harfouche, H. Wang, and Y. Li, Scientific Reports **7**, 1 (2017).
[138] R. Tang, C. Jiang, W. Qian, J. Jian, X. Zhang, H. Wang, and H. Yang, Scientific Reports **5**, 1 (2015).
[139] J. C. Dyre, Physical Review B **48**, 12511 (1993).
[140] N. Hitmi, C. LaCabanne, and R. Young, Journal of Physics and Chemistry of Solids **47**, 533 (1986).
[141] S. Nakamura, H. Takeda, and K. Yamashita, Journal of Applied Physics **89**, 5386 (2001).
[142] N. Hitmi, C. LaCabanne, and R. Young, Journal of Physics and Chemistry of Solids **49**, 541 (1988).
[143] A. H. Rajabi, M. Jaffe, and T. L. Arinzeh, Acta Biomaterialia **24**, 12 (2015).
[144] B. Tandon, J. J. Blaker, and S. H. Cartmell, Acta Biomaterialia **73**, 1 (2018).
[145] M. H. Shamos and L. S. Lavine, Nature **213**, 267 (1967).
[146] S.-W. Yu, S.-T. Kuo, W.-H. Tuan, Y.-Y. Tsai, and C.-H. Su, Materials Letters **65**, 3522 (2011).
[147] Q. Wang, Q. Chen, J. Zhu, C. Huang, B. W. Darvell, and Z. Chen, Materials

Chemistry and Physics **109**, 488 (2008).
[148] N. Wada, N. Horiuchi, K. Mukougawa, K. Nozaki, M. Nakamura, A. Nagai, T. Okura, and K. Yamashita, Materials Research Bulletin **74**, 50 (2016).
[149] S. Itoh, S. Nakamura, T. Kobayashi, K. Shinomiya, and K. Yamashita, Calcified Tissue International **78**, 133 (2006).
[150] S. Itoh, S. Nakamura, M. Nakamura, K. Shinomiya, and K. Yamashita, Artificial Organs **30**, 863 (2006).
[151] M. Nakamura, A. Nagai, T. Hentunen, J. Salonen, Y. Sekijima, T. Okura, K. Hashimoto, Y. Toda, H. Monma, and K. Yamashita, ACS Applied Materials & Interfaces **1**, 2181 (2009).
[152] S. Bodhak, S. Bose, and A. Bandyopadhyay, Acta Biomaterialia **5**, 2178 (2009).
[153] C. Fu, K. Savino, P. Gabrys, A. Zeng, B. Guan, D. Olvera, C. Wang, B. Song, H. Awad, Y. Gao, and M. Z. Yates, Chemistry of Materials **27**, 1164 (2015).
[154] A. K. Dubey, G. Tripathi, and B. Basu, Journal of Biomedical Materials Research Part B: Applied Biomaterials **95**, 320 (2010).
[155] A. K. Dubey and B. Basu, Journal of the American Ceramic Society **97**, 481 (2014).
[156] A. K. Dubey and K.-i. Kakimoto, Materials Science and Engineering: C **63**, 211 (2016).
[157] Y. Zhang, L. Chen, J. Zeng, K. Zhou, and D. Zhang, Materials Science and Engineering: C **39**, 143 (2014).
[158] A. Dubey, B. Basu, K. Balani, R. Guo, and A. Bhalla, Ferroelectrics **423**, 63 (2011).
[159] S. Best, A. Porter, E. Thian, and J. Huang, Journal of the European Ceramic Society **28**, 1319 (2008).
[160] B. L. Phoon, C. W. Lai, J. C. Juan, P.-L. Show, and G.-T. Pan, International Journal of Hydrogen Energy **44**, 14316 (2019).
[161] Q. Li, C. W. Kartikowati, S. Horie, T. Ogi, T. Iwaki, and K. Okuyama, Scientific Reports **7**, 1 (2017).
[162] Y. Wang, D. Zhang, C. Wen, and Y. Li, ACS Applied Materials & Interfaces **7**, 16018 (2015).
[163] S. L. Hirsh, D. R. McKenzie, N. J. Nosworthy, J. A. Denman, O. U. Sezerman, and M. M. Bilek, Colloids and Surfaces B: Biointerfaces **103**, 395 (2013).
[164] V. Hlady and J. Buijs, Current Opinion in Biotechnology **7**, 72 (1996).
[165] F. Bartolomeu, M. Sampaio, O. Carvalho, E. Pinto, N. Alves, J. Gomes, F. S. Silva, and G. Miranda, Journal of the Mechanical Behavior of Biomedical Materials **69**, 128 (2017).
[166] B. Gross, Physical Review **66**, 26 (1944).
[167] W. Cui, X. Li, C. Xie, H. Zhuang, S. Zhou, and J. Weng, Biomaterials **31**, 4620 (2010).
[168] C. Nah, S. H. Han, J.-H. Lee, M.-H. Lee, S. D. Lim, and J. M. Rhee, Composites Part B: Engineering **35**, 125 (2004).
[169] R. Subasri, D. Matusch, H. Näfe, and F. Aldinger, Journal of the European Ceramic

Society **24**, 129 (2004).
[170] I. Mobasherpour, M. S. Heshajin, A. Kazemzadeh, and M. Zakeri, Journal of Alloys and Compounds **430**, 330 (2007).
[171] A. Monshi, M. R. Foroughi, and M. R. Monshi, World Journal of Nano Science and Engineering **2**, 154 (2012).
[172] T. Klaytae, P. Panthong, and S. Thountom, Ceramics International **39**, S405 (2013).
[173] C.-H. Chang and Y.-H. Shen, Materials Letters **60**, 129 (2006).
[174] A. J. Ruys, *Alumina Ceramics: Biomedical and Clinical Applications* (Woodhead Publishing, 2018).
[175] U. Balachandran and N. Eror, Journal of the American Ceramic Society **65**, c54 (1982).
[176] P. I. Gouma and M. J. Mills, Journal of the American Ceramic Society **84**, 619 (2001).
[177] W. Taylor and A. Murray, Solid State Communications **31**, 937 (1979).
[178] S. Qin, X. Wu, F. Seifert, and A. I. Becerro, Journal of the Chemical Society, Dalton Transactions , 3751 (2002).
[179] A. Karakuscu, M. Cologna, D. Yarotski, J. Won, J. S. Francis, R. Raj, and B. P. Uberuaga, Journal of the American Ceramic Society **95**, 2531 (2012).
[180] N. Horiuchi, S. Nakaguki, N. Wada, K. Nozaki, M. Nakamura, A. Nagai, K. Katayama, and K. Yamashita, Journal of Applied Physics **116**, 014902 (2014).
[181] K. H. Müller, M. Motskin, A. J. Philpott, A. F. Routh, C. M. Shanahan, M. J. Duer, and J. N. Skepper, Biomaterials **35**, 1074 (2014).
[182] D. E. Newbury and N. W. Ritchie, Scanning **35**, 141 (2013).
[183] C. P. Klein, J. de Blieck-Hogemrst, J. Wolket, and K. De Groot, Biomaterials **11**, 509 (1990).
[184] H. R. Ramay and M. Zhang, Biomaterials **25**, 5171 (2004).
[185] P. Feng, M. Niu, C. Gao, S. Peng, and C. Shuai, Scientific Reports **4**, 1 (2014).
[186] M. A. Saifi and L. Cross, Physical Review B **2**, 677 (1970).
[187] A. Linz Jr, Physical Review **91**, 753 (1953).
[188] I. K. Sharp and R. Lightwood, Injury **14**, 523 (1983).
[189] J. W. Zimmerman, H. Jimenez, M. J. Pennison, I. Brezovich, D. Morgan, A. Mudry, F. P. Costa, A. Barbault, and B. Pasche, Chinese Journal of Cancer **32**, 573 (2013).
[190] O. Korostynska, A. A. Gandhi, A. Mason, A. Al-Shamma'a, and S. A. Tofail, in *Key Engineering Materials*, Vol. 543 (Trans Tech Publ, 2013) pp. 26–29.
[191] R. Augustine, U. G. Kalappura, and K. Mathew, Microwave and Optical Technology Letters **50**, 2931 (2008).
[192] T. Hoshina, R. Sase, J. Nishiyama, H. Takeda, and T. Tsurumi, Journal of the Ceramic Society of Japan **126**, 263 (2018).
[193] A. Tkach, J. S. Amaral, S. Zlotnik, V. S. Amaral, and P. M. Vilarinho, Journal of the European Ceramic Society **38**, 605 (2018).
[194] M. T. Sebastian, *Dielectric materials for wireless communication* (Elsevier, 2010).

[195] S. Y. Wong, J. Hassan, and M. Hashim, Solid State Science and Technology **17**, 57 (2009).
[196] L. Wang, X. Deng, J. Li, G. Zhang, C. Wang, and K. Su, Materials Research Innovations **17**, 190 (2013).
[197] X.-G. Tang and H. L.-W. Chan, Journal of Applied Physics **97**, 034109 (2005).
[198] M. Menendez, A. Ishihara, S. Weisbrode, and A. Bertone, Clinical Orthopaedics and Related Research **468**, 1157 (2010).
[199] A. Bertone, D. Lipson, J. Kamei, A. Litsky, and S. Weisbrode, Clinical Orthopaedics and Related Research **446**, 278 (2006).
[200] C. Goldstein, S. Sprague, and B. A. Petrisor, Journal of Orthopaedic Trauma **24**, S62 (2010).
[201] M. Griffin and A. Bayat, Eplasty **11** (2011).
[202] H. Han, C. Davis III, and J. C. Nino, The Journal of Physical Chemistry C **118**, 9137 (2014).
[203] M. Zubair Ansari and N. Khare, Journal of Applied Physics **117**, 025706 (2015).
[204] I. Shlimak, *Is hopping a science?: selected topics of hopping conductivity* (World Scientific, 2015).
[205] S. Pattipaka, A. James, and P. Dobbidi, Journal of Alloys and Compounds **765**, 1195 (2018).
[206] T. Lin, S. Young, C. Kung, H. Chen, M. Kao, M. Chang, and C. Ou, IEEE Transactions on Nanotechnology **13**, 425 (2013).
[207] T. Hu and B. Shklovskii, Physical Review B **74**, 054205 (2006).
[208] A. Somoza, M. Ortuno, and M. Pollak, Physical Review B **73**, 045123 (2006).
[209] A. Zabrodskiĭ and K. Zinov'eva, ZhETF Pisma Redaktsiiu **37**, 369 (1983).
[210] S. Pattipaka, M. Peddigari, and P. Dobbidi, Materials Science and Engineering: B **252**, 114470 (2020).
[211] E. Bäuerlein, *Handbook of biomineralization* (Wiley-VCH, 2007).
[212] M. T. Buscaglia, M. Viviani, V. Buscaglia, L. Mitoseriu, A. Testino, P. Nanni, Z. Zhao, M. Nygren, C. Harnagea, D. Piazza, and C. Galassi, Physical Review B **73**, 064114 (2006).
[213] A. Najafinezhad, M. Abdellahi, H. Ghayour, A. Soheily, A. Chami, and A. Khandan, Materials Science and Engineering: C **72**, 259 (2017).
[214] C. Drouet, BioMed Research International **2013**, 1 (2013).
[215] J. A. Rincón-López, J. A. Hermann-Muñoz, N. Cinca-Luis, B. Garrido-Domiguez, I. García-Cano, J. M. Guilemany-Casadamon, J. M. Alvarado-Orozco, and J. Munoz-Saldana, Crystal Growth & Design **19**, 5005 (2019).
[216] E. Skwarek, W. Janusz, V. Gun'ko, E. Pakhlov, V. Zarko, and K. Gdula, Adsorption **22**, 725 (2016).
[217] H.-M. Kim, T. Himeno, M. Kawashita, T. Kokubo, and T. Nakamura, Journal of the Royal Society Interface **1**, 17 (2004).
[218] J. Coreno and O. Coreno, Journal of Biomedical Materials Research Part A **75**, 478

(2005).
[219] M. B. López, B. Rand, and F. Riley, Journal of the European Ceramic Society **20**, 107 (2000).
[220] D. Furlong and G. Parfitt, Journal of Colloid and Interface Science **65**, 548 (1978).
[221] Y. Gu, B. Tay, C. Lim, and M. Yong, Biomaterials **26**, 6916 (2005).
[222] L. M. Pandey and S. K. Pattanayek, Applied Surface Science **257**, 4731 (2011).
[223] A. I. Rubinstein, R. F. Sabirianov, and F. Namavar, Nanotechnology **27**, 415703 (2016).
[224] K. Kandori, S. Tsuyama, H. Tanaka, and T. Ishikawa, Colloids and Surfaces B: Biointerfaces **58**, 98 (2007).
[225] S. Samimi, N. Maghsoudnia, R. B. Eftekhari, and F. Dorkoosh, *Characterization and Biology of Nanomaterials for Drug Delivery* (Elsevier, 2019).
[226] E. A. Vogler, Biomaterials **33**, 1201 (2012).
[227] V. Saxena and L. M. Pandey, Journal of Trace Elements in Medicine and Biology **57**, 126416 (2020).
[228] R. T. Candidato Jr, C. Thouzellier, and L. Pawłowski, Journal of Biomedical Materials Research Part B: Applied Biomaterials **106**, 2101 (2018).
[229] X. D. Zhu, H. S. Fan, C. Y. Zhao, T. Ikoma, M. Tanaka, J. Y. Chen, and X. D. Zhang, in *Key Engineering Materials*, Vol. 309 (Trans Tech Publ, 2006) pp. 73–76.
[230] K. Bazaka and M. V. Jacob, Electronics **2**, 1 (2013).
[231] E. Romero, *Powering biomedical devices* (Academic Press, 2013).
[232] I. Firkowska-Boden, X. Zhang, and K. D. Jandt, Advanced Healthcare Materials **7**, 1700995 (2018).
[233] S. Datta, S. Jana, A. Das, A. Chakraborty, A. R. Chowdhury, and P. Datta, Bioactive Materials **5**, 569 (2020).
[234] B. Feng, Z. Jinkang, W. Zhen, L. Jianxi, C. Jiang, L. Jian, M. Guolin, and D. Xin, Biomedical Materials **6**, 015007 (2011).
[235] B. Amin, M. A. Elahi, A. Shahzad, E. Porter, and M. O'Halloran, Biomedical Physics & Engineering Express **5**, 022001 (2019).
[236] A. Das, E. Barua, S. K. Mushahary, A. Bhardwaj, V. Saxena, L. Pandey, A. Deoghare, and P. Dobbidi, Materials Letters **304**, 130668 (2021).
[237] A. K. Dubey, A. EA, K. Balani, and B. Basu, Journal of the American Ceramic Society **96**, 3753 (2013).
[238] T. Tariverdian, A. Behnamghader, P. B. Milan, H. Barzegar-Bafrooei, and M. Mozafari, Ceramics International **45**, 14029 (2019).
[239] O. Gokcekaya, K. Ueda, T. Narushima, and C. Ergun, Materials Science and Engineering: C **53**, 111 (2015).
[240] J. Knowles, S. Callcut, and G. Georgiou, Biomaterials **21**, 1387 (2000).
[241] M. Rouahi, E. Champion, O. Gallet, A. Jada, and K. Anselme, Colloids and Surfaces B: Biointerfaces **47**, 10 (2006).
[242] C. Combes and C. Rey, Acta Biomaterialia **6**, 3362 (2010).

[243] H. Rahmani and E. Salahinejad, Ceramics International **44**, 19200 (2018).
[244] Y.-C. Liu, Y.-T. Lee, T.-C. Huang, G.-S. Lin, Y.-W. Chen, B.-S. Lee, and K.-L. Tung, ACS Applied Bio Materials **4**, 2523 (2021).
[245] W. Zhang, Y. Shen, H. Pan, K. Lin, X. Liu, B. W. Darvell, W. W. Lu, J. Chang, L. Deng, D. Wang, and W. Huang, Acta Biomaterialia **7**, 800 (2011).
[246] V. Aina, L. Bergandi, G. Lusvardi, G. Malavasi, F. E. Imrie, I. R. Gibson, G. Cerrato, and D. Ghigo, Materials Science and Engineering: C **33**, 1132 (2013).
[247] Q. Zhang, J. Zhai, L. Kong, and X. Yao, Journal of Applied Physics **112**, 124112 (2012).
[248] W. Huo, Y. Chen, Z. Zhang, J. Liu, S. Yan, J.-M. Wu, X. Zhang, and J. Yang, Journal of the American Ceramic Society **101**, 1737 (2018).
[249] L. Zhang, P. Wu, Y. Li, Z.-Y. Cheng, and J. C. Brewer, Composites Part B: Engineering **56**, 284 (2014).
[250] P. Wang, Y. Li, and Y. Lu, Journal of the European Ceramic Society **31**, 2005 (2011).
[251] L. Wang, W. Ren, P. Shi, X. Chen, X. Wu, and X. Yao, Applied Physics Letters **97**, 072902 (2010).
[252] T. Hu, J. Juuti, H. Jantunen, and T. Vilkman, Journal of the European Ceramic Society **27**, 3997 (2007).
[253] X. Lu, Y. Tong, H. Talebinezhad, L. Zhang, and Z.-Y. Cheng, Journal of Alloys and Compounds **745**, 127 (2018).
[254] R. Waser and R. Hagenbeck, Acta Materialia **48**, 797 (2000).
[255] M. Arbatti, X. Shan, and Z.-Y. Cheng, Advanced Materials **19**, 1369 (2007).
[256] A.-M. Yousefi, H. Oudadesse, R. Akbarzadeh, E. Wers, and A. Lucas-Girot, Nanotechnology Reviews **3**, 527 (2014).
[257] S. Rabha and P. Dobbidi, Journal of Materials Science: Materials in Electronics **30**, 5327 (2019).
[258] A. S. Roy, S. Gupta, S. Sindhu, A. Parveen, and P. C. Ramamurthy, Composites Part B: Engineering **47**, 314 (2013).
[259] T. Iglesias, G. Vilao, and J. C. R. Reis, Journal of Applied Physics **122**, 074102 (2017).
[260] Y. Tanaka, T. Iwasaki, M. Nakamura, A. Nagai, K. Katayama, and K. Yamashita, Journal of Applied Physics **107**, 014107 (2010).
[261] F. Kremer and A. Schönhals, *Broadband dielectric spectroscopy* (Springer Science & Business Media, 2002).
[262] S. Kasamatsu and O. Sugino, Physical Chemistry Chemical Physics **20**, 8744 (2018).
[263] T. Matsumoto, M. Okazaki, M. Inoue, S. Yamaguchi, T. Kusunose, T. Toyonaga, Y. Hamada, and J. Takahashi, Biomaterials **25**, 3807 (2004).
[264] G. Yin, Z. Liu, J. Zhan, F. Ding, and N. Yuan, Chemical Engineering Journal **87**, 181 (2002).
[265] J. Liu, H. Jiang, and X.-Y. Liu, The Journal of Physical Chemistry B **110**, 9085

(2006).
[266] A. Serro, M. Bastos, J. C. Pessoa, and B. Saramago, Journal of Biomedical Materials Research Part A **70**, 420 (2004).
[267] A. Z. Alshemary, A. E. Pazarceviren, A. Tezcaner, and Z. Evis, RSC Advances **6**, 68058 (2016).
[268] M. Frasnelli, F. Cristofaro, V. M. Sglavo, S. Dirè, E. Callone, R. Ceccato, G. Bruni, A. I. Cornaglia, and L. Visai, Materials Science and Engineering: C **71**, 653 (2017).
[269] X. Fang, O. K. Tan, Y. Y. Gan, and M. S. Tse, Sensors and Actuators B: Chemical **149**, 381 (2010).
[270] M. Tagaya, T. Ikoma, S. Migita, M. Okuda, T. Takemura, N. Hanagata, T. Yoshioka, and J. Tanaka, Materials Science and Engineering: B **173**, 176 (2010).
[271] H. Jiao, K. Zhao, T. Bian, and Y. Tang, Journal of Alloys and Compounds **715**, 73 (2017).
[272] A. Svensson, E. Nicklasson, T. Harrah, B. Panilaitis, D. Kaplan, M. Brittberg, and P. Gatenholm, Biomaterials **26**, 419 (2005).
[273] V. Karageorgiou and D. Kaplan, Biomaterials **26**, 5474 (2005).
[274] R. K. Saini, L. P. Bagri, and A. Bajpai, Colloids and Surfaces B: Biointerfaces **177**, 211 (2019).
[275] Y.-P. Lu, M.-S. Li, S.-T. Li, Z.-G. Wang, and R.-F. Zhu, Biomaterials **25**, 4393 (2004).
[276] A. Das, A. K. Chikkala, G. P. Bharti, R. R. Behera, R. S. Mamilla, A. Khare, and P. Dobbidi, Journal of Alloys and Compounds **739**, 729 (2018).
[277] C.-M. Xie, X. Lu, K.-F. Wang, F.-Z. Meng, O. Jiang, H.-P. Zhang, W. Zhi, and L.-M. Fang, ACS Applied Materials & Interfaces **6**, 8580 (2014).
[278] T. Kokubo, Acta Materialia **46**, 2519 (1998).
[279] B. Tandon, A. Magaz, R. Balint, J. J. Blaker, and S. H. Cartmell, Advanced Drug Delivery Reviews **129**, 148 (2018).
[280] S. Lang, S. Tofail, A. Kholkin, M. Wojtaś, M. Gregor, A. Gandhi, Y. Wang, S. Bauer, M. Krause, and A. Plecenik, Scientific Reports **3**, 1 (2013).
[281] C. Daish, R. Blanchard, K. Fox, P. Pivonka, and E. Pirogova, Annals of Biomedical Engineering **46**, 525 (2018).
[282] M. Hartig, U. Joos, and H.-P. Wiesmann, European Biophysics Journal **29**, 499 (2000).
[283] L. Xia, Y. Xie, B. Fang, X. Wang, and K. Lin, Chemical Engineering Journal **347**, 711 (2018).
[284] N. W. Hrabe, P. Heinl, B. Flinn, C. Körner, and R. K. Bordia, Journal of Biomedical Materials Research Part B: Applied Biomaterials **99**, 313 (2011).
[285] M. M. Bilek, Applied Surface Science **310**, 3 (2014).
[286] P. Hameed, V. Gopal, S. Bjorklund, A. Ganvir, D. Sen, N. Markocsan, and G. Manivasagam, Colloids and Surfaces B: Biointerfaces **173**, 806 (2019).
[287] J. Xie, J. Hu, L. Fang, X. Liao, R. Du, F. Wu, and L. Wu, Surface and Coatings

Technology **384**, 125223 (2020).
[288] R. Behera, A. Das, A. Hasan, D. Pamu, L. Pandey, and M. Sankar, Materials Science and Engineering: C **114**, 111033 (2020).
[289] A. Hasan and L. M. Pandey, Applied Surface Science **505**, 144611 (2020).
[290] E. Barua, A. B. Deoghare, S. Chatterjee, and P. Sapkal, Ceramics International **45**, 20331 (2019).
[291] R. Nawang, M. Z. Hussein, K. A. Matori, C. A. C. Abdullah, and M. Hashim, Results in Physics **15**, 102540 (2019).
[292] B. Basu, S. K. Swain, and D. Sarkar, RSC Advances **3**, 14622 (2013).
[293] K. Zhang, Y. Fan, N. Dunne, and X. Li, Regenerative Biomaterials **5**, 115 (2018).
[294] S. Vohra, K. M. Hennessy, A. A. Sawyer, Y. Zhuo, and S. L. Bellis, Journal of Materials Science: Materials in Medicine **19**, 3567 (2008).
[295] S. Staehlke, H. Rebl, and B. Nebe, Cell Biology International **43**, 22 (2019).
[296] L. Saldaña, F. Bensiamar, A. Boré, and N. Vilaboa, Acta Biomaterialia **7**, 4210 (2011).
[297] E. M. Czekanska, M. J. Stoddart, J. R. Ralphs, R. Richards, and J. Hayes, Journal of Biomedical Materials Research Part A **102**, 2636 (2014).
[298] S. Pattipaka, A. Joseph, G. P. Bharti, K. J. Raju, A. Khare, and D. Pamu, Applied Surface Science **488**, 391 (2019).
[299] I. Chang, S. Woo, M. H. Lee, J. H. Shim, Y. Piao, and S. W. Cha, Applied Surface Science **282**, 463 (2013).
[300] S. H. Maxian, J. P. Zawadsky, and M. G. Dunn, Journal of Biomedical Materials Research **27**, 111 (1993).
[301] B. K. Sarma, P. Barman, B. Sarma, A. Das, and A. R. Pal, Materials Letters **185**, 387 (2016).
[302] A. Bigi, E. Boanini, B. Bracci, A. Facchini, S. Panzavolta, F. Segatti, and L. Sturba, Biomaterials **26**, 4085 (2005).
[303] Z. Li, L. Yubao, Z. Yi, W. Lan, and J. A. Jansen, Journal of Biomedical Materials Research Part A **93**, 269 (2010).
[304] M. M. Gentleman and E. Gentleman, International Materials Reviews **59**, 417 (2014).
[305] K. Cai, J. Bossert, and K. D. Jandt, Colloids and Surfaces B: Biointerfaces **49**, 136 (2006).
[306] M. Padial-Molina, P. Galindo-Moreno, J. Emilio Fernández-Barbero, F. O'Valle, A. Belén Jódar-Reyes, J. Luis Ortega-Vinuesa, and P. J. Ramón-Torregrosa, Acta Biomateralia **7**, 771 (2011).
[307] T. Sawase, R. Jimbo, K. Baba, Y. Shibata, T. Ikeda, and M. Atsuta, Clinical Oral Implants Research **19**, 491 (2008).
[308] F. Kremer and A. Schönhals, in *Broadband Dielectric Spectroscopy* (Springer, 2003) pp. 99–129.
[309] A. Opitz, A. Falchier, C.-G. Yan, E. M. Yeagle, G. S. Linn, P. Megevand,

A. Thielscher, R. Deborah A, M. P. Milham, A. D. Mehta, and C. E. Schroeder, Scientific Reports **6**, 1 (2016).
[310] M. Abazari and A. Safari, Applied Physics Letters **97**, 262902 (2010).
[311] V. Khopkar and B. Sahoo, Physical Chemistry Chemical Physics **22**, 2986 (2020).
[312] L. Wang, W. Ren, P. Shi, and X. Wu, Journal of Applied Physics **115**, 034103 (2014).
[313] S. J. Novick and J. S. Dordick, Biomaterials **23**, 441 (2002).
[314] L. Jeurgens, W. Sloof, F. Tichelaar, and E. Mittemeijer, Physical Review B **62**, 4707 (2000).
[315] B. Wang, Q. Lin, C. Shen, J. Tang, Y. Han, and H. Chen, Journal of Colloid and Interface science **431**, 1 (2014).
[316] W.-J. Lee, H.-G. Kim, and S.-G. Yoon, Journal of Applied Physics **80**, 5891 (1996).
[317] K. P. Surendran, A. Wu, P. M. Vilarinho, and V. M. Ferreira, Journal of Applied Physics **107**, 114112 (2010).
[318] R. K. Aaron, D. M. Ciombor, and B. J. Simon, Clinical Orthopaedics and Related Research (1976-2007) **419**, 21 (2004).

# Vita

Mr. Apurba Das was born and brought up in Guwahati, Assam. He completed his graduation with Physics Honours in 2013 from Cotton College, affiliated to Gauhati University, Assam. Thereafter, he obtained a postgraduate degree in Physics from Gauhati University, Assam in 2015. Subsequently, he had enrolled into the Ph.D programme at Indian Institute of Technology Guwahati in 2016 after qualifying the Graduate Aptitude Test in Engineering (GATE). He has earned the Senior Research Fellowship in 2018 by Indian Institute of Technology Guwahati.